

Marc Rüdiger

Analysis and Simulation of Crystalline Silicon Solar Cells

Fraunhofer-Institut für
Solare Energiesysteme ISE

Analysis and Simulation of Crystalline Silicon Solar Cells

Marc Rüdiger

FRAUNHOFER VERLAG

Kontakt:

Fraunhofer-Institut für Solare Energiesysteme ISE
Heidenhofstraße 2
79110 Freiburg
Telefon +49 761/4588-5150
Fax +49 761/4588-9342
E-Mail info@ise.fraunhofer.de
URL www.ise.fraunhofer.de

Bibliografische Information der Deutschen Nationalbibliothek

Die Deutsche Nationalbibliothek verzeichnet diese Publikation in der Deutschen Nationalbibliografie; detaillierte bibliografische Daten sind im Internet über <http://dnb.d-nb.de> abrufbar.
ISBN (Print): 978-3-8396-0638-4

D 352

Zugl.: Konstanz, Univ., Diss., 2013

Druck: Mediendienstleistungen des
Fraunhofer-Informationszentrum Raum und Bau IRB, Stuttgart

Für den Druck des Buches wurde chlor- und säurefreies Papier verwendet.

© by **FRAUNHOFER VERLAG**, 2013

Fraunhofer-Informationszentrum Raum und Bau IRB
Postfach 80 04 69, 70504 Stuttgart
Nobelstraße 12, 70569 Stuttgart
Telefon 07 11 9 70-25 00
Telefax 07 11 9 70-25 08
E-Mail verlag@fraunhofer.de
URL <http://verlag.fraunhofer.de>

Alle Rechte vorbehalten

Dieses Werk ist einschließlich aller seiner Teile urheberrechtlich geschützt. Jede Verwertung, die über die engen Grenzen des Urheberrechtsgesetzes hinausgeht, ist ohne schriftliche Zustimmung des Verlages unzulässig und strafbar. Dies gilt insbesondere für Vervielfältigungen, Übersetzungen, Mikroverfilmungen sowie die Speicherung in elektronischen Systemen.

Die Wiedergabe von Warenbezeichnungen und Handelsnamen in diesem Buch berechtigt nicht zu der Annahme, dass solche Bezeichnungen im Sinne der Warenzeichen- und Markenschutz-Gesetzgebung als frei zu betrachten wären und deshalb von jedermann benutzt werden dürften.

Soweit in diesem Werk direkt oder indirekt auf Gesetze, Vorschriften oder Richtlinien (z.B. DIN, VDI) Bezug genommen oder aus ihnen zitiert worden ist, kann der Verlag keine Gewähr für Richtigkeit, Vollständigkeit oder Aktualität übernehmen.

Analysis and Simulation of Crystalline Silicon Solar Cells

Dissertation

zur Erlangung des akademischen Grades
eines Doktors der Naturwissenschaften (Dr. rer. nat.)

an der Universität Konstanz
Mathematisch-Naturwissenschaftliche Sektion
Physik

vorgelegt von

Marc Rüdiger

durchgeführt am

Fraunhofer Institut für Solare Energiesysteme ISE
Freiburg im Breisgau

Tag der mündlichen Prüfung: 15. April 2013

1. Referent: Prof. Dr. Gerhard Willeke
2. Referent: Prof. Dr. Thomas Dekorsy

To Carla and Mila

Table of contents

Table of contents	i
1 Introduction.....	1
1.1 Motivation	1
1.2 Silicon solar cell concepts in production and their restrictions.....	2
1.3 Thesis outline.....	6
2 Physical background of charge carriers in silicon	9
2.1 Band structure of semiconductor material.....	9
2.2 Charge carrier densities in silicon	11
2.3 Carrier transport of electrons and holes.....	15
2.4 Generation and recombination of excess carriers.....	16
2.5 Recombination mechanisms	17
2.5.1 Radiative recombination	18
2.5.2 Auger recombination	18
2.5.3 Bulk defect recombination.....	19
2.5.4 Surface recombination	22
2.6 Free carrier absorption.....	23
3 Simulation of crystalline silicon solar cells	27
3.1 Solar cell parameters	27
3.2 Analytical approach: one- and two-diode model.....	28
3.3 Numerical simulation	30
3.4 Optical simulation	32
3.4.1 Transfer matrix method for computing optically thin layers.....	33
3.4.2 Modeling of rear side reflectance properties	34
3.5 Electrical simulation.....	39
3.5.1 Surface recombination velocity S_0 of Al_2O_3 passivated silicon interfaces	41
3.5.2 From injection dependent lifetime to solar cell parameters.....	44

4	Free carrier absorption models for silicon solar cell applications.....	49
4.1	Motivation.....	49
4.2	Sample preparation.....	50
4.3	Simulation setup.....	51
4.4	Comparison of existing parameterizations.....	52
4.4.1	Free carrier absorption in boron doped regions.....	53
4.4.2	Free carrier absorption in phosphorus doped regions.....	55
4.5	Discussion.....	56
4.6	Conclusions.....	61
5	Numerical description of highly aluminum-doped silicon.....	63
5.1	Introduction.....	63
5.2	Electric properties of aluminum in silicon.....	64
5.3	Experimental results.....	65
5.4	Simulations.....	66
5.4.1	Influence of Auger recombination.....	68
5.4.2	Influence of defect recombination.....	69
5.4.3	Influence of lateral doping inhomogeneities.....	72
5.4.4	Influence of incomplete ionization of aluminum acceptor atoms.....	73
5.4.5	Discussion.....	76
5.5	Conclusions.....	77
6	<i>n</i> -type silicon solar cells with aluminum-doped rear p^+ emitter.....	79
6.1	Introduction.....	79
6.2	Comparison: experiment and simulation.....	80
6.2.1	Calibration of numerical simulations.....	80
6.2.2	Parameters.....	83
6.3	Analysis of phosphorus n^+ front surface field.....	85
6.4	Influence of <i>n</i> -type Si bulk and front contact finger distance.....	87
6.5	Analysis of aluminum p^+ rear emitter.....	92
6.6	Conclusions.....	95

7	Lateral conductance effects of locally contacted rear surface passivated silicon solar cells	97
7.1	PERC structure on <i>p</i> -type silicon featuring laser-fired contacts	97
7.1.1	Simulation setup.....	98
7.1.2	Optimum rear contact distance L_p	100
7.1.3	Current density-voltage behavior.....	102
7.2	Consideration of global bulk effects.....	105
7.2.1	Modeling of lumped series resistance losses	105
7.2.2	High level injection effects	107
7.3	Consideration of local bulk effects.....	109
7.4	Recombination losses in the bulk material.....	115
7.5	Optimization of analytical modeling	116
7.5.1	Comparison of analytical and numerical modeling	117
7.5.2	High level injection effects in analytical modeling	119
7.5.3	Injection dependent analytical simulation results	122
7.6	Conclusions	124
8	Bifacial <i>n</i> -type silicon solar cells for upconversion applications	127
8.1	Introduction	127
8.2	Optimizing the solar cell structure using simulation models	131
8.2.1	Solar cell simulation model	131
8.2.2	Modeling the impact of upconversion onto the solar cell performance	131
8.2.3	Optimization of anti-reflection coatings	135
8.2.4	Assessment of efficiency potential	141
8.3	Fabrication of bifacial solar cells	144
8.3.1	Fabrication parameters.....	144
8.3.2	Measurement results	148
8.4	Measurements of bifacial solar cells with upconverter	150
8.4.1	Method to determine the external quantum efficiency of the system of solar cell and upconverter.....	150

8.4.2	Used upconverter samples and optical coupling with solar cell	152
8.4.3	Results	154
8.5	Conclusions.....	157
9	Conclusions and outlook	159
10	Bibliography.....	163
11	Appendix	181
11.1	Abbreviations.....	181
11.2	Glossary	184
11.3	Physical constants	191
12	List of publications.....	193
12.1	Refereed journal papers	193
12.2	Refereed papers presented at international conferences	195
12.3	Diploma thesis	198
13	Deutsche Zusammenfassung und Ausblick.....	199
	Danksagung	205

1 Introduction

1.1 Motivation

Since the beginning of the industrial revolution, the environment has been changed massively. The Intergovernmental Panel on Climate Change IPCC declared in its report in 2007 [1] as a scientific and diplomatic consensus that global warming of the past 50 years might be caused predominantly by the humankind. But it might be possible that the temperature increase before 1956 is caused by changes of the solar irradiation and recent changes might be substantially influenced as well by natural sources.

Nowadays, even former skeptics of climate change, like Prof. R. Muller from Berkeley University/California, go a step further and confirm that humankind is nearly the only reason for global warming. As a result of his “Berkeley Earth Surface Temperature Project”, the temperature increase (shown in Fig. 1.1) is clearly related to the fingerprints of carbondioxide and volcanic activities (which can influence the global temperature temporarily due to fine particles in the atmosphere), but cannot be correlated to changes of the solar irradiation [2, 3].

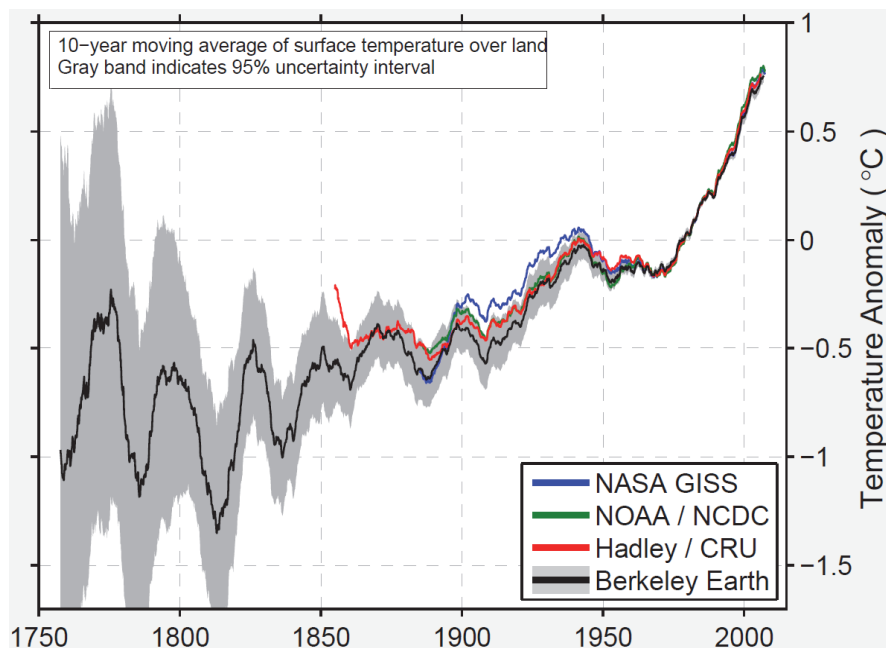


Fig. 1.1: Decadal land-surface average temperature. The results of the recently published data of the “Berkeley Earth Surface Temperature Project” [2, 3] confirm previously published climate data [4-7]. Results show that the average temperature of the earth surface increased by about $\Delta T = 1.5^{\circ}\text{C}$ during the past 250 years. This includes an increase of 0.9°C in the past 50 years. The graph has been taken from [2].

In order to achieve the goal, defined by the IPCC in 2001 [8], to limit global warming to 2°C in order to avoid serious consequences for the humankind, it is necessary to drastically reduce carbon dioxide emissions. On base of a special report of the German Advisory Council on Global Change WBGU [9] it is necessary to reduce the emissions that much that from 2050 nearly no further carbon dioxide should reach the atmosphere. Currently, around 40% of the world's greenhouse gas emissions trace back to the electricity generation from fossil fuels. Therefore, it is indispensable to massively expand electricity generation by renewable energy sources such as wind, hydro and solar energy in order to achieve a well-balanced energy mix, not restricted by any limited resources. In addition, storage technologies like e.g. storage pools or underground hydrogen/methane storages need to be established in order to regulate natural generation fluctuations caused by the fluctuating availability of renewable energies and, thus, to guarantee security of power supply.

Due to its nearly unlimited potential [10], photovoltaic solar energy will play a major role in the transformation process towards a renewable energy supply. Photovoltaics allows the direct conversion of solar energy into electricity. Its area of application ranges from mini-solutions like e.g. cell phone chargers over autonomous one household power supplies and mini-grids to smart-grids and power stations in the megawatt range, providing energy for thousands of households.

The market share of silicon (Si) based mono- and multicrystalline solar cells in comparison to other materials used for solar cell production remains high, due to the broad availability of the feedstock, technically relatively mature industrial processes and a tough competition on the market. A brief overview of actual Si solar concepts implemented in industrial production and its main physical loss mechanisms is given in the following chapter. The results are published in [11].

1.2 Silicon solar cell concepts in production and their restrictions

To make photovoltaic electricity more competitive on the market against the production of electricity via conventional energy sources, it is crucial to drive down their costs per generated power unit. On technological level this can be achieved by decreasing the costs in the production chain or by increasing the solar cell efficiency (by maintaining the same production costs) in order to find the economic optimum of process costs and efficiency. The cost aspect of solar cell production might be subject elsewhere. Here, the focus is set on the efficiency potential of different solar cell

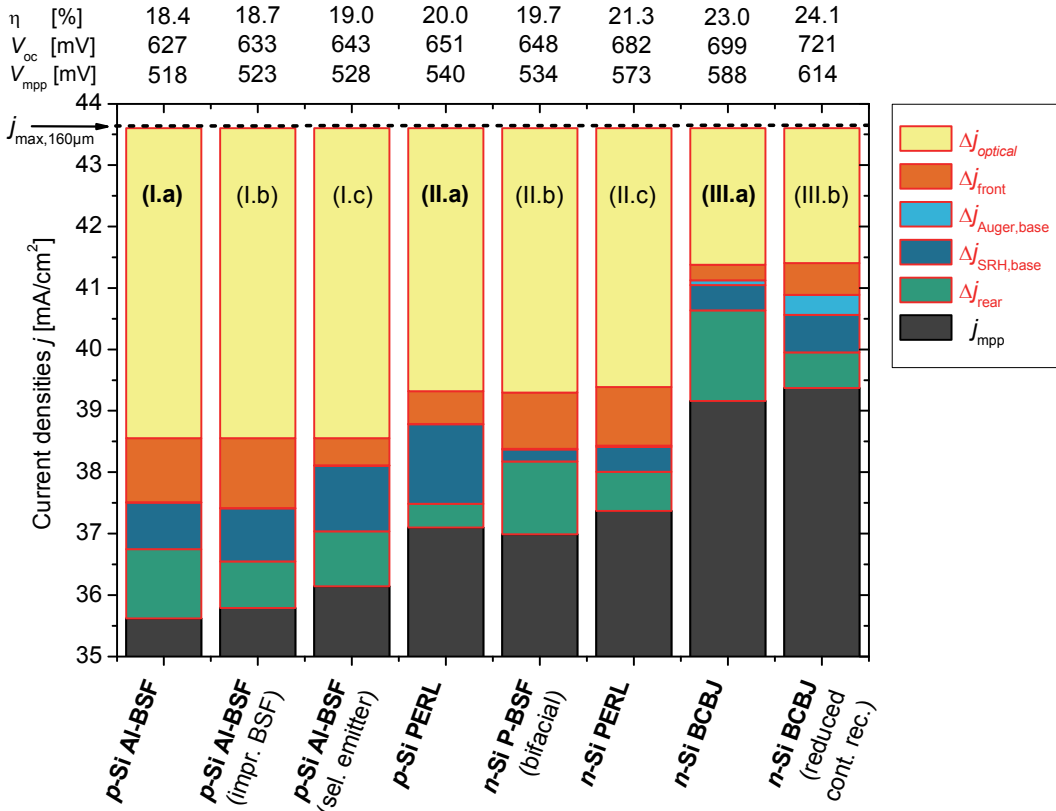


Fig. 1.2: Overview of the current density losses Δj of several Si solar cell concepts in industrial production. Δj is separated in optical and electrical losses, latter separated in recombination losses occurring in the front region, in the base or in the rear region of the device. j_{mpp} denotes the usable current density under operating conditions.

structures. Thereby, it is important to analyze the loss mechanisms of each solar cell concept and to be aware of their main losses in order to identify the certain efficiency restrictions. In the following, a rough overview of selected industrially relevant Si solar cell concepts and their main current loss mechanisms is given, calculated in the context of this work, without claiming to provide completeness.

In Fig. 1.2, the numerically calculated usable current density j_{mpp} under operating conditions (mpp for “maximum power point”) of each considered solar cell concept is shown by the lowermost part of the columns (dark grey), followed by the occurring current density losses Δj (framed in red). The numerical calculations of the devices are based on a consistent set of parameters, allowing a comparison of the structures. To handle the complexity of the considered structures and to describe them accurately including high injection and lateral conductance effects, 2D and 3D simulations are necessary, which are performed with Sentaurus Device [12]. In order to evaluate the occurring Δj , respectively, it is convenient to separate the loss channels concerning optical losses $\Delta j_{optical}$ and losses occurring at the front side Δj_{front} (contacts, surfaces

and losses occurring in the front diffusions), in the base material Δj_{base} and at the rear side Δj_{rear} (contact, surfaces and losses occurring in the rear diffusions) of the solar cell. The corresponding recombination currents are spatially integrated. The base current density losses are further separated into losses occurring by defect recombination $\Delta j_{\text{SRH,base}}$ (also called SRH for ‘‘Shockley-Read-Hall’’ recombination; see Chap. 2.5.3) and by Auger recombination $\Delta j_{\text{Auger,base}}$ (see Chap. 2.5.2). $j_{\text{max},160\mu\text{m}} = 43.6 \text{ mA/cm}^2$ denotes the theoretical current density maximum for a $160 \mu\text{m}$ thick wafer featuring Lambertian light trapping [13]. $160 \mu\text{m}$ is the base thickness used for all considered structures in Fig. 1.2. The optical losses $\Delta j_{\text{optical}} = j_{\text{max},160\mu\text{m}} - j_{\text{gen}}$ are defined as the difference of this theoretical maximum and the actually generated photo-current density j_{gen} within the corresponding device, featuring the main loss mechanism (Fig. 1.2, uppermost yellow part of the columns). Resistive losses are taken into account, but are not separately shown. The mentioned physical parameters as well as the efficiency η , the open-circuit voltage V_{oc} and the voltage V_{mpp} under operating conditions are introduced in detail in Chap. 2 and 3.

The denotation of the cell structures in Fig. 1.2 and Fig. 1.3 is consistent. Structures denoted with b or c in Fig. 1.2 differ only marginally from the corresponding structures with the same Roman numeral illustrated in Fig. 1.3. The solar cell structure (I.a) represents a Czochralski (Cz) grown low-cost p -Si solar cell with screen-printed front side contacts and full-area Al-BSF and full-area rear contact. In order to decrease the rather high rear recombination (Fig. 1.2, (I.a), green), the applied Al paste might be improved [14, 15], leading to structure (I.b) in Fig. 1.2. The structure features a decreased Δj_{rear} , but as a consequence of the increased V_{mpp} and more available charge

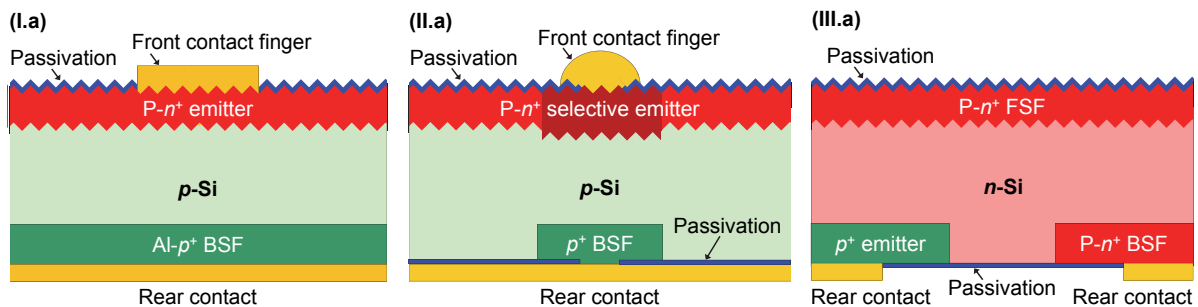


Fig. 1.3: Three exemplary schemata of solar cell concepts in industrial production (shown are the standard domains). (I.a) denotes a standard monocrystalline p -Si solar cell with screen-printed front side contact fingers, single front side emitter, full-area Al- p^+ back surface field (BSF) and full-area rear contact. (II.a) features optimized front contact fingers, a selective front emitter, local p^+ BSF with a passivated rear side and local rear contact openings, commonly known as PERL structure. In (III.a), a back-contact back-junction Si solar cell concept with full-area front surface field (FSF) is shown.

carriers in the bulk (due to the decreased rear recombination), the recombination losses at the front and in the base increase. The dominating electrical recombination loss remains in the front region, i.e. emitter, due to a high doping concentration in this area of the solar cell and an insufficient surface passivation in (I.b). By front metal pastes which are able to contact lowly doped emitters [16] or by introducing a selective emitter featuring a decreased doping concentration below the front passivation to achieve an improved blue response and a high doping concentration below the front contacts, the emitter recombination can be reduced (Fig. 1.2, (I.c)). A strong reduction of Δj_{front} (orange) is observed, while the base (blue) and rear (green) recombination losses increase. A good overview of the manifold selective emitter technologies for the realization of selective emitters is given in [17].

Concepts featuring dielectric rear side passivation [18-21], as shown in Fig. 1.3 (II.a), feature a significantly reduced rear side recombination and better internal reflectance properties, leading to a reduced $\Delta j_{\text{optical}}$. A loss recombination analysis of such a *p*-Si PERL solar cell approach is shown in Fig. 1.2 (II.a). Here, as recombination losses at the front and at the rear are already relatively low, the base dominates the recombination. The material quality of industrially used boron-doped Cz *p*-Si is limited by light-induced degradation, caused by metastable BO-complexes [22, 23]. The efficiency values shown for all *p*-Si solar cells in Fig. 1.2 represent the solar cell in a fully degraded state, i.e. fully activated BO-complex. Recombination losses might be further decreased by a reduction of the interstitial oxygen concentration $[O_i]$ or by substituting the B by e.g. P, as phosphorus-doped *n*-Si is not affected by such degradation effects. The loss analysis of a bifacial *n*-Si solar cell concept [24] featuring a full-area B- p^+ emitter and a full-area P- n^+ BSF is shown in Fig. 1.2 (II.b), featuring a strong reduction of $\Delta j_{\text{SRH,base}}$. Due to the significantly enhanced carrier lifetimes of *n*-Si Cz bulk material (compared to fully degraded *p*-Si Cz), the B emitter might be placed as well on the rear side of the solar cell, as reported in [25, 26]. Compared to full-area BSFs, local BSFs above the rear contacts of *n*-Si PERL solar cells [27-29] reduce the rear side recombination, as shown in Fig. 1.2 (II.c), leading to a significant increase in V_{oc} . Structure (II.c) features relatively low recombination losses in all three considered regions (front, base and rear) of the solar cell, but not at least due to shading losses, caused by the front metal fingers and busbars, a significant optical current density loss remains.

A further significant decrease of the optical losses and, thus, a step towards higher solar cell efficiencies, can be achieved by transferring all contacted areas to the rear side of the solar cell, avoiding front side metal shading losses. Such a back-contact back-junction (BCBJ) *n*-Si solar cell concept [30] is exemplarily shown in Fig. 1.3

(III.a); the corresponding loss analysis can be seen in Fig. 1.2 (III.a). Here, Auger recombination in the base region starts to play a role. Actual activities on BCBJ solar cells are reported in [31-33]. As the bulk and surface recombination losses are already significantly reduced, especially the contact recombination becomes a dominating loss mechanism in this structure. Thus, a modified rear side geometry might decrease electrical shading losses [34], due to decreased lateral diffusion paths, leading to increased short-circuit current densities. A reduced contact recombination, as also achieved with heterojunction solar cells [35], might lead to V_{oc} values far beyond 700 mV [36, 37].

To further reduce the optical losses and, thus, to increase the efficiency, the absorption of long-wavelength light has to be increased. This could be achieved e.g. by a diffractive rear side structure, which reflects light, impinging on the rear side of the solar cell. The light is reflected under a very small angle (i.e. nearly parallel to the solar cell surface) in order to enhance the optical path length of the light within the solar cell and, thus, the absorption probability [38, 39]. Using all these presented features, efficiencies up to 26% are technologically achievable with silicon solar cells [40].

1.3 Thesis outline

Chapter 2 deals with the physical basics of interest for the presented work. A precise description of the charge carrier densities, which depend on the doping concentration, temperature, and illumination of the sample, is given. The mechanisms of excess carrier recombination are described in detail. Furthermore, free carrier absorption and existing parameterizations given in literature are presented, which play a major role in Chap. 4.

Chapter 3 introduces the main concepts of the simulation of crystalline silicon solar cells. The analytical approach of the one- and two-diode model and the tools for advanced 2D and 3D numerical simulation are given. Therefore, the model basis used for the numerical calculations in this work is presented and the diversity of numerical modeling is supported by examples for optical and electrical simulations.

Chapter 4 is concerned with free carrier absorption, a parasitic absorption process which might reduce significantly the incident usable photon flux in highly doped silicon. Existing parameterizations, mostly set up on the base of data in the mid-wavelength infrared, are evaluated in the wavelength range $\lambda = 1.0 - 2.0 \mu\text{m}$, including the relevant range for silicon solar cells. It turns out that the existing models show in

this wavelength range significant deviations. Thus, new parameters are presented in order to enhance the quantification of photogeneration losses.

In *Chapter 5*, an advanced method for precise modeling of highly aluminum-doped p^+ silicon is presented, leading to excellent agreement of numerical and experimental data within a broad range. The influence of different recombination mechanisms on the saturation current densities of aluminum-doped silicon surfaces for different aluminum profiles is analyzed. It is demonstrated that incomplete ionization affects the profile characteristics significantly and, therefore, has to be accounted for in accurate modeling of highly aluminum-doped silicon.

On base of the method developed in Chap. 5, a detailed analysis on the optimization of n -type silicon solar cells with Al-alloyed rear p^+ emitter for industrial applications by means of 2D and 3D numerical simulation is presented in *Chapter 6* in order to identify the potential and the limiting factors of this cell concept. This solar cell concept combines well known low cost process steps of standard silicon solar cells (see Fig. 1.2 (I.a-c)) with the benefit of n -type silicon bulk material featuring significantly reduced base recombination losses.

Chapter 7 focuses on lateral conductance effects of locally contacted rear surface passivated silicon solar cell concepts. Such effects need to be investigated in most cases via 3D numerical simulations, as charge carrier might pass lateral distances in the range of millimeters. Calculations of p -type silicon solar cell structures are presented, focusing on the optimum rear contact distances. High injection effects of solar cells featuring highly resistive base material are discussed, which have a strong impact on their performance. Furthermore, an existing analytical model for optimum rear contact distance calculations is extended in order to account for these high injection effects.

Chapter 8 is concerned with the optimization of bifacial n -type silicon solar cells for upconversion applications. Anti-reflection layer systems are numerically defined in order to fulfill the specific requirements of the setup. Based on the calculation results, solar cells were fabricated and quantum efficiency measurements of a system consisting of a solar cell and a prototype erbium based upconverter could be established, exceeding previously published results, with respect to the illumination intensity.

Chapters 9 finally summarizes this work and gives an outlook, which challenges still have to be faced.

2 Physical background of charge carriers in silicon

In this chapter the fundamentals of semiconductor physics are briefly introduced. The focus is set on carrier transport of electrons and holes and the different recombination mechanisms in semiconductors. Additionally, free carrier absorption and existing parameterizations given in literature are presented. Further details may be found for example in [41-43].

2.1 Band structure of semiconductor material

The free electron model in solid state physics provides an insight e.g. in the electrodynamic properties, thermal capacity and thermal and electrical conductivity of metals, but needs to be extended for the explanation of the differences of metals, semiconductors and insulators. Whereas the electrical resistance of pure metals can hold $\rho = 10^{-10} \Omega\text{cm}$ at very low temperatures, pure insulators feature resistances up to $\rho = 10^{22} \Omega\text{cm}$. The specific resistance of semiconductors is ranged between these values and depends on the influence of external parameters like temperature or magnetic field.

For the electrical conductivity it is important to know how electrons respond to an applied electric field. Electrons within a crystalline structure are arranged in energy bands, which are separated by so-called *band gaps*, which can be seen in Fig. 2.1.

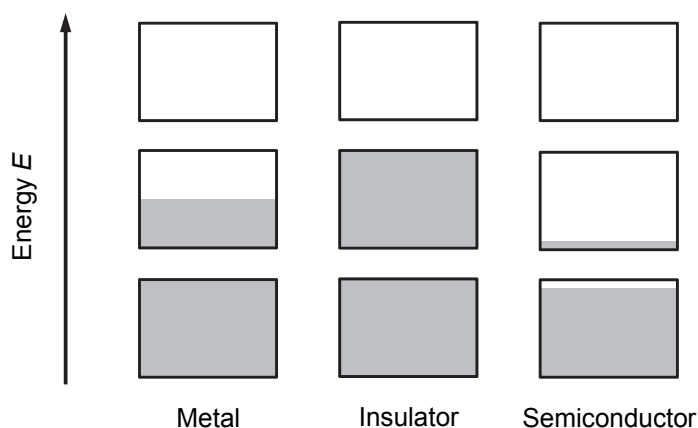


Fig. 2.1: Schematic of the occupation of allowed energy states of electrons for metal, insulator and semiconductor. The vertical extension of the rectangles marks the allowed energy states, the shaded areas the with electrons occupied states. A semiconductor (like silicon) becomes an insulator at $T = 0 \text{ K}$. Above this temperature, a certain amount of charge carriers is thermally excited.

Within these band gaps energy states are forbidden due to the interaction within the wave functions of conduction electrons and the ionic structure of the lattice atoms. If the allowed energy bands are fully occupied or empty the crystal acts as an insulator because electrons cannot move under the influence of an electric field. Typical band gap energies within the highest fully occupied energy band (valence band) and the lowest unoccupied energy band (conduction band) are in the range of several electron volts (eV). The crystal behaves like a metal, if one or more bands are partially occupied, approximately between 10 and 90%. A semiconductor behaves like an insulator at $T = 0$ K, but becomes conductive under excitation. Its band gap energy $E_g = E_C - E_V$, the difference of the lowest energy in the conduction band E_C and the highest energy within the valence band E_V , is temperature dependent and normally given in units of electron volts (eV).

For crystalline silicon (c-Si), the wave vectors of the maximum energy of the valence band and the minimum energy of the conduction band do not match in phase space, as shown in Fig. 2.2, which is characteristic for an indirect semiconductor.

The temperature-dependence of the band gap energy E_g in Si can be expressed by the parameterization [44]

$$E_g(T) = E_{g,0} - \frac{\alpha T^2}{\beta + T}, \quad (2.1)$$

with $E_{g,0} = 1.175$ eV at a temperature $T = 0$ K, $\alpha = 4.73 \times 10^{-4}$ eV/K and $\beta = 636$ K.

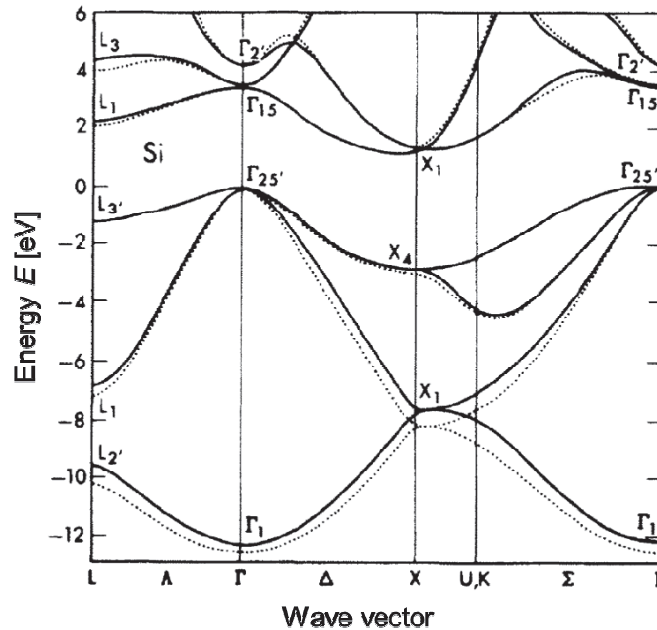


Fig. 2.2: Band structure for crystalline silicon, calculated with the non-local (solid) and the local (dashed) pseudo potential method, respectively. From Ref. [45].

2.2 Charge carrier densities in silicon

The densities of electrons in the conduction band dn and holes in the valence band dp , respectively, with the energy E in the energy interval dE are derived by the density of states $D_{C/V}$ and the occupation probability $f(E)$ to

$$\begin{aligned} dn(E) &= D_C(E)f(E)dE \\ dp(E) &= D_V(E)(1-f(E))dE \end{aligned} \quad (2.2)$$

As electrons are fermions, their probability $f(E)$ is given by the Fermi-Dirac distribution function

$$f(E) = \frac{1}{1 + \exp\left(\frac{E - E_F}{k_B T}\right)} \quad (2.3)$$

k_B denotes the Boltzmann constant and T the absolute Temperature. The Fermi energy E_F is also referred to as electro-chemical potential η_e , as it can be describes as well as sum of the chemical potential μ_e and the electrical energy $-e\phi$:

$$E_F = \eta_e = \mu_e - e\phi \quad (2.4)$$

The densities of allowed states in the valence band D_V and in the conduction band D_C are given by

$$\begin{aligned} D_V(E) &\propto (m_h^*)^{3/2} (E_V - E)^{1/2} \\ D_C(E) &\propto (m_e^*)^{3/2} (E - E_C)^{1/2} \end{aligned} \quad (2.5)$$

with the effective masses of electrons m_e^* and holes m_h^* , respectively.

An integration over the energy intervals shown in Eq. (2.2) lead to the sum of the electrons per volume element in the conduction band and the sum of the holes per volume element in the valence band,

$$n = \int_{E_C}^{\infty} D_C(E)f(E)dE \quad \text{and} \quad p = \int_0^{E_V} D_V(E)(1-f(E))dE \quad (2.6)$$

This expression can be approximated for non-degenerated semiconductors with $E_C - E_F \gg k_B T$ and $E_F - E_V \gg k_B T$ by the Boltzmann distribution. Thus, Eq. (2.6) simplifies to

$$n_0 = N_C \exp\left(-\frac{E_C - E_F}{k_B T}\right) \quad \text{and} \quad p_0 = N_V \exp\left(-\frac{E_F - E_V}{k_B T}\right) \quad (2.7)$$

in thermal equilibrium. n_0 denotes the equilibrium electron concentration in the conduction band, p_0 the equilibrium hole concentration in the valence band and N_C and N_V the effective densities of states in the conduction band and the valence band, respectively. With the temperature-dependence of the effective masses of electrons and holes, the effective densities of states can be written as [44]

$$N_{C/V}(T, m_{e/h}^*(T)) = 2 \left(2\pi m_{e/h}^* k_B T / h^2\right)^{3/2}, \quad (2.8)$$

where h is the Planck's constant. The density-of-states effective electron mass

$$m_e^* = 6^{2/3} \left(m_t^{*2} m_l^*\right)^{1/3} \quad \text{with} \quad m_l^* = 0.9163 m_0 \quad (2.9)$$

contains the transversal and longitudinal effective electron masses m_t^* and m_l^* and the equivalent conduction band minima [44, 46]. In silicon, m_t^* is best described by the temperature of the energy gap [46]:

$$\frac{m_t^*(T)}{m_0} = 0.1905 \frac{E_{g,0}}{E_g(T)}. \quad (2.10)$$

The product of the equilibrium concentrations introduced in Eq. (2.7) defines the intrinsic carrier concentration n_i , which remains independent of the Fermi energy E_F :

$$n_i \equiv \sqrt{n_0 p_0} = \sqrt{N_C N_V} \exp\left(-\frac{E_g}{2k_B T}\right). \quad (2.11)$$

At $T = 300$ K a commonly used value is $n_i = 1.0 \times 10^{10} \text{ cm}^{-3}$ [47], which has been determined without taking band gap narrowing in the experiment into account [48]. Thus, the data have been reinterpreted by Altermatt *et al.* and revised to $n_i = 9.65 \times 10^9 \text{ cm}^{-3}$ [48]. Latter value is used in this work.

The effect of band gap narrowing [49] has to be accounted for especially at high injection and high doping densities, which leads to a reduction of the band gap E_{bgn} , resulting in an effective intrinsic carrier concentration

$$n_{i,\text{eff}} = n_i \exp\left(\frac{E_{\text{bgn}}}{2k_B T}\right). \quad (2.12)$$

For an undoped *intrinsic* semiconductor, the electron density in the conduction band equals the hole density in the valence band and, thus, for the Fermi energy follows:

$$E_F \equiv E_i = \frac{E_C + E_V}{2} + \frac{k_B T}{2} \ln\left(\frac{N_V}{N_C}\right) . \quad (2.13)$$

E_i is commonly used as the energy level in an intrinsic semiconductor.

In case of an *extrinsic* semiconductor, some lattice atoms are substituted by in general group III or V elements of the periodic table in case of Si as group IV element. These so-called *dopants* with relatively low concentrations of 0.1 to 100 ppm in comparison to the base material, influences significantly its electrical conductivity.

Group V elements such as phosphorus (P) feature an additional valence electron, which is not in a covalent bond to a neighbor atom. Only a small amount of energy in the range of several meV is required to release these extra electrons from its bonding and shift it into the conduction band and become unbounded from individual atoms, contributing to the electrical conductivity. Group V dopants in Si behave like electron donors, forming an *n*-type semiconductor.

Doping with group III elements, where the fourth valence electron is missing, creates a so-called *hole* in the Si lattice, which can be easily shifted to the valence band. They behave as acceptors, resulting in a *p*-type semiconductor. At room temperature nearly all dopant atoms are ionized, contributing to the electrical conductivity.

Thus, the doping concentration N_{dop} is several orders of magnitude larger, compared to the intrinsic carrier concentration n_i , resulting in a classification of the electrons and holes into *majority* and *minority* charge carriers (see Eq. (2.11)). Assuming a negligible contribution of the intrinsic carriers to the majority carrier concentration and complete ionization of all dopant atoms, nearly always the case at $T = 300$ K, it follows:

$$\begin{aligned} p_0 = N_A \quad \text{and} \quad n_0 = \frac{n_i^2}{N_A} \ll p_0 \quad \text{for } p\text{-type Si} \quad , \\ n_0 = N_D \quad \text{and} \quad p_0 = \frac{n_i^2}{N_D} \ll n_0 \quad \text{for } n\text{-type Si} \quad . \end{aligned} \quad (2.14)$$

N_A is the acceptor concentration and N_D the donor concentration, respectively.

Due to the additional charge carriers that doping introduces into the semiconductor, the position of the Fermi level shifts according to

$$\begin{aligned}
E_F &= E_V + k_B T \ln\left(\frac{N_V}{N_A}\right) \quad \text{for } p\text{-type Si} \quad , \\
E_F &= E_C - k_B T \ln\left(\frac{N_C}{N_D}\right) \quad \text{for } n\text{-type Si} \quad ,
\end{aligned}
\tag{2.15}$$

which can be directly derived from Eq. (2.7). Combining this equation with Eq. (2.13), it follows

$$E_F - E_i = \mp \frac{E_g}{2} \pm k_B T \ln\left(\frac{\sqrt{N_C N_V}}{N_{\text{dop}}}\right)
\tag{2.16}$$

for the difference between intrinsic energy level and Fermi energy level. The upper and lower signs hold for p -type and n -type semiconductors, respectively.

Charge neutrality must be always satisfied, regardless of the type of doping:

$$n_0 + N_A = p_0 + N_D \quad .
\tag{2.17}$$

The majority carrier concentration in a doped semiconductor has been considered as temperature-independent in the previous part. This assumption is valid for a large temperature range around room temperature, where the intrinsic carriers have a negligible influence on the overall conduction and all dopant atoms are ionized. However, at sufficient low or high temperatures these assumptions have to be extended.

By illuminating a semiconductor, photons with energies $E_\gamma > E_g$ generate electron hole pairs (see Chap. 2.4). Therefore, the density of electrons and holes, respectively, increase above their values in the dark:

$$n > n_0 \quad \text{and} \quad p > p_0 \quad .
\tag{2.18}$$

To describe at once electron and hole densities in this illuminated state, the Fermi energy E_F splits according to the generalized Planck radiation law into two different so-called Quasi Fermi distributions $E_{F,e}$ and $E_{F,h}$ with its corresponding occupation probabilities f_C and f_V , respectively [50].

Hence, the density of the electrons in the conduction band and the density of the holes in the valence band can be determined according to

$$n = N_C \exp\left(\frac{E_{F,e} - E_C}{k_B T}\right) \quad \text{and} \quad p = N_V \exp\left(\frac{E_V - E_{F,h}}{k_B T}\right) \quad .
\tag{2.19}$$

As a consequence, the product of the electron and hole densities,

$$n p = n_i^2 \exp\left(\frac{E_{F,e} - E_{F,h}}{k_B T}\right) = n_i^2 \exp\left(\frac{\eta}{k_B T}\right) > n_i^2, \quad (2.20)$$

is larger than the square of the intrinsic density n_i . Thereby, $\eta = E_{F,e} - E_{F,h}$ determines the separation of the Quasi Fermi energies.

The electro-chemical potentials, introduced in Eq. (2.4), change to

$$\begin{aligned} \eta_e &= \mu_e - q\phi = \mu_{e,0} + k_B T \ln\left(\frac{n}{N_C}\right) - q\phi = +E_{F,e} \\ \eta_h &= \mu_h + q\phi = \mu_{h,0} + k_B T \ln\left(\frac{p}{N_V}\right) + q\phi = -E_{F,h}, \end{aligned} \quad (2.21)$$

with the chemical potential of the electrons μ_e and of the holes μ_h [51]. Fig. 2.3 illustrates a schematic band diagram of an illuminated semiconductor.

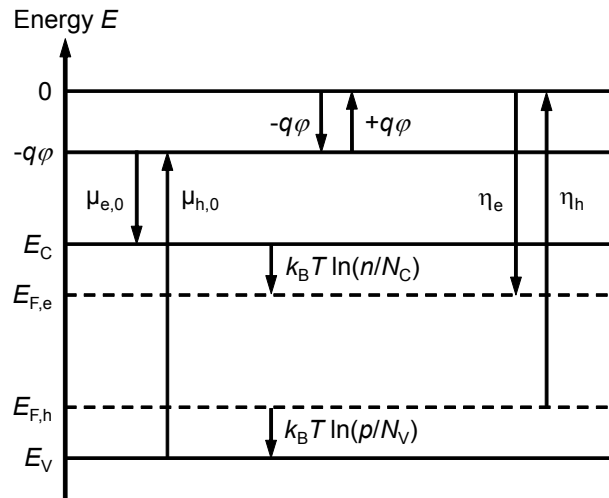


Fig. 2.3: Schematic band diagram of an illuminated semiconductor. $\eta_{e/h}$ denotes the electron chemical potential as sum of the chemical potential $\mu_{e/h}$ and the electric energy $\mp q\phi$ for electrons and holes, respectively.

2.3 Carrier transport of electrons and holes

Three different sets of equations are needed to describe carrier transport in semiconductors.

The electrostatic potential is the solution of the Poisson equation and holds:

$$\Delta\varphi = -\nabla\vec{E} = -\frac{\rho_p}{\varepsilon \cdot \varepsilon_0} \quad . \quad (2.22)$$

Thereby, φ denotes the electrostatic potential, and ε and ε_0 the electrical field constant in a medium and in vacuum, respectively. The relation connects the electric field \vec{E} with the density of volume charge ρ_p :

By the continuity equations for electrons and holes, the time related change in carrier densities is set into relation to the corresponding generation rates $G_{n/p}$ and recombination rates $R_{n/p}$ and the local change of the current densities $j_{n/p}$:

$$\frac{\partial n}{\partial t} = G_n - R_n + \frac{\nabla j_n}{q} \quad \text{and} \quad \frac{\partial p}{\partial t} = G_p - R_p + \frac{\nabla j_p}{q} \quad . \quad (2.23)$$

The mechanisms of carrier generation and recombination are discussed in more detail in Chapter 2.4.

For the drift-diffusion model, the current densities for electrons and holes are given by:

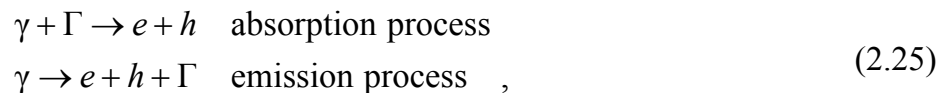
$$j_n = n \cdot \mu_n \cdot \nabla E_{F,e} \quad \text{and} \quad j_p = p \cdot \mu_p \cdot \nabla E_{F,h} \quad , \quad (2.24)$$

where μ_n and μ_p denote the mobilities of the electrons and holes, respectively. It can be seen, that a current only occurs due to a change in the electro chemical potentials, which is important for the understanding of solar cell devices.

2.4 Generation and recombination of excess carriers

By the absorption of photons in semiconductor material, whose energy E_γ is larger than the band gap E_g : $E_\gamma > E_g$, additional electron hole pairs are generated. As silicon is an indirect semiconductor (see Chap. 2.1), an additional phonon is needed for the transition of an electron from the maximum of the valence band to the minimum of the conduction band.

By the absorption of a photon γ , one or more phonons Γ can be absorbed or emitted:



while always energy and momentum conservation holds. Due to this three-particle-process, the absorption coefficient is relative low for indirect semiconductors in comparison to those of direct semiconductors. Also, the absorption around the band gap energy E_g is blurred because of a small, but non-zero energy contribution of the phonons.

The via photon absorption optically generated electron hole pairs are called excess carriers Δn and Δp for electrons and holes, respectively. Thus, the total carrier density is the sum of excess and equilibrium carrier density:

$$n = \Delta n + n_0 \quad \text{and} \quad p = \Delta p + p_0 \quad . \quad (2.26)$$

In a semiconductor with constant optical excitation $G_{\text{illu}} > G_0$ in thermal equilibrium, the generation is counterbalanced by a constant recombination rate $R_{\text{illu}} = G_{\text{illu}} > R_0$. Thereby, G_0 and R_0 indicate the thermal generation and recombination without optical excitation, respectively. Directly after turning-off the external illumination, the excess carriers Δn and Δp recombine subsequently with the net recombination rate $R = R_{\text{illu}} - R_0$, until thermal equilibrium is reached again. With the assumption of charge neutrality and $\Delta n = \Delta p$, which implies the absence of minority carrier trapping centers, the time-dependent decay of the excess carriers is defined by

$$\frac{\partial \Delta n(t)}{\partial t} = -R(\Delta n(t), n_0, p_0) \quad . \quad (2.27)$$

Based on this mathematical expression, the excess carrier lifetime

$$\tau(\Delta n, n_0, p_0) \equiv \frac{\Delta n}{R(\Delta n, n_0, p_0)} \quad (2.28)$$

is defined. The excess carrier lifetime is referred to as minority carrier lifetime.

The total recombination rate R_{total} can be calculated from the sum of the single recombination rates, as the different recombination rates R_i occur independently from each other. Hence, the total excess carrier lifetime τ_{total} results from the inverse sum of the reciprocal carrier lifetimes τ_i :

$$R_{\text{total}} = \sum_i R_i \quad \text{and} \quad \frac{1}{\tau_{\text{total}}} = \sum_i \frac{1}{\tau_i} \quad . \quad (2.29)$$

2.5 Recombination mechanisms

In the following the different recombination channels are introduced, which are relevant for this work. The intrinsic recombination mechanisms, which can be distinguished in radiative and Auger band-to-band recombination, will be described, as well as the extrinsic recombination mechanisms due to defects levels featuring energy levels within the band gap E_g .

2.5.1 Radiative recombination

The radiative recombination is the direct inverse of the optical generation mechanism. An electron from the conduction band and a hole from the valence band recombine directly, while emitting a photon with the appropriate energy. The radiative recombination rate

$$R_{\text{radiative}} = g_{\text{eh}} B (n p - n_{\text{i,eff}}^2) \quad . \quad (2.30)$$

is dependent linearly on the concentrations of the excess carriers. Thereby, B is the coefficient of radiative recombination, which contains directly the information about the quantum-mechanical probability of a transition of an electron from the conduction band into the valence band. Due to the necessary presence of at least one phonon for a transition in silicon as an indirect semiconductor (see Chap. 2.4), the transition probability is with $B_{\text{LLI}}(T = 300 \text{ K}) = 4.73 \times 10^{-15} \text{ cm}^3 \text{ s}^{-1}$ [52] under low-level injection (LLI) by orders of magnitude lower, compared to values of direct semiconductors.

The factor g_{eh} denotes an enhancement factor due to the influence of the Coulomb force between electrons and holes. Due to the fact that electron-hole pairs can only recombine if their wave functions overlap in space, the Coulomb attraction at low carrier densities of an electron and a hole increases this overlap. Towards higher carrier densities than $\sim 1 \times 10^{15} \text{ cm}^{-3}$, electron-hole pairs become effectively screened by the increasing amount of electrons and holes, decreasing the overlap of their wave functions. In this regime, electrons and holes can be treated as an ideal gas in general. Further details of the dependence of B on varying injection and dopant densities at different temperatures are given in Ref. [53].

In low-level injection (LLI) conditions, the carrier lifetime of the radiative recombination can be calculated according to its definition (see Eq.(2.28)) for a p -type and an n -type semiconductor:

$$\tau_{\text{radiative}}^{\text{LLI,p}} = \frac{1}{B p_0} \quad \text{and} \quad \tau_{\text{radiative}}^{\text{LLI,n}} = \frac{1}{B n_0} \quad . \quad (2.31)$$

2.5.2 Auger recombination

Auger band-to-band recombination is a non-radiative recombination process and, in general, is the dominating recombination process at high dopant densities in Si solar cells. The energy that is released by the recombination of an electron and a hole is transferred to a third particle. This can be an electron in the conduction band, a so-called eeh process, or a hole in the valence band, an ehh process. Subsequently, this

energy is released to phonons of the lattice structure of the semiconductor and relaxes thermally. Auger recombination can be expressed as:

$$R_{\text{Auger}} = (g_{\text{eeh}} C_n n + g_{\text{ehh}} C_p p) (n p - n_{i,\text{eff}}^2) \quad , \quad (2.32)$$

with the temperature-dependent Auger coefficients C_n for the *eeh* process and C_p for the *ehh* process [54-56]. These coefficients were already determined in the 1970ies by e.g. Dziawior and Schmid [57] at high dopant densities to $C_n = 2.8 \times 10^{-31} \text{ cm}^6 \text{ s}^{-1}$ and $C_p = 9.9 \times 10^{-32} \text{ cm}^6 \text{ s}^{-1}$. As Auger recombination is influenced by screening as well (see Chap. 2.5.1), the enhancement factors g_{eeh} and g_{ehh} has been introduced in the 90ties [54, 58] to correct C_n and C_p , respectively, towards lower carrier densities.

A widely used parameterization has been published by Kerr and Cuevas [59]. Unfortunately, this cannot be used in numerical device modeling due to its polynomial expression with a disadvantageous derivative, which might cause problems especially in space charge layers [60].

Recently, a new parameterization could be presented [61] shifting the Auger limit towards higher lifetimes. These new and even more accurate results could be experimentally determined by advanced surface passivation techniques enabling very low surface recombination rates [62, 63], which will be introduced in Chap. 3.5.1.

The low-level injection (LLI) lifetime of the Auger recombination process can be displayed as

$$\tau_{\text{Auger}}^p = \frac{1}{C_p p_0^2} \quad \text{and} \quad \tau_{\text{Auger}}^n = \frac{1}{C_n n_0^2} \quad (2.33)$$

for a *p*-type and an *n*-type semiconductor, respectively.

2.5.3 Bulk defect recombination

Impurities and crystal defects can generate energy levels in the band gap of a semiconductor. Free charge carriers can recombine via these impurities in a two- or multiple-step process. This extrinsic recombination channel strongly depends on the concentration of the impurity, but is in Si solar cell applications mostly the dominating recombination channel at low and intermediate dopant densities. W. Shockley and W.T. Read [64], and almost at the same time R.N. Hall [65] with studies on the properties of germanium, proposed a theory to describe carrier recombination via impurity levels. This so-called Shockley-Read-Hall (SRH) recombination is essential for some considerations in this work.

The four elementary processes of free carrier interaction with an impurity level within the band gap are shown in Fig. 2.4. If a defect center is occupied with an electron, latter can either be emitted into the conduction band (i) or a hole from the valence band can be captured (iii). If the defect center is vacant, a hole from the conduction band can be captured (ii) or a hole can be emitted into the valence band (iv). Commonly, interactions with the conduction band are described by using electrons and interactions with the valence band by using holes.

By combining processes (ii) and (iii), the defect acts as a recombination center, which reflects in a typical recombination process via defect levels. For the combination of the inverse processes, (i) and (iv), the defect acts as a generation center, which can be neglected [66], in general. Combining processes (i) and (ii) or as well (iii) and (iv), the captured carrier is emitted back into the band where it came from. Thus, the defect level acts as a so-called trap level. Therefore, a defect acts as a recombination or a trap center, depending on the more probable process: a second capture process of a second carrier or thermal reemission of the captured carrier. This depends mainly on the capture cross sections of the impurity, the temperature and as well on the Fermi energy level [66].

For calculating the net recombination rate of electrons and holes via an impurity level, it is essential to know the time-dependent carrier densities in the valence and conduction band. For the capture rates c_n^* and c_p^* in Fig. 2.4 hold

$$c_n^* = c_n n = (\sigma_n v_{th,n}) n \quad \text{and} \quad c_p^* = c_p p = (\sigma_p v_{th,p}) p \quad . \quad (2.34)$$

The capture coefficients are denoted by c_n and c_p and the capture cross sections by σ_n and σ_p for electrons and holes, respectively. $v_{th,n}$ and $v_{th,p}$ stand for the thermal charge

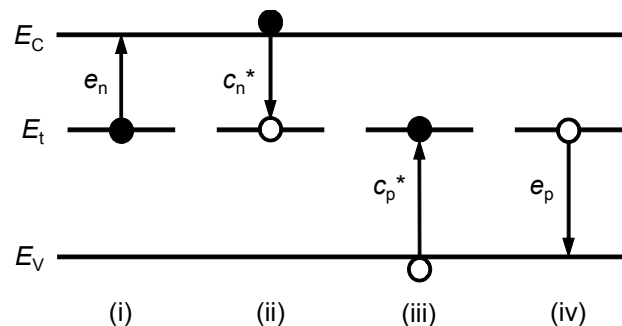


Fig. 2.4: Description of the elementary processes of free carrier interaction with an impurity level within the band gap: (i) electron emission, (ii) electron capture, (iii) hole capture, and (iv) hole emission.

carrier velocities, which are the averaged velocities of the quasi-free electrons and holes in the conduction band and in the valence band, respectively [46]:

$$v_{\text{th},n/p} = \left(\frac{8 k_B T}{\pi m_{\text{th},e/h}^*} \right)^{1/2} . \quad (2.35)$$

Thereby, $m_{\text{th},e}^* = 0.275 m_0$ and $m_{\text{th},h}^* = 0.410 m_0$ express the thermal effective electron and hole masses with m_0 as the electron rest mass.

For considering the whole ensemble instead of a single defect center, the defect concentration N_t and the occupation probability with an electron f_t , described by the Fermi-Dirac distribution, are introduced. Due to the proportionality of the product $N_t f_t$ and the total electron emission and of the product $N_t (1 - f_t)$ and the total electron capture, the derivatives of the carrier densities with respect to time in the conduction band and in the valence band, respectively, can be expressed as:

$$\begin{aligned} \left(\frac{dn}{dt} \right)_{\text{GR}} &= \text{(i)} - \text{(ii)} = [c_n n N_t (1 - f_t)] - [e_n N_t f_t] = 0 \\ \left(\frac{dp}{dt} \right)_{\text{GR}} &= \text{(iv)} - \text{(iii)} = [c_p p N_t f_t] - [e_p N_t (1 - f_t)] = 0 . \end{aligned} \quad (2.36)$$

Due to the principle of detailed balance, each process must be in equilibrium with its inverse process [67] and, thus, the derivatives equal zero. With Eq. (2.36) and Eq. (2.7), the emission rates e_n and e_p can be given as:

$$\begin{aligned} e_n &= c_n n \frac{1 - f_t}{f_t} \equiv c_n n_1 \quad \text{with} \quad n_1 \equiv N_C \exp\left(-\frac{E_C - E_t}{k_B T}\right) \\ e_p &= c_p p \frac{f_t}{1 - f_t} \equiv c_p p_1 \quad \text{with} \quad p_1 \equiv N_V \exp\left(-\frac{E_t - E_V}{k_B T}\right) . \end{aligned} \quad (2.37)$$

Thereby, n_1 and p_1 denote the SRH densities.

Under non-equilibrium conditions with an external excitation, e.g. illumination, the electron and hole densities n and p are increased. By reaching steady-state conditions, the derivatives of the carrier densities with respect to time equal each other: $dn/dt = dp/dt$. Together with Eq. (2.36) and (2.37), the net SRH recombination rate can be expressed as:

$$R_{\text{SRH}} = \frac{(n p - n_{i,\text{eff}}^2)}{\tau_{n0}(p + p_1) + \tau_{p0}(n + n_1)} . \quad (2.38)$$

Thereby, it can be shown that Eq. (2.38) is also valid under transient conditions, although it was derived under steady-state conditions. The capture time constants of electrons and holes are defined as

$$\tau_{n0} \equiv \frac{1}{N_t \sigma_n v_{th,n}} \quad \text{and} \quad \tau_{p0} \equiv \frac{1}{N_t \sigma_p v_{th,p}} \quad . \quad (2.39)$$

By assuming negligible trapping of minority carriers ($\Delta n = \Delta p$) and by using Eqs. (2.26), the SRH lifetime reads:

$$\tau_{SRH} = \frac{\tau_{n0} (p_0 + p_1 + \Delta n) + \tau_{p0} (n_0 + n_1 + \Delta n)}{p_0 + n_0 + \Delta n} \quad . \quad (2.40)$$

With the definition of the symmetry factor k as the ratio of the carrier capture cross sections, the SRH lifetime can be expressed as:

$$\tau_{SRH} = \tau_{n0} \left[\frac{p_0 + p_1 + \Delta n}{p_0 + n_0 + \Delta n} + k \frac{n_0 + n_1 + \Delta n}{p_0 + n_0 + \Delta n} \right] \quad \text{with} \quad k \equiv \frac{\sigma_n}{\sigma_p} = \frac{\tau_{p0}}{\tau_{n0}} \quad . \quad (2.41)$$

Thereby, the second equals sign in the definition of k only holds, if the difference between the thermal velocities of electrons and holes is neglected. This assumption is justified, since in general the carrier capture cross sections of electrons and holes, respectively, deviate by orders of magnitude.

Under low-level injection conditions (LLI), which means $\Delta n, \Delta p \ll N_{dop}$, Eq. (2.41) simplifies for a p -type and n -type semiconductor to

$$\tau_{SRH}^{LLI,p} = \tau_{n0} \left[1 + \frac{p_1}{p_0} + k \frac{n_1}{p_0} \right] \quad \text{and} \quad \tau_{SRH}^{LLI,n} = k \tau_{n0} \left[1 + \frac{n_1}{n_0} + \frac{1}{k} \frac{p_1}{n_0} \right] \quad , \quad (2.42)$$

respectively. By further assuming a deep defect level with $E_t \approx E_i$, the corresponding low level injection SRH lifetimes simplify to

$$\tau_{SRH}^{LLI,p} = \tau_{n0} \quad \text{and} \quad \tau_{SRH}^{LLI,n} = k \tau_{n0} = \tau_{p0} \quad . \quad (2.43)$$

2.5.4 Surface recombination

The crystallographic structure at the surface of a semiconductor features an abrupt discontinuity, leading to the emergence of unsaturated bonds, so-called *dangling bonds*. These act as very effective recombination centers and produce, like any disorder of the crystal symmetry, energy states, which are located mostly within the band structure.

As solar cells feature large-areas, it is important to reduce surface recombination by surface passivation. Mostly, deposited dielectric layers with a fixed charge Q_f are used to saturate the dangling bonds and/or to reduce the minority carrier density close to the surface by the fixed charge. The defect density at the interface of the semiconductor and the dielectric layer is in general sufficiently small and Q_f is sufficiently large. Thus, the trapped charge in these states, due to their occupation statistics, can be neglected and the surface recombination rate

$$R_{\text{surface}} = \frac{(n_s p_s - n_{i,\text{eff}}^2)}{\frac{p_s + p_1}{S_n} + \frac{n_s + n_1}{S_p}} \quad (2.44)$$

can be described analogously to SRH bulk recombination. n_s and p_s denote the carrier densities and S_n and S_p the surface recombination velocities at of electrons and holes, respectively.

The surface recombination velocity quantifies the quality of a surface, equivalent to the excess carrier lifetime in the bulk material, and is given in units of cm/s:

$$S_{\text{eff}} \equiv \frac{R_{\text{surface}}}{\Delta n_s} \quad (2.45)$$

S_{eff} can be interpreted as the velocity of the current of bulk carriers towards the surface. Thus, the surface recombination velocity is limited to thermal velocity (see Eq. (2.35)), which is in the range of 1×10^7 cm/s.

2.6 Free carrier absorption

Free carrier absorption is a parasitic absorption process, which reduces the light intensity but does not create electron-hole pairs. Thereby, photons are absorbed by either free electrons or holes, leading to a transition between states in the same (intraband absorption) or in a different (interband absorption; e.g. transitions between two conduction bands) band. Thus, the photon energy is lost due to thermalization processes. At photon energies close to the band gap, free carrier absorption can effectively compete with the generation of electron-hole pairs and, thus, might decrease solar cell efficiency. Although free carrier absorption can be neglected for wavelengths $\lambda < 1000$ nm in general, for longer wavelengths it can become significant, especially in regions with high carrier concentrations.

In classical theory [68], free carrier absorption shows a quadratic behavior in λ and linear behavior in the doping concentration N (n or p , respectively):

$$\alpha_{\text{FCA},n/p}(\lambda, N) = \frac{q^3}{4\pi^2 \epsilon_0 c^3 n_{\text{Si}} m_{e/h}^{*2} \mu_{n/p}} \cdot \lambda^2 \cdot N \quad . \quad (2.46)$$

ϵ_0 is the permittivity in vacuum, n_{Si} the refractive index of silicon, m^* the effective mass, μ the carrier mobility and a quadratic behavior of the wavelength λ .

With the assumption, that $\mu(N)$ is independent on N , free carrier absorption can, thus, be written as

$$\frac{\alpha_{\text{FCA},n}}{\text{cm}^{-1}} = C_{\text{FCA},n} \left(\frac{\lambda}{\mu\text{m}} \right)^\xi \frac{n}{\text{cm}^{-3}} \quad \text{and} \quad \frac{\alpha_{\text{FCA},p}}{\text{cm}^{-1}} = C_{\text{FCA},p} \left(\frac{\lambda}{\mu\text{m}} \right)^\varphi \frac{p}{\text{cm}^{-3}} \quad , \quad (2.47)$$

for n -type and p -type doped semiconductors, respectively. The unitless coefficient $C_{\text{FCA},n/p}$ includes the constants given in Eq. (2.46) and the exponents ξ and φ are 2.

Schroder *et al.* [69] evaluated experimentally determined absorption coefficients α_{Si} as a function of carrier concentration for the wavelengths $\lambda = 4, 5$ and $10 \mu\text{m}$. For these wavelengths, best agreement to the experimental data was achieved with

$$C_{\text{FCA},n}^{\text{Schroder}} = 1.0 \times 10^{-18} \quad \text{and} \quad C_{\text{FCA},p}^{\text{Schroder}} = 2.7 \times 10^{-18} \quad . \quad (2.48)$$

The fits showed as well a quadratic behavior of λ with ξ ; $\varphi = 2$ (see 2.46). Schroder *et al.* [69] mentioned, that this free carrier absorption theory might yet not be thoroughly developed.

Beyond the Schroder parameters, another widespread empirical and simple to use expression is given by Green [70] for photon energies $h\nu > 0.5 \text{ eV}$ and charge carrier densities around 10^{18} cm^{-3} :

$$\begin{aligned} C_{\text{FCA},n}^{\text{Green}} &= 2.6 \times 10^{-18} \quad \text{and} \quad \xi = 3 \quad , \\ C_{\text{FCA},p}^{\text{Green}} &= 2.7 \times 10^{-18} \quad \text{and} \quad \varphi = 2 \quad , \end{aligned} \quad (2.49)$$

improving the results of Schroder for p -type Si, but showing for n -type Si a different coefficient and a cubic behavior of $\alpha_{\text{FCA},n}$ with λ ($\xi = 3$) (see Eq. 2.46). The cubic behavior follows from the evaluation of experimentally determined absorption coefficients [71] of doped n -type Si material, shown in Fig. 2.5. In heavily doped Si material, a linear region can be seen for $\lambda > 5 \mu\text{m}$, attributed to intraband free carrier absorption [70], featuring approximately a quadratic behavior of the wavelength. At $2 \mu\text{m} < \lambda < 4 \mu\text{m}$ a characteristic hump appears at all considered doping levels, due to interband transitions within the two lowest conduction bands crossing at the wave

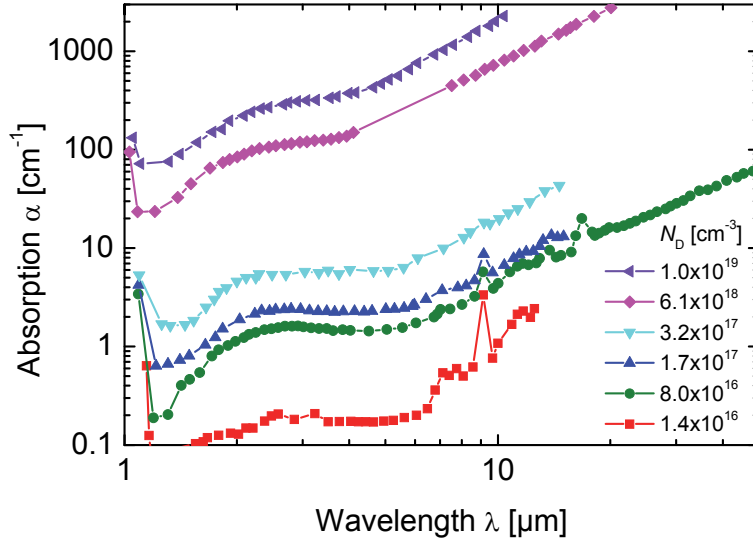


Fig. 2.5: Absorption coefficient as a function of wavelength for six different *n*-type Si samples at room-temperature (data from [71]). More details to the functional behavior at $\lambda = 1.2 - 2 \mu\text{m}$ will be given in Chap. 4.

vector \mathbf{X} (see Fig. 2.2) [70], which does not appear in *p*-type Si material. Due to this additional hump, an additional structure occurs for $1.2 \mu\text{m} < \lambda < 2 \mu\text{m}$, attributed to inter-valence band transitions [72] and, thus, Green evaluated an approximately cubic dependence of $\alpha_{\text{FCA},n}$ on λ (i.e. $\xi = 3$) [70].

Despite proposed more precise models [73, 74] for the dependence of the contribution of free carriers to the absorption coefficient α_{FCA} , former FCA parameterizations found more widespread application, due to its simplicity. Isenberg and Warta [75] quantified deviations of the Schroder parameterization and discrepancies of up to half an order of magnitude for an appropriate description of FCA for heavily doped layers. They proposed a parameterization, based on data at $\lambda = 5 \mu\text{m}$, for the wavelength range from 1.2 to 8 μm , based on the semi-classical approach of Ref. [73]:

$$C_{\text{FCA},n/p}^{\text{Isenberg}} = C_{\text{FCA},n/p}(\lambda) \cdot \frac{N}{\text{cm}^{-3}} \cdot \left(\frac{\lambda}{\mu\text{m}} \right)^2 \cdot \left(1 + A \left[1 + \text{erf} \left\{ m \log \frac{N}{N_0} \right\} \right] \right) . \quad (2.50)$$

Thereby, the dimensionless carrier absorption coefficient C_{FCA} is a function of λ . A and m are dimensionless fit parameters describing the deviation of the function $\alpha_{\text{FCA}}(N)$ from a linear model and N_0 is a carrier concentration used for normalization. The parameters for $\lambda = 1.2 \mu\text{m}$ are shown in Tab. 2.1, more parameters are given in Ref. [75].

Tab. 2.1: Parameters of the empirical Isenberg FCA model for a wavelength $\lambda = 1.2 \mu\text{m}$ [75].

	C_{FCA}	A	m	$N_0 [\text{cm}^{-3}]$
<i>n</i> -type Si	4.45×10^{-11}	5.75	0.67	6.3×10^{18}
<i>p</i> -type Si	10.72×10^{-11}	2.59	0.76	3.2×10^{18}

In conclusion, it can be noticed that all published free carrier studies presented in this chapter are based on the evaluation of experimental absorption data. Schroder [69] determined his parameterization with experimental data at $\lambda = 4, 5$ and $10 \mu\text{m}$, far beyond the range of $\lambda = 1.0 - 1.2 \mu\text{m}$, which is relevant for Si solar cells. Here, parasitic absorption processes can take place competing with the absorption of the Si material. Also the parameterization of Isenberg [75] is based on data at $\lambda = 5 \mu\text{m}$, even though parameters are given for $\lambda = 1.2 \mu\text{m}$ (see Tab. 2.1). Only the parameterization for *n*-type Si of Green [70] is evaluated at the range $\lambda = 1.2 - 2 \mu\text{m}$ close to the wavelength range, relevant for Si solar cells.

Thus, a comparison of the here presented models in the range of $\lambda = 1.0 - 2.0 \mu\text{m}$, including the relevant range of parasitic absorption in Si solar cells ($\lambda = 1.0 - 1.2 \mu\text{m}$), will be presented and discussed in detail in Chap. 4 and a new parameterization valid in this range is introduced.

3 Simulation of crystalline silicon solar cells

The main concepts of the simulation of crystalline Si solar cells are introduced. The analytical approach of the one- and two-diode model and the tools for advanced 2D and 3D numerical simulation are given. Therefore, the model basis used for the numerical calculations in this work is presented and the diversity of numerical modeling is supported by examples for both, optical and electrical simulations.

3.1 Solar cell parameters

The most important solar cell parameters can be extracted from the current density-voltage (IV) curve, which can be seen exemplarily in Fig. 3.1. The IV curve is typically performed under standard illumination conditions, which means an illumination intensity of 1000 W/m^2 and the AM1.5G spectrum with the spectral distribution according to IEC 60904-3 standard [76] at a temperature $T = 25^\circ\text{C}$. The maximum of the power curve of a solar cell defines the so-called maximum power point (mpp), the point at optimum working conditions with maximum yield. The quotient of maximum power density $P_{\text{mpp}} = V_{\text{mpp}} \cdot j_{\text{mpp}}$ and the product of open-circuit voltage V_{oc} and short-circuit current density j_{sc} defines the fill factor

$$FF = \frac{V_{\text{mpp}} \cdot j_{\text{mpp}}}{V_{\text{oc}} \cdot j_{\text{sc}}} . \quad (3.1)$$

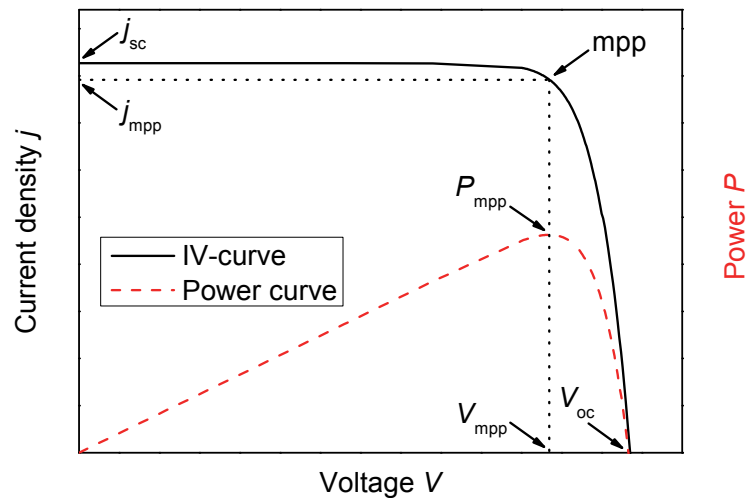


Fig. 3.1: IV curve and power curve of a Si solar cell under illumination conditions.

The fill factor is not only smaller than 1 due to the exponential behavior of the IV curve, but can be also reduced by resistive losses and non-ideal diode behavior.

Finally, the conversion efficiency η of a solar cell is defined by the quotient of the output power density P_{mpp} and the incident light power density P_{in} :

$$\eta = \frac{P_{\text{mpp}}}{P_{\text{in}}} = \frac{V_{\text{mpp}} j_{\text{mpp}}}{P_{\text{in}}} = \frac{V_{\text{oc}} j_{\text{sc}} FF}{P_{\text{in}}} \quad (3.2)$$

3.2 Analytical approach: one- and two-diode model

A basic analytical understanding of the characteristics of solar cells can be achieved by considering its diode behavior. The fundamental physics of a diode, which is fundamentally a two-terminal electronic component with asymmetric transfer characteristic, have been firstly introduced by Shockley [77] in 1949.

Based on the following assumptions:

- Low-level injection (LLI) conditions
- Generation profile independent of minority carrier density or position
- Box-shaped n - and p -type Si regions
- Infinitely extended semiconductor
- Non-recombination losses at the space-charge region

the coupled system of the differential equations given in Chap. 2.3 can be solved analytically. The current density generated by a solar cell, holds in the so-called *one-diode model*:

$$j(V) = j_0 \left(\exp \left[\frac{q (V - j(V) R_s)}{n_1 k_B T} \right] - 1 \right) + \frac{V - j(V) R_s}{R_p} + j_{\text{sc}} \quad (3.3)$$

Thereby, V is the external voltage applied to the solar cell, $n_1 = 1$ is the ideality factor for the above mentioned assumptions and $j_{\text{sc}} < 0$. R_s and R_p account for the contribution of additional series and parallel resistance losses, respectively. j_0 is the dark saturation current density in the base and emitter volume and holds

$$j_0 = q n_i^2 \left(\frac{D_e}{N_A L_e} + \frac{D_h}{N_D L_h} \right) . \quad (3.4)$$

$D_{e/h}$ are the diffusion constants for electrons and holes, which are correlated to the diffusion lengths $L_{e/h}$, respectively, via:

$$L_{e/h} = \sqrt{D_{e/h} \tau} . \quad (3.5)$$

The short-circuit current density j_{sc} in Eq. (3.3) is given by the integrated photo-generation G_{ph} within $L_{e/h}$:

$$j_{sc} = q \int_{-L_h}^{+L_e} G_{ph} dx . \quad (3.6)$$

A comprehensive derivation of the one-diode-equation can be found e.g. in [78].

The *two-diode model* is an extension of Eq. (3.3). It takes additionally into account for recombination in areas with almost the same charge carrier density of electrons and holes, especially the space-charge region, which is described by the second term with the dark saturation current density j_{02} :

$$j(V) = j_{01} \left(\exp \left[\frac{q(V - j(V) R_s)}{n_1 k_B T} \right] - 1 \right) + j_{02} \left(\exp \left[\frac{q(V - j(V) R_s)}{n_2 k_B T} \right] - 1 \right) + \frac{V - j(V) R_s}{R_p} + j_{sc} . \quad (3.7)$$

Here, j_{01} is equivalent to j_0 in Eq. (3.3). The second ideality factor n_2 equals 2 under idealized conditions, including the assumption of only one defect level in the middle of the band gap. More complex recombination mechanisms in real solar cells often lead to $n_1 \neq 1$ and also $n_2 \neq 2$ [79, 80]. The equivalent circuit diagram of the one- and two-diode model is shown in Fig. 3.2.

In [81], a comprehensive description of the different effects of the parameters in the two-diode model is given, leading to a broad basic understanding of the physical behavior of Si solar cells. However, for more accurate modeling of solar cells concerning e.g. the recombination behavior of multiple defect levels or multi-dimensional current effects, more precise models are required, which in general cannot be solved analytically, and require numerical algorithms.

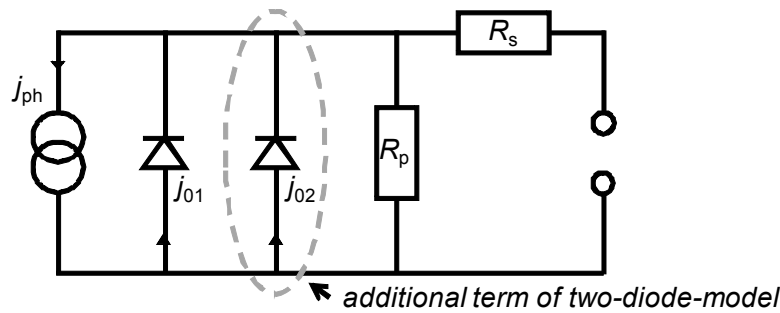


Fig. 3.2: Equivalent circuit diagram of the one- and two-diode model. The first diode describes recombination in the base and in the emitter volume. The second diode (additional term of two-diode model) describes recombination in the space-charge region. Parasitic series resistance R_s and parallel resistance R_p losses are accounted for. The photogenerated current density j_{ph} equals the short-circuit current density j_{sc} in this model.

3.3 Numerical simulation

Even if a crystalline Si solar cell is a relatively simple pn -junction structure in comparison to many other semiconductor devices, its optimization is a complex task and the coupled semiconductor equations introduced in Chap. 2.3 often cannot be solved with analytical approaches. Thus, the set of equations needs to be solved numerically at discrete points, which have to be distributed reasonably to the device geometry, forming a so called simulation mesh structure. Thereby, many different dimensions, by orders of magnitude different, have to be handled in one model. Whereas a monocrystalline Si solar cell has a diameter in the two-digit centimeter range, cell thicknesses are in the range of $180\ \mu\text{m}$, and the smallest device structures feature sizes of nanometers. But due to the highly symmetric structure of a solar cell, it is sufficient to model a geometrically irreducible *standard domain*. For example, a 2D standard domain of a screen-printed industrial p -type Si solar cell (left) includes only half of the front contact finger width, as shown in Fig. 3.3 (left). A 3D standard domain of e.g. a back-contact back-junction solar cell with point-like contacts includes a quarter of the rear contact area of the p - and n -type contact, respectively, shown in Fig. 3.3 (right). By mirroring at the boundaries of such an element of symmetry, the entire structure can be constructed. The standard domain of cells featuring line contacts instead of point-like structures mostly reduce to a 2D structure, featuring a significant computational effort. However, 3D structures with point-like contacts should not be approximated by 2D models [60], as it might cause errors in both, the resistive and the recombination losses.

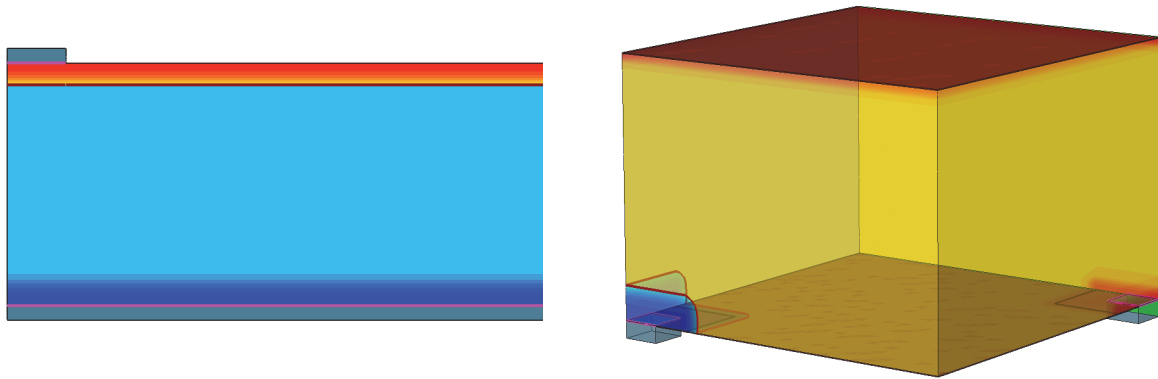


Fig. 3.3: Geometrically irreducible standard domain for numerical simulations in 2D (left) for a full-area rear surface metallized solar cell with front contact fingers and in 3D (right) for a back-contact back-junction solar cell with point-like rear contacts.

In Fig. 3.4 an excerpt of a simulation mesh geometry is shown. The refinement needs to be very small meshed at the surfaces, where short wavelength light is coupled into the solar cell, as it is absorbed within the first nanometers. Furthermore, diffusion profiles need to be meshed sufficiently, depending on their density gradient. Close to the metal contacts the mesh has to be adapted to account for current-crowding effects [82]. Basically, the mesh needs to be fine enough in all regions, where parameters vary significantly with distance.

In contrast to diodes, as used e.g. on standard printed circuit boards, solar cells operate in reverse direction. Thereby, free carriers are generated by the sunlight, implying for solar cell simulation a calculation of a carrier generation profile G . As solar cells in first order approximation are non-light-emitting diodes, the optical and the electrical simulation can be decoupled and calculated in different setups, taking advantage of their different standard domains.

In the following, the optical and electrical numerical simulation will be explained in more detail based on the specifically used physical models, as they are of great importance for an accurate minimization of recombination and resistive losses. The chapters will be accompanied by several simulation examples, underlining versatility of numerical modeling.

In the present thesis, the solar cell simulation program Sentaurus TCAD from Synopsys [12] is used, which unifies optical and electrical as well as process simulation tools, and provides a broad range of physical models, based on Fermi-Dirac statistics. The presented calculations are performed with the program releases from A-2008.09 to G-2012.06.

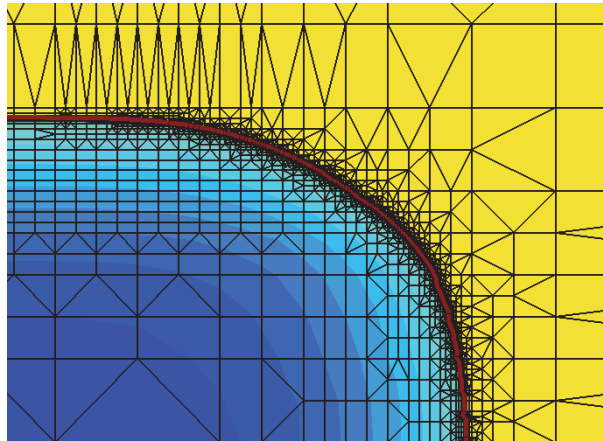


Fig. 3.4: Excerpt of a simulation mesh geometry. The discrete mesh points need to be more finely distributed in regions where an input or an output variable changes significantly over distance, like e.g. the doping concentration at the pn-junction.

3.4 Optical simulation

For the calculation of reflection, transmission and space-resolved absorption of the solar cell a fully 3D Monte Carlo ray tracer is used. Ray tracing is a common simulation method based on the equations of geometrical optics. Whereas the standard domain for planar surfaces reduces to a 1D structure, for textured surfaces it incorporates a quarter of an inverted or upright pyramid with an aperture angle of 70.5° ¹ and a pyramid height of about 5 to 10 μm , as exemplarily shown in Fig. 3.5. The wave-optical nature of light is neglected, thus, ray tracing is only suitable for structures whose dimensions are much larger than the wavelength of light. This requirement is adequately met for conventional crystalline solar cell thicknesses and the mentioned pyramidal heights, but not for anti-reflection coatings (ARCs) with thicknesses of a few nanometers. Latter will be discussed in Chap. 3.4.1.

To obtain the photogeneration rate G , which is important for device modeling, a ray tracing simulation is carried out separately for each wavelength of a given spectrum².

¹ To roughen the surface of monocrystalline (100) orientated Si surfaces, a wet-chemical etching process with KOH is typically used. Due to the direction-orientated etching character of alkalines along the crystallographic structure of Si, pyramids with an opening angle of 70.5° appear.

² Typically in the wavelength range $\lambda = 300 - 1200 \text{ nm}$ for Si solar cell simulations, as it starts with the minimum relevant wavelength of the AM1.5G spectrum and ends slightly above the maximum wavelength, which can be absorbed by crystalline Si at $T = 300 \text{ K}$, due to its band gap structure.

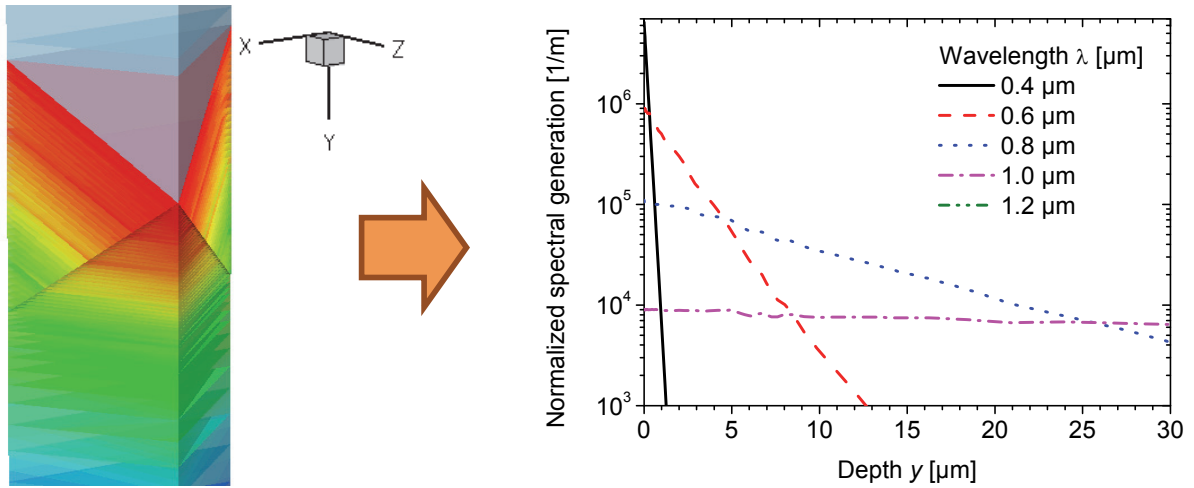


Fig. 3.5: The optical standard domain features a quarter of a pyramid. Via symmetric boundary conditions, a pyramidal structure is formed. The position-dependent photogeneration rate $G(x,y,z,\lambda)$ is projected onto a line, which is perpendicular to the solar cell.

G follows from the integration over the considered wavelength range, convoluted with the solar spectrum AM1.5G. For incorporating the result into the device model, the position-dependent $G(x,y,z,\lambda)$ is projected onto a line, which is perpendicular to the solar cell (y -axis in Fig. 3.5). This 1D profiles $G(y,\lambda)$ can be imported into the electrical simulation and mapped laterally onto its entire standard domain.

3.4.1 Transfer matrix method for computing optically thin layers

The thicknesses of the anti-reflection coatings (ARCs), deposited onto the Si surfaces to improve physical passivation and optical reflection properties, feature the same order of magnitude like the incident wavelength of light. Thus, coherence effects have to be accounted for in simulations of such thin multilayer systems, which can be realized via the so-called *transfer matrix method* (TMM), based on the Fresnel equations.

Thereby, the influence of a single layer is described by a 2×2 transfer matrix, containing information about thickness and refractive index of the considered layer, as well as angle dependencies perpendicular to the surface. A multiplication with the incident wave vector, consisting of an electric and a magnetic field component, leads to the resulting electromagnetic wave vector. Latter contains all information to calculate the resulting refraction and transmission fractions including their directions, which are transferred in the following back to the ray tracer. A more detailed description of the TMM may be found in [83].

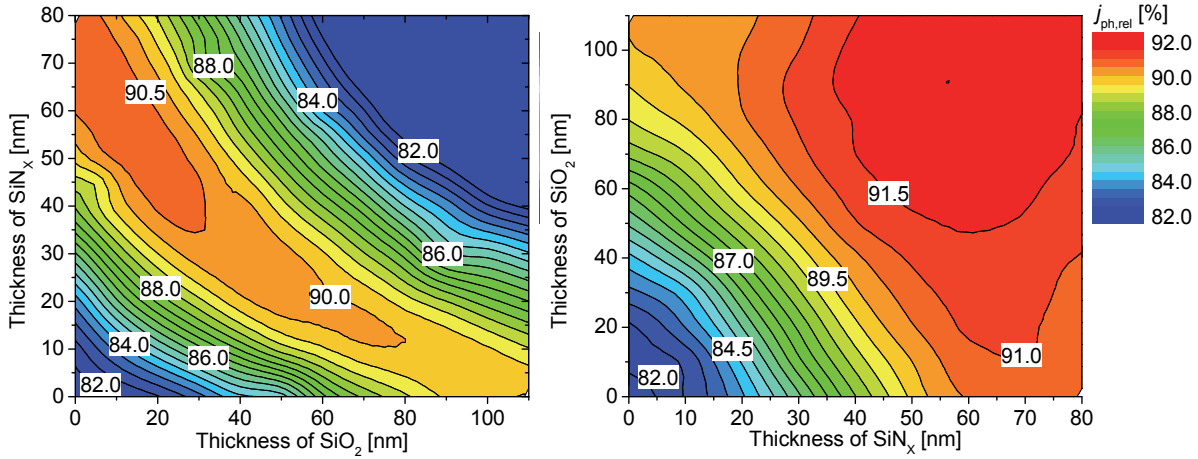


Fig. 3.6: Simulated variation of a front side dielectric stack system consisting of Si/SiO₂/SiN_x/air (left) and Si/SiN_x/SiO₂/air (right) on top of a 250 μm thick Si wafer. The rear side reflectance is set to 92.5%. In both graphs, the dielectric layer next to the Si bulk material is set as abscissa.

With this algorithm, also stacks of several thin layers can be calculated. Thus, by varying the thicknesses of the considered stacks, the system can be optimized in order to maximize the resulting photogeneration current density j_{ph} . Such an optimization is shown in Fig. 3.6 for a front side stack system consisting of Si/SiO₂/SiN_x/air (left) as well as Si/SiN_x/SiO₂/air (right). The simulated Si wafer features a thickness of 250 μm. The refractive index $n_{Si}(\lambda)$ and the extinction coefficient $k_{Si}(\lambda)$ of Si have been applied according to [84], while for the corresponding values for SiN_x and SiO₂, the predefined tables in Sentaurus TCAD [12] have been used. The rear side features a reflectance of $R_0 = 92.5\%$ and $\omega = 75$ (see Chap. 3.4.2), according to experimental data. The resulting photogeneration current densities $j_{ph,rel}$ are given in %, relative to the incident current density j_{in} . Thus, a change in the order of the dielectric layers results in a completely different optimum, due to the different refractive indices of the considered stack systems. Please note, that these results are only based on optical considerations. The surface passivation properties of the stack systems on top of the bulk material may feature different recombination losses at the interface.

3.4.2 Modeling of rear side reflectance properties

Rear surface reflectance properties of thin dielectric layers can be simulated analogously to the in Chap. 3.4.1 introduced TMM model, additionally implementing a rear side reflector like e.g. Al with its appropriate optical properties. To consider a

specific rear surface roughness, the rear surface of the simulation setup can be triangulated in smaller planar triangular pieces, as recently presented [85]. In this so-called *tilted-mirrors-model*, the degree of roughness can be determined via imported 3D microscope images.

Another convenient and widely used empirical approach is given by the so-called empirical *Phong model* [86]. In this model, the incident light beam is reflected according to its incident angle α at the rear surface with an angle independent degree of reflectance R_0 . Thereby, the reflected beam is widened by a cosine function around the reflected direction by the Phong-exponent ω . The intensity distribution holds:

$$I = I_0 \cos^\omega \alpha \quad . \quad (3.8)$$

The smaller ω , the more diffuse becomes the reflected beam, which is illustrated e.g. in [78]. I_0 is the intensity of the incident beam, I the resulting reflected beam intensity. The influence of R_0 and ω on the simulated reflection is shown in Fig. 3.7. In this example, the wafer thickness is 200 μm and the front side features random pyramids and an anti-reflection (AR) SiN_x layer with a thickness of 65 nm. As R_0 increases, less photons are absorbed by the rear surface, increasing the reflectance significantly in the long wavelength range. A decrease of ω leads to a decrease of the reflectivity, as more light is absorbed within the bulk material.

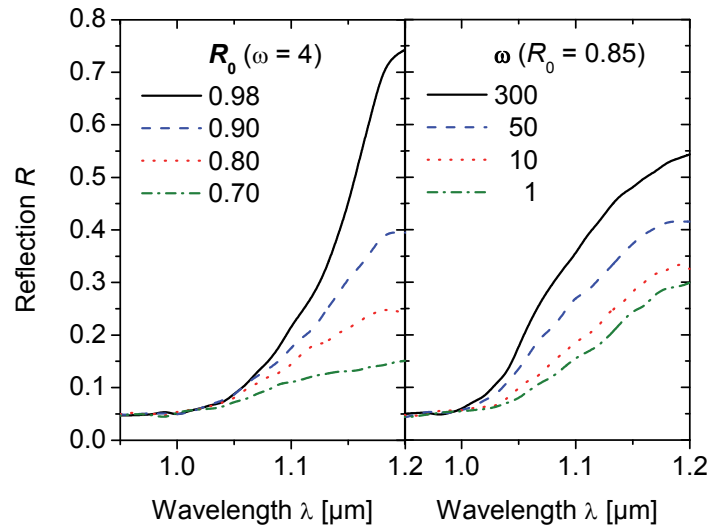


Fig. 3.7: Parameter variation of the empirical Phong model. With increasing rear side reflectivity R_0 and Phong-exponent ω , the reflectivity increases.

Diffractive rear side structures

In the course of making crystalline solar cells thinner with thicknesses well below 100 μm , conventional light trapping techniques do not provide sufficient absorption of the long wavelength range of the solar spectrum. Thus, the improvement of light trapping is an important topic in recent solar cell research [87-91] and requires advanced modeling tools [92-95]. Diffractive rear side structures like gratings or photonic crystals are one possibility to achieve longer path lengths. An introduction to photonic structures may be found in Ref. [96]. Wave optical 2D or 3D effects can be calculated via methods like finite different time domain (FDTD) or rigorous coupled wave analysis (RCWA). Such coupled methods require both, optical near field information for calculating the local absorption in the Si bulk material and the far field information for the determination of reflection, transmission and absorption spectra. Whereas FDTD is integrated in Sentaurus TCAD, RCWA has to be calculated separately and simulation results have to be imported into the semiconductor device simulation of Sentaurus Device [92, 93].

Rear reflectance properties of bifacial solar cells

Modeling the rear reflectance properties of bifacial solar cells features additional requirements. Thereby it is convenient to adapt the simulation method according to the considered layer system. A modeling approach is developed in this work³, allowing the investigation of the rear side illumination of solar cells with different rear side reflectors. This will be exemplarily shown for the following investigated test structures. The results are published in [97]. Here, the optical properties of planar cells (pp), random pyramids only on the front side (tp) and random pyramids on front and rear side (tt) (Fig. 3.8, insets) have been considered with different rear layer systems, shown in Tab. 3.1.

Thereby, the Si bulk material of all test samples features a thickness of 200 μm and a dielectric layer stack of 10 nm Al_2O_3 and 65 nm AR- SiN_x on both sample sides. Whereas configuration (i) and (ii) have been simulated as mentioned before via the in Chap. 3.4.1 introduced TMM model for the simulation of the dielectric layers with a Ag rear side reflector with its appropriate optical properties, the diffuse rear reflectors (iii) – (vi) are modeled with two separate simulations for front and rear side. These

³ The model and the results presented here have been developed in close cooperation with J. Frank, whose diploma thesis has been supervised by the author of this work and S. Fischer in the framework of his PhD thesis.

Tab. 3.1: Overview of the different rear side reflectors, which are combined with the three test structures, shown in Fig. 3.8 (insets).

No.	Configuration	Description
i	Metallized (Ag)	100 nm Ag applied by vapor deposition
ii	Air + Ag	Ag mirror behind wafer, air gap within wafer and Ag
iii	White paint	Rear side painted with white acrylic paint
iv	Air + white paint	Glass plate with white paint is located behind the wafer
v	Air + paper	Multiple layers of white paper are located behind the wafer
vi	Air + PTFE	Sintered PTFE powder, 1 cm thick, behind the wafer

reflectors are assumed in good approximation to be Lambertian, so that the rear illumination is distributed by $\cos(\theta)$. With the reflection $R_R(\lambda)$ of the diffusive rear reflectors (iii)–(vi) (see Tab. 3.1), respectively, for the absorption $A(\lambda)$ and reflectance $R(\lambda)$ of the system wafer/reflector follows:

$$\begin{aligned}
 A(\lambda) &= A_f(\lambda) + T_f(\lambda) \cdot R_R(\lambda) \cdot A_r(\lambda) \cdot \frac{1}{1 - R_r(\lambda) \cdot R_R(\lambda)} \quad , \\
 R(\lambda) &= R_f(\lambda) + T_f(\lambda) \cdot R_R(\lambda) \cdot T_r(\lambda) \cdot \frac{1}{1 - R_r(\lambda) \cdot R_R(\lambda)} \quad .
 \end{aligned}
 \tag{3.9}$$

The absorptions $A_{f/r}(\lambda)$, reflections $R_{f/r}(\lambda)$, and transmissions $T_{f/r}(\lambda)$ are calculated for front (f) and rear (r) side illumination, respectively. The fractions in both equations result from a geometric series due to multiple reflections within wafer and a rear surface reflector. This expression is applicable for the reflectors (iv)–(vi), but inadequate for (iii) because of the lack of air gap, as interference effects of the rear anti-reflection layer cannot be considered. As the reflection of (iii) could only be experimentally measured against the refractive index of air ($n = 1$), the Fresnel formulas are used to correct the measured reflection against AR-SiN_x with $n \approx 2$.

Within the experimental data and simulations, good qualitative agreement could be achieved [97]. By the simulations, the resulting photocurrent densities for the considered rear reflectors are determined and shown in Fig. 3.8. The simulated photocurrent density j_{ph} for each wafer type is shown as baseline in dark gray without any additional rear reflector and the photocurrent increase Δj_{ph} resulting of the rear

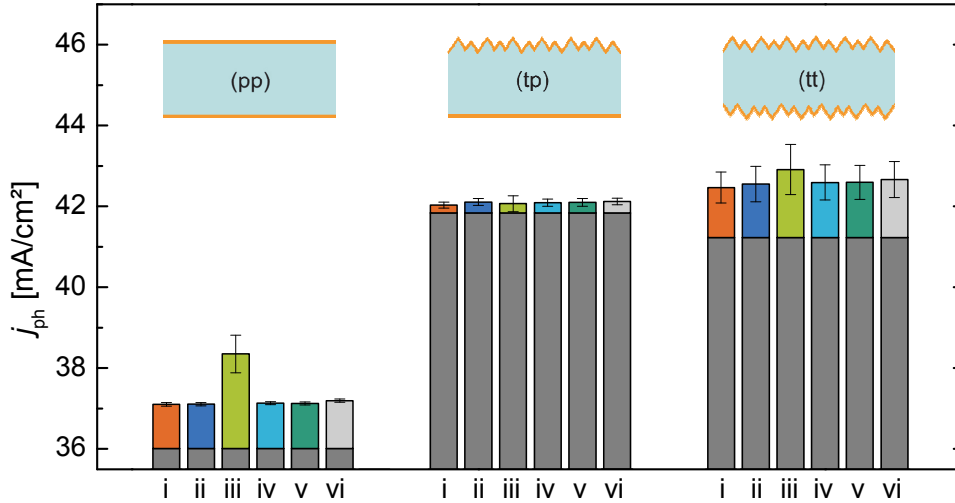


Fig. 3.8: Simulated photocurrent density j_{ph} for each wafer type without rear reflector (dark gray) and the photocurrent increase Δj_{ph} resulting of the rear reflectors $i - vi$ (colored). The rear reflector configurations are given in Tab. 3.1.

reflector configurations (i) – (vi) (see Tab. 3.1). As expected, due to the lower reflectivity at textured front surfaces [98], it appears a significant difference within samples with planar (Fig. 3.8, left) and textured front surfaces (Fig. 3.8, middle). Furthermore, the influence of the rear side reflectors for one-sided textured wafers is relatively low, as the incident light is mostly totally reflected at the rear side, due to the angular optical path of the photons resulting from the optical refraction of the textured front side. Both-sided textured wafers (Fig. 3.8, right) feature slightly lower light trapping than one-sided textured wafers, resulting in a lower j_{ph} . With the structured rear surface, less total internal reflection occurs, leading to a higher transmission at the rear side. With an appropriate rear side reflector, even enhanced light trapping properties might be achievable.

For the wafers featuring planar surfaces, a direct application of a diffuse reflector (like e.g. white paint) might lead to the best light trapping enhancement, while both, direct and diffuse reflectors featuring an air gap within wafer and reflector feature much less enhancement. When the light is reflected at the rear side outside the wafer, even very obliquely incident light reentering the Si is refracted towards the perpendicular by an angle to the vertical line of at most 17° , which corresponds to a path length enhancement of only 4.4% to the perpendicular. However, when the diffuse reflector is applied directly onto the rear side of the wafer, the refraction to the perpendicular can be avoided and, thus, longer light paths are achievable, due to total internal reflection at the front side.

3.5 Electrical simulation

The aim of electrical modeling of a semiconductor solar cell is the description of its physical properties by using appropriate models. For the numerical calculation of the solar cell characteristics, the in Chap. 2.3 introduced coupled system of the continuity equations for electrons and holes and the Poisson equation are solved at discrete grid points in space. Due to the symmetry of the discretization element with N vertices, the set of equations yields $3N$ equations.

When incorporating the optical generation profile (see Chap. 3.4) it is convenient to scale the generation rate by the amount of shading and neglect the shading due to the front metal fingers.

For the numerical solution of equations (2.22) and (2.23), the containing parameters need to be described correctly in order to achieve sufficiently high precision capability. As solar cells are limited by the minority carrier current in contrast to a majority carrier current limitation in most semiconductor circuit technologies, models such as for the intrinsic carrier density, minority carrier mobility and the recombination at passivated surfaces had to be refined for photovoltaic demands. A consistent set of models and parameters for the simulation of Si solar cells is given in Tab. 3.2, as used in this work, which agrees with the recently published values proposed by Altermatt [60].

Unfortunately, the more accurate model for Auger recombination from Kerr and Cuevas [59] and Richter *et al.* [61] might not be used for numerical modeling. Due to their polynomial expressions, calculations might lead to uncertainties in regions with abruptly changing concentrations by orders of magnitude, like it is the case e.g. in the space charge region [60]. Therefore, the model of Dzierwor and Schmidt [57] is used, although it is known that it underestimates the recombination rate below carrier concentrations of 10^{18} cm^{-3} due to screening effects, corrected subsequently by the enhancement factors g_{eh} and g_{hh} (see Eq. (2.32)). The recently published model of Richter *et al.* [61] is a modification of the Kerr parameterization [59], as measured bulk charge carrier lifetimes exceeded the Auger limit in [59]. Thus, the parameterization in [61] would be the model of choice, if the mentioned numerical problems could be tackled.

SRH surface recombination depends strongly on the surface morphology and the deposition circumstances, but can influence the solar cell performance significantly. Corresponding parameterizations for SiN_x and SiO_2 passivated interfaces for phosphorus-diffused surfaces might be found e.g. in [99] and for boron-diffused

Tab. 3.2: The set of models and parameters for numerical simulations used in this work.

	Description/model/parameter
Equations solved	Semiconductor equations (see Chap. 2.3)
Temperature	$T = 300$ K
Free carrier statistics	Fermi-Dirac
Intrinsic carrier density	$n_i = 9.65 \times 10^9 \text{ cm}^{-3}$ [48]
Free carrier mobility	Klaassen's unified mobility model [100, 101]
Band gap narrowing	Schenk [49]
Recombination:	
- Radiative	$B = 4.73 \times 10^{-15} \text{ cm}^3 \text{ s}^{-1}$ [102]
- Auger	Dziewior and Schmid [57] <i>Temperature dependence</i> [103]: $C_{n,p} = (A+B(T/T_0)+C(T/T_0)^2) \cdot (1+H \cdot \exp(-(n,p)/N_0))$ $A = 2.8 \times 10^{-31} \text{ cm}^6 \text{ s}^{-1}$, $2.8 \times 10^{-31} \text{ cm}^6 \text{ s}^{-1}$ $B = 0$, $-1.239 \times 10^{-32} \text{ cm}^6 \text{ s}^{-1}$ $C = 0$, $3.231 \times 10^{-32} \text{ cm}^6 \text{ s}^{-1}$ $H = 8$, 8 $N_0 = 2.5 \times 10^{17} \text{ cm}^{-3}$, $2.5 \times 10^{17} \text{ cm}^{-3}$
- SRH (bulk)	SRH model (Eq. (2.38)) <i>B-doped Cz Si (degraded lifetime τ_d due to BO-complexes):</i> $\frac{\tau_d}{\mu\text{s}} = 2 \cdot 7.675 \times 10^{45} \cdot \left(\frac{[\text{B}_s]}{\text{cm}^{-3}} \right)^{-0.824} \cdot \left(\frac{[\text{O}_i]}{\text{cm}^{-3}} \right)^{-1.748}$ [22, 23] $\Rightarrow \tau_{n0} = 1.1/2.03 \cdot \tau_d$; ⁴ $E_t = E_c - 0.41$; $k = 9.3$ [104]

⁴ Follows from the condition, that all lifetime measurements in the referenced literature have been performed at the same relative injection level $\Delta n/N = 0.1$.

surfaces in [105]. Due to its excellent passivation properties, Al_2O_3 becomes more and more important for Si surface passivation, especially on boron-doped surfaces due to its negative surface charges. Until now only one parameterization of Al_2O_3 passivated boron-doped surfaces is published to the authors knowledge [106], based on experimental data with a restricted range of boron surface concentrations from 2×10^{18} to $2 \times 10^{19} \text{ cm}^{-3}$. Thus, a more comprehensive parameterization will be introduced in Chap. 3.5.1.

Due to texturing, the solar cell surface increases and, thus, S_0 as well in comparison to the passivation on planar surfaces. Here, the difference in recombination is substantially greater than the difference in surface area of 1.73 [107]. Additionally, variations in the passivation quality on the pyramidal tips and valleys may occur due to the stress at the surface morphology and non-uniform doping concentrations, leading to a further increase of S_0 [107]. Therefore, for textured surfaces, the empirical factor of 3 for the increase of S_0 on textured surfaces is used according to [108], if only exists a parameterization for planar surfaces.

3.5.1 Surface recombination velocity S_0 of Al_2O_3 passivated silicon interfaces

Firstly presented in the 1980th for Si solar cell passivation schemes [62, 63], the dielectric Al_2O_3 provides an excellent level of surface passivation on highly B-doped Si surfaces [109, 110], due to a very good chemical saturation of the dangling bonds at the Si surface. In combination with its negative fixed charges of $-9.9 \times 10^{13} \text{ cm}^{-2}$ [111] it is also able to passivate effectively lowly B-doped Si surfaces [109, 110, 112]. First solar cell results featuring Al_2O_3 passivation have been presented in 2008 [113] and a comprehensive overview of Al_2O_3 passivation schemes is recently published by Dingemans and Kessels in [114].

As it is essential for accurate numerical simulation to have reliable values for the surface recombination velocities of Al_2O_3 passivated surfaces, dependent on the surface doping concentration, a parameterization is set up for B-doped Si surfaces.

As the surface recombination velocity S_0 depends, in general, on the doping concentration N_{surf} at the Si surface [115-117], a set of planar 10 Ωcm FZ n -Si test samples with different symmetrically diffused B-doped profiles have been produced and effectively passivated with 20 nm thick atomic layer deposited (ALD) Al_2O_3 . The doping profiles feature surface doping concentrations in the range from 3×10^{18} to

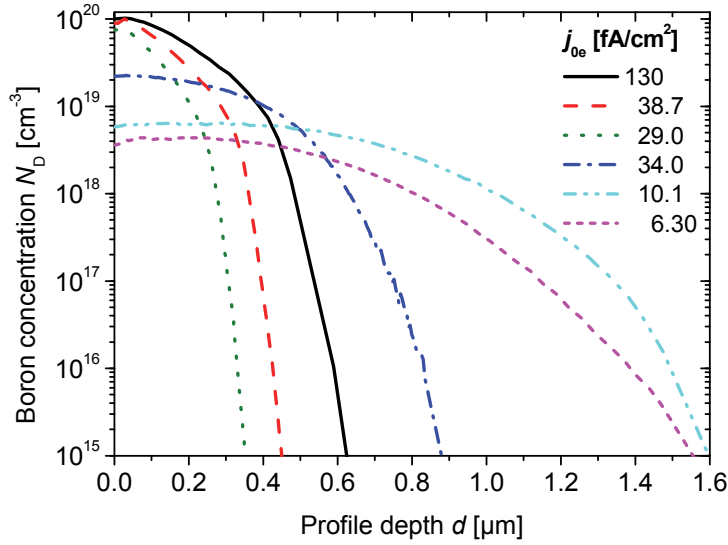


Fig. 3.9: Overview of the boron diffusion profiles used for the determination of S_0 . The profiles were determined by ECV measurements. The given j_{0e} are determined according to the method of Kane and Swanson [118].

$1 \times 10^{20} \text{ cm}^{-3}$, as shown in Fig. 3.9. The saturation current density j_{0e} of all samples have been determined according to Kane and Swanson [118]:

$$\frac{1}{\tau_{\text{eff}}} - \frac{1}{\tau_{\text{Aug}}} = \frac{1}{\tau_{\text{SRH}}} + \frac{2 \cdot j_{0e}}{q \cdot n_i^2 \cdot W} \Delta n \quad . \quad (3.10)$$

W is the thickness of the test wafer and j_{0e} the saturation current density of the emitter and the interface.

To determine S_0 of Al_2O_3 passivated non-diffused p -Si surfaces, test samples with bulk resistivities of 1, 10, and 100 Ωcm are effectively passivated as well. The upper limit of S_0 ($\Delta n = 10^{15} \text{ cm}^{-3}$) is determined via quasi-steady state photoconductance (QSSPC) measurements, as holds:

$$\frac{1}{\tau_{\text{eff}}} = \frac{1}{\tau_{\text{bulk}}} + \frac{2S_{\text{eff}}}{W} \geq \frac{2S_0}{W} \quad . \quad (3.11)$$

This estimate is most accurate, while the base doping is low. With increasing base doping, the Auger recombination in the bulk increases, which might lead to an increasing overestimation of S_0 .

Via numerical modeling, j_0 of a solar cell might be accessed according to the one-diode equation (3.3) under V_{oc} conditions:

$$j_0 = \frac{j_{sc}}{\exp\left(\frac{q V_{oc}}{k_B T}\right) - 1} = \frac{q[R(V_{oc}) - R(j_{sc})]}{\exp\left(\frac{q V_{oc}}{k_B T}\right) - 1} = j_{0e} + j_{0,residual} \quad (3.12)$$

Thereby, $j_{0,residual}$ includes the residual fraction of j_0 , which is not included in j_{0e} . The relation $j_{sc} = q[R(V_{oc}) - R(j_{sc})]$ follows from the equilibrium conditions of generation and recombination of free carriers at open-circuit and short-circuit conditions. In analogy to the separation of j_0 in j_{0e} and $j_{0,residual}$, the recombination rate can be divided by the same manner. Thus, j_{0e} can be expressed as

$$j_{0e} = \frac{q[R_e(V_{oc}) - R_e(j_{sc})]}{\exp\left(\frac{q V_{oc}}{k_B T}\right) - 1} \quad (3.13)$$

As the recombination rate R_e and all other shown parameters can be accessed via the simulation, the saturation current density j_{0e} can be determined [105]. Thereby, $R_e(S_0) = R_{e,SRH} + R_{e,Auger} + R_{e,surf}(S_0)$ consists of the sum of the SRH and Auger recombination and the surface recombination, which itself is a function of S_0 .

A simulation setup, according to the experimental test structures is set up, featuring the same base resistivity, thickness and bulk properties. The diffusion profiles (see Fig. 3.9) have been included in the simulation on the rear side, while the front side features a very shallowly doped Gaussian phosphorus profile, to calculate the diode characteristics. The emitter profile features a peak concentration of $N_{peak} = 1 \times 10^{16} \text{ cm}^{-2}$ and a depth $d = 0.1 \text{ } \mu\text{m}$ to reduce most effectively Auger and SRH recombination losses. To determine S_0 at the boron diffused rear side as the only free parameter in the simulation, it can be adjusted in order to achieve the same j_{0e} as determined via the experiment. The resulting S_0 values are shown in Fig. 3.10. The error bars of the determined S_0 values result of an estimated experimental error for the determination of j_{0e} of 10%.

Doping dependent surface recombination velocities are accounted for in Sentaurus Device, the device modeling tool of Sentaurus TCAD, according to the following parameterization:

$$S_0 = S_{const} \left[1 + S_{ref} \left(\frac{N_{D,surf}}{N_{ref}} \right)^\gamma \right] \quad (3.14)$$

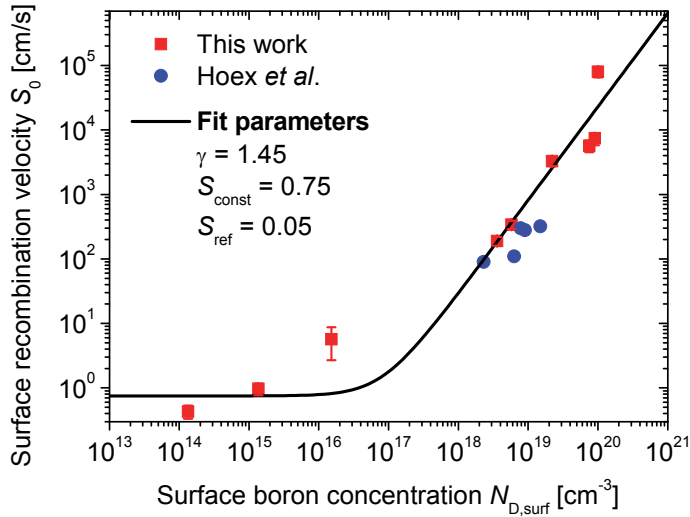


Fig. 3.10: The values obtained in this work for S_0 are plotted against the boron doping concentration $N_{D,surf}$ at the Si surface (squares). The fitting results are shown by using the parameterization according to Eq. (3.14) (line). Literature data of Hoex *et al.* [106] (blue) are in good accordance to the obtained data.

Here, $N_{D,surf}$ is the boron concentration at the Si surface, and S , S_{ref} and γ are free parameters. Latter can be determined by a least square fit to the experimental data, whereas the reference doping concentration holds $N_{ref} = 10^{16}$ cm/s.

The fitting results are shown in Fig. 3.10. In addition, the published S_0 values of Hoex *et al.* [106] are plotted, which are in very good agreement with the determined parameterization. In this doping range, the slope of $S_0(N_D)$, characterized by the parameter γ , is well reproduced. At low doping concentrations, especially the value at $N_D = 1.5 \times 10^{16}$ cm⁻³, shows stronger deviations, due to an increased Auger recombination within the non-diffused 1 Ω cm FZ *p*-Si material, as mentioned before.

3.5.2 From injection dependent lifetime to solar cell parameters

An example for the capabilities of numerical simulations for the evaluation of local lateral charge carrier flow effects, as occurring e.g. in multicrystalline (mc) Si solar cells, is given in the following.

In spatially resolved optical images of effectively passivated mc carrier lifetime samples, like e.g. performed with photoluminescence (PL) imaging under steady-state conditions, local lateral minority charge carrier flows through the base occur. Here, minority charge carriers flow from regions with high charge carrier density to regions featuring lower charge carrier densities. Therefore, PL images are blurred dependent on the local carrier lifetime, as the effect is limited by the bulk diffusion length. In mc Si solar cells, such currents occur as well, but additional majority carrier compensation currents occur in the emitter, flowing from high to low lifetime regions, dependent on

the operating conditions of the solar cell. Such effects are very difficult to quantify experimentally.

In Fig. 3.11 the standard domain of a mc Si solar cell is shown for j_{sc} , mpp and V_{oc} operating conditions in order to investigate this effect via 2D simulations. Within this simplified standard domain, two regions with significantly different charge carrier lifetime are assumed, representing the mc character of the wafer: one grain with $\tau = 100 \mu\text{s}$ ($w = 0 - 600 \mu\text{m}$) and the other featuring a tenfold lower carrier lifetime of $\tau = 10 \mu\text{s}$ ($w = 600 - 900 \mu\text{m}$). The excess charge carrier density is represented by the coloring and the current flow by the arrows, which are indicating the technical current direction (i.e. the opposite direction to the electron flow). A local flow of minority charge carriers through the base from high to low lifetime regions is observed in all considered operating conditions. Whereas these compensation currents are restricted by the minority carrier diffusion length, emitter currents are able to reallocate the charge carrier concentrations on a larger scale. Under V_{oc} conditions a significant current through the emitter from the high to the low lifetime regions can be observed, having its origin in the upper part of the bulk region, as can be seen in Fig. 3.11 (lowermost). In contrast, in j_{sc} and mpp conditions the current flows to the contacts, due to the gradient of the Quasi Fermi level. In order to quantify the impact of the high carrier lifetime region, another simulation has been set up, featuring a homogeneous carrier lifetime of $\tau = 10 \mu\text{s}$ through the entire width of the standard domain. It turned out that due to the neighboring region featuring a higher carrier lifetime, the integrated excess carrier density is enhanced by 6% under j_{sc} , by 23% under mpp and by 63% under V_{oc} conditions. As under j_{sc} conditions no increase can be observed close to the emitter region, the resulting enhancement is solely caused by a minority carrier flow through the base. Under mpp and V_{oc} conditions both occurs, a compensation current passing the base region and a current passing the emitter. These compensation currents were experimentally determined in [119].

The results of these considerations play an important role e.g. in a recently presented method to analyze spatially resolved solar cell efficiency limitations of mc bulk material due to bulk recombination [120, 121]. Here, spatially resolved PL images, determining the local bulk lifetimes $\tau_{\text{bulk},xy}$ of effectively surface passivated Si wafers, are combined with solar cell simulations, performed with the 1D numerical simulation tool PC1D [122]. This procedure allows the comparison of different material qualities directly on efficiency level, without mixing material limitations and limitations due to the solar cell structure, as occurring by solar cell measurements. Further details of the method may be found in [120, 121]. PL imaging is well suited for solar cell

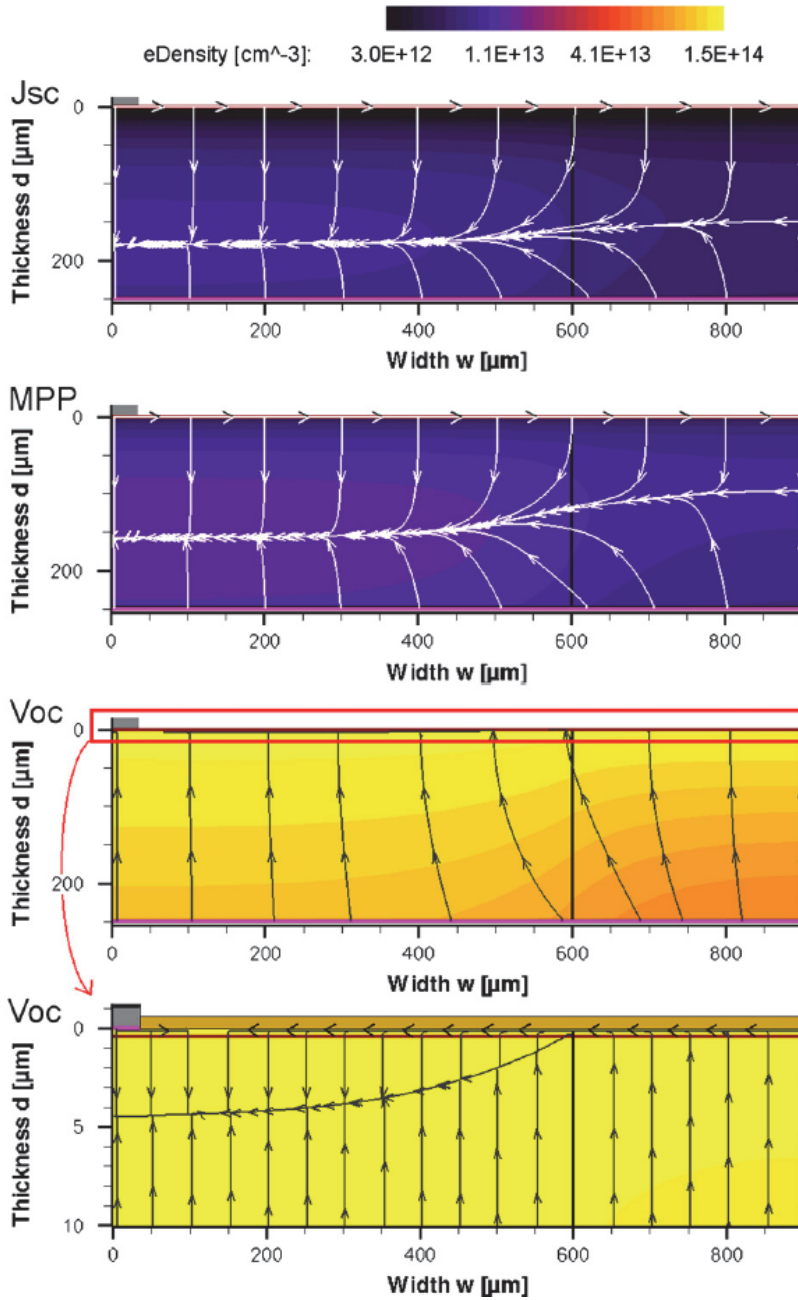


Fig. 3.11: Numerical simulations of the standard domain of a multicrystalline p -Si solar cell with n^+ -emitter at the front side, metal contact in the upper left corner and a full-area Al back surface field. The bulk lifetime for $w = (0 - 600) \mu\text{m}$ holds $100 \mu\text{s}$, whereas for $w = (600 - 900) \mu\text{m}$ it holds $10 \mu\text{s}$. Shown are the electron density distribution (color legend) and the electron current density (indicated by the arrows in technical current direction; the number of arrows is arbitrary) for j_{sc} , mpp and V_{oc} conditions. The calculations have been published in [121].

predictions, as they feature the same compensating current effects, as observed in the numerical simulations. Results are exemplarily shown in Fig. 3.12 for a multicrystalline p -Si wafer featuring a lowly doped front emitter with a sheet resistance $R_{sh} = 90 \Omega/\text{sq}$ and a full-area Al back surface field (BSF). The measurements have been performed after light induced degradation. For better comparison of the different

parameter losses, the images are scaled to the maximum achievable value for non-limiting bulk lifetime, respectively. For the images showing V_{oc} , j_{sc} and PPF_{bulk} , the minimum features 94% of the maximum value, and for $P\eta_{bulk}$ the minimum features 88% of its maximum value. Here, PPF_{bulk} denotes the maximum fill factor, only limited by the recombination in the bulk material and, thus, $P\eta_{bulk}$ the corresponding maximum efficiency. It can be observed that PPF_{bulk} is reduced at the grain boundaries and dislocation clusters due to the injection dependent lifetime. Compared to the fill factor FF_0 of an ideal diode, about 1% absolute is globally lost, limiting the actual fill factor FF of the solar cell.

For comparison to measured results of the completely processed solar cells, the spatially resolved data shown in Fig. 3.12 were averaged to global values. As no emitter compensation currents occur under j_{sc} conditions, these data were averaged arithmetically. Under V_{oc} and PPF conditions, the emitter compensation currents were simulated via Spice network simulations [123] and the data were averaged on lifetime level to global values via the harmonic mean in the diffusion length. Results are presented in Tab. 3.3, indicating very good agreement of measurements and via PC1D or Sentaurus Device performed simulations. To account for the global injection dependent lifetime $\tau_{bulk}(\Delta n)$ of the wafer in Sentaurus Device, a measurement of $\tau_{bulk}(\Delta n)$ has been fitted via two independent SRH defect levels and adopted in the device simulation. An external series resistance has been assumed in order to simulate the FF correctly.

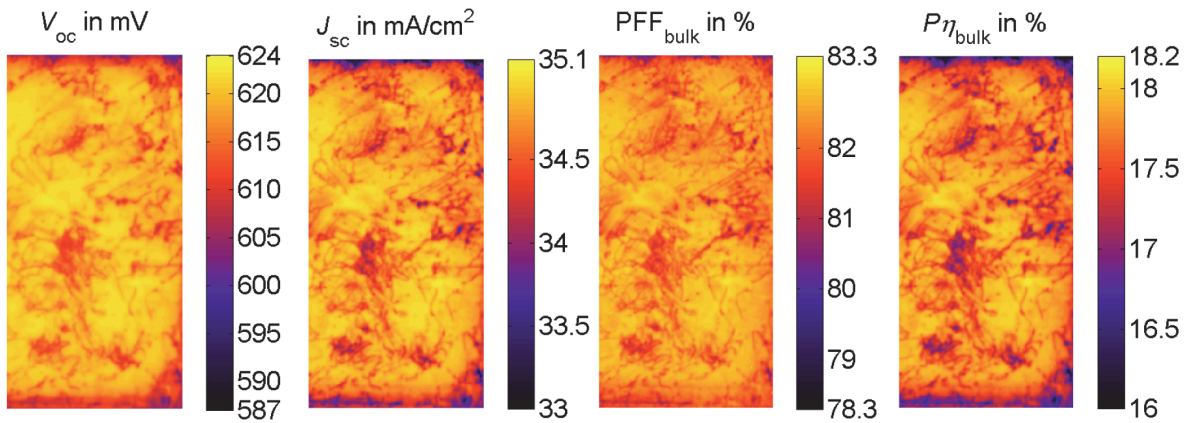


Fig. 3.12: Analysis of a multicrystalline p-Si wafer with full-area Al BSF. Shown are spatially resolved images of V_{oc} , j_{sc} , PPF_{bulk} and $P\eta_{bulk}$, determined from the measured lifetime and the solar cell simulation. Each image is scaled to its highest lifetime (FF_0 is used as maximum for the highest achievable voltage). The minimum is 94% of that maximum for the V_{oc} , j_{sc} and PPF_{bulk} images and 88% for the $P\eta_{bulk}$ image. The figure has been taken from [120].

Tab. 3.3: Comparison of simulation results established by PC1D and Sentaurus Device to experimentally measured data. The results are published in [120].

	Measured data	PC1D	Sentaurus
Open-circuit voltage V_{oc} [mV]	619 ± 1	617	619
Short-circuit current j_{sc} [mA/cm ²]	34.7 ± 0.1	34.7	34.7
Fill factor FF [%]	78.8 ± 0.2	82.3 (PFF_{bulk})	78.9
Efficiency η [%]	16.9 ± 0.0	17.6 ($P\eta_{bulk}$)	17.0

4 Free carrier absorption models for silicon solar cell applications

Free carrier absorption (FCA) is a parasitic absorption process which might reduce significantly the amount of photons, potentially generating electron-hole pairs in highly doped Si. Existing parameterizations have been introduced in Chap. 2.6. Here, the presented parameterizations will be evaluated in the wavelength range $\lambda = 1.0 - 2.0 \mu\text{m}$, including the relevant range for Si solar cells. New parameters will be presented in order to enhance the quantification of photogeneration losses. The results of this chapter are published in [124].

4.1 Motivation

As mentioned in Chap. 2.6, most free carrier absorption parameterizations have been set up by evaluating absorption data in the range $\lambda \geq 4 \mu\text{m}$ and, thus, far beyond the range of $\lambda = 1.0 - 1.2 \mu\text{m}$, which is relevant for Si solar cells. Due to simplicity, the models of Schroder [69] and Green [70] are based on an elementary formula structure, assuming linearity in the doping concentration N and assuming a fixed mobility μ , which is not dependent on N (see Eq. (2.47)). This might cause a good agreement to experimental data in the evaluated wavelength range, but could cause deviations in other considered ranges. However, Isenberg [75] figured out inconsistencies by using the classical model of Schroder [69] at $\lambda = 5 \mu\text{m}$ and developed a physically more profound parameterization as given in Eq. (2.50), based on more precise models [73, 74]. So far it is unclear, which model should be used for modeling free carrier absorption effects within Si solar cells.

In the following, the presented FCA parameterizations will be evaluated in the wavelength range $\lambda = 1.0 - 2.0 \mu\text{m}$ by comparing simulated optical reflection curves with a broad set of experimental data for samples featuring different boron and phosphorus diffused profiles. Comparing reflection curves enables the evaluation of FCA effects directly in the wavelength range, relevant for Si solar cells. In this context, parameters for the simplified model are optimized in order to achieve an enhanced description of the influence of FCA in Si solar cells for the considered wavelength range.

4.2 Sample preparation

To evaluate the influence of FCA via reflection measurements, test samples were produced on 100 Ωcm p -type Si base material, as shown in Fig. 4.1. The samples feature a thickness of 250 μm and were textured on the front side through a lithographic process with inverted pyramids to increase the effect of FCA by extending the path length of the incident light. Additionally, a precisely defined surface is achieved, enhancing the accuracy of numerical simulation of the structure. An 80 nm thick SiN_x anti-reflection layer has been deposited through plasma enhanced chemical vapor deposition (PECVD) at the front side, while at the shiny etched planar rear surface, 110 nm SiO_2 have been thermally grown. On top of SiO_2 layer at the rear side, a 1 μm silver layer has been thermally evaporated to achieve a high internal reflection to further extend the optical path length. Although four samples did not receive any diffusion profile and act as reference for the numerical simulations, the rest of the samples feature different boron and phosphorus diffused profiles covering a broad range of different sheet resistances. Two different sample structures have been fabricated: (a) only the rear side has been diffused and (b) front and rear side feature the same diffusion profile. Using diffused doping profiles instead of samples with constant doping reduces the accuracy of the FCA calculations. On the other hand, this setup with diffused profiles is the relevant one for solar cells based on crystalline Si.

The diffusion profiles used are shown in Fig. 4.2. The sheet resistance values R_{sh} are the mean of two or three four-point probe measurements at different positions of the planar sample side, and are given together with their standard deviation of the mean.

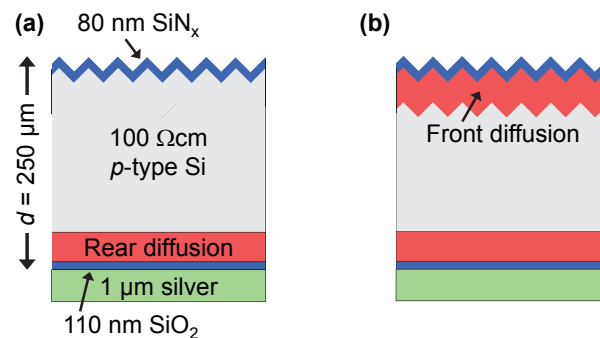


Fig. 4.1: Schematic sketch of the test samples produced for the analysis of free carrier absorption (FCA) losses. Two variations have been set up: (a) only the rear side has been diffused and (b) front and rear side feature the same diffusion profile. The used boron and phosphorus profiles are shown in Fig. 4.2.

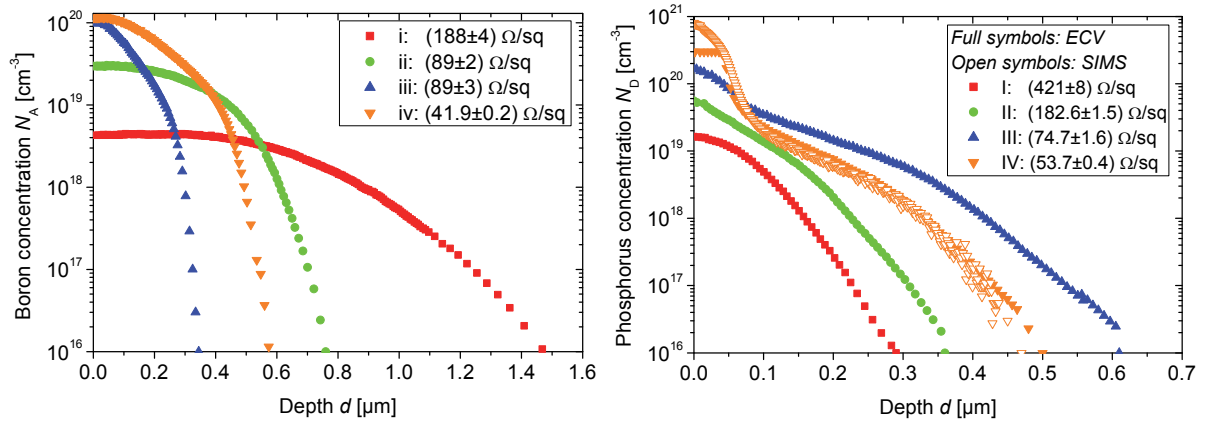


Fig. 4.2: Boron (left) and phosphorus (right) diffusion profiles, used for the evaluation of FCA losses. The profiles have been measured via ECV (closed symbols) and SIMS (open symbols).

To avoid measurement uncertainties due to the high-low junction structure of both-sided B diffused samples, only one sided diffused samples have been measured. The profiles have been measured by electrochemical capacitance–voltage (ECV) measurements, using a WEP-CVP21 profiler and a diluted ammonium bifluoride (NH_4HF_6) electrolyte [125]. Because the first three to five measurement points of ECV measurements in general show parasitic influences and do not reflect the real doping concentration, the profile curves have been extrapolated to the surface. As in ECV measurements the electrically active concentration of B and P diffusion profiles is detected, the P doping profile (IV) with a very high surface concentration above the solubility limit of $3 \times 10^{20} \text{ cm}^{-3}$ [126, 127], shown in Fig. 4.2 (right, open symbols), has been measured additionally with secondary ion mass spectroscopy (SIMS) for comparison. Within a profile depth of $d = 0 - 50 \text{ nm}$ the gap of electrically active and total P concentration, measured by SIMS, can be clearly seen. An analytical calculation of R_{sh} of profile (IV) leads to $R_{\text{sh,ECV}}(\text{IV}) = 54.7 \text{ } \Omega/\text{sq}$ for the ECV measured profile, which is in acceptable accordance to the measured value of $R_{\text{sh,meas}}(\text{IV}) = 53.7 \text{ } \Omega/\text{sq}$. For the SIMS measured profile, the analytical calculation yields $R_{\text{sh,SIMS}} = 50 \text{ } \Omega/\text{sq}$, as expected far below the measurement. For all these calculations, the mobility model by Klaassen [100, 101] has been used. As FCA depends on the electrically active carrier concentration, the ECV measured profile has been used for the calculations.

4.3 Simulation setup

To evaluate the influence of FCA absorption resulting from different B and P doping profiles (see Fig. 4.2), the sample structure has been set up in a numerical device simulator. A 3D structure has been used to track the light paths within the Si material

through a raytracer, as explained in Chap. 3.4. This is able to consider an implemented arbitrary functional behavior of α_{FCA} . The 80 nm thick SiN_x anti-reflection coating has been simulated via the transfer matrix method, to consider wave optical effects. More details are given in Chap. 3.4.1. The refractive index of SiN_x has been determined by spectral ellipsometry from planar reference samples. In the analyzed spectral range, the applied refractive index of SiN_x varies only slightly from $n = 2.02$ at $\lambda = 1 \mu\text{m}$ to $n = 2.01$ at $\lambda = 2 \mu\text{m}$. Absorption within the SiN_x thin film occurs only for $\lambda < 0.5 \mu\text{m}$. In the Si bulk, the Lambert-Beer law [128] has been applied. A boron base doping concentration of $N_A = 1.34 \times 10^{14} \text{ cm}^{-3}$ has been applied, which corresponds to 100 Ωcm bulk material. The measured doping profiles are applied to each face of the inverted pyramids. This constitutes an idealization, as the diffusion at the edges of the inverted pyramids is probably different compared with a flat surface. However as the pyramids are rather large ($18.5 \times 18.5 \mu\text{m}$ base area), the influence of the edges is rather small. At the rear side of the sample structure, the Phong model (introduced in Chap. 3.4.2) has been used to describe the slight surface roughness of the shiny etched rear surface. The complex refractive index of Si is taken from [84]. As shown by Isenberg and Warta [75], the change of the real part n of the refractive index of Si because of free carriers in the doping (10^{15} to 10^{21} cm^{-3}) and the spectral range ($1 \mu\text{m} < \lambda < 2 \mu\text{m}$) treated is smaller than 15%, which is neglected, compared with the change of its imaginary part k by several orders of magnitude. Physical models have been used according to Tab. 3.2.

The rear side of the numerical simulation setup has been calibrated, as this is the only unknown set of free parameters. This is done through a reference cell, which does not have any doping diffusion and, thus, features a very high measured $R_{\text{sh,ref}} = (4000 \pm 300) \Omega/\text{sq}$. The measured spectral reflectance of the reference sample is shown for the wavelength range $\lambda = 1.0 - 2.0 \mu\text{m}$ in Fig. 4.3 (black, line). With a Phong coefficient $\omega = 800$ and a reflection rate of $R = 0.990$ at the rear side of the sample, excellent agreement with the measured reflectance could be achieved, as can be seen in Fig. 4.3 (black, dash). This setup is used for all simulations presented in this chapter. The simulation of the reference sample is independent of the used FCA model, as FCA does not have any effect on the very lowly doped 100 Ωcm bulk material. In the following simulation results, only the FCA models are varied.

4.4 Comparison of existing parameterizations

In the following subsections, a comparison of simulated reflection data using the existing FCA parameterizations to experimentally determined reflection data is presented. The spectrally resolved reflectance has been measured by a spectral

photometer Cary500i from Varian. The measured sample is illuminated by a monochromatic light beam and the reflected light is detected by a lead sulfide (PbS) photodiode. To consider the diffuse reflected light as well, the sample has been placed in a highly reflective Ulbricht sphere, covered with the diffuse reflecting material polytetrafluoroethylene, commercially known as Teflon. Before each measurement, for calibration reasons, a baseline without sample and a measurement with a white standard had been performed.

As the test samples feature textured surfaces, light coupled into the samples passes a certain lateral distance until it might be coupled out again after multiple internal reflections. This effect could potentially lead to underestimated reflectance, as light could leave the sample outside the measurement area. To quantify this potential reflection loss, the fraction of illuminated and measured area has been varied from 0.02 – 0.5, more precisely the illuminated area has been varied by changing the aperture of the incident light beam. Thereby, no difference in the reflection data could be observed, indicating no reflection losses by this effect. For the presented measurements, an illumination fraction of 20% has been used.

The optical spectroscopy has been performed by a Fourier-spectrometer with detectors sensitive to wavelengths between 400 nm and 2200 nm. Cross check reflection measurements have been performed at a second reflection measurement setup using a Fourier transformation spectrometer, allowing the measurement of the hemispheric and the diffuse part of the reflectance. The measurements yield the same results within an error of ~1% absolute of the reflectance and, thus, confirming the correctness of the measurements.

4.4.1 Free carrier absorption in boron doped regions

In Fig. 4.3, the reflection measurements of the reference sample (black, line) and of the test samples with the corresponding Boron diffusion profiles (colored, lines), given in Fig. 4.2 (left), are shown. Thereby, the left column shows results for the test samples featuring only a diffusion at the rear side, while the right column shows the samples featuring diffusions at the front and rear side. Here and in the following figures of this chapter, the indication “*p*-Si” and “*n*-Si” denote the doping type of the diffusion profile, whereas the base doping type is not changed. The base doping concentration is sufficiently low, not contributing to FCA.

In the first row of Fig. 4.3, calculated reflection curves are shown including the FCA parameterization of Schroder, as given in Eq. (2.48), in the following denoted as

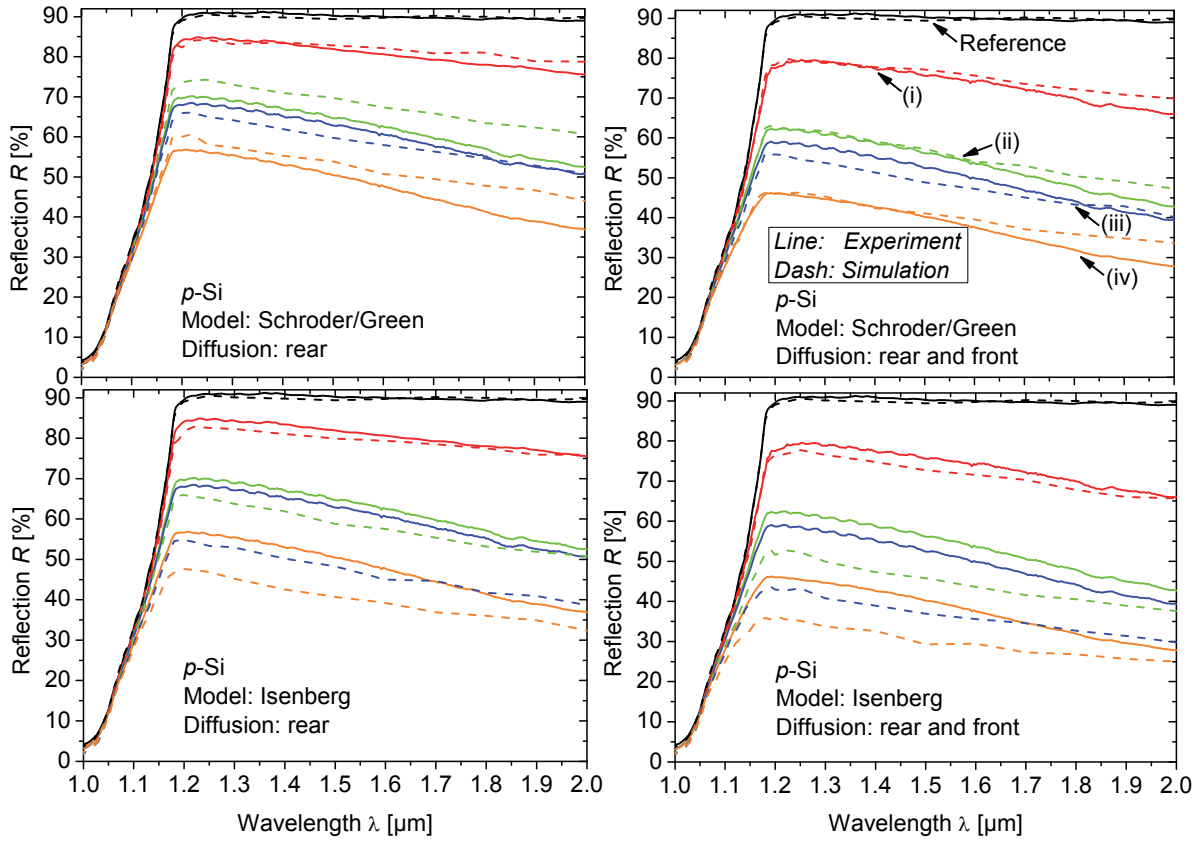


Fig. 4.3: Comparison of experimentally determined (line) and calculated (dash) reflection curves for samples featuring different boron diffusion profiles, which can be seen in Fig. 4.2. The influence of FCA is calculated with different models in the different rows (dash), respectively. Results are shown for test samples featuring only rear side diffusions (left) or diffusions on both sides (right) (cf. Fig. 4.1).

Schroder model. Green presented the same parameterization for *p*-Si. The second row shows calculations of reflection curves, including the parameterization of Isenberg *et al.* as shown in Eq. (2.50), and named *Isenberg model* in the following. Calculation results are shown dashed in the same color, as the corresponding experimental result.

Results calculated with the Schroder model for the both-sided diffused samples in Fig. 4.3 (above, right) show good agreement to the experimental data in the range $\lambda = 1.0 - 1.2 \mu\text{m}$. Only profile (iii) shows a deviation of about 5% absolute around $\lambda = 1.2 \mu\text{m}$. Also for the rear side diffused samples, the agreement is fairly good, not exceeding a difference of 5% in reflection. But it can be noticed, that the slope of calculated data for one-sided and both-sided diffused samples in the range $\lambda = 1.2 - 2.0 \mu\text{m}$ are slightly different to the experimental data, leading to an increasing mismatch towards $\lambda = 2.0 \mu\text{m}$.

Having a look at the reflection results based on the Isenberg model (Fig. 4.3, below), it can be observed that for samples with the very lowly diffused profile (i) similar results

as for the Schroder model are achieved. The slope in the range $\lambda > 1.2 \mu\text{m}$ might fit even a little bit better. In samples with the more heavily doped B diffusions (ii) – (iv) the Isenberg model tends to result in an overestimation of FCA in the range $\lambda = 1.0 - 1.2 \mu\text{m}$. With increasing FCA influence, the deviation of the slope within simulation and experiment at $\lambda > 1.2 \mu\text{m}$ increases.

However, examining the entire set of data, results calculated with the Schroder model show better accordance to the set of experimental data in the considered wavelength range, than the results calculated with the Isenberg model.

4.4.2 Free carrier absorption in phosphorus doped regions

In Fig. 4.4 the experimentally determined reflection curves (line) are shown for the samples featuring different phosphorus diffusion profiles, given in Fig. 4.2 (right), for one-sided (left) and both-sided (right) diffused samples. The calculated results (dash) feature the different FCA models; each row is calculated with the same model.

While calculations with the Schroder model feature good accordance for samples with B doped diffusions, as shown in the previous chapter (see Fig. 4.3), in Fig. 4.4 (above) for samples with P doped diffusion profiles, the model underestimates the influence of FCA by far. All calculated reflection curves are well above the experimental data at $\lambda = 1.2 \mu\text{m}$, exceeding the results by 5 to 20% absolute. Here, the slope of the calculated data at $\lambda = 1.2 - 2.0 \mu\text{m}$ again differs from the slope of the experimental data.

The results calculated with the Green model (Fig. 4.4, middle) feature a contrary behavior. While the accordance to the experimental data of the lowest doped samples (with profile (I)) is better, the Green model tends to overestimate the influence of FCA for most profile configurations, yielding a difference to the experimental data by about 10% absolute. Same tendency can be seen for the results calculated with the Isenberg model (Fig. 4.4, below). For the samples with profiles (II) – (IV), in all cases the effect of FCA is significantly overestimated in the considered wavelength range, even more than by the results calculated with the Green model.

While the slopes of the calculated results from the Schroder and the Isenberg model feature the behavior with a slightly lower slope than observed in the experimental data, the slope of the calculated results using the Green model tends to be slightly too high, due to the cubic behavior in wavelength (see Eq. (2.49)).

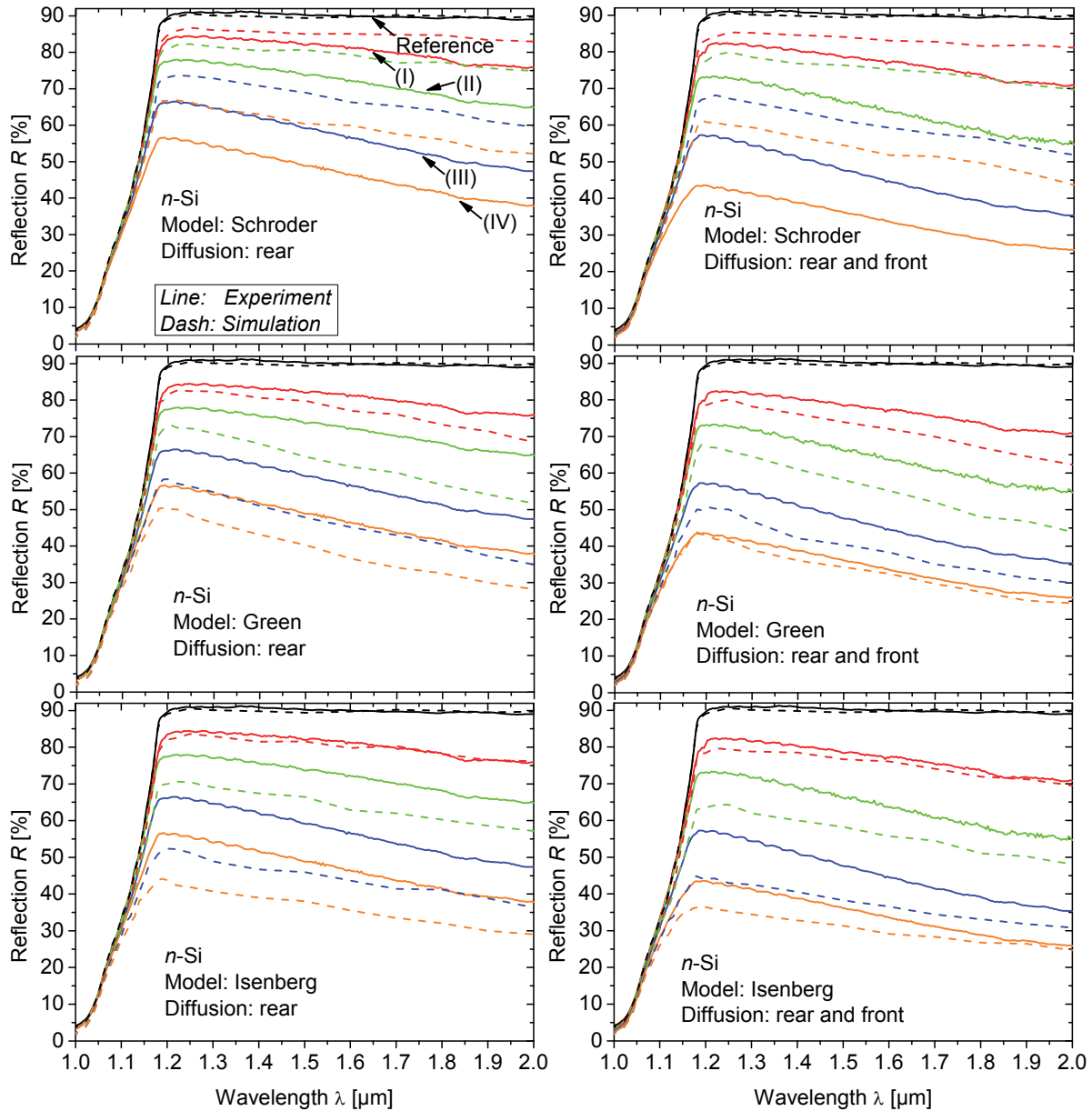


Fig. 4.4: Comparison of experimentally determined (line) and calculated (dash) reflection curves for samples featuring different phosphorus diffusion profiles, which can be seen in Fig. 4.2. The influence of FCA is calculated with different models in the different rows (dash), respectively. Results are shown for test samples featuring rear side diffusions (left) or diffusions on both sides (right) (cf. Fig. 4.1).

4.5 Discussion

From the evaluated data shown in Fig. 4.3 and Fig. 4.4 can be concluded that the simulations featuring the FCA parameterizations from literature (see Chap. 2.6) give deviating results. Whereas the results calculated with the Schroder model for the B diffused samples are in fairly good accordance with the experimental data, simulations with the Isenberg model overestimate the influence of FCA in the considered wavelength range. For the calculations of the samples with P diffusion profiles, the

Green model appears to describe the influence of FCA best within the considered models, even though a resulting difference within experimental data and simulations of $\sim 10\%$ occurs. Calculation results with the Schroder model underestimate the effect of FCA, whereas with the Isenberg model the influence of FCA is again significantly overestimated. Although the Isenberg model is the parameterization based on the most enhanced physical model, it does not seem to be appropriate in the wavelength range considered in this study. However, calculations with all presented parameterizations show deviations of the slope in the wavelength range $\lambda = 1.2 - 2.0 \mu\text{m}$ because of the different exponential dependence of α_{FCA} on λ .

Because of the observed discrepancies between the modeled and measured data for the wavelength range $\lambda = 1.2 - 2.0 \mu\text{m}$ a new set of parameters is determined. Based on the simple functional structure for the description of FCA losses, given in Eq. (2.47), a variation of $C_{\text{FCA},n}$, $C_{\text{FCA},p}$, ξ , and φ has been set up for the entire set of data, consisting of 16 reflection curves: eight curves from the test samples featuring B diffusion profiles and eight curves from the test samples featuring P diffused profiles. For each parameter set p' (samples with B or P doped profiles, respectively) the spectral reflectance $R_{\text{sim},i}(p', \lambda)$ ($i = 1, \dots, n'$) of all n' samples have been simulated and the mean absolute errors MAE to the experimentally determined reflection curves $R_{\text{measured},i}(\lambda)$ ($i=1, \dots, n'$), respectively, have been determined:

$$MAE = \frac{1}{n'} \cdot \sum_{i=1}^{n'} \left(\frac{1}{m'} \sum_{j=1}^{m'} |R_{\text{sim},i}(p', \lambda_j) - R_{\text{measured},i}(p', \lambda_j)| \right) . \quad (4.1)$$

Equal weight has been given to each wavelength λ_j ($j = 1, \dots, m'$). The MAE of the entire set of data is minimized for the following sets p'_{min} of parameters:

$$\begin{aligned} \frac{\alpha_{\text{FCA},p}}{\text{cm}^{-1}} &= 2.6 \cdot 10^{-18} \cdot \left(\frac{\lambda}{\mu\text{m}} \right)^{2.4} \cdot \frac{p}{\text{cm}^{-3}} \quad \text{and} \\ \frac{\alpha_{\text{FCA},n}}{\text{cm}^{-1}} &= 1.8 \cdot 10^{-18} \cdot \left(\frac{\lambda}{\mu\text{m}} \right)^{2.6} \cdot \frac{n}{\text{cm}^{-3}} , \end{aligned} \quad (4.2)$$

valid for the wavelength range $\lambda = 1.0 - 2.0 \mu\text{m}$. The spectral reflectances calculated with this set of parameters are shown in Fig. 4.5 for the set of samples featuring B diffusions (above) and for the set of samples featuring P diffusions (below). Whereas the reflection data feature a maximum deviation of $\sim 5\%$ absolute within experimental and simulated data, the overall agreement is significantly enhanced. Because of the adapted exponential behavior, the slopes of the calculated data coincide very well with

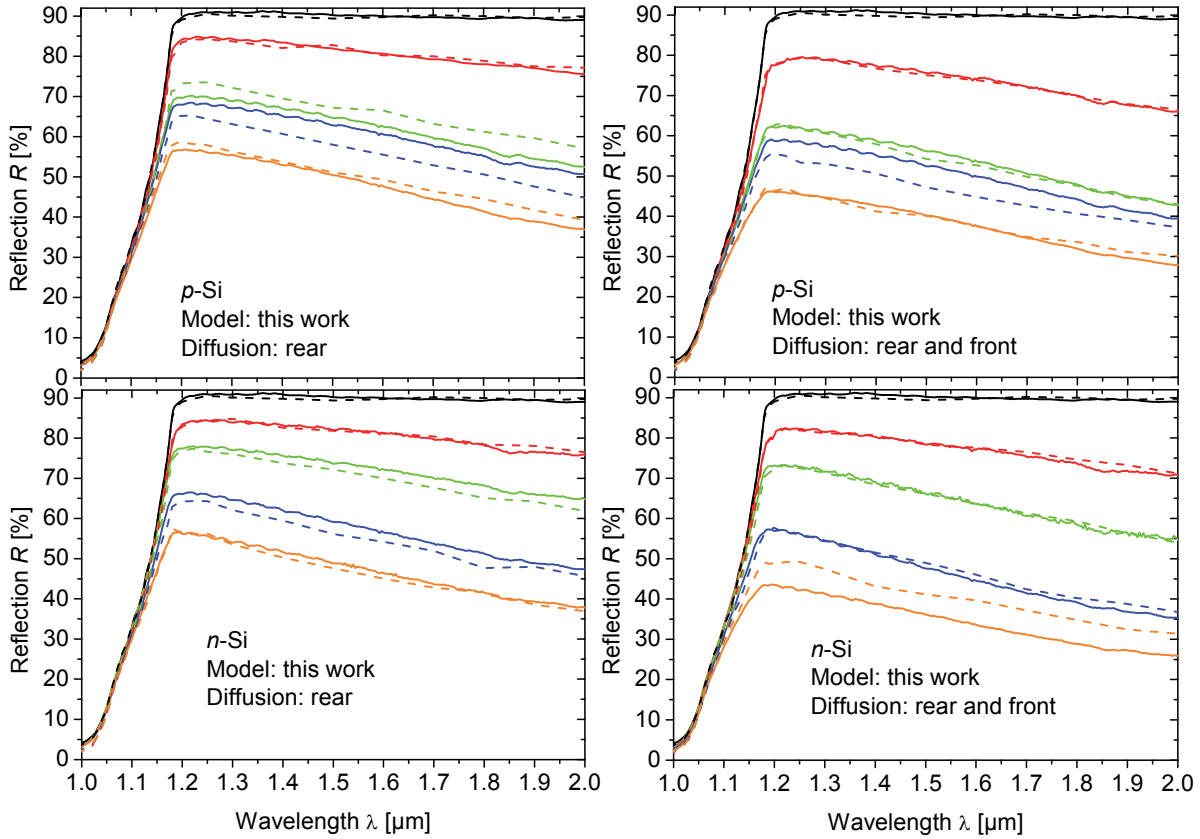


Fig. 4.5: Comparison of experimentally determined (line) and calculated (dash) reflection curves for samples featuring different boron (above) and phosphorus (below) diffusion profiles, which can be seen in Fig. 4.2. The influence of FCA is calculated with the set of parameters, given in Eq. (4.2).

the experimental data, indicating an exponential behavior of the wavelength of about 2.5 for n - and p -Si in contrast to previously published assumptions.

In Fig. 4.6 experimental data given in literature (symbols) are plotted for Si:P in comparison with the parameterization presented in this study (lines), and the parameterization of Green (dashed lines). As no experimental data are available for p -type Si for $\lambda < 2.4 \mu\text{m}$, a comparison with the presented parameterization is not possible. For n -Si, a detail of the experimental data from Spitzer [71] (symbols), which is an excerpt of Fig. 2.5. For comparison, the parameterization presented in this work (solid lines) and the parameterization of Green (dashed lines) are plotted. It can be observed that the parameterization of Green, which is based on these data, is for $N_D < 10^{18} \text{ cm}^{-3}$ higher than the experimental data at $\lambda = 1.2 - 2.0 \mu\text{m}$, overestimating FCA slightly. This result is consistent with the observations made in Fig. 4.4. Here, Eq. (4.2) seems to fit slightly better the experimental data. For $N_D > 10^{18} \text{ cm}^{-3}$ contrary behavior can be observed, the Green model appears to fit the data best. But as the experimental data for $N_D = 6.1 \times 10^{18} \text{ cm}^{-3}$ and $1 \times 10^{19} \text{ cm}^{-3}$ might be incorrect for the

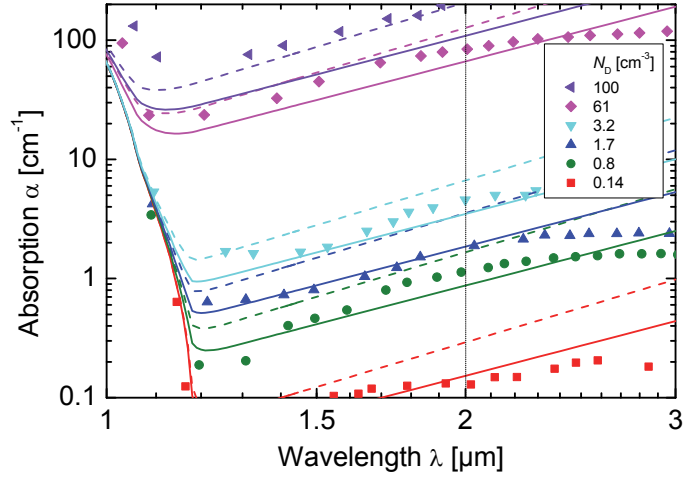


Fig. 4.6: Comparison of the FCA parameterization (solid lines) determined in this work for $< 2.5 \mu\text{m}$ and the Green parameterization (dashed lines) for $< 2.5 \mu\text{m}$, which is set up based on the shown experimental data [71] (symbols) for P doped Si.

following reason. At $\lambda = 1.0 - 1.2 \mu\text{m}$ the measured absorption coefficient α is significantly higher in comparison with the very precise $\alpha_{\text{Si}}(\lambda)$ data for band-to-band absorption from Green [84] probably indicating an overestimation of the measured α . Thus, α_{FCA} might be overestimated for the experimental values of Spitzer for these doping concentrations. Toward high doping concentrations, deviations might be caused as well by the negligence of nonlinearity effects in n . Linear behavior in n is assumed in the parameterizations for both this work (see Eq. (4.2)) and that of Green (see Eq. (2.49)). As well for the highest doping concentration $N_{\text{D}} = 10^{19} \text{cm}^{-3}$ the latter parameterization predicts an absorption coefficient α_{FCA} smaller than the experimental data (for $\lambda = 1.0 - 1.7 \mu\text{m}$). A change of the real part of the refractive index at high doping concentrations might not be the reason for the deviations, as the influence is very small for $\lambda < 2 \mu\text{m}$ (see Fig. 3 in [75]). In addition, the use of the Phong-model is deemed to be related neither to the deviations at high doping concentrations, as very good accordance of simulated and experimentally determined reflection data of the reference sample could be achieved (see Fig. 4.3).

From the numerical simulation setup, the photogenerated current density loss Δj_{ph} caused by FCA can be quantified. In Fig. 4.7, Δj_{ph} is shown versus the area doping concentration N_{dose} , consisting of the integral of the doping concentration N_{dop} over the sample thickness. Here, the base doping concentration has been varied and, thus, N_{dose} consists of the product of N_{dop} and the sample thickness. Results from simulations with Eq. (4.2) are plotted (line) in comparison to the results by applying the different parameterizations discussed above. Additionally, the relative deviation to the results calculated with Eq. (4.2) are shown (Fig. 4.7, above). Δj_{ph} from calculations with the

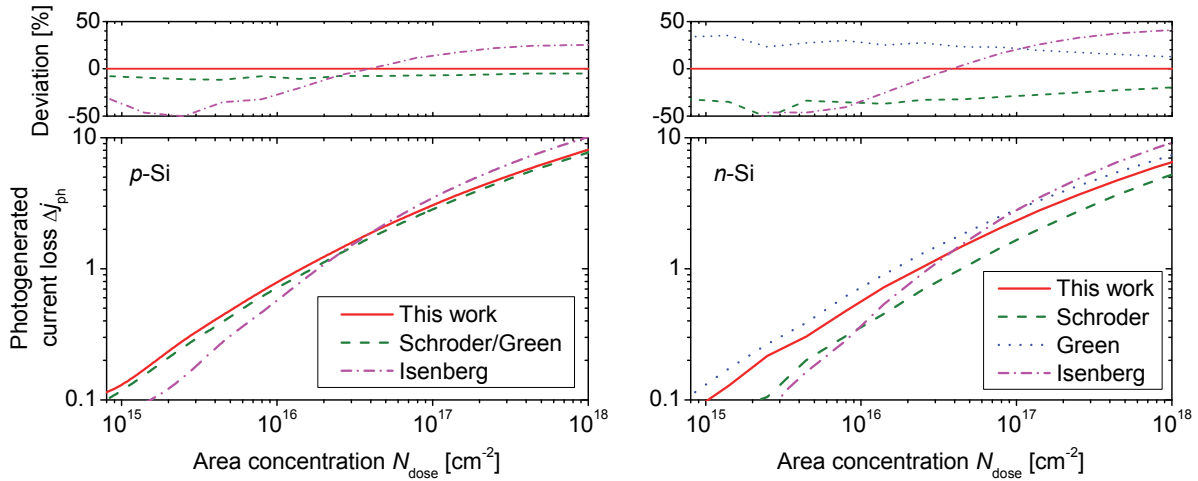


Fig. 4.7: Photogenerated current density loss Δj_{ph} caused by FCA versus the area doping concentration N_{dose} , consisting of the integral of the doping concentration N_{dop} over the sample thickness. Results from simulations with Eq. (4.2) and are plotted (line) in comparison to the results by applying the different parameterizations discussed before.

Schroder model is underestimated by 10% over the whole considered N_{dose} range. Due to the non-linearity of the Isenberg model, its application leads to up 50% lower Δj_{ph} for $N_{dose} < 4 \times 10^{16} \text{ cm}^{-2}$. For $N_{dose} > 4 \times 10^{16} \text{ cm}^{-2}$, Δj_{ph} might be up to 25% higher than the presented parameterization.

In Fig. 4.8, Δj_{ph} by using Eq. (4.2) is exemplarily shown for varied Gaussian profiles on textured (above) and planar (below) surfaces for both, B (left) and P doped (right) Si. Due to the increased surface for textured surfaces and, thus, an increased doping concentration after diffusion, the effect of FCA is significantly increased as well. Furthermore, a significantly increased optical refraction at textured front surfaces leads to an increased path length within the material and to multiple internal reflections, causing an increased influence of FCA as well. The FCA losses for the examined diffusion profiles given in Fig. 4.2 have been quantified as well and are shown in Tab. 4.1. For B doped profiles, Δj_{ph} varies between $< 0.05 \text{ mA/cm}^2$ for the very shallowly doped profile (i) on planar surfaces, up to a significant calculated influence of $\Delta j_{ph} = 0.6 \text{ mA/cm}^2$ for profile (iv) on textured surfaces. The calculations show for the considered P doped profiles a loss range of $\Delta j_{ph} = < 0.05 - 0.4 \text{ mA/cm}^2$. If Δj_{ph} of profile (IV) is calculated via the surface corrected SIMS profile instead of the ECV profile, the loss caused by FCA would be overestimated within 0.1 and 0.2 mA/cm^2 . Thus, when SIMS measurements of P doped profiles are included in numerical device simulations, profile concentrations above $3 \times 10^{20} \text{ cm}^{-3}$ should be corrected, according to its solubility limit [126].

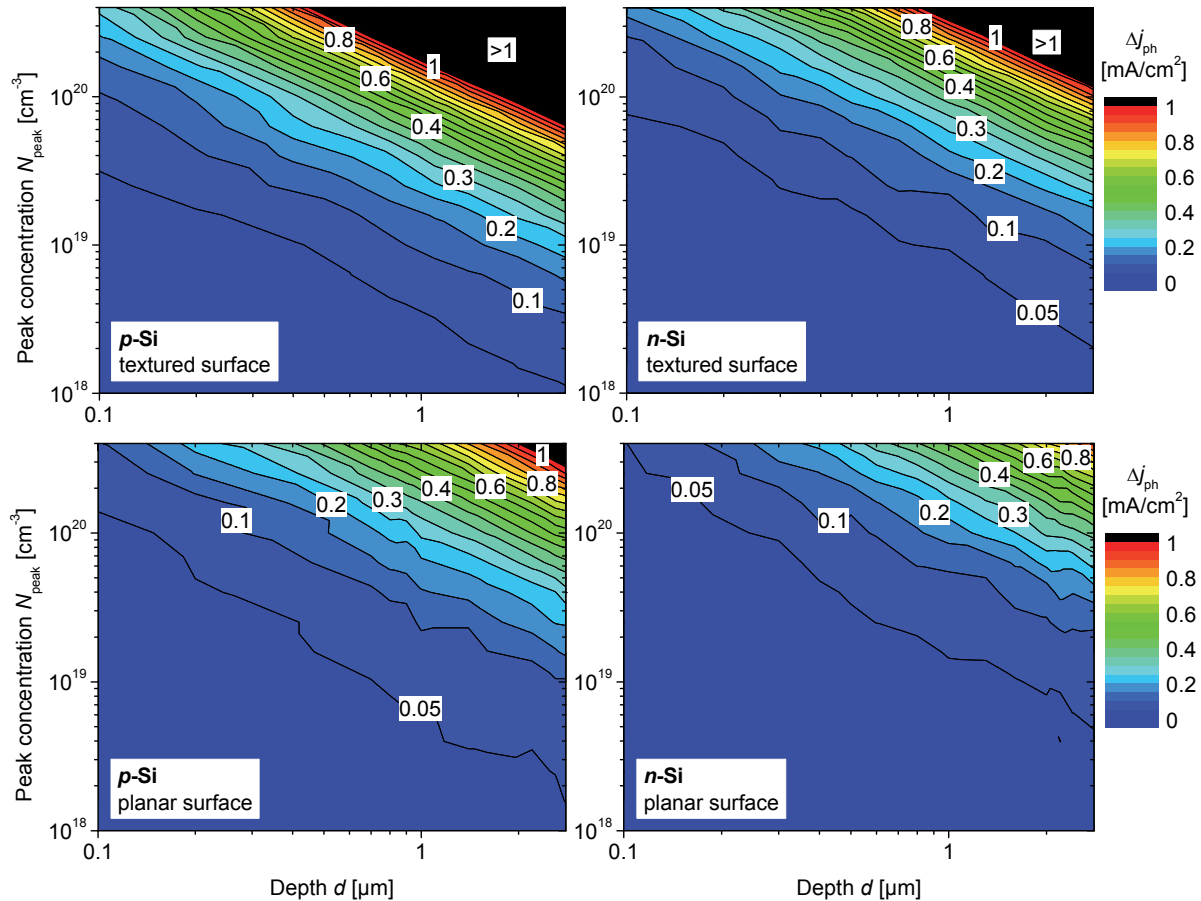


Fig. 4.8: Photogenerated current density losses Δj_{ph} , exemplarily shown for varied Gaussian profiles on textured (above) and planar (below) surfaces for B (left) and P doped (right) Si.

By calculating the Δj_{ph} losses shown in Tab. 4.1 with the Green parameterization, same results can be observed for the B doped profiles (i - iv). For the P doped profiles (I - IV), the resulting Δj_{ph} values differ by a factor of about 0.5, which is a relevant underestimation of the effect of FCA.

The results shown in Fig. 4.8 and Tab. 4.1 indicate that FCA is a nonnegligible loss mechanism in highly doped Si, which plays an important role for an accurate description of the device current density and should be considered in device simulations.

4.6 Conclusions

In this chapter, existing free carrier absorption models were evaluated according to their validity within the wavelength range $\lambda = 1.0 - 2.0 \mu\text{m}$. This included the relevant range where FCA could potentially decrease the photogenerated current density j_{ph} in highly doped Si. Therefore, test samples were produced featuring different B and P

Tab. 4.1: Δj_{ph} caused by FCA for the examined diffusion profiles given in Fig. 4.2. The losses have been calculated by the use of Eq. (4.2).

Profile	Dopant	Sheet resistance R_{sh} [Ω/sq]	Photogenerated current density loss Δj_{ph} [mA/cm^2]	
			Textured	Planar
i	B	188 ± 4	0.1	< 0.05
ii	B	89 ± 2	0.3	0.1
iii	B	89 ± 3	0.4	0.1
iv	B	41.9 ± 0.2	0.6	0.3
I	P	421 ± 8	< 0.05	< 0.05
II	P	182.6 ± 1.5	0.1	< 0.05
III	P	74.7 ± 1.6	0.2	0.1
IV	P	53.7 ± 0.4	0.4	0.2

doped diffusion profiles, covering a broad range of sheet resistances, and the corresponding reflection curves were measured. Based on numerical device simulations, the same test structures were simulated, including the different FCA parameterizations from Schroder [69], Green [70] and Isenberg [75]. Significant deviations of the simulated reflection curves could be observed by comparing the results of the different parameterizations found in the literature. Whereas simulations including the Schroder parameterization for B doped Si – which is identical to the Green parameterization for Si:B – showed fairly good agreement with the experimental data, most other simulations showed significant differences to the set of experimental data, including Si:P and Si:B, over- or underestimating the effect of FCA.

Therefore, based on the classical theory [68], new parameters for the quantification of FCA losses have been set up, achieving very good agreement with the experimental data. Based on this parameterization, losses on j_{ph} due to FCA are quantified for different doping concentrations and explicitly for the investigated experimental profiles on textured and planar surfaces. The results illustrate that FCA is a nonnegligible loss mechanism in highly doped Si solar cells, which plays an important role for an accurate description of device current density losses. Because of the simplistic formula structure, the parameterization might be easily implemented in numerical simulation tools.

5 Numerical description of highly aluminum-doped silicon

In this chapter an advanced method for precise modeling of highly aluminum-doped p^+ silicon is presented, leading to excellent agreement of numerical and experimental data within a broad range. The influence of different recombination mechanisms on the saturation current densities of Al-doped Si surfaces for different Al profiles has been analyzed. Lateral doping inhomogeneities and the effect of incomplete ionization have been examined in detail. It is demonstrated that incomplete ionization affects the profile characteristics significantly and, therefore, has to be accounted for in accurate modeling of highly Al-doped Si. The results of this chapter have been published in Ref. [129, 130].

5.1 Introduction

Numerical device simulations of silicon (Si) regions with aluminum (Al) doping have been a challenging task so far. Considering Al atoms as acceptor occupancies, according to the description of boron (B), the saturation current densities of Al-doped p^+ Si (Al- p^+) regions are calculated too low, leading to significantly overestimated open-circuit voltages in solar cell simulations. Recently, a minority carrier lifetime parameterization as a function of the Al acceptor density N_A has been reported for simulation purposes [99, 131] in order to account for the lifetime limiting defect in Al-doped Si, which may be caused by the formation of aluminum–oxygen (Al–O) defect complexes [132-134]. However, it will be shown that the current models are not suitable to describe highly Al-doped Si in good accordance with experimental data, such as the saturation current density j_0 or the open-circuit voltage V_{oc} of solar cells. Thus, in this chapter, the effect of Auger and Shockley–Read–Hall (SRH) recombination [64, 65] on the saturation current densities j_0 of Al- p^+ regions will be analyzed in detail. Furthermore, the influence of lateral Al doping profile inhomogeneities and incomplete ionization of the Al acceptor atoms is determined. Here, data for the Al–O defect complexes given in literature are combined with an incomplete ionization model for Al acceptors and a Gaussian-weighted depth distribution of Al doping profiles. Excellent agreement with measured results within a broad range of data has been achieved. It is demonstrated that the effect of incomplete ionization of Al acceptors is an important mechanism in Al-doped Si and has to be accounted for in accurate solar cell modeling.

5.2 Electric properties of aluminum in silicon

Al is an element that is omnipresent as a grown-in impurity in the processing of many semiconductor devices. In Si solar cells, for instance, it is mostly present in the back surface field (BSF) region as well as in the metal contact paste.

The diffusivity of interstitial Al in Si [135]

$$D = 4.73 \text{ cm}^2\text{s}^{-1} \exp\left(-\frac{3.35 \text{ eV}}{k_B T}\right) \quad \text{for } (850^\circ\text{C} \leq T \leq 1290^\circ\text{C}) \quad (5.1)$$

is relatively low compared to the diffusivity of transition metals. Hence, Al is not very likely introduced into the wafer bulk by unintentional diffusion during device processing. However, if Al is already present as a grown-in impurity in the starting material, it can act as an electrically active defect with detrimental consequences for the electrical material quality.

As a group III element in the periodic table, it features a well known shallow acceptor level at $E_t - E_V = 69 \text{ meV}$ [136] with E_t as trap energy level and E_V as energy of the

Tab. 5.1: Defect levels and capture cross sections for Al-contaminated Si reported in literature.

Reference	Defect energy level E_t [eV]	Capture cross section σ [cm ²] symmetry factor k
Marchand <i>et al.</i> [137]	$E_V + 0.216$	
	$E_V + 0.316$	
	$E_V + 0.402$	
	$E_C - 0.389$	
Davis <i>et al.</i> [132]	$(E_V + 0.43) \pm 0.05$	$\sigma_p = 1.4 \times 10^{-14}$ $\sigma_n = 5.7 \times 10^{-15}$
	$(E_V + 0.47) \pm 0.03$	
Schmidt <i>et al.</i> [138]	$E_C - (0.45 \dots 0.90)$	
Rosenits <i>et al.</i> [133, 134]	$(E_V + 0.44) \pm 0.02$	$\sigma_p = 3.6 \times 10^{-17}$ $\sigma_n = 3.6 \times 10^{-15}$ ($k = 100$)

valence band edge, which makes it a potential doping substance for p -type Si. In addition, Al and Al-related defect centers are also presumed to exhibit deep energy levels in the Si band gap. However, despite a couple of investigations in the past on Al-related defect centers in Si [132, 137-140], the results of these investigations were contradictory or failed to give an unambiguous set of defect parameters. A selection of the found energy levels is summarized in Tab. 5.1.

5.3 Experimental results

Highly Al-doped p^+ Si regions can easily be formed by alloying of Al pastes, screen-printed onto the surface of Si wafers, during a short high-temperature firing step. These Al- p^+ regions are commonly used as BSFs in p -type Si solar cells and can also be used as rear emitters in n -type Si solar cells [141, 142] (see Chap. 6). A wide range of test samples has been prepared on high-quality 100 Ωcm p -type boron-doped float-zone (FZ) Si material. These samples differ in Al- p^+ depth and surface passivation and have been characterized in detail [143, 144]. One part of the samples features non-passivated Al- p^+ surfaces, whereas the second part exhibits effectively passivated surfaces. For the surface passivation, atomic-layer-deposited aluminum oxide (Al_2O_3) or plasma-enhanced-chemical-vapor-deposited amorphous Si (a-Si) layers have been applied. The opposite non-Al-doped sample surfaces have been passivated by silicon nitride (SiN_x), leading to asymmetric structures as shown schematically in Fig. 5.1. For evaluation reasons, p -type Si base material is used, since the Al doping profile properties do not depend on the kind of bulk doping. The Al doping profiles have been detected by electrochemical capacitance–voltage (ECV) measurements, using a WEP-CVP21 profiler and a diluted ammonium bifluoride (NH_4HF_6) electrolyte [125]. The saturation current densities $j_{0,\text{Al}}$ of the Al- p^+ regions have been determined via the quasi-steady-state photoconductance (QSSPC) method by which the transient decay of photogenerated carriers is measured [118, 145]. Under high-level injection conditions the recombination rate in the Al- p^+ region has a quadratic dependence on the carrier density and is, therefore, separable from the linear recombination rate in the base and at the surfaces. Thus, the reciprocal instantaneous decay time $1/\tau_{\text{eff}}(\Delta n)$ dependent on the minority carrier density Δn is given by

$$\frac{1}{\tau_{\text{eff}}(\Delta n)} = \frac{1}{\tau_{\text{SRH}}} + \frac{1}{\tau_{\text{A,CE}}(\Delta n)} + \frac{1}{qn_i^2 d} \cdot j_{0,\text{total}} \cdot \Delta n \quad (5.2)$$

and, thus, the saturation current density $j_{0,\text{total}}$ can be extracted from the slope of the plot of these two parameters. τ_{SRH} denotes the SRH lifetime, $\tau_{\text{A,CE}}$ the Coulomb-

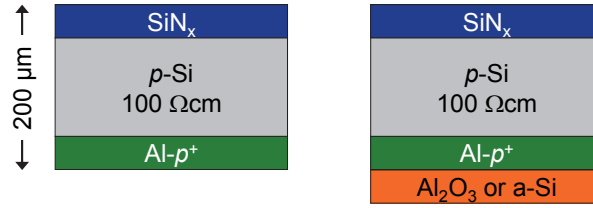


Fig. 5.1: Schematic of the test samples, prepared on high-quality 100 Ωcm boron-doped p -type float-zone (FZ) Si material. The samples differ on the rear side in $\text{Al-}p^+$ depth and surface passivation. One part of the samples features non-passivated $\text{Al-}p^+$ surfaces (left), whereas the second part exhibits effectively passivated surfaces (right).

enhanced Auger lifetime, q the elementary charge, n_i the intrinsic carrier density, and d the sample thickness. For the asymmetric samples, the saturation current density $j_{0,\text{Al}} = j_{0,\text{total}} - j_{0,\text{residual}}$ of the $\text{Al-}p^+$ region can be extracted by determining $j_{0,\text{residual}}$ with the help of an additional symmetric reference sample without $\text{Al-}p^+$ region featuring SiN_x passivated surfaces. Due to the very good passivation properties of the SiN_x and the low doping concentration of the FZ Si base material, $j_{0,\text{residual}}$ is negligible and, thus, $j_{0,\text{Al}}$ can be determined very well. Measured saturation current densities of $\text{Al-}p^+$ regions with different doping profiles are shown in Fig. 5.4 (squares).

5.4 Simulations

For the numerical determination of saturation current densities $j_{0,\text{Al}}$ via one- and two-dimensional simulations, an asymmetric sample structure equivalent to the experiment (see Fig. 5.1) has been set up in Sentaurus TCAD [12]. As base material, p -type boron-doped Si with a resistivity of 100 Ωcm has been assumed supplying lifetimes close to the Auger limit. In order to calculate the current density-voltage characteristic of the device, a non-recombining front contact and a rear contact with adjustable surface recombination velocity have been used. By determining the short-circuit current density j_{sc} and the open-circuit voltage V_{oc} , the saturation current density $j_{0,\text{total}}$ of the entire system can be calculated via the one-diode equation. With the saturation current density $j_{0,\text{residual}}$ extracted from the simulation of the symmetric reference, $j_{0,\text{Al}} = j_{0,\text{total}} - j_{0,\text{residual}}$ of the $\text{Al-}p^+$ region can be calculated.

As detected by ECV measurements, the Al doping profile curve starts at a surface concentration of $\sim 1 \times 10^{18} \text{ cm}^{-3}$, rises to a maximum value of $\sim 3 \times 10^{18} \text{ cm}^{-3}$ at a depth of some μm and decreases there rapidly, as shown exemplarily in Fig. 5.2. At the interface of the Al-doped p^+ Si and the Si bulk, the profile is broadly blurred due to lateral thickness inhomogeneities of the $\text{Al-}p^+$ region [125]. Scanning electron

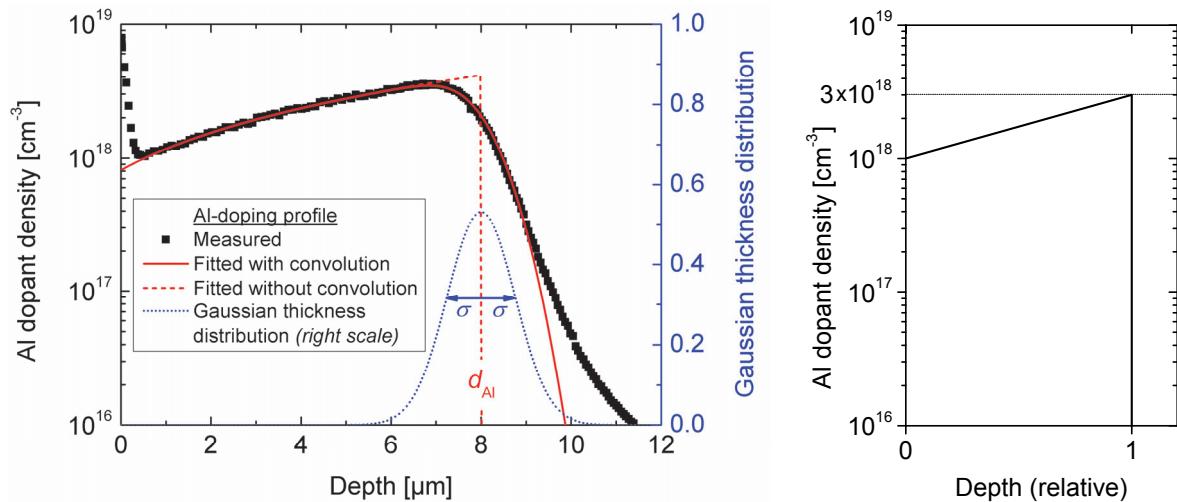


Fig. 5.2: Al dopant density in Si as a function of depth measured by ECV (left). The Gaussian-shaped characteristic [125] of the profile decay is mainly caused by lateral doping inhomogeneities of the Al-doped region within the measuring area. Thus, according to Ref. [146], the determined profiles have been assumed as a convolution of the real Al profile and a Gaussian function. d_{Al} stands for the depth, at which the profile decreases abruptly. For numerical simulations, an empirical Al doping profile has been set up (right). Thereby, the artifact at the surface (steep increase of Al dopant density) [143, 147] has been neglected.

microscope (SEM) images indicate an abrupt profile decrease due to a sharp contrast at the Al- p^+ /Si bulk interface (see Fig. 5.3). Thus, the measured Al doping profiles have been fitted by a convolution of an abrupt profile, which is applied to the simulations, and a Gaussian distribution [146]. Thereby, the steep increase of the dopant density near the surface involved by Al residuals [143, 147] has been neglected.

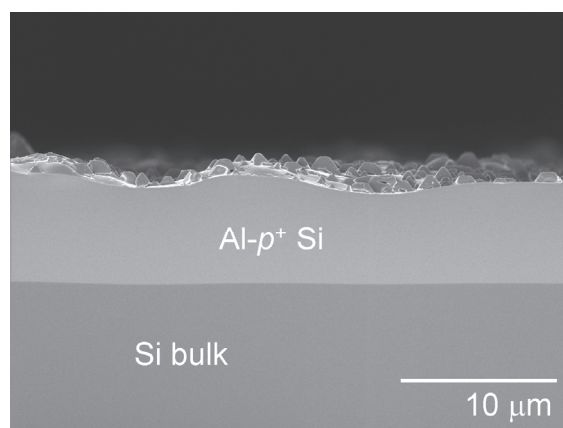


Fig. 5.3: Cross-sectional SEM image of an Al-doped p^+ region at the Si surface. The Al doping profile ends abruptly, clearly indicated by the sharp contrast at the interface between the Al- p^+ region and the Si bulk. Thickness inhomogeneities within the ECV measurement area ($\varnothing = 3.55 \text{ mm} \pm 0.06 \text{ mm}$) lead to the Gaussian-shaped characteristics of the measured profiles (see Fig. 5.2).

Tab. 5.2: Parameters used for simulations of the saturation current densities $j_{0,Al}$ of Al-doped Si.

Parameter	Unit	Numerical value
Resistivity of p -Si base material	Ωcm	100
Capture time constant for minority carriers τ_{n0}	ms	35
Thickness of Si base material d	μm	200
Temperature T	K	300
Intrinsic carrier concentration n_i	cm^{-3}	9.65×10^9 [48, 148]
Degeneracy factor g		$\frac{1}{4}$
Surface recombination velocity S_0		
for minority carriers	cm/s	1×10^0
for majority carriers	cm/s	1×10^7

Excellent accordance of the numerical fits and the experimental data has been achieved, as demonstrated in Fig. 5.2. The parameters used for the simulations are summarized in Tab. 5.2. For depth variations of the Al- p^+ regions, an empirical Al doping profile has been set up consisting of an exponential increase from $N_A = 1 \times 10^{18} \text{ cm}^{-3}$ at the surface to a maximum value of $N_A = 3 \times 10^{18} \text{ cm}^{-3}$ at the Al- p^+ /Si interface and an abrupt decay (Fig. 5.2, right).

It is important to mention that the ECV technique detects the *total* Al doping concentrations, that means electrically active (ionized) and non-active (non-ionized) Al atoms [125, 146]. By this method, the Al density is determined from capacitance measurements, and the capacitance (due to the space charge region) is unaffected by incomplete ionization [149, 150] because all dopants are ionized in space charge regions (the Fermi level is situated far from the Al dopant levels due to band bending). As incomplete ionization extensively affects the electrically active concentration of Al acceptors in Si within the doping range of 10^{17} to 10^{19} cm^{-3} , relevant for the profiles discussed in this work, it has to be considered carefully for accurate modeling of highly Al-doped Si, see Chap. 5.4.4.

5.4.1 Influence of Auger recombination

In order to analyze the influence of Auger recombination on the saturation current densities of Al- p^+ regions, only Auger recombination (see Chap. 2.5.2) has been taken

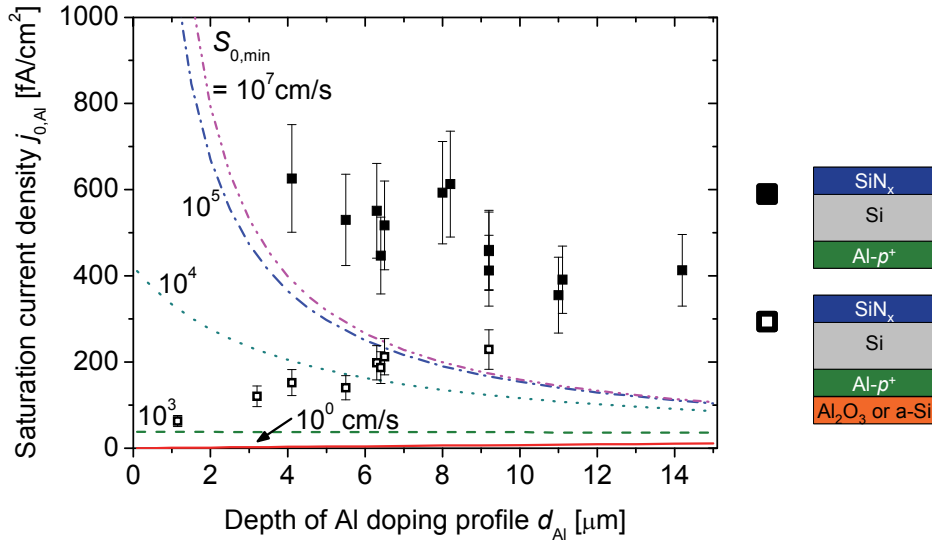


Fig. 5.4: Measured saturation current densities $j_{0,Al}$ (squares) with surface-passivated (open) and non-surface-passivated (closed) Al- p^+ regions and calculated influence of Auger recombination (lines), without taking defect recombination into account. The profile depth and the minority carrier surface recombination velocity $S_{0,min}$ have been varied.

into account for the device simulations. The depth d_{Al} (see Fig. 5.2), at which the Al doping profile decreases abruptly, and the minority carrier surface recombination velocity $S_{0,min}$ of the Al-doped sample side have been varied. Experimental results are shown in Fig. 5.4. Considering perfectly passivated surfaces ($S_{0,min} = 10^0$ cm/s), very low saturation current densities $j_{0,Al} \leq 10$ fA/cm² occur, even for deep Al profiles with $d_{Al} = 15$ μm. For $S_{0,min} = 10^3$ cm/s, the $j_{0,Al}(d_{Al})$ characteristics remain nearly constant, not exceeding 50 fA/cm². With increasing $S_{0,min}$ values, $j_{0,Al}$ rises quite quickly, especially for very low Al profile depths. Due to the thinner Al- p^+ depths, the barrier for the minority carriers to the surface is relatively reduced, leading to enhanced recombination at the surface and a significant increase in $j_{0,Al}$. In the range of $S_{0,min} = 10^5$ cm/s to 10^7 cm/s (thermal velocity for Si at $T = 300$ K), $j_{0,Al}$ does not change significantly. This means that the maximum $j_{0,Al}$ curve is still far below the measured $j_{0,Al}$ values for non-surface-passivated Al- p^+ regions (Fig. 5.4, closed squares), indicating that Auger recombination is not the limiting recombination path, in agreement with Ref. [151].

5.4.2 Influence of defect recombination

Al and Al-related centers form electrically active deep energy levels close to the Si midgap, leading to high recombination and, thus, reducing the minority carrier lifetime. The carrier lifetime limiting defect in Al-doped Si can be related to Al–O defect complexes [132, 133, 140]. An overview of experimentally determined defect levels and capture cross sections for Al-doped Si taken from literature is given in Tab.

5.1. While the energy of the deep defect level $E_t - E_V$ is quite well known and the results reported by different authors show little deviation, the results for the capture cross section σ_h of the holes differ by one order of magnitude. For the capture cross section σ_n of the electrons, only one value was found in literature.

For defect modeling via SRH theory [64, 65], the general description of carrier generation and recombination at a single defect level, the entire defect parameter set consisting of E_t , σ_e , and σ_h and the defect concentration N_t is required. Due to low-level injection (LLI) conditions in the considered Al-doped Si region and for a deep defect level, the SRH minority carrier lifetime equals the minority carrier capture time constant τ_{n0} , as given in Eq. (2.39). Since the exact value of σ_n is based on only one reference and the defect density N_t , assumed to be dependent on N_A , is unknown, the product of the effective defect density $N_t^*(N_A) \equiv N_t(N_A)\sigma_n \propto N_A$ acts as a free parameter in the simulations.

With increasing N_t^* values, the saturation current density rises within the whole Al- p^+ depth range due to an elevated recombination activity, as indicated by the arrow in Fig. 5.5. Furthermore, with increasing N_t^* values, recombination occurs rather at defects in the bulk than at the surface. This results in a shifting of the convergence value of the calculated characteristics for $S_{0,min} = 10^7$ cm/s and 10^0 cm/s to decreased d_{Al} values. Please note that the N_t^* values given in Fig. 5.5 indicate the effective defect density at

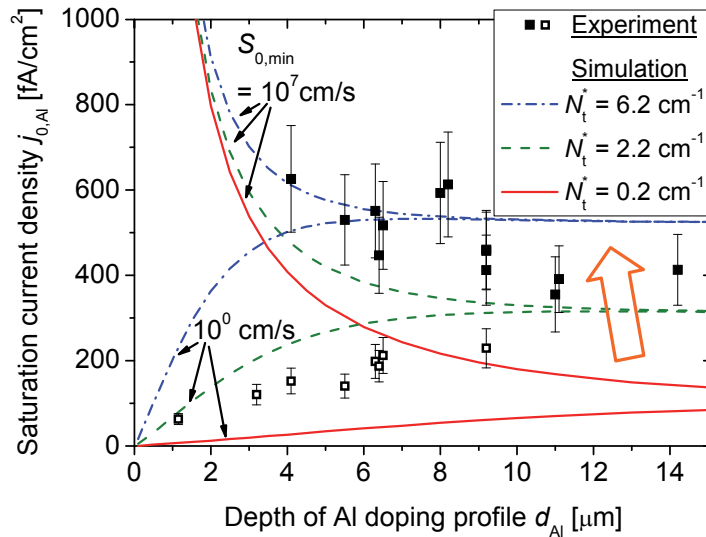


Fig. 5.5: Measured saturation current densities $j_{0,Al}$ (squares) and calculated influence of Auger and SRH recombination (lines) for varied effective defect densities $N_t^* \equiv N_t\sigma_n$. The two curves for each N_t^* value indicate calculations for passivated ($S_{0,min} = 10^0$ cm/s) and non-passivated ($S_{0,min} = 10^7$ cm/s) Al- p^+ surfaces, respectively.

the maximum acceptor concentration $N_t^*(N_{A,\max}) = N_t^*(3 \times 10^{18} \text{ cm}^{-3})$. As a first order approximation, the Al–O complex scales linearly with the Al concentration, therefore $N_t^* \propto N_A$ has been chosen. Due to the LLI conditions, the simulation of Al-doped Si can be considered as independent of the correct set of defect parameters for the Al–O complex (see Eq. (2.39)). However, to determine the absolute defect concentration N_t , knowledge of the minority carrier capture cross section σ_n is required. Recently, a minority carrier lifetime parameterization as a function of the Al acceptor density N_A has been reported for simulation purposes [99, 131], based as well on SRH theory and referred to as the $\tau_{\text{Altermatt}}$ model:

$$\frac{\tau_{\text{Altermatt}}}{\mu\text{s}} = \frac{1}{\left(\frac{N_A}{\text{cm}^{-3}}\right)^{1.5048} \cdot 2.8339 \cdot 10^{-24} \cdot f}. \quad (5.3)$$

The scaling factor $f = 2 \times 10^{-3}$ [152] is given as dimensionless quantity in literature. For comparison to the SRH model under LLI conditions (see Eq. (2.39)), the parameterization has been applied to the empirical Al doping profiles. The results for the numerically calculated $j_{0,\text{Al,Altermatt}}$ are shown in Fig. 5.6 (dashed). By comparing Eqs. (2.39) and (5.3), both approaches depict a very similar structure and, thus, a good correlation between $j_{0,\text{Al,SRH}}$ (with $N_t^* = 1.7 \text{ cm}^{-1}$) and $j_{0,\text{Al,Altermatt}}$ can be observed, especially for non-surface-passivated Al- p^+ regions (Fig. 5.6). For surface-passivated Al- p^+ regions, the relative difference does not exceed 20%.

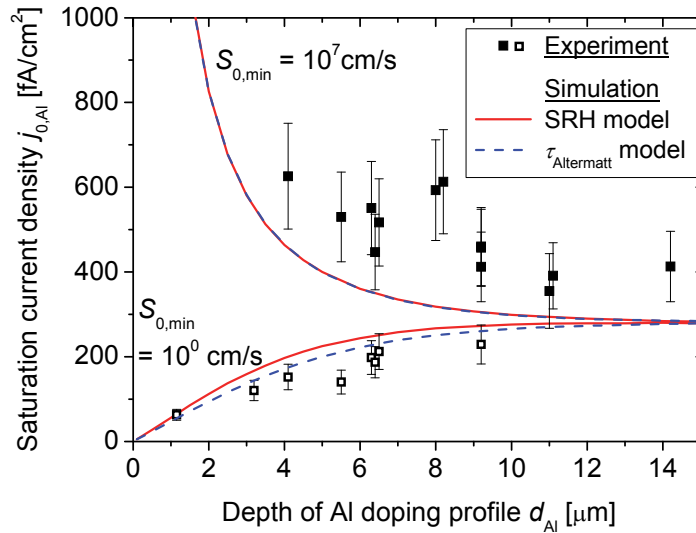


Fig. 5.6: Measured saturation current densities $j_{0,\text{Al}}$ (squares) and calculated influence of Auger and SRH recombination with $N_t^* = 1.7 \text{ cm}^{-1}$ (referred to as SRH model) and the lifetime parameterization ($\tau_{\text{Altermatt}}$ model) proposed in Refs. [99] and [131].

Nevertheless, both simulation results do not fit very well to the experimentally obtained results, leading to strongly underestimated saturation current densities for non-passivated Al-doped Si surfaces.

5.4.3 Influence of lateral doping inhomogeneities

In Fig. 5.3, an SEM image of the cross section of the Al-doped p^+ region at the Si surface is shown. Significant lateral thickness inhomogeneities of such regions in the micrometer range can be clearly seen (see Fig. 5.3). This is much smaller than the typical diameter of the measurement area of commonly used techniques to analyze the composition of solid surfaces like ECV, which is in general in the range of millimeters. As a consequence of this insufficient resolution, a measurement of an Al doping profile exhibits a Gaussian distribution of the decay at the Al- p^+ /Si interface. Thus, a measured Al doping profile can be considered as a convolution of the “real” abrupt profile and a Gaussian distribution [146], as mentioned before, leading to a non-abrupt decrease (see Fig. 5.2).

To quantify the effect of Al- p^+ thickness inhomogeneities on the saturation current densities, the standard deviations σ of the normal distributions of all measured and fitted profiles have been determined, resulting in a medium absolute standard deviation $\bar{\sigma}_{\text{abs}} = 0.75 \mu\text{m}$, as shown in Fig. 5.7. For the simulations, the Gaussian distribution is discretized into seven parts, each with a width of 1σ . The Al doping profiles (according to Fig. 5.4, inset) have been set up with 3σ deviation. The normalized

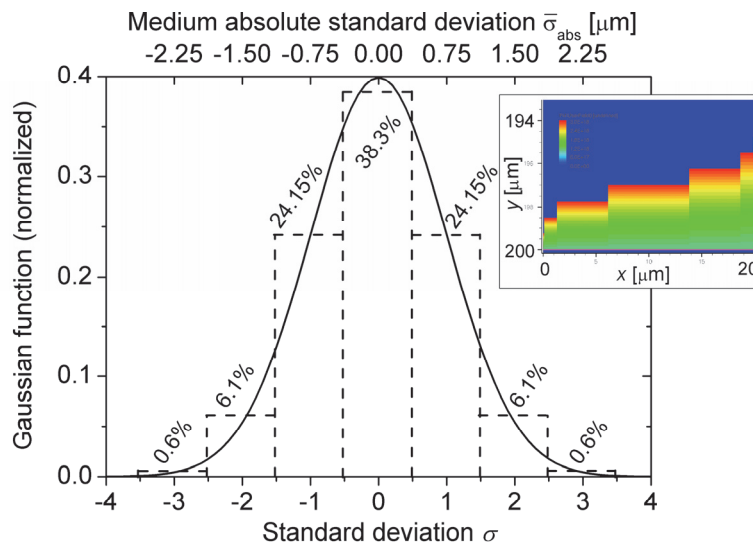


Fig. 5.7: Gaussian function vs. standard deviation σ . The medium variation of the measured depth $\Delta d = 0.75 \mu\text{m}$ has been determined from fits to the measured ECV profiles (see Fig. 5.2). The different depths have been accounted for in the simulations (inset), according to their Gaussian probability.

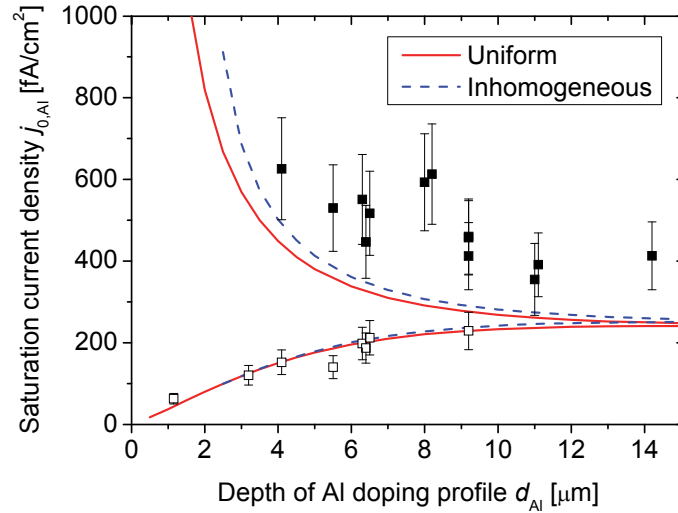


Fig. 5.8: Measured saturation current densities $j_{0,Al}$ (squares) and calculated influence of Auger and SRH recombination without (dash dotted) and with (dotted) taking Al- p^+ thickness inhomogeneities into account (see Fig. 5.7). For non-surface-passivated thin Al- p^+ regions, a lower shielding for the minority carriers in the Si bulk leads to increased recombination at the surface and, thus, to an increase of $j_{0,Al}$.

integral of the Gaussian distribution indicates the probability of the specific depths. This has been accounted for in the profile width in device simulations, schematically shown in Fig. 5.7 (inset). In these simulations, the total width of the shown variation is small compared to the sample thickness of the considered element (1:10) in order to minimize lateral effects. In Fig. 5.8 the influence of an Al profile depth variation on the saturation current density is shown with (dotted) and without (dash dotted) taking inhomogeneities into account. While no changes can be considered for the $j_{0,Al}$ characteristics of Al- p^+ regions with passivated surfaces ($S_{0,min} = 10^0$ cm/s), $j_{0,Al}$ increases for non-passivated surfaces ($S_{0,min} = 10^7$ cm/s). With decreasing thickness of the Al- p^+ region, $j_{0,Al}$ increases due to an increased impact of the high recombination active surface, caused by the thin Al- p^+ profiles. The influence of inhomogeneities becomes significant for profile depths below 6 μm with a relative increase by more than 10%. Nevertheless, inhomogeneities do not result in a strong increase of $j_{0,Al}$ for non-passivated Al- p^+ regions to values as high as the experimental data.

5.4.4 Influence of incomplete ionization of aluminum acceptor atoms

For increasing dopant densities in Si (of acceptors or donors, respectively), the Fermi level E_F approaches the valence or conduction band edge. Thus, the occupation of localized dopant levels increases, leading to incomplete ionization (i.i.) of the dopant atoms [153]. Thereby, the free carrier density is significantly lower than the dopant density, although all dopant atoms replace Si atoms within its crystalline lattice structure. As has been presented by Altermatt and co-workers [149, 150], the most relevant doping range for i.i. is $10^{17} - 10^{19}$ cm^{-3} (relevant for Al doping profiles), even

at room temperature. Since the ionization energy $E_{\text{dop},0} = 69 \text{ meV}$ of Al acceptors is much higher than those of boron acceptors (44 meV) or phosphorus donors (46 meV), the influence of i.i. in Si is correspondingly much greater for Al than for B or P. Calculations show that in the considered doping range, 20%–50% of the substitutional Al atoms do not contribute to the hole concentration [146], which significantly influences the carrier mobilities as well.

In Sentaurus TCAD, the predefined model for the fraction of ionized acceptor atoms $N_A/N_{A,0}$ is given by

$$\frac{N_A}{N_{A,0}} = \frac{1}{1 + g_A \frac{p}{p_1}} \quad \text{with} \quad p_1 = N_V \cdot \exp\left(-\frac{E_A - E_V}{k_B T}\right) \quad \text{for} \quad N_A < N_{\text{crit}}. \quad (5.4)$$

N_V denotes the effective density of states at the edge of the valence band, E_V the upper limit of the valence band energy, k_B the Boltzmann constant, and T the temperature. g_A is the inverse of the degeneracy factor $g = 1/4$, which is the convergence limit of the i.i. model proposed by Altermatt and coworkers [149, 150] for low doping concentrations. The functional behavior is shown in Fig. 5.9. In this more generalized i.i. model, as a main difference from the model implemented in Sentaurus TCAD, $g_A = g_A(T, N_A, n, p)$ is a function of T, N_A, n and p . This leads to a smooth transition to complete ionization instead of a hard transition enforced by a step function. But as not sufficient experimental data could be found in literature on Al-doped Si, which is necessary for a firm experimental base for this i.i. model, the i.i. model implemented in Sentaurus

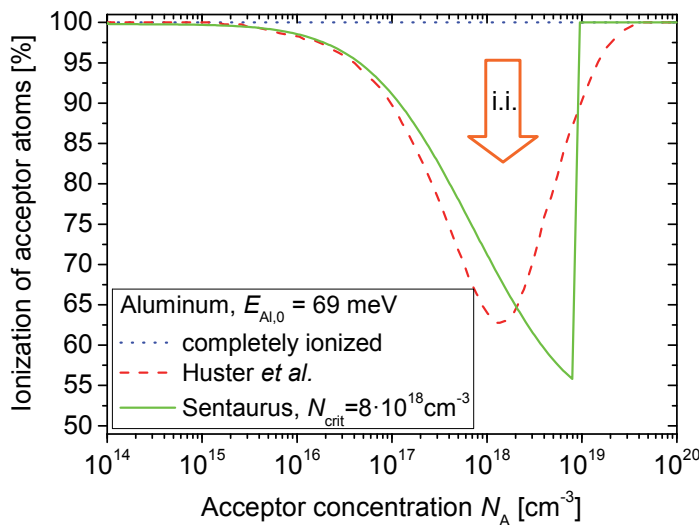


Fig. 5.9: Effect of incomplete ionization (i.i.) dependent on the acceptor concentration N_A . Shown are the results of the simulations with the integrated model in Sentaurus TCAD (line) and calculations by Huster and Schubert (Ref. [146]).

TCAD with the default parameters [12] have been used. $E_{\text{dop},0}$ for Al acceptors in Si was taken from literature and a critical doping concentration N_{crit} for the Mott (metal-insulator) transition above $8 \times 10^{18} \text{ cm}^{-3}$ was used. For comparison, calculations made by Huster and Schubert [146] are shown in Fig. 5.9, which feature a smooth transition as well. Unless the models differ significantly for $N_A > 3 \times 10^{18} \text{ cm}^{-3}$, the fraction of ionization of the acceptor atoms for $N_A \leq 3 \times 10^{18} \text{ cm}^{-3}$ is on the same order of magnitude, which is the relevant range for this work. However, Huster and Schubert point out in their work [146] that their calculations are to be interpreted in a qualitative manner and do not represent calibrated quantities. As the theoretical model used for these calculations is unclear, the results should be interpreted as a guide line.

Due to incomplete ionization of the Al atoms, the resulting electrically active dopant concentration is significantly decreased, as shown exemplarily in Fig. 5.10.

With N_t^* as the only free parameter, excellent agreement of measured and calculated $j_{0,\text{Al}}$ values is achieved by taking i.i. in Sentaurus TCAD device simulations (Fig. 5.11, line) into account. By additionally accounting for inhomogeneities, the same tendencies as shown in Fig. 5.8 occur [129]. Increased saturation current densities can only be observed for profile depths below $6 \mu\text{m}$ in combination with very high surface recombination velocities. Nevertheless, the effect of incomplete ionization has by far a more pronounced impact on $j_{0,\text{Al}}$ and, thus, inhomogeneities can be neglected in most device simulations. Calculating the saturation current densities from the measured and not from the empirical Al doping profiles leads to very good agreement with the

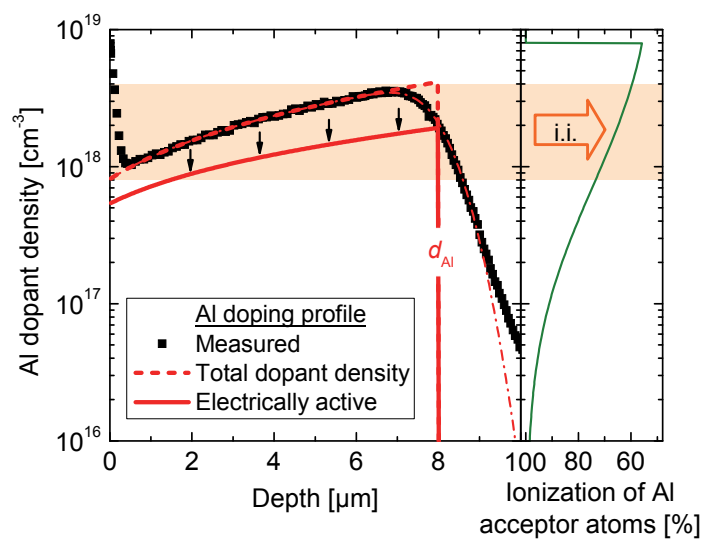


Fig. 5.10: Al doping profile measured by ECV (squares). Due to incomplete ionization of the Al atoms (right), the resulting electrically active dopant concentration (line, left) is significantly decreased.

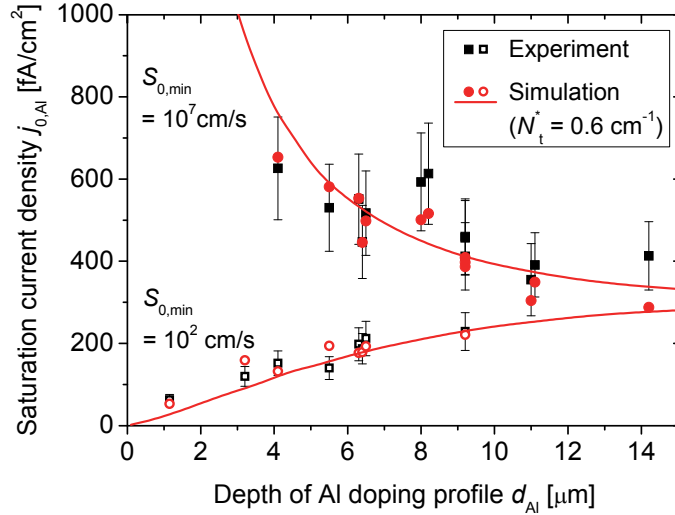


Fig. 5.11: Measured saturation current densities $j_{0,Al}$ (black, squares) and calculated (red) influence of Auger and SRH recombination taking incomplete ionization of the Al acceptors into account. Numerical simulations are performed with the empirically determined profile (see Fig. 5.2, right) (lines). In addition, each simulation result is calculated with the corresponding measured profile and shown at the same Al profile depth (circles). The influence of profile inhomogeneities has been neglected. Excellent agreement of measured and calculated $j_{0,Al}$ values has been achieved.

measured $j_{0,Al}(d_{Al})$ data, as summarized in Fig. 5.11. In these calculations, a more realistic surface recombination velocity $S_0 = 100$ cm/s has been assumed for passivated surfaces (open symbols) [106]. Each simulated $j_{0,Al}$ value (circle) corresponds to the measured data point (square) at the same profile depth.

5.4.5 Discussion

With the result $N_t^* = 0.6$ cm⁻¹ given in Chap. 5.4, an average SRH lifetime in the Al- p^+ region of $\tau_{Al-p^+} = 270$ ns can be determined by using Eq. (2.39). This value is twice as high as the lifetime determined by Schmidt *et al.* ($\tau_{Al-p^+} \geq 130$ ns) [151], which is mentioned as a lower limit for τ_{Al-p^+} . With σ_n taken from Davis *et al.* (see Tab. 5.1) and N_t^* determined in this work, the maximum total defect concentration N_t can be calculated to be in the range of 10^{14} cm⁻³. But as the capture cross section σ_n for the deep Al defect level in Si is only based on one result from literature, the determined N_t should be understood as a rough estimate.

A comparison of experimental data with simulation results of the open-circuit voltage V_{oc} of n -type Si solar cells with non-surface-passivated Al- p^+ rear emitter quantifies the impact of the discussed simulation models. Results are given in Tab. 5.3. By accounting for the Al atoms simply as acceptor occupancies, calculations show an overestimation of V_{oc} of 16 mV to the measured value. Incorporating the $\tau_{Altermatt}$ model in the same device simulation leads to a decrease of the simulated V_{oc} , due to a

Tab. 5.3: *Experimental data and simulation results for an n-type Si solar cell with Al- p^+ rear emitter. By accounting for the Al atoms simply as acceptor occupancies (1), calculations show an overestimation of the open-circuit voltage V_{oc} of 16 mV. Whereas incorporating the $\tau_{\text{Altermatt}}$ model (2) still leads to a significant overestimation, the model presented in this work (3) shows very good agreement with the measured values.*

n -Si solar cell with Al- p^+ rear emitter profile		Defect model for the Al- p^+ region	Incomplete ionization model	Open-circuit voltage V_{oc}
Experiment (see Chap. 6.2)				640
Simulation	(1)	No	No	656
	(2)	$\tau_{\text{Altermatt}}(N_A)$ (Eq. (5.3))	No	650
	(3)	(Eq. (2.39))	Yes	641

decreased SRH lifetime in the Al- p^+ region, but the result still overestimates the measured results significantly. By implementing the model presented in this work, very good agreement to the measured results could be achieved, as can be seen in Tab. 5.3. More details on the solar cell structure and the specific simulations are given in Chap. 6. This leads to the conclusion that incomplete ionization has to be accounted for in accurate modeling of highly Al-doped Si.

5.5 Conclusions

In this chapter an advanced method for accurate modeling of highly Al-doped Si has been introduced. (i) The effects of different recombination losses on the saturation current densities of Al- p^+ regions, (ii) the influence of lateral profile inhomogeneities, and (iii) incomplete ionization of the Al acceptors have been analyzed in detail. The simulation results have been validated within a broad range of experimental data. As a result, it could be demonstrated that defect recombination in highly Al-doped Si seems to be the major loss mechanism. Depth inhomogeneities especially influence thin profiles with high recombination active surfaces, but in most cases these can be neglected in device simulations. However, due to a much higher ionization energy compared to other acceptor atoms, as for example boron, incomplete ionization has an explicit impact on the saturation current densities, due to a significant decrease of the

electrically active Al concentration. Taking this effect into account, excellent agreement of measured and calculated $j_{0,Al}$ values has been achieved. The average SRH lifetime in the Al- p^+ region has been determined to $\tau_{Al-p^+} = 270$ ns. Furthermore, measured data of an n -type Si solar cell, where the Al-doped Si acts as p^+ rear emitter, have been compared to simulations accomplished applying the presented model, demonstrating very good accordance. From that it can be concluded that SRH recombination in combination with incomplete ionization has to be accounted for in accurate modeling of highly Al-doped Si.

6 *n*-type silicon solar cells with aluminum-doped rear p^+ emitter

A detailed analysis on the optimization of n^+np^+ silicon solar cells with aluminum-alloyed rear p^+ emitter for industrial applications by means of two- and three-dimensional numerical simulations is presented in order to identify the potential and the limiting factors of this solar cell concept. Based on simulations with excellent agreement to experimental data, a complete and continuative study is shown, analyzing gradually three different regions of the solar cell. Firstly, the front side is investigated by discussing the influence of different uniform and selective front surface fields. Secondly, the influence of the base is discussed and how doping concentrations and pitch variations influence each other. Finally, the rear side of this solar cell concept is analyzed, how profile variations and locally contacted Al-alloyed rear p^+ emitters influence the cell performance. The content of this chapter has been published in Refs. [154, 155].

6.1 Introduction

A comprehensive one-dimensional modeling of industrial *n*-type silicon solar cells with aluminum-alloyed rear p^+ (Al- p^+) emitter was already set up by Nagel and Schmiga *et al.* in 2006 [156], based on experimental cell results of 17% reported in Ref. [141] and predicting efficiencies of more than 18% by means of PC1D simulations [122]. Since then a lot of effort has been spent to improve this solar cell concept by (i) optimizing the rear Al- p^+ emitter, (ii) improving the phosphorus-diffused n^+ front surface field (FSF) covered by a SiN_x anti-reflection coating and (iii) applying aerosol-printed and silver-plated front contact fingers, leading to measured efficiencies of 18.2% in 2009 [157] and reaching the theoretical predictions.

Recently, an efficiency of 19.3% [142] has been achieved for the best industrial-type n^+np^+ solar cell on phosphorous-doped 10 Ωcm float-zone (FZ) Si material by further improvements including the front surface field and applying an anti-reflection stack consisting of a 10 nm SiO_2 passivation layer and a 65 nm SiN_x anti-reflection coating. A similar efficiency of 19.4% has been reached for a cell on Czochralski-grown Si featuring an additional selective FSF and a screen-printed contact grid [158]. Due to these new improvements, the experimental results exceed by far the theoretical predictions made by Nagel *et al.*. Further promising results have been reported by

other groups which underlines the relevance of this topic for photovoltaic research and development [159-164].

Thus, in this chapter, a complete and continuative analysis on the optimization of *n*-type Si solar cells with Al-alloyed rear *p*⁺ emitter is presented, taking 2D effects of this cell concept into account, which have not been considered in previous work. Furthermore, the consequences of omitting the full-area FSF is discussed in detail, applying highly doped local *n*⁺⁺ FSF areas only below the front contacts. Moreover, for different base doping concentrations, FSF effects are analyzed.

6.2 Comparison: experiment and simulation

6.2.1 Calibration of numerical simulations

To calibrate the calculations, a 19.3% efficient *n*⁺*np*⁺ Al back junction solar cell [142], fabricated at Fraunhofer ISE, has been simulated numerically. A schematic sketch of the solar cell structure is shown in Fig. 6.1. In extension to the experimentally applied uniform FSF, a selective FSF is indicated, consisting of a full-area FSF and additional highly doped areas locally below the front contacts, referred to as “local FSFs” in the following. The realized *n*-type Si solar cell features an industrially feasible front side metallization of an aerosol-printed and Ag-plated contact grid with a front finger distance *w* of 1600 μm. The front surface is textured by random pyramids and has a uniform phosphorus-doped *n*⁺ FSF with a peak doping concentration $N_{\text{peak}} = 5 \times 10^{19} \text{ cm}^{-3}$ and a sheet resistance $R_{\text{sh}} = 90 \text{ } \Omega/\text{sq}$. As anti-reflection coating a

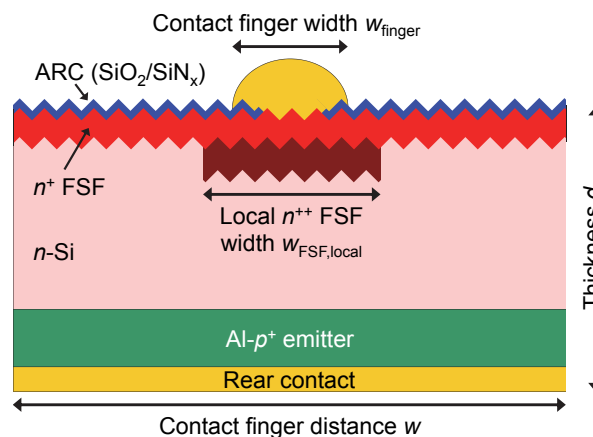


Fig. 6.1: Schematic sketch of the *n*⁺*np*⁺ Al back junction Si solar cell, which is investigated via simulations. Here, a selective FSF is already implemented, consisting of a full-area *n*⁺ FSF and additional highly doped *n*⁺⁺ areas locally below the front contacts (local FSFs). The standard domain used for simulations is half of the shown element.

stack consisting of a 10 nm SiO₂ and a 65 nm SiN_x layer has been used. The full-area Al- p^+ rear emitter features a doping profile with a thickness $d_{Al} \approx 8 \mu\text{m}$ (see Chap. 5).

To model the electrical performance of the above described solar cells via the smallest and geometrically irreducible standard domain (half of the element that is shown in Fig. 6.1), numerical 2D simulations under standard test conditions (25°C, 1-sun illumination intensity, AM1.5G spectrum) have been carried out. The optics has been simulated separately in an optical symmetry element via ray tracing assuming upright pyramids (see Chap. 3.4). The transfer matrix method has been used to calculate the propagation of plane waves through the thin layers of the SiO₂/SiN_x anti-reflection coating (ARC). The results, 1D wavelength and penetration depth dependent generation profiles have been coupled into the 2D electrical device simulation. Internal reflection at the rear side of the cell has been accounted for by the Phong model [86], leading to very good agreement of the simulated and the experimentally measured reflection curves in the range above 360 nm (see Fig. 6.2). The difference in the reflection curves for $\lambda < 360$ nm can be directly seen as well in the EQE characteristics. But due to the small photon density of the incident light below $\lambda = 360$ nm, counting 1.5% of the whole photon flux of the AM1.5G-spectrum, there is a negligible influence on the simulation results. The parameters used for the simulations are summarized in Tab. 6.1.

In Chap. 5 it has been discussed that for the description of Al-doped p^+ regions, defect recombination has to be considered, as the effective lifetime [129, 151] in these

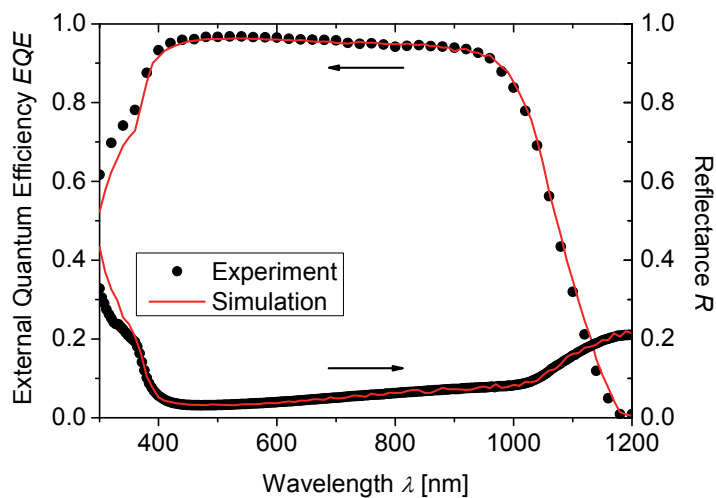


Fig. 6.2: External quantum efficiency and reflectance of measurement and simulation for the n^+np^+ Al back junction Si solar cell [142]. Excellent agreement could be achieved for wavelengths above 360 nm. Due to the low photon density below 360 nm in the AM1.5G-spectrum there is a negligible influence on the simulation results.

Tab. 6.1: Parameters used for the simulation of the n-type Si solar cell featuring a full-area screen-printed Al- p^+ rear emitter and an aerosol-printed and Ag-plated front contact grid.

Parameter	Unit	Numerical value
Thickness d	μm	200
Front finger distance w	μm	1600
Geometrical front contact finger width w_{finger}	μm	60
Shadowing loss (for $w = 1600 \mu\text{m}$)	%	6.0
Base doping concentration N_D	cm^{-3}	4.5×10^{14} ($\sim 10 \Omega\text{cm}$)
n^+ FSF profile	-	measured
Al- p^+ emitter profile	-	measured
Depth of Al- p^+ emitter d_{Al}	μm	8
Low level injection bulk lifetime τ_{eff}	ms	25
Optical reflection	-	adapted to meas.
Internal Phong reflection R_{Phong}	-	0.7
Phong exponent ω_{Phong}	-	4
Front surface recombination velocity $S_{0,\text{front}}$	cm/s	4×10^3
Surface recombination velocity at contacts $S_{0,\text{contact}}$	cm/s	1×10^7
Series resistance for contacts, fingers and busbars $R_{\text{s,ext}}$	Ωcm^2	0.6

regions is strongly reduced, mainly driven by aluminum-oxygen complexes [132, 133]. However, due to a much higher ionization energy of Al compared to other acceptor atoms, as for example boron, incomplete ionization additionally impacts the saturation current densities significantly and has to be accounted for in accurate device simulations [125, 129]. A comparison of numerical simulations and experimental results shows excellent agreement in terms of quantum efficiencies and current density-voltage characteristics and, thus, all relevant solar cell parameters, as demonstrated in Fig. 6.2 and Fig. 6.3, respectively.

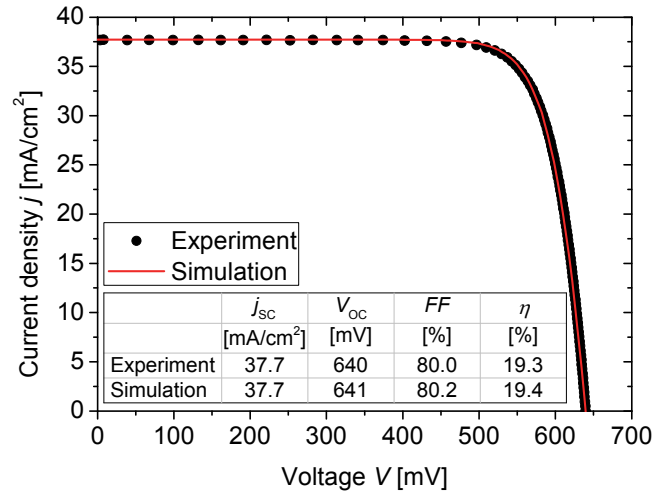


Fig. 6.3: *IV curve and electrical solar cell parameters of measurement and simulation for the n^+np^+ Al back junction Si solar cell [142]. Excellent agreement could be achieved.*

6.2.2 Parameters

For the numerical simulations of the n^+np^+ Al back junction Si solar cell, the phosphorus doping profile of the n^+ FSF is assumed as an error function profile and the Al doping profile of the p^+ rear emitter as an abrupt profile with an acceptor surface concentration of $N_A = 1 \times 10^{18} \text{ cm}^{-3}$ exponentially increasing to $3 \times 10^{18} \text{ cm}^{-3}$ at a depth of $8 \mu\text{m}$, as shown in Fig. 5.2. The front finger distance is set to $w = 1200 \mu\text{m}$ (in contrast to $w = 1600 \mu\text{m}$, used in Chap. 6.2.1).

The shadowing losses of the front contacts have been accounted for in the following manner: A geometrical front finger width $w_{\text{finger}} = 60 \mu\text{m}$ has been measured. A shadowing loss of 6% has been considered in the standard domain for a front contact distance $w = 1600 \mu\text{m}$, including the fingers and also the two busbars. Due to the rounded shape of the silver-plated contacts, about 14% [165] of the reflected light at the metallized surface is additionally coupled into the device contributing to the generation current. For variation of w the shadowing losses change, which has been adopted in the calculations of the standard domain.

By varying the phosphorus peak doping concentration of the n^+ FSF, a change in the surface recombination velocity $S_{0,\text{front}}$ has to be considered as well. Thus, a parameterization of $S_{0,\text{front}}$ for an effective surface passivation with SiO_2 dependent on the FSF surface concentration $N_{\text{FSF,peak}}$ for phosphorus-doped Si surfaces proposed by Cuevas *et al.* [166] has been applied. To account for the surface enlargement due to the front surface texturing, $S_{0,\text{front}}$ from the parameterization has been multiplied by a factor of 2 for simulations. The surface recombination velocity at the contacts has been set to thermal velocity. The intrinsic density of states ($n_i = 9.65 \times 10^9 \text{ cm}^{-3}$) and band

gap narrowing have been accounted for according to Ref. [60]. Calculations are based on Fermi-Dirac statistics. For the minority capture time constants τ_{p0} of the base material, Auger-limited lifetimes of Kerr *et al.* [59] have been used. For the defect parameters of the Shockley-Read-Hall (SRH)-model, a defect level $E_t = E_i$ and a symmetry factor $k \equiv \sigma_n/\sigma_p = 1$ have been assumed. E_i denotes the Fermi energy in an intrinsic semiconductor and σ_n and σ_p are the capture cross sections for electrons and holes, respectively.

Three different FSF profiles are investigated in detail, chosen according to their contactability by different metallization techniques, which are summarized in Tab. 6.2. Profiles (a) and (b) are both examples for industrially relevant POCl_3 -diffused FSF profiles. While (a) reflects a typical profile used in mass production, (b) represents a profile after a drive-in process, which is quite similar to the FSF profile measured by ECV of the $\eta = 19.3\%$ solar cell discussed in Chap. 6.2.1. While profile (b) can only be contacted via advanced metallization techniques like aerosol- or inkjet-printing in combination with plated contacts due to the lower $N_{\text{FSF,peak}}$ value, profile (a) can also be contacted via a standard screen-printing process. The third profile (c) reflects a POCl_3 -diffused profile for high-efficiency applications, but could also be achieved on an industrial level, for example via promising techniques like ion implantation [167, 168], requiring an adequate metallization technique. Please note that the high surface concentration in profile (a) is very sensitive to Auger recombination and, thus, might result in slightly different results compared to simulations with measured profiles featuring a kink-and-tail behavior.

Tab. 6.2: *Three different phosphorus-doped FSFs have been investigated in detail. Profile (a) can be contacted via a standard screen-printing process, while profile (b) and (c) can only be contacted via advanced metallization techniques like aerosol or inkjet printing in combination with plated contacts, due to the lower peak concentration $N_{\text{FSF,peak}}$.*

Profile	$N_{\text{FSF,peak}}$ [cm^{-3}]	d_{FSF} [μm]	R_{sh} [Ω/sq]	Metallization type
(a)	5×10^{20}	0.2	55	“standard”
(b)	5×10^{19}	0.5	140	“advanced”
(c)	5×10^{18}	1.0	280	“high η ”

6.3 Analysis of phosphorus n^+ front surface field

For the analysis of the n^+np^+ solar cell, the phosphorus doping error function profile of the FSF has been varied in peak concentration $N_{\text{FSF,peak}}$ and profile depth d_{FSF} to determine the influence of different FSFs. The surface recombination velocities $S_{0,\text{front}}$ are adjusted according to Ref. [22], respectively. In Fig. 6.4 the calculated short-circuit current densities j_{sc} and efficiencies η are shown for full-area uniform n^+ FSFs and a phosphorus base doping concentration (i) $N_{\text{D}} = 5.0 \times 10^{15} \text{ cm}^{-3}$ ($\rho \approx 1 \text{ }\Omega\text{cm}$) and (ii) $N_{\text{D}} = 4.5 \times 10^{14} \text{ cm}^{-3}$ ($\rho \approx 10 \text{ }\Omega\text{cm}$). Furthermore, results are displayed for a selective FSF on $10 \text{ }\Omega\text{cm}$ base material (iii), thereby using profile (a) (see Table II) as additional local n^{++} FSF below the front contact fingers.

- (i) From the simulations for $1 \text{ }\Omega\text{cm}$ base material, a strong overall decrease of j_{sc} of more than 2 mA/cm^2 absolute can be assessed, compared to j_{sc} in $10 \text{ }\Omega\text{cm}$ bulk material. As observed in Ref. [156, 169], this effect results from a strong increase of the minority carrier concentration in the FSF with increasing bulk doping concentration. This higher minority carrier concentration in the FSF leads to higher recombination and, thus, to a lower charge collection probability of the minority carriers at the rear side contact, resulting in a decreased j_{sc} . Furthermore, for FSFs with very low peak doping concentrations at the surface, a stronger decrease of j_{sc} is obtained for (i) compared to (ii) in Fig. 6.4. Due to the higher bulk doping concentration, the barrier for the minority carriers to the front surface is relatively lowered, leading to more recombination at the front surface and a decrease of j_{sc} in the range of very shallow FSFs.
- (ii) Examining j_{sc} for $10 \text{ }\Omega\text{cm}$ bulk material indicates high values of $\geq 38 \text{ mA/cm}^2$ over a broad range, decreasing towards higher doped FSF profiles, mainly due to increased Auger recombination losses. V_{oc} does not change remarkably within 1 and $10 \text{ }\Omega\text{cm}$ bulk material, reaching a maximum value of $\sim 640 \text{ mV}$ at FSF peak concentrations around 10^{19} cm^{-3} . Under high injection conditions prevailing in $10 \text{ }\Omega\text{cm}$ bulk material during solar cell operation at the maximum power point (mpp), device simulations show a ‘‘conductivity modulation’’ [170] due to the vertical gradient of the carrier concentration. With lower FSF peak doping concentrations ($N_{\text{FSF,peak}} \leq 10^{19} \text{ cm}^{-3}$) and shallower depths, significant efficiency losses due to decreasing V_{oc} and FF values for $10 \text{ }\Omega\text{cm}$ base material are obtained, whereas for $1 \text{ }\Omega\text{cm}$ base material the FF values remain stable at a high level over the whole varied range. The minority carriers in $10 \text{ }\Omega\text{cm}$ base material are less effectively shielded from the highly recombination-active front contact.

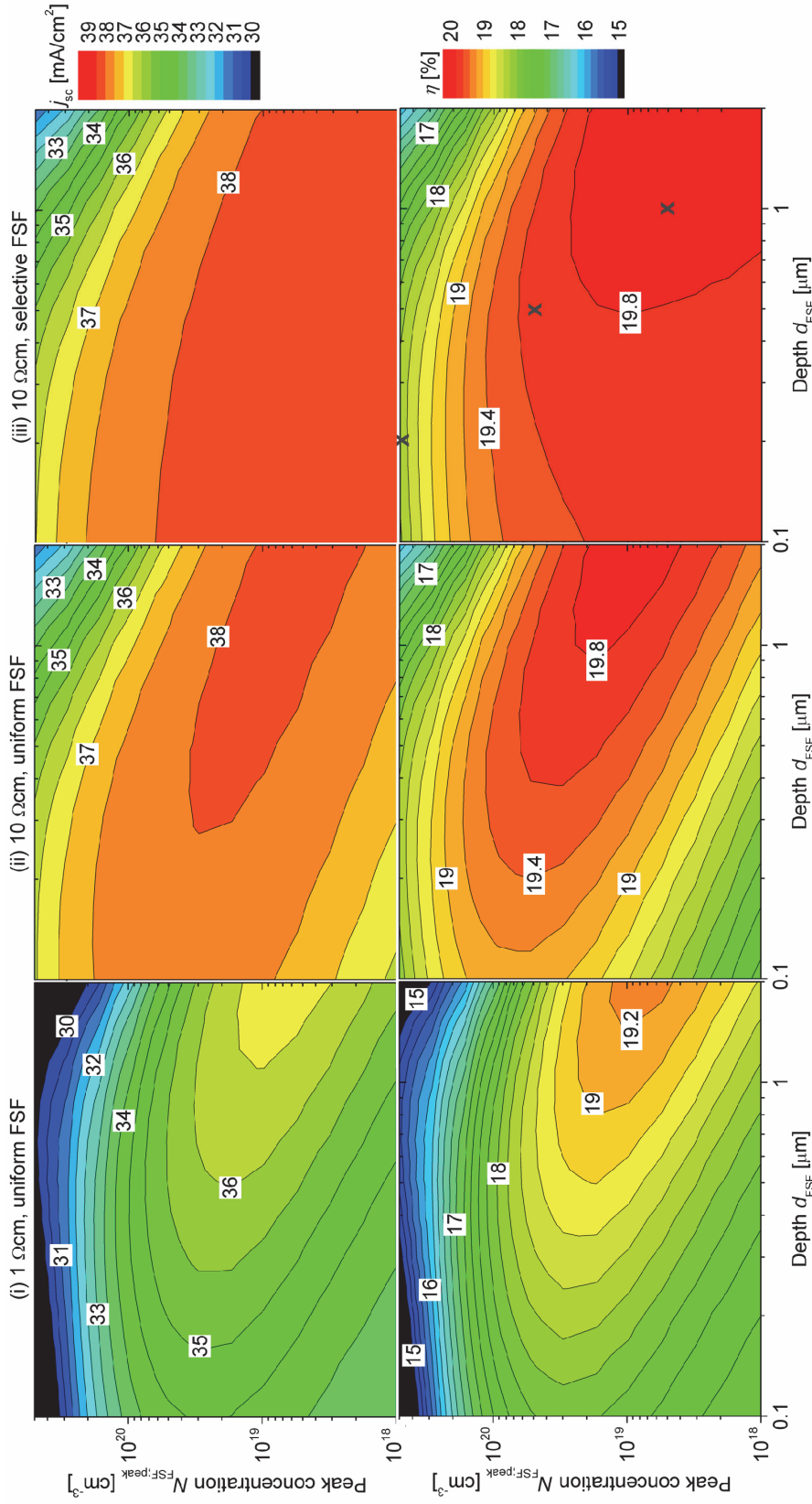


Fig. 6.4: Variation of the FSF peak concentration $N_{FSF,peak}$ and the profile depth d_{FSF} of the n^+np^+ Al back junction Si solar cell with a base doping concentration (i) $N_D = 5.0 \times 10^{15} \text{ cm}^{-3}$ ($\rho = 1 \text{ } \Omega\text{cm}$) and (ii), (iii) $4.5 \times 10^{14} \text{ cm}^{-3}$ ($\rho = 10 \text{ } \Omega\text{cm}$). For (i) and (ii) a uniform FSF and for (iii) a selective FSF is applied. Shown are the cell parameters short-circuit current density j_{sc} and efficiency η for a cell thickness $d = 200 \text{ } \mu\text{m}$, a front finger distance $w = 1200 \text{ } \mu\text{m}$ and a contact width $w_{finger} = 60 \text{ } \mu\text{m}$. At the rear side an Al-p⁺ emitter with a thickness of $8 \text{ } \mu\text{m}$ has been applied. The three crosses (below, right) indicate the profile parameters used for further variations (see Tab. 6.2).

To verify this assumption, further calculations assuming negligible minority carrier surface recombination at the front contact have accomplished (not shown). Here, no V_{oc} losses are observed anymore. The enhanced recombination at the metal contact/silicon (metal/semiconductor) interface leads to a significant decrease of the carrier concentration at mpp conditions in the bulk, resulting in an increase of the effective series resistance, driving mainly the FF drop. Furthermore, due to the elevated resistivity, most of the lateral majority carrier current passing the FSF enters the front contact directly at the edge, leading to current crowding [82]. Finally, qualitatively bulk resistivities (i) and (ii) lead to the same conclusion: best solar cell efficiencies are achieved for deeply diffused profiles with peak concentrations around $1 \times 10^{19} \text{ cm}^{-3}$. Due to the lowered charge collection probability for $1 \text{ } \Omega\text{cm}$ material, lower efficiencies of nearly 1% absolute are expected.

- (iii) By comparing the simulations done on $10 \text{ } \Omega\text{cm}$ base material for a full-area uniform (ii) and a selective FSF (iii) (additional profile (a), Tab. 6.2 with $w_{\text{FSF,local}} = 100 \text{ } \mu\text{m}$ locally below the front contacts), no difference in the results occurs for $N_{\text{FSF,peak}}$ values above $5 \times 10^{19} \text{ cm}^{-3}$ due to an effective shielding of the minority carriers from the highly recombination-active front contact. Below $5 \times 10^{19} \text{ cm}^{-3}$, the local highly doped FSF acts as excellent minority carrier barrier under the contacts. Thus, the reduction of the full-area FSF doping concentration does not lead to a reduction of the carrier concentration and a drop of V_{oc} and FF . As a result, η increases continuously by decreasing $N_{\text{FSF,peak}}$ due to a constantly decreasing saturation current density in the FSF. This leads inevitably to the question whether a full-area FSF is needed or local FSFs below the contacts are sufficient, which will be discussed in Chap. 6.4.

6.4 Influence of n -type Si bulk and front contact finger distance

In this section, the phosphorus base doping concentration of the n^+np^+ Al back junction Si solar cell is varied in a broad range, covering resistivities from $0.1 \text{ } \Omega\text{cm}$ until nearly $100 \text{ } \Omega\text{cm}$ (Fig. 6.5). Additionally, the influence of the front finger distance w is examined. At the rear side an $8 \text{ } \mu\text{m}$ deep Al- p^+ emitter and at the front side a P- n^+ FSF with $N_{\text{FSF,peak}} = 5 \times 10^{19} \text{ cm}^{-3}$ (Tab. 6.2, (b)) have been included in the simulations. The lifetimes have been accounted for according to the Auger limit of the base doping concentrations N_D (see Chap. 2.5.2).

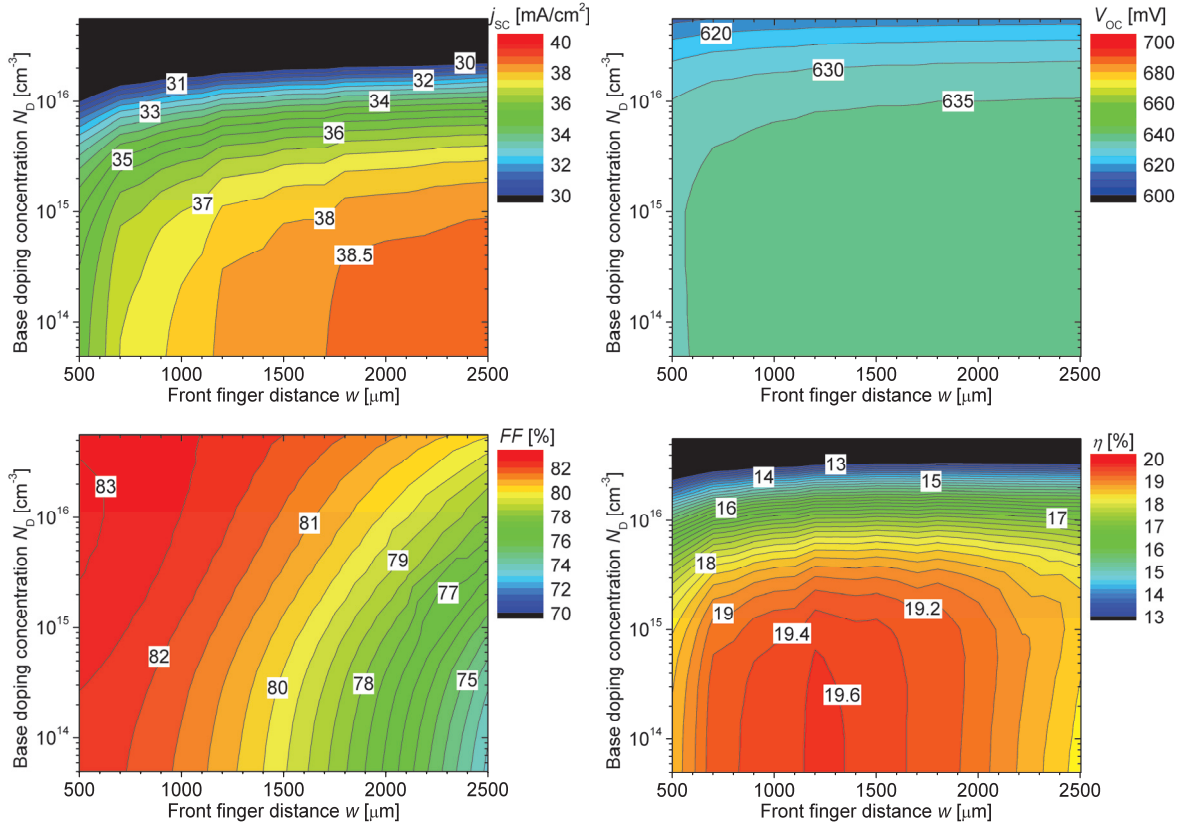


Fig. 6.5: Variation of the phosphorus base doping concentration N_D and the front finger distance w of the n^+np^+ Al back junction Si solar cell. For the FSF, profile (b) (Tab. 6.2) has been used and an Al-p⁺ emitter with a depth $d_{Al} = 8 \mu\text{m}$ has been assumed. Shown are the cell parameters short-circuit current density j_{sc} , open-circuit voltage V_{oc} , fill factor FF and efficiency η for a cell thickness $d = 200 \mu\text{m}$ and a contact width $w_{finger} = 60 \mu\text{m}$.

Towards higher N_D values, a continuous decrease of V_{oc} and j_{sc} is obtained, which is even more pronounced for $N_D > 10^{16} \text{cm}^{-3}$. As already mentioned in Chap. 6.3, this effect results from a strong increase of the minority carrier concentration in the FSF with increasing bulk doping concentration [156, 169] and, thus, a lowered charge collection probability of the minority carriers at the rear side contact, leading to a decreased j_{sc} . As expected, j_{sc} decreases as well when front finger distances are reduced due to the constant finger width $w_{finger} = 60 \mu\text{m}$. The smaller w becomes, the more the fraction of incident light coupling into the solar cell decreases.

A contrary behavior is observed in respect of the fill factor. The larger w , the more pronounced lateral current effects become. As a consequence of a continuously increasing series resistance, the FF decreases. Due to opposite characteristics of j_{sc} and FF depending on the front finger distance, a maximum in the efficiency appears in the range of around $w \approx 1200 \mu\text{m}$, slightly below the front finger distance of the realized solar cell described in Chap. 6.2.

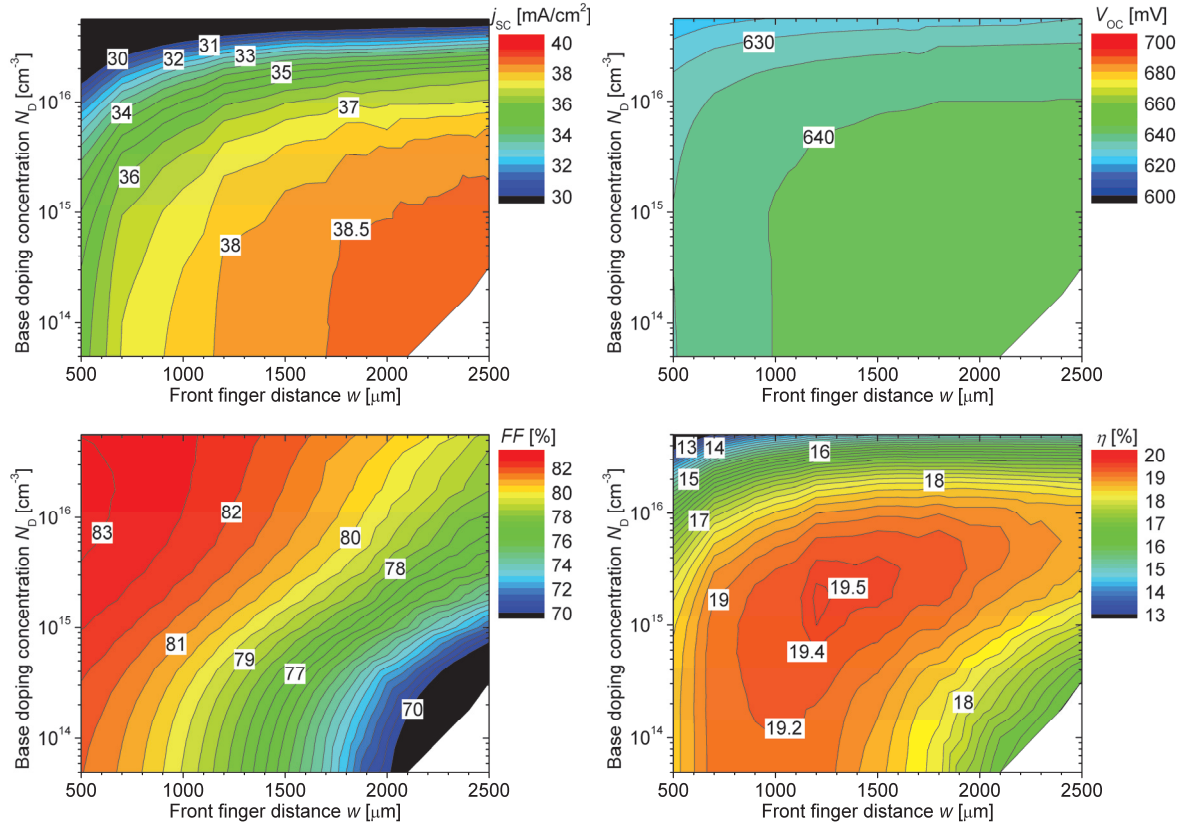


Fig. 6.6: Variation of the phosphorus base doping concentration N_D and front finger distance w of the n^+np^+ Al back junction Si solar cell. Calculations are analogous to Fig. 6.5, but without full-area FSF. Only local FSFs (Tab. 6.2, (a)) with a width of $100 \mu\text{m}$ have been applied below the front contact fingers. A surface recombination velocity $S_{0,front} = 10 \text{ cm/s}$ has been assumed, according to measured results. Compared to Fig. 6.5, similar peak efficiencies are achievable.

Interestingly, comparable efficiencies of up to 19.5% are achieved by omitting the full-area FSF and only applying highly doped local FSFs below the front metal contacts (Table II, (a)), as demonstrated in Fig. 6.6. For simulation, $100 \mu\text{m}$ wide local FSF areas have been assumed. Due to lowered Auger recombination and a decreased effective surface recombination velocity, an increase of j_{sc} especially for $N_D > 1 \times 10^{15} \text{ cm}^{-3}$ and an overall increase of V_{oc} by about 5 mV are obtained in comparison to the results in Fig. 6.5, leading to improved efficiencies for base doping concentrations above $N_D = 1 \times 10^{15} \text{ cm}^{-3}$ ($< 5 \Omega\text{cm}$). Towards lower N_D values and especially for larger finger distances w , the lateral conductivity becomes insufficient and significantly increased internal series resistances are induced. As a consequence, the FF drops remarkably, limiting the efficiency. From these simulations, the conclusions can be drawn that the optimal N_D amounts to around $2 \times 10^{15} \text{ cm}^{-3}$, which corresponds to 2 - 3 Ωcm base material, well suitable for industrial application. When omitting the full-area FSF, a very effective surface passivation is even more essential.

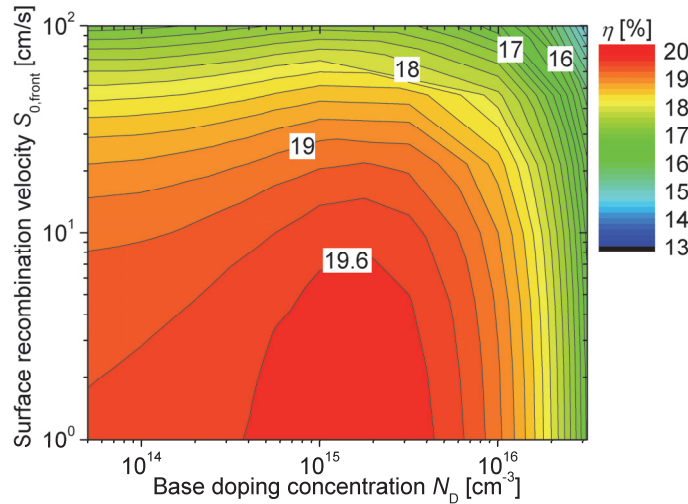


Fig. 6.7: Influence of the surface recombination velocity $S_{0,front}$ on the efficiency η (compare to Fig. 6.6). A front finger distance $w = 1200 \mu\text{m}$ has been applied. The n^+np^+ Al back junction Si solar cell without full-area FSF is highly sensitive to variations in the front surface passivation quality.

For the simulation, the surface recombination velocity $S_{0,front} = 10 \text{ cm/s}$ has been assumed on the base of experimentally achieved results and, thus, realizing lower $S_{0,front}$ values might lead to even higher efficiencies, as shown in Fig. 6.7.

The influence of different FSF profiles on the cell performance is summarized in Fig. 6.8, where the efficiency is plotted as a function of the base doping concentration N_D . The front finger distance has been chosen in the range $w = 1200 - 1300 \mu\text{m}$, according to the best front finger distance for each combination. On the left hand side, variations for “advanced” metallization techniques with printed seed layers and plated contacts are shown, allowing contacting phosphorus-doped surfaces with concentrations down to $N_D = 5 \times 10^{19} \text{ cm}^{-3}$ and achieving narrower finger widths of $w_{finger} = 60 \mu\text{m}$ [171]. On the right hand side, results for “standard” metallization techniques like screen-printing are shown, necessitating surface concentrations of approximately $5 \times 10^{20} \text{ cm}^{-3}$ and being limited to finger widths of $100 \mu\text{m}$. For profile abbreviations see Tab. 6.2.

Whereas in Fig. 6.8 (left) the efficiency of cells featuring profile (b) as full-area FSF has a strong dependence on the base doping concentration (absolute reduction of η by 1% absolute, comparing 1 and $10 \Omega\text{cm}$), η can be significantly increased, especially on $1 \Omega\text{cm}$ material, by reducing $N_{FSF,peak}$ and implementing a selective FSF (combination (c) & (b)). On high-resistivity base material this would lead to an efficiency reaching nearly 20%. As mentioned before, comparable efficiencies are achieved by omitting the full-area FSF and only applying local FSF areas below the front contacts. This local FSF with the driven-in profile (b) does not remarkably improve the efficiency

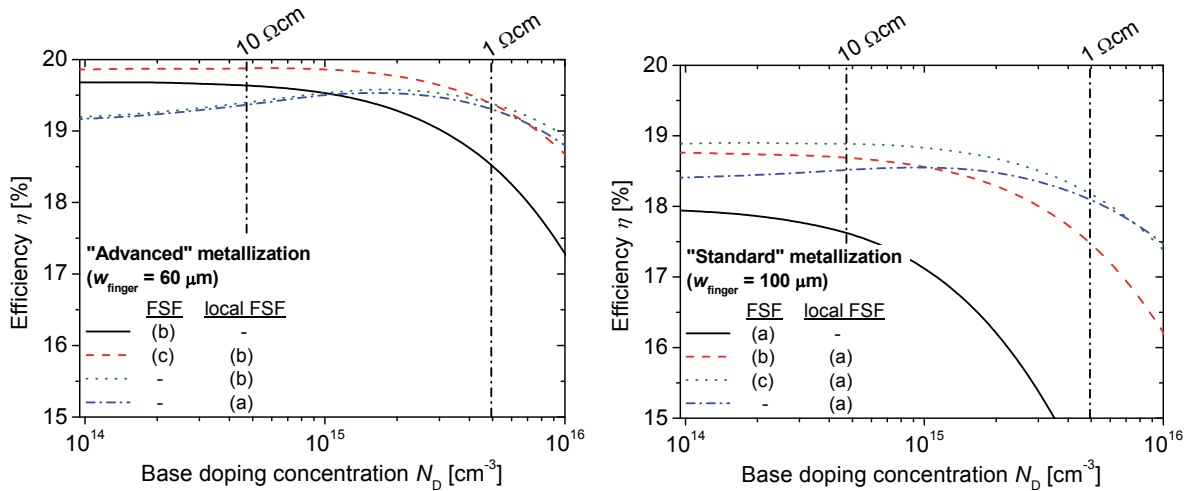


Fig. 6.8: Influence of different uniform and selective FSFs on the efficiency η . On the left, variations for “advanced” metallization techniques are shown, allowing contacting lowly doped surfaces and achieving narrower finger widths. On the right, results for standard metallization techniques like screen-printing are shown. The profile abbreviations are given in Tab. 6.2. According to the best front finger distance for each combination, $w = 1200 - 1300 \mu\text{m}$ has been chosen.

compared to the same architecture with the more industrially adequate profile (a) (see Fig. 6.8). An industrially feasible approach for realizing such structures is provided by laser chemical processing (LCP), enabling diffusion profiles with $N_{\text{peak}} = 2.5 \times 10^{20} \text{ cm}^{-3}$ and depths of $1.0 \mu\text{m}$ with high throughput, leading to sheet resistances of $\sim 15 \Omega/\text{sq}$ [172].

Due to increased shadowing losses by standard screen-printed metallization (Fig. 6.8, right, with $w_{\text{FSF,local}} = 200 \mu\text{m}$ locally below the front contacts) the efficiency is overall decreased by at least 0.8% absolute (comparing the local FSF (a) for both metallization types, dash dot). A full-area FSF (a) leads to a strong decrease of η , due to significantly increased Auger recombination within the FSF. Here the application of an industrially feasible selective FSF (dash) improves the solar cell performance by 1% absolute for $10 \Omega\text{cm}$ base material. Again, same efficiencies are achievable only with local FSFs for industrially relevant 2 - 3 Ωcm base material, if surface recombination velocities $S_{0,\text{front}} \leq 10 \text{ cm/s}$ can be achieved.

Until now, in this study, concrete values of the effective minority carrier lifetime τ_{eff} for n -type FZ Si have been assumed for calculations. The dependence of the cell efficiency on τ_{eff} is exemplarily demonstrated in Fig. 6.9 for 1 (left) and $10 \Omega\text{cm}$ (right) base material. For $1 \Omega\text{cm}$ base material and bulk lifetimes above 1 ms, best results are achieved with bulk thicknesses in the range $100 - 180 \mu\text{m}$, whereas for $10 \Omega\text{cm}$ material and lifetimes $> 10 \text{ ms}$ the optimal thickness is beyond $300 \mu\text{m}$, due to

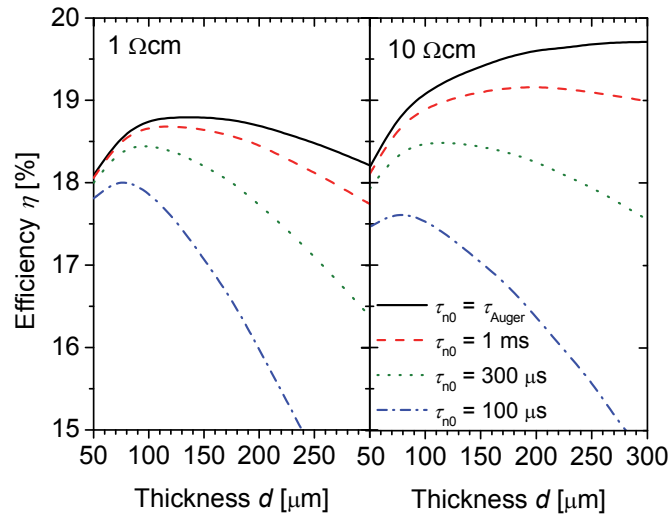


Fig. 6.9: Influence of bulk minority carrier lifetime τ and the wafer thickness d on the efficiency η for 1 and 10 Ωcm n-type Si base material. A front finger pitch $w = 1200 \mu\text{m}$ has been assumed with $w_{\text{finger}} = 60 \mu\text{m}$. For the FSF, profile (b) (Tab. 6.2) has been applied.

an enhanced absorption of incident photons and sufficiently high effective diffusion lengths of the minority carriers. For $\tau_{\text{eff}} \approx 300 \mu\text{s}$ a cross-over point is observed, leading to enhanced efficiencies for 1 Ωcm base material. In high-resistivity materials higher j_{sc} values can be reached, but towards low lifetimes the strongly decreasing FF overcompensates this benefit. Nevertheless, for $\tau_{\text{eff}} < 1 \text{ ms}$, in contrast to p -type Si solar cells, the diffusion length of the minority carriers limits the current and, thus, the efficiency, as the minority carriers - predominantly generated at the front side of the wafer - have to diffuse to the rear side, passing the entire wafer thickness before reaching the junction.

6.5 Analysis of aluminum p^+ rear emitter

The thickness d_{Al} of non-passivated highly Al-doped Si regions essentially influences the saturation current density $j_{0,\text{Al}}$, as discussed in Chap. 5. Here, d_{Al} needs to be preferably thick in order to achieve lowest $j_{0,\text{Al}}$ values. For effectively surface passivated Al- p^+ regions holds a contrary behavior: the thinner the Al- p^+ region, the lower is $j_{0,\text{Al}}$.

For n^+np^+ Si solar cells featuring non-passivated full-area Al-doped rear p^+ emitters, the $j_{0,\text{Al}}$ increase for thicker Al- p^+ emitter leads to a significant V_{oc} increase and, thus, improved efficiencies η , as displayed by Fig. 6.10 (dash dot). The V_{oc} decreases with decreasing thickness of the Al- p^+ emitter due to enhanced recombination of minority carriers at the non-passivated fully metallized rear side.

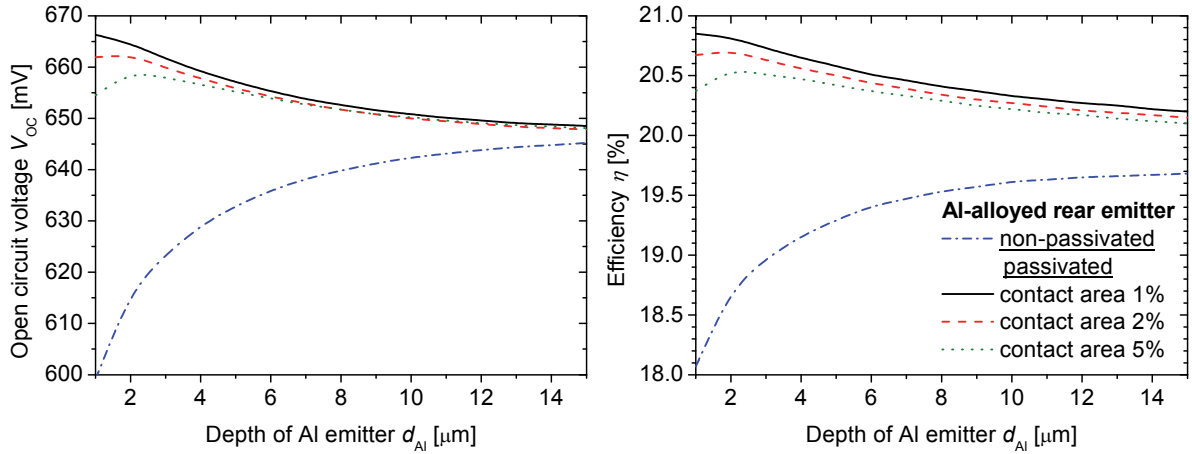


Fig. 6.10: Variation of the thickness d_{Al} of the full-area Al- p^+ rear emitter. Shown are the open-circuit voltage V_{oc} and efficiency η for non-passivated and passivated rear emitters, the latter with varying contact metallization coverage at the rear side.

An effectively passivated rear surface of the full-area Al-doped rear p^+ emitter leads to very clearly reduced $j_{0,Al}$ values (see Chap. 5) and, thus, to a significant improvement of V_{oc} in the range of 15 – 20 mV, as has been reported recently [143, 144, 157, 173, 174]. This V_{oc} benefit can be directly seen in the 2D simulation in Fig. 6.10 for Al- p^+ thicknesses of $d_{Al} \approx 8 \mu\text{m}$. Please note that an initially e.g. $8 \mu\text{m}$ thick Al- p^+ area thickness after surface passivation to a thickness of about $4 \mu\text{m}$, due to surface preparation and an etch back process. In the shown simulations, in addition to the non-passivated n^+np^+ solar cell results, the rear contact metallization fraction has been varied. Thereby, the passivated part of the rear surface features with $S_{0,\text{rear,pass}} = 0 \text{ cm/s}$ perfect passivation properties. The rear contact distance L_P has been set to $530 \mu\text{m}$. For passivated Al- p^+ emitters the behavior inverts, resulting in increasing V_{oc} values with decreasing thicknesses. Metallization coverage fractions of 1% are normally used. Increasing this fraction results in a decrease of V_{oc} mainly for relatively thin Al emitters (full-area Al- p^+ emitters usually have thicknesses around $4 - 8 \mu\text{m}$, depending on the amount of printed Al paste and alloying conditions [175]).

In addition, j_{sc} is significantly influenced due to a rear side passivation as well. The passivation enhances the reflection properties at the rear surface by 16% ($R_{\text{Phong}} = 0.86$) in the long wavelength range above $\lambda = 1000 \text{ nm}$, leading to an increase of j_{sc} by 1.5 mA/cm^2 .

In order to account properly for lateral conductance effects in locally contacted surface-passivated Al- p^+ emitters of n^+np^+ Si solar cells, an advanced 3D simulation model is necessary. A 3D standard domain according to the rear side has been chosen, approximating the front side as fully contacted to decouple front and rear contact distances. The FSF profile (b) (Tab. 6.2) and an effective front surface recombination

velocity of $S_{0,\text{eff}} = 10^4$ cm/s have been used for calculations, to match the front side j_0 value of the 2D simulation model. The carrier generation has been reduced by 6%, according to the shadowing losses caused by the front metallization grid. The simulation results shown in the following are based on 3D simulations. A detailed description of such a 3D standard domain for simulation purposes is given in Chap. 7. Here, the focus is set on the solar cell behavior.

In Fig. 6.11, the influence of the rear contact point distance L_P and the thickness of the full-area Al- p^+ emitter d_{Al} on the fill factor and the efficiency are shown. The surface recombination velocity of the passivated rear is set to $S_{0,\text{rear}} = 100$ cm/s [129], whereas the rear reflectance properties have not been changed. Whereas j_{sc} does not change significantly over the whole considered parameter range, V_{oc} increases strongly towards thinner Al- p^+ regions (not shown) due to significantly reduced saturation current densities $j_{0,e}$, limited at $d_{\text{Al}} \leq 2$ μm by contact recombination. V_{oc} behaves nearly independent on L_P , as the rear side metallization fraction has been kept constant at 1%. Due to a non-sufficient lateral conductivity towards very thin Al- p^+ emitters, the FF decreases with increasing L_P . The tradeoff between V_{oc} and FF results in an optimal rear contact distance of 500 μm for an Al- p^+ emitter thickness d_{Al} of around 2 μm . This L_P results in a contact point diameter of 50 μm , which can be realized.

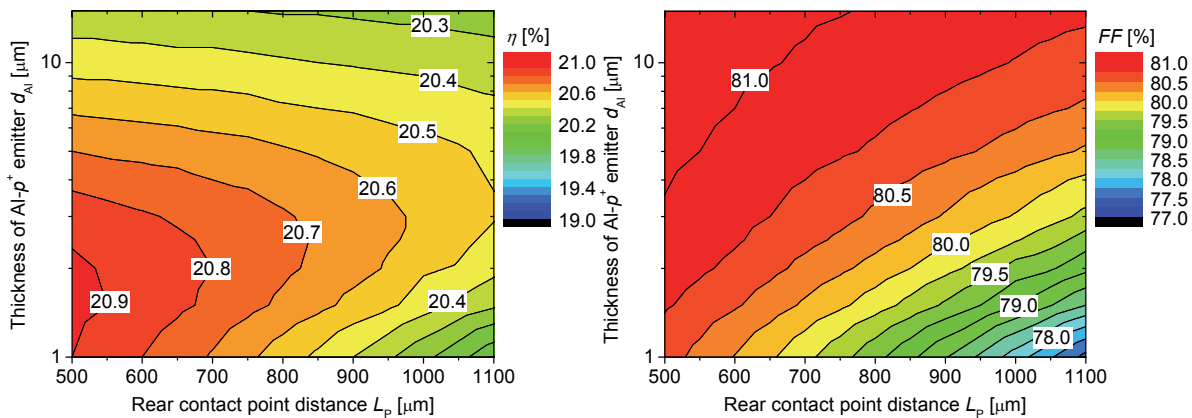


Fig. 6.11: Influence of the rear contact point distance L_P and the thickness of the Al- p^+ emitter d_{Al} on fill factor FF and efficiency η . The surface recombination velocity of the passivated rear emitter has been set to $S_{0,\text{rear}} = 100$ cm/s [129]. To decouple front and rear side contact distances in these 3D simulations, the front side of the cell has been assumed to be fully metallized. FSF (b) (see Tab. 6.2) and an effective front surface recombination velocity of $S_{0,\text{eff}} = 10^4$ cm/s have been used for calculations to achieve the same j_0 values as in the real solar cell. The carrier generation has been reduced by 6%, according to the shadowing losses caused by the front side metallization. The rear side metallization fraction has been kept constant at 1%.

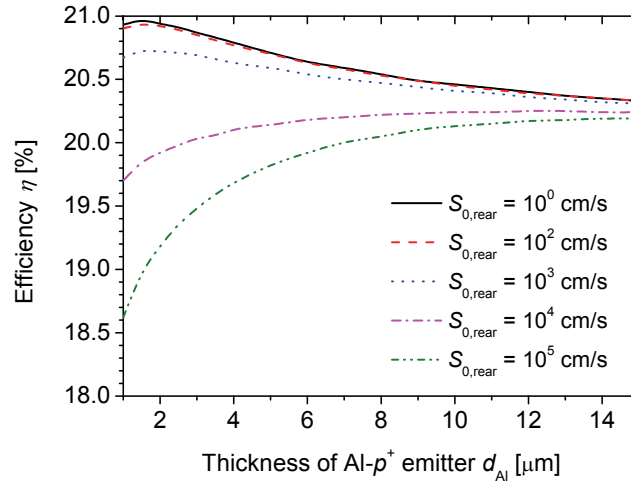


Fig. 6.12: Influence of the thickness d_{Al} of the Al- p^+ emitter and the rear surface recombination velocity $S_{0,rear}$ on the efficiency η of the n^+np^+ Al back junction Si solar cell ($10 \Omega\text{cm}$). The front side properties have been chosen according to Fig. 6.11.

In Fig. 6.12 the rear surface recombination velocity $S_{0,rear}$ of the surface-passivated Al- p^+ emitter has been varied in a broad range and its influence on η is shown. With a realistic $S_{0,rear} = 100 \text{ cm/s}$, an efficiency potential of 20.9% is determined for n^+np^+ Al back junction Si solar cells. For $S_{0,rear} > 10^3 \text{ cm/s}$ $j_{0,e}$ increases significantly leading to a decrease of η .

6.6 Conclusions

In this chapter, a detailed analysis of the potential of n -type Si solar cells with Al-alloyed rear p^+ emitter for industrial applications by means of 2D and 3D numerical simulations has been presented. In order to identify the efficiency limiting factors, this solar cell has been calculated by sequentially focusing on effects of the front side, the bulk material and the rear side.

In summary, promising improvements of the n^+np^+ Al back junction cell concept are:

- (i) Lowering the front finger distance slightly leads to an increase of the efficiency by 0.2% absolute.
- (ii) A further decreased phosphorus peak doping concentration of the full-area uniform front surface field results in an efficiency increase; it becomes even more effective with the use of a selective FSF.
- (iii) The application of local highly doped FSF areas below the front contacts without full-area FSF has a similar efficiency potential, if an effective front surface passivation with $S_{0,front} \leq 10 \text{ cm/s}$ is provided.

- (iv) The implementation of an additional passivation layer on the surface of the rear Al- p^+ emitter leads to significantly decreased recombination and, thus, to a significant V_{oc} improvement of 15 – 20 mV. In combination with an increase of j_{sc} by 1.5 mA/cm², due to improved internal reflection properties, the efficiency increases by 1% absolute and beyond, even with rear surface recombination velocities up to $S_{0, rear} = 1 \times 10^3$ cm/s.

Thus, for n^+np^+ solar cells with non-passivated full-area Al- p^+ rear emitter, conversion efficiencies of up to 20% are realistic. Additionally, an effective surface passivation of the Al- p^+ emitter should increase the efficiency by 1% absolute, leading to an efficiency potential close to 21% for this solar cell concept.

7 Lateral conductance effects of locally contacted rear surface passivated silicon solar cells

In this chapter, lateral conductance effects of locally contacted rear surface passivated p-Si solar cell concepts (commonly known as PERC structure) are investigated. In most cases such effects need to be modeled via 3D numerical simulations, as charge carrier might pass lateral distances in the range of millimeters. Therefore, in the chapters 7.1 - 7.4 the focus is set on numerical optimum rear contact distance calculations, discussing high injection effects occurring at locally rear contacted solar cell concepts featuring highly resistive base material. In chapter 7.5, an existing analytical model for optimum rear contact distance calculations is extended in order to account for these high injection effects. Results of chapter 7 are published in [176, 177].

7.1 PERC structure on p-type silicon featuring laser-fired contacts

Monocrystalline boron-doped Si solar cells featuring local rear contacts and passivated rear surfaces, introduced by Blakers *et. al.* in 1989 [178], allow higher conversion efficiencies than conventional industrial devices exhibiting full-area Al back surface fields. One approach to realize local rear contacts is the laser-fired contact (LFC) technology [179], which is suitable for thin wafer processing and high industrial throughput. To achieve best performances, it is crucial to choose an appropriate rear contact design according to the used Czochralski-grown p-type Si material and its resistivity. Since the introduction of this cell concept, various optimization studies based on numerical simulations have been published. First publications focused on high efficiency structures [180-188] and, later on in 2002, as well industrial quality Si material has been considered by Catchpole and Blakers [189]. Recently, a comprehensive analytical study [190] has been presented to estimate the optimum bulk resistivity and corresponding contact distances. These analytical calculations were restricted to low level injection (LLI) conditions, which can lead to errors for high resistivity material with higher lifetime and will be discussed in more detail in Chap. 7.5. In this chapter, 3D numerical simulations are presented, accounting for injection level dependent recombination and transport mechanisms, and thus, achieving more accurate results for high resistivity material. The optimum rear contact distances L_p for different solar cell thicknesses and a broad range of nominal bulk

resistivities ρ_0 are calculated. These variations are presented for (i) high-quality float-zone (FZ) and (ii & iii) Czochralski (Cz)-grown p -Si material with a very low and a very high oxygen content in the bulk material, which detrimentally influences the effective carrier lifetimes τ_{eff} .

7.1.1 Simulation setup

For accurate simulations of locally contacted rear surface passivated p -Si solar cells it is crucial to take the bulk material properties into account. Thus, three different material qualities have been considered in this study: (i) float-zone (FZ) with an Auger-limited bulk carrier lifetime and (ii & iii) Czochralski (Cz)-grown material with its fundamental limitations of stable lifetime τ_d in B-doped Cz-Si, according to

$$\frac{\tau_d}{\mu\text{s}} = 2 \times 7.675 \cdot 10^{45} \cdot \left(\frac{[\text{B}_s]}{\text{cm}^{-3}} \right)^{-0.824} \cdot \left(\frac{[\text{O}_i]}{\text{cm}^{-3}} \right)^{-1.748} \quad (7.1)$$

published by Bothe *et al.* in 2004 [22]. The interstitial oxygen concentration $[\text{O}_i]$ and the boron concentration $[\text{B}_s]$ are given in units of cm^{-3} and τ_d in μs . The factor of 2 in Eq. (7.1) has been added to the originally presented equation in order to take the permanent improvement of excess carrier lifetime due to high-temperature processes in solar cell processing into account and, thus, a reduction of the interstitial oxygen concentration [22, 23]. Here, a low (ii) $[\text{O}_i] = 6 \times 10^{17} \text{ cm}^{-3}$ and a very high (iii) $[\text{O}_i] = 1 \times 10^{18} \text{ cm}^{-3}$ interstitial oxygen contamination have been considered, which mark the lower and upper limit of $[\text{O}_i]$ in Cz-grown p -Si, respectively. For the Cz material, the capture time constant for excess minority carriers $\tau_{n0} = 1.1/2.03 \cdot \tau_d$ is used, which follows from Eq. (7.1) and the condition, that all lifetime measurements in [22] have been performed at the same relative injection level $\Delta n/N = 0.1$. The defect energy level E_t and the symmetry factor k is chosen according to Rein *et al.* [104]. In order to focus on the rear side properties, a non-recombination active front side with full-area transparent electrode has been assumed for the simulations. Thus, there is no lateral current flow in the emitter and the front side has a negligible impact on the simulated cell performance. Please note that a non-ideal front surface with a realistic emitter dark saturation current density $j_{0,e}$ would lead to slightly lower minority carrier densities. For optical purposes, a front surface textured with random pyramids and a 75 nm SiN_x anti-reflection coating has been implemented. Shading losses of the front contact have been neglected in this study. Realistic rear side reflectance conditions by means of the Phong-model have been chosen [191]. Two different approaches for modeling the properties at and near the rear contact have been used. In Chap. 7.1, the surface recombination velocities $S_{0,\text{met}}(N_A)$ for the excess minority carriers at the rear contact depending on the doping concentration N_A have been considered by

$$S_{0,\text{met}}(N_A) = S_0 + \alpha \cdot e^{\beta(N_A + N_0)}. \quad (7.2)$$

according to Ref. [192] with $S_0 = -900$ cm/s, $\alpha = 22.1$ cm/s, $\beta = 1.29 \times 10^{-16}$ cm³ and $N_0 = 3.40 \times 10^{16}$ cm⁻³. All surface recombination velocities are given in cm/s. In the second approach, which is applied from the beginning of Chap. 7.2, a Gaussian BSF profile is applied locally in the area of the rear contact, featuring a peak concentration $N_{\text{peak}} = 10^{20}$ cm⁻³ and a depth $d_{\text{BSF}}(N_A = 10^{16}$ cm⁻³) = 0.1 μm , which corresponds to $R_{\text{sh}} = 400$ Ω/sq . Here, the surface recombination velocity $S_{0,\text{met}} = 10^7$ cm⁻³ at the rear contact equals the thermal velocity.

$S_{0,\text{pass}}$ values for the excess minority carriers at the thermally grown SiO₂ passivated rear side are determined empirically from a standard industrial process:

$$\frac{S_{0,\text{pass}}(N_A)}{\text{cm/s}} = 23 \cdot \left(\frac{N_A}{1.5 \times 10^{15} \text{ cm}^{-3}} \right)^{0.41}. \quad (7.3)$$

The formula has the same structure as published in [193], but with other values for the parameters, which have been adapted to experimental data. Each rear contact features a quadratic shape with an edge length of 80 μm , independent from the rear contact distance L_P . This equals the surface of a circle with a diameter $h_{\text{LFC}} = 90$ μm , which is achievable by laser-processing on industrial level. The standard domain is shown in Fig. 7.1. Calculations are based on Fermi-Dirac statistics. The complete set of simulation parameters used in this study is given in Tab. 3.2.

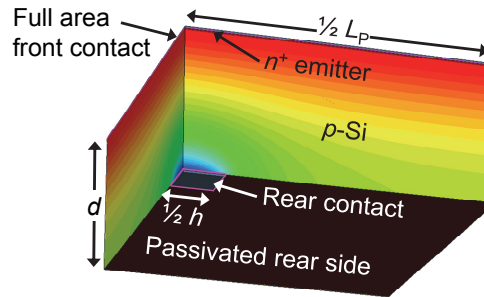


Fig. 7.1: Schematic of the standard domain of a monocrystalline p-type Si solar cell with passivated rear surface for numerical simulations. With a constant rear contact point width $h = 80$ μm according to industrially achievable laser points, the following parameters have been varied in the given ranges: the nominal base resistivity from $\rho_0 = 0.1$ Ωcm to about 20 Ωcm , the rear contact distance $L_P = 200 - 1000$ μm and the thickness $d = 80 - 200$ μm (see Fig. 7.2). To focus on the bulk and rear side recombination effects, the front side has been considered as a 1D non-recombination active transparent front side electrode with a very shallow phosphorus doped emitter, avoiding significant Auger recombination losses. The colors of the bulk material indicate the distribution of the excess carrier density Δn in arbitrary units at the mpp.

7.1.2 Optimum rear contact distance L_p

In Fig. 7.2 numerically simulated conversion efficiencies η for a standard domain of monocrystalline p -type Si solar cells with passivated rear surfaces are shown as a function of the nominal base resistivity $\rho_0 = 0.5 - 10 \text{ } \Omega\text{cm}$, the rear contact distance L_p and the thickness h are shown. Due to the fixed size of the rear contact area, the metallization fraction f increases towards small L_p and, thus, more recombination occurs at the rear side of the solar cell. As a consequence, the open-circuit voltage V_{oc} decreases. This relative decrease is much stronger for materials with higher bulk lifetime, due to a higher V_{oc} for high L_p . Thus, the FZ material shows a larger variation in the efficiency. Towards high L_p , higher lateral series resistance and spreading resistance losses [194-199] occur, leading to a strong decrease in the fill factor FF and reducing mainly the efficiency. Therefore, the optimum L_p is formed by a trade-off between V_{oc} and FF . As a result of a significantly reduced excess minority carrier lifetime τ_{eff} in the bulk towards lower quality materials, here considered with an increasing amount of oxygen in the bulk material, the optimum shifts towards thinner solar cell thicknesses and lower L_p .

A decreasing FF is strongly coupled with resistance losses. In the presented modeling solely series resistance losses are present, as the standard domain is free of parallel resistance losses. In Fig. 7.3, the fill factor losses towards high L_p , leading to the η decrease in Fig. 7.2, are shown for a fixed solar cell thickness $d = 170 \text{ } \mu\text{m}$. The FF is shown for FZ and Cz bulk material, the latter with a very high $[O_i]$, representing the worst case monocrystalline Cz material, consistently to Fig. 7.2. In the following, if Cz material is mentioned, it is referred to an O_i content of $[O_i] = 1 \times 10^{18} \text{ cm}^{-3}$.

If the fill factor losses would be caused exceptionally by the series resistance, which would be mainly driven by the base resistivity, the losses should be the same for the considered FZ and Cz bulk material. But as can be seen in Fig. 7.3, the losses diverge with increasing base resistivity, especially for increasing L_p , due to high injection effects. Therefore, for a deeper understanding, the lumped series resistance R_s will be modeled in Chap. 7.2.1. In addition, it is known that injection dependent recombination also leads to FF losses [200]. This effect will be considered and analyzed in Chap. 7.4.

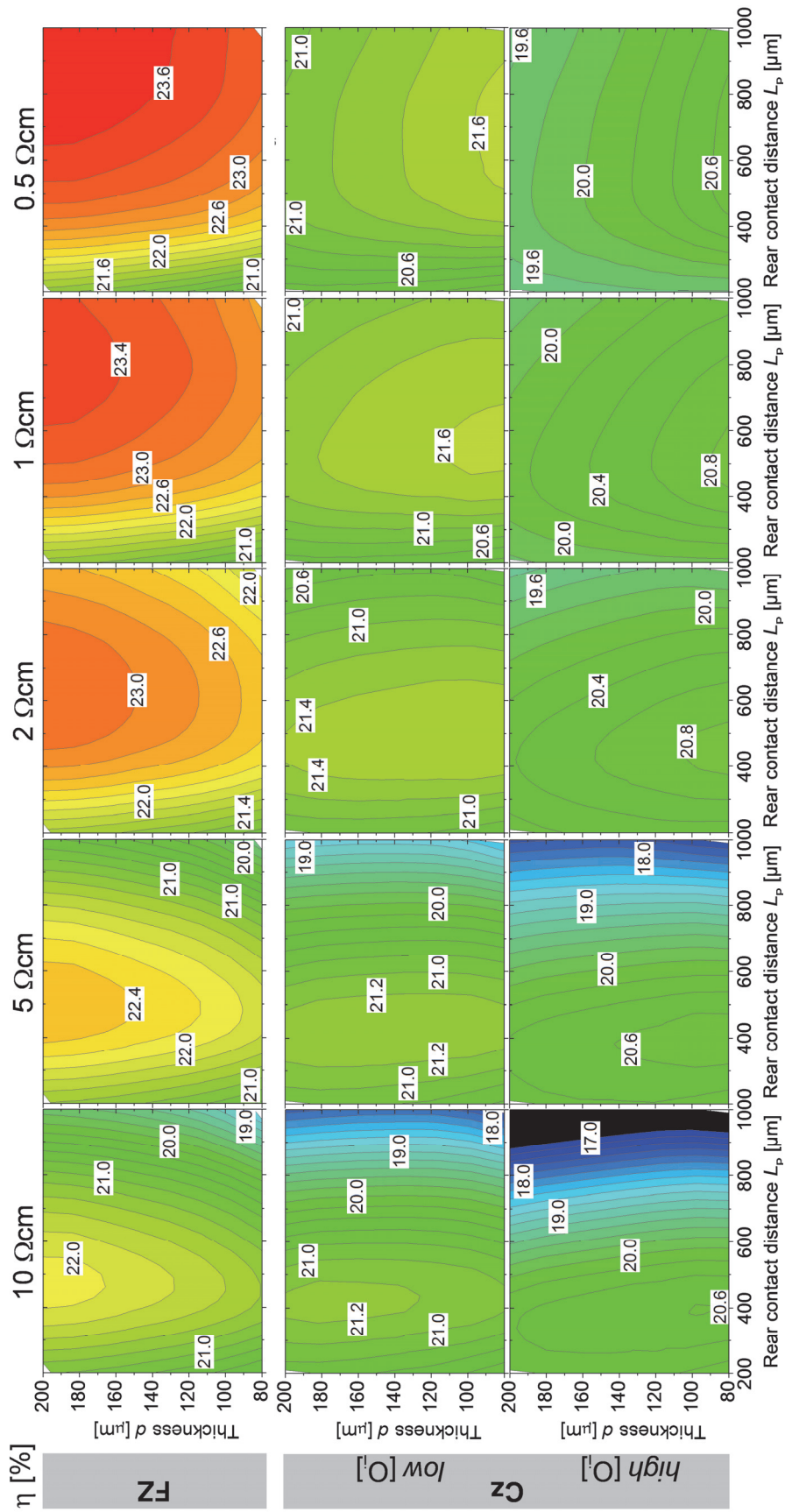


Fig. 7.2: Simulated conversion efficiencies η for monocrystalline p-type Si material featuring nominal base resistivities ρ_0 from 0.5 to 10 Ωcm . Three different material qualities have been calculated (float-zone (FZ) and Czochralski(Cz)-grown material with two different realistic oxygen contaminations $[O_i] = 6 \times 10^{17} \text{ cm}^{-3}$ and $1 \times 10^{18} \text{ cm}^{-3}$). In order to focus on the bulk and rear side recombination properties, a non-recombination active front side with neglected shading effects due to the front side metallization has been assumed for the 3D numerical simulations.

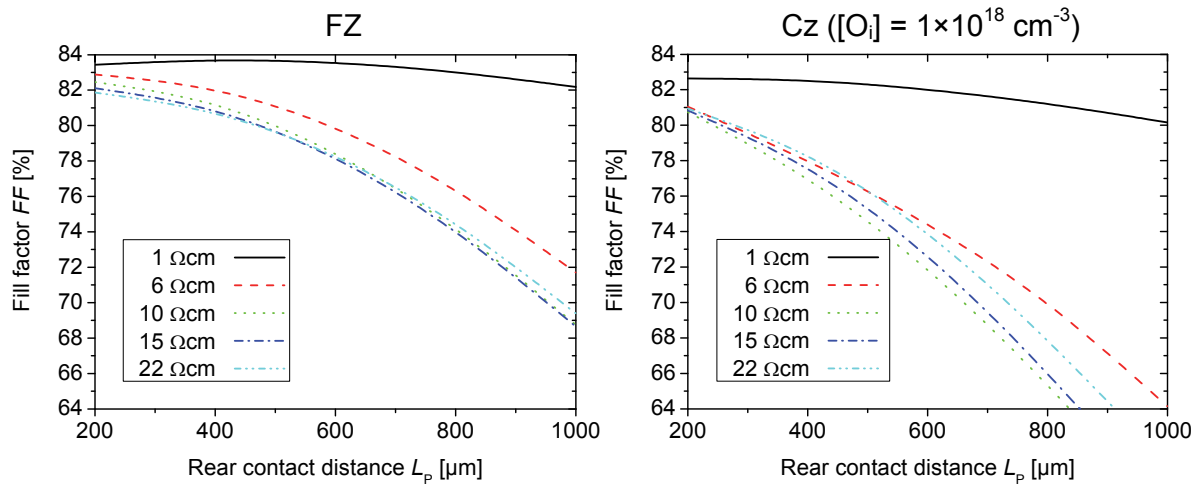


Fig. 7.3: Fill factor FF versus rear contact distance L_p and different nominal base resistivities ρ_0 for numerically calculated locally contacted rear surface passivated p -Si solar cells with FZ (left) and Cz bulk material (right), featuring $[O_i] = 1 \times 10^{18} \text{ cm}^{-3}$. The losses diverge with increasing ρ_0 , especially for increasing L_p , due to high injection effects.

7.1.3 Current density-voltage behavior

The current density-voltage (IV) characteristics for the considered FZ and Cz bulk material for different base resistivities ρ_0 are shown in Fig. 7.4 for a fixed rear contact distance $L_p = 1000 \mu\text{m}$. For FZ base material (Fig. 7.4, left), an increase of resistivity from 1 to 6 Ωcm results clearly in the characteristic current dependent voltage decrease, as an indicator of series resistance losses [81]. With further increasing resistivities, an additional current density decrease can be observed. At high resistivities, the IV characteristics show similarities to the typical behavior appearing if the parallel resistance R_p would be decreased – the current density starts to decrease already at very low voltages around 100 mV. But in this case, R_p losses can be excluded, as the simulated structure is free of R_p influences.

While in FZ base material j_{sc} and V_{oc} remain relatively constant under variation of ρ_0 , in the considered Cz bulk material (Fig. 7.4, right) both parameters decline towards low resistive material, as a consequence of the severely degraded lifetime. This results in a very small $\tau_{n0} = 13 \mu\text{s}$ for 1 Ωcm Cz material. The same resistivity behavior is observed as for FZ bulk material. Thereby, in Fig. 7.4 (right) a cross-over point appears at $500 \text{ mV} < V < 550 \text{ mV}$. With increasing ρ_0 the current density decrease starts at lower V , whereas higher V_{oc} values can be observed.

To rebut the suspect, that this behavior could appear from the applied model for $S_{0,\text{met}}$, the IV curves have been recalculated with $S_{0,\text{met}} = 10^7 \text{ cm/s}$ and a Gaussian BSF boron

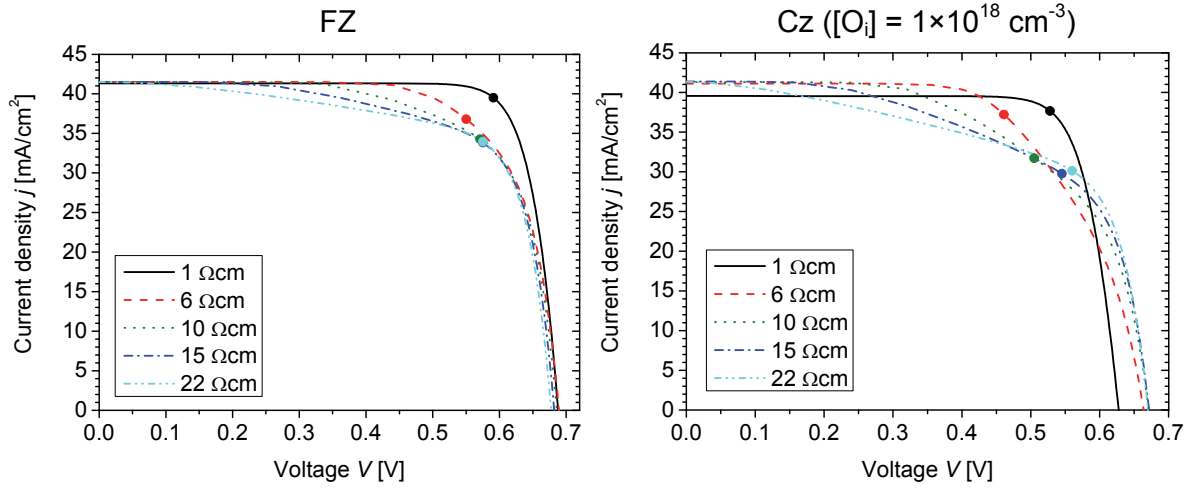


Fig. 7.4: Simulation of the IV curve for different bulk resistivities at a fixed rear contact distance $L_P = 1000 \mu\text{m}$ and $d = 170 \mu\text{m}$ for FZ (left) and Cz bulk material (right) with $[O_i] = 1 \times 10^{18} \text{cm}^{-3}$. The surface recombination velocities $S_{0,met}(N_A)$ have been considered according to Eq. (7.2).

diffusion profile locally at the rear contact. Results are shown in Fig. 7.5. The BSF profile features a peak concentration $N_{\text{peak}} = 10^{20} \text{cm}^{-3}$ and a depth $d_{\text{BSF}}(N_A = 10^{16} \text{cm}^{-3}) = 0.1 \mu\text{m}$, corresponding to $R_{\text{sh}} = 400 \Omega/\text{sq}$. This reflects an arbitrary BSF doping profile, as the determination of local BSF doping profiles formed by an LFC process is quite challenging. By comparing the results with Fig. 7.4, a slight shift of V_{oc} can be observed for increasing ρ_0 . But overall, the main IV features are observed, as described before.

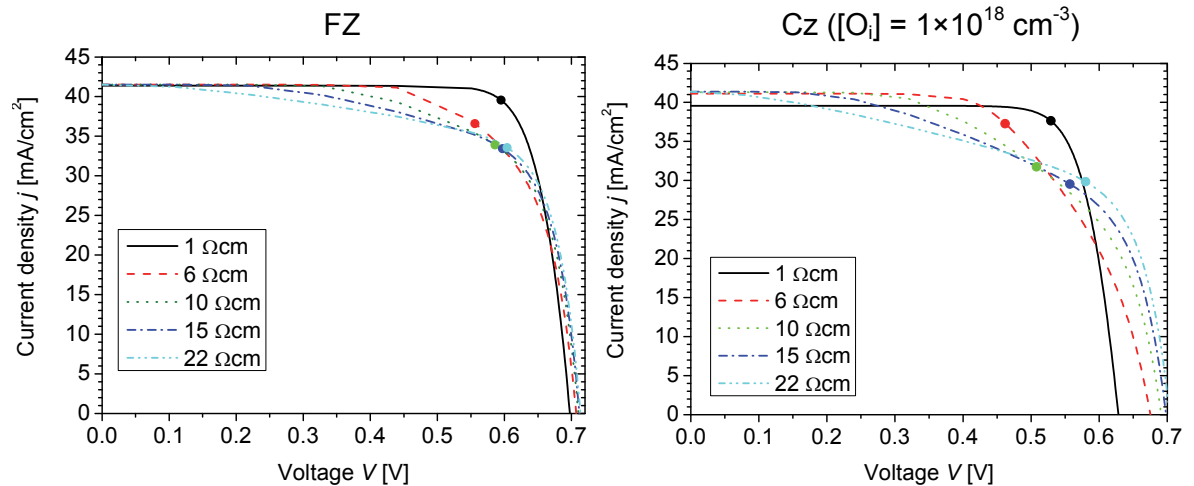


Fig. 7.5: Simulation of the IV curve for different bulk resistivities at a fixed rear contact distance $L_P = 1000 \mu\text{m}$ and $d = 170 \mu\text{m}$ for FZ (left) and Cz bulk material (right) with $[O_i] = 1 \times 10^{18} \text{cm}^{-3}$. The IV curves shown in Fig. 7.4 have been recalculated with $S_{0,met} = 10^7 \text{cm/s}$ and a local Gaussian BSF boron diffusion profile with $R_{\text{sh}} = 400 \Omega/\text{sq}$ at the rear contact.

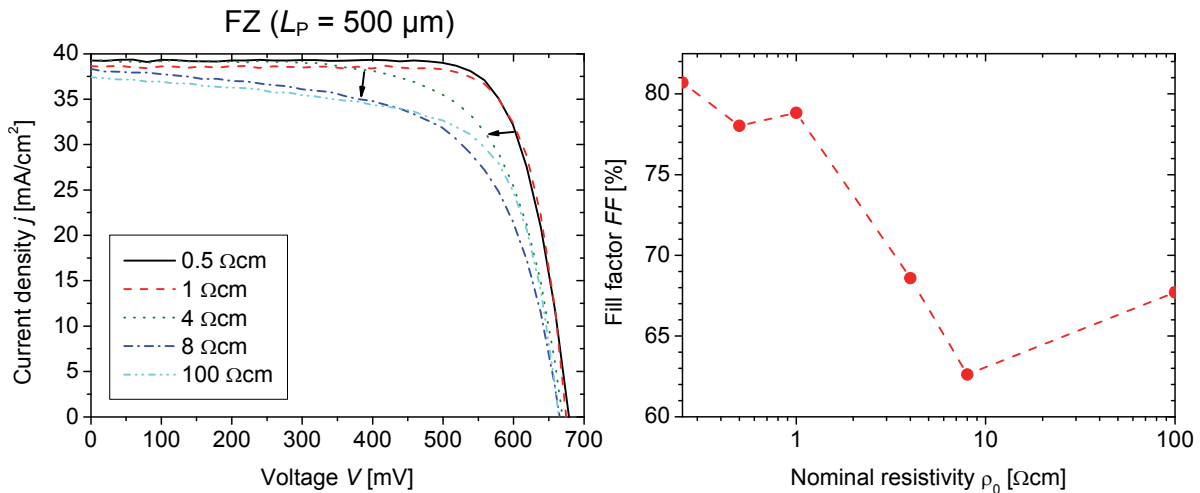


Fig. 7.6: Experimentally determined IV curves for different bulk resistivities at a fixed rear contact distance $L_p = 500 \mu\text{m}$ (left) and $d = 250 \mu\text{m}$ with its corresponding FFs (right). The solar cells are taken from a batch, fabricated at Fraunhofer ISE in the framework of the doctoral thesis of A. Grohe [201].

The discussed IV characteristics shown in the simulations in Fig. 7.4 and Fig. 7.5 can also be observed in measured IV curves of proper solar cells, fabricated at Fraunhofer ISE in the framework of the doctoral thesis of A. Grohe [201]. The results of a part of his batch named *NRP7* are shown in Fig. 7.6. These boron doped FZ p -Si PERC solar cells feature, equivalent to the simulated structure, a full-area front emitter and LFCs at the rear side of the solar cell. The bulk resistivity has been varied in a broad range from 0.25 to 100 Ωcm , while the rear contact distance has been set fixed to $L_p = 500 \mu\text{m}$ (Fig. 7.6, left). More details on the processing of the solar cells may be found in [201].

As appearing in the simulations, an increase of the bulk resistivity from 0.5 to 4 Ωcm features the same tendency of decreasing j at high voltages $V > 400 \text{ mV}$. With further increasing ρ_0 , the j drop begins as well at much lower voltages, implying a negative slope of the generally constant running current behavior at low voltages $V < 400 \text{ mV}$. Additionally, the observed increase of the FF for $\rho_0 > 10 \Omega\text{cm}$ (Fig. 7.3) can also be found in the experimental data (Fig. 7.6, right).

For a more detailed analysis, in Chap. 7.2.1 the series resistance losses of the presented results will be calculated explicitly and in Chap. 7.2.2 high level injection effects will be discussed in detail.

7.2 Consideration of global bulk effects

7.2.1 Modeling of lumped series resistance losses

Determining lumped series resistance losses in Si solar cells is essential, as solar cells are able to produce high currents of several ampere. Thereby, a broad variety of different methods exist, like e.g. fitting the two-diode function to a dark IV curve, comparing a one-sun with a dark IV curve or a $\text{Suns}V_{oc}$ measurement, a computation of the area under a one-sun IV curve, or comparing two or more IV curves measured at different illumination intensities. But thereby, not all methods are recommended according to their reliability and robustness, as turned out in the review of Pysch *et al.* [202]. Latter method, the extraction of R_s from a set of IV curves determined at different illumination intensities, firstly suggested in 1960 by Swanson [203], turned out as one of the methods of choice, also favored in [204] as it might be theoretically more accurate than R_s extractions attained by alternative methods. Furthermore, it might be an easy to use method, as it could be potentially integrated in IV testers including flasher, which measure multiple illumination intensities simultaneously, determining R_s as a function of current density [204].

In this study, R_s is determined via simulations under operating conditions at a V slightly above the maximum power point (mpp), according to [202]. Thereby, the IV curve is determined at three different illumination intensities: at (i) one-sun illumination and at (ii) +10% and (iii) -10% of the standard illumination conditions, leading to a shift in j_{sc} , proportional to the illumination variation [203, 205]. R_s results out of the shift in voltage and is determined via a fit to the calculated data pairs, as illustrated in Fig. 7.7.

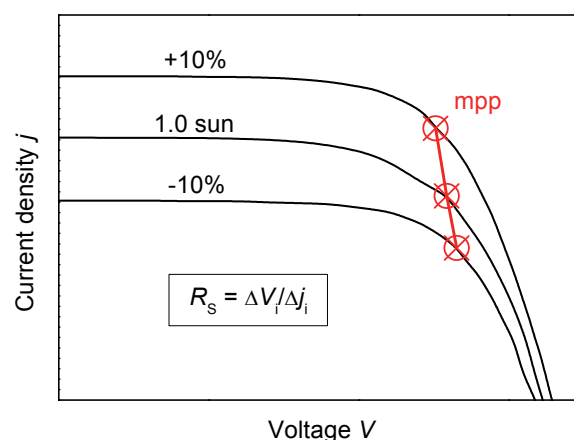


Fig. 7.7: Schematic for the determination of the lumped series resistance R_s in the presented simulations. The IV curve is determined at three different illumination intensities slightly above the maximum power point (mpp), according to [202].

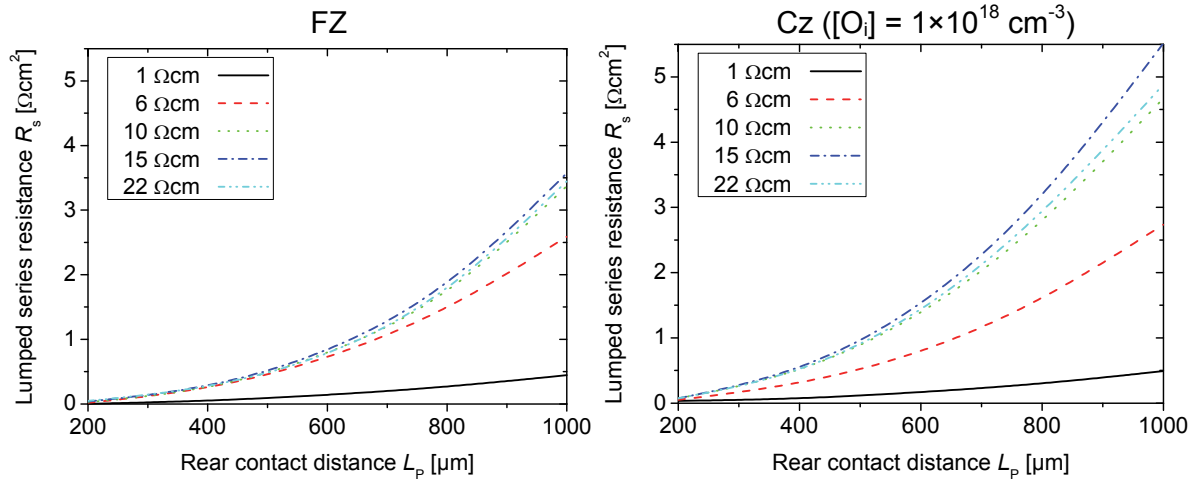


Fig. 7.8: Calculated lumped R_s losses, considering the same standard domain with $d = 170 \mu\text{m}$, as used for the determination of the FF in Fig. 7.3. Thereby, the observed FF s and R_s 's can be correlated very well.

In Fig. 7.8, the calculated R_s values are shown, considering the same standard domain, as used for the determination of the FF in Fig. 7.3. Thereby, the observed FF and R_s values can be correlated very well as expected, exhibiting qualitatively the same tendencies. In this case, the results are confirming the suspicion, that series resistance losses are not mainly driven by the bulk resistivity, but by injection dependent effects.

As the difference of lumped R_s losses within the considered FZ and Cz bulk material becomes prominent at high L_p , R_s losses at the mpp as a function of nominal bulk resistivity at a fixed $L_p = 1000 \mu\text{m}$ are analyzed in Fig. 7.9. Indicated by the black dotted line, for comparison, an analytical expression for dark series resistance losses from Cox and Strack [194] is shown, reflecting a linear behavior of R_s dependent on the nominal bulk resistivity ρ_0 (apparent exponential behavior due to logarithmic x-scale). The numerical simulation of R_s for FZ bulk material in Fig. 7.9 (red, line) shows for $\rho_0 < 4 \Omega\text{cm}$ the same linear behavior, as does the analytical expression. For $4 \Omega\text{cm} < \rho_0 < 15 \Omega\text{cm}$, R_s rises less than linear to a maximum of $R_s(15 \Omega\text{cm}) \approx 3.5 \Omega\text{cm}^2$, which is less than the half of $R_{s,\text{Cox\&Strack}}(15 \Omega\text{cm})$. This behavior is reflected in the FF losses in Fig. 7.9, with a minimum slightly shifted to smaller ρ_0 . Above $\rho_0 = 15 \Omega\text{cm}$, R_s decreases detrimentally; the FF shows the same increasing tendency (blue, line), but much smoother. Standard domains with higher nominal resistivities than $26 \Omega\text{cm}$, could not be calculated, as numerical solver problems were encountered. Calculations with Cz bulk material in Fig. 7.9 (red, dash) hold similar behavior: linearity until $\rho_0 \approx 7 \Omega\text{cm}$ according to the analytical equation, followed by a non-linear rise to a maximum of $R_s(\rho_0 = 15 \Omega\text{cm}) \approx 5.5 \Omega\text{cm}^2$. Thus,

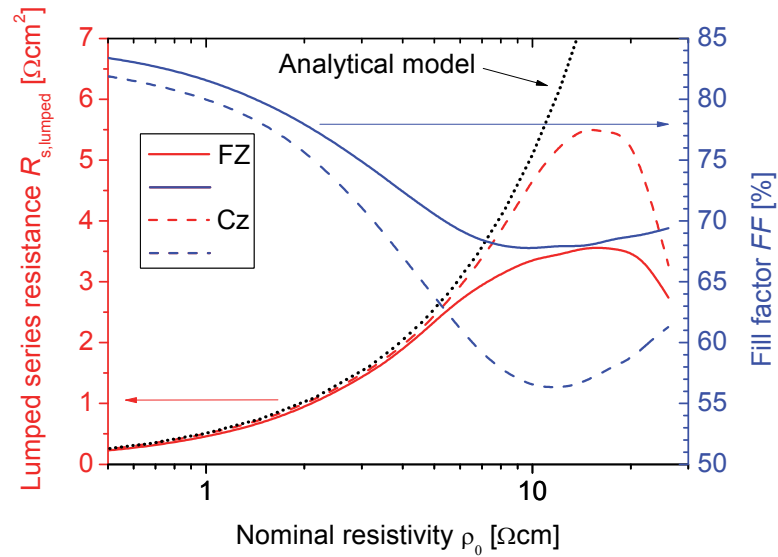


Fig. 7.9: Numerical simulations of the lumped series resistance R_s (red) and the fill factor FF (blue) for FZ (line) and Cz (dash) bulk material. For comparison, an analytical model from Cox and Strack [194] for the series resistance $R_{s,Cox\&Strack}$ is shown (black, dotted), which behaves linear in ρ_0 . The standard domain geometry holds $L_P = 1000 \mu\text{m}$ and $d = 170 \mu\text{m}$.

non-linearity starts at higher ρ_0 , compared to the simulations featuring FZ bulk material, but attaining the maximum at around the same ρ_0 , but with a much higher $R_{s,lumped}$ value according to the degraded lifetime of the Cz bulk material. Again, for $\rho_0 > 15 \Omega\text{cm}$, R_s decreases detrimentally, which does not reflect as much in the corresponding FF behavior (Fig. 7.9, blue, dash).

The observations done in Fig. 7.9 will be discussed and the occurring effects will be clarified in the following.

7.2.2 High level injection effects

The observed non-linear behavior in Fig. 7.9 for FZ ($\rho_0 > 4 \Omega\text{cm}$) and Cz ($\rho_0 > 7 \Omega\text{cm}$) bulk material is caused by injection dependent effects, as shown in Fig. 7.10. Here, the given carrier concentrations are bulk average values at one-sun illumination and under mpp operation conditions. The base doping concentration N_A scales linearly with the nominal bulk resistivity ρ_0 , independently of whether it is FZ or Cz bulk material.

As can be seen in Fig. 7.10 for FZ bulk material, with increasing ρ_0 , the minority carrier density Δn increases continuously, attaining higher values than the base doping concentration at a nominal resistivity of about $7 \Omega\text{cm}$, where the ratio $\Delta n/N_A = 1$. For $\rho_0 > 7 \Omega\text{cm}$, Δn is further increasing (but with decreasing slope) and converging at

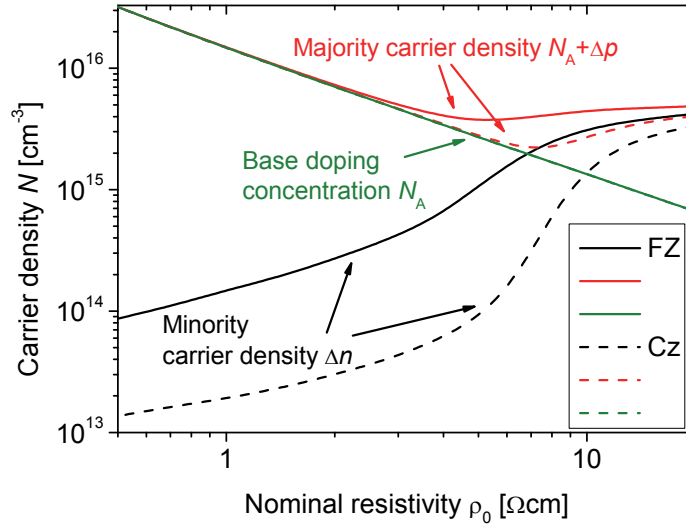


Fig. 7.10: Carrier densities for FZ and Cz bulk material ($[O_i] = 1 \times 10^{18} \text{ cm}^{-3}$). The given carrier concentrations are bulk average values at one-sun illumination and under mpp operation conditions. It illustrates that the observed non-linear behavior in Fig. 7.9 for FZ ($\rho_0 > 4 \text{ } \Omega\text{cm}$) and Cz ($\rho_0 > 7 \text{ } \Omega\text{cm}$) bulk material is caused by injection dependent effects.

high level injection (HLI) conditions ($\Delta n > 10 \cdot N_A$) towards a certain carrier density. Thus, the majority carrier densities $p = N_A + \Delta p$ for $\rho_0 < 4 \text{ } \Omega\text{cm}$ is dominated by N_A , as the material is in low level injection (LLI) conditions. For $\rho_0 > 4 \text{ } \Omega\text{cm}$ it holds $p > N_A$ as consequence of the significant Δn increase. Here, the transition from LLI conditions to HLI starts, which is reflected as well in the starting non-linear R_s behavior in Fig. 7.9 around $4 \text{ } \Omega\text{cm}$. As a result of conductivity modulation [170], the effective resistivity is not defined solely by N_A anymore and the effective series resistance decreases. Interestingly, the majority carrier density p features a minimum at $\rho_0 \approx 5 \text{ } \Omega\text{cm}$ and, further, increases similarly to Δn , due to $\Delta n = \Delta p$. The high $\Delta n/N_A$ ratios of the transition and HLI regime result in reduced series resistances, in comparison to the nominal resistances taking only N_A into account.

For Cz bulk material, the same behavior as for FZ material can be observed in Fig. 7.10. Due to the significantly lower lifetimes in comparison to FZ bulk material, Δn is constantly lower, not attaining higher values than the base doping concentration until a nominal resistivity of about $10 \text{ } \Omega\text{cm}$. Thus, $p > N_A$ holds for $\rho_0 > 7 \text{ } \Omega\text{cm}$, again explaining the starting R_s non-linearity obtained in Fig. 7.9 around $7 \text{ } \Omega\text{cm}$. With further increasing ρ_0 , Δn_{FZ} and Δn_{Cz} are approaching each other, as the SRH lifetime of Cz bulk material in HLI holds $\tau_{\text{SRH,HLI}} = \tau_{\text{n0}} + \tau_{\text{p0}}$ and, thus, is significantly increased in comparison to LLI conditions with $\tau_{\text{SRH,LLI}} = \tau_{\text{n0}}$.

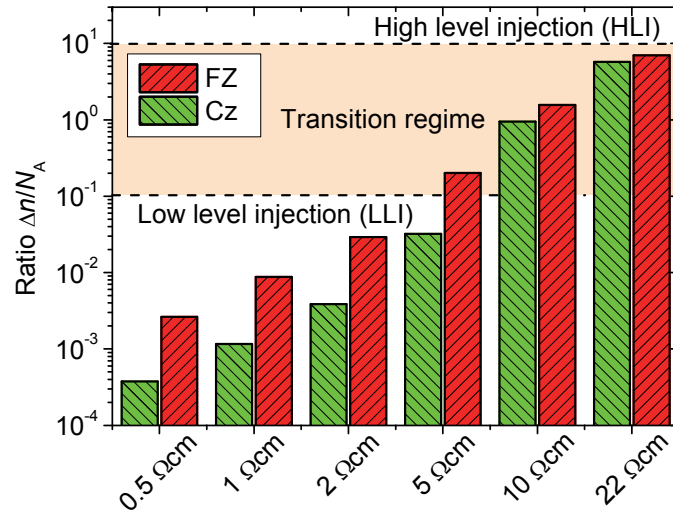


Fig. 7.11: Ratio of the average excess minority carrier density Δn in the bulk material at the maximum power point and doping concentration N_A for FZ and Cz material with $[O_i] = 1 \times 10^{18} \text{ cm}^{-3}$. The different material properties influence the transition to HLI and, thus, the series resistances in the bulk.

In Fig. 7.11 the transition from LLI to HLI conditions is illustrated according to the ratio of minority carrier density and base doping concentration $\Delta n/N_A$. Thereby, HLI is defined as mentioned before and LLI is defined as $\Delta n < 0.1 \cdot N_A$. Due to the significantly higher lifetimes in FZ compared to Cz material, Δn and, thus, $\Delta n/N_A$ is higher for all considered resistivities, leaving LLI at about $\rho_0 = 3 - 4 \Omega\text{cm}$. In contrast, LLI in Cz material is left at higher resistivities above $\rho_0 = 6 - 8 \Omega\text{cm}$, dependent on $[O_i]$. Please note that the ratios indicated in Fig. 7.11 will slightly move towards lower values, if a non-ideal front surface passivation is assumed.

Therefore, the starting non-linear behavior of the lumped R_s around $\rho_0 = 4 - 10 \Omega\text{cm}$ shown in Fig. 7.9 can be explained by injection dependent effects. But for $\rho_0 > 20 \Omega\text{cm}$ in Fig. 7.9, the strong R_s decrease, which does not fully coincide with the corresponding FF losses, could not be clarified with the considered global bulk effects. Also, the behavior of the IV curves for high ρ_0 , shown in Fig. 7.5 remains still unclear. Thus, it is appropriate to investigate local bulk effects occurring within the 3D standard domain, which is done in Chap. 7.3.

7.3 Consideration of local bulk effects

The majority carrier density distributions $p = N_A + \Delta p$ of the calculated FZ p -Si 3D standard domain with $L_p = 1000 \mu\text{m}$ are shown in Fig. 7.12 for $\rho_0 = 1, 10$ and $22 \Omega\text{cm}$. Thereby, the rear side contact is located below on the right hand side. The density distributions are shown for two fixed voltages at $V_1 = 500 \text{ mV}$ (left) and $V_2 = 650 \text{ mV}$

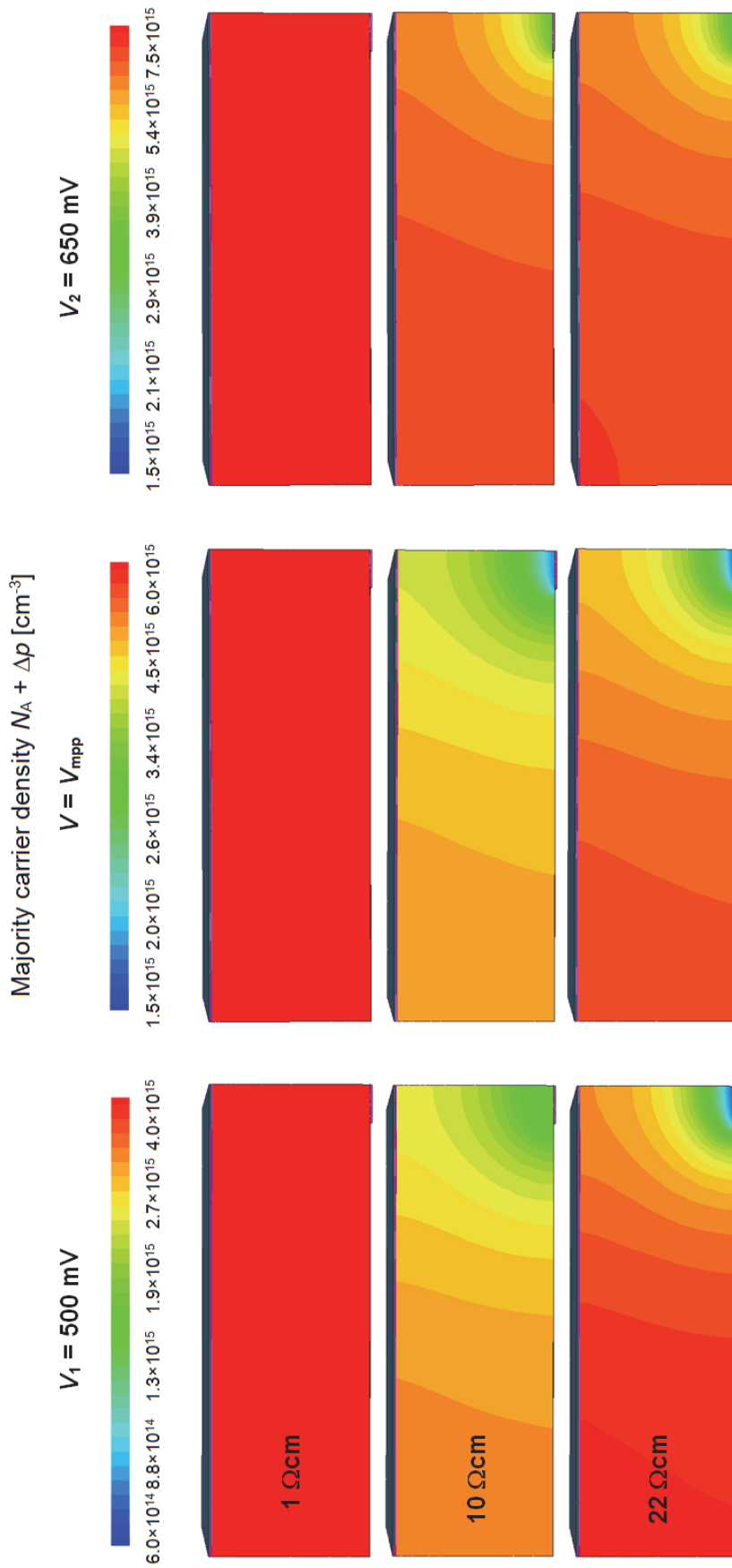


Fig. 7.12: Majority carrier density distribution of the 3D standard domain at $V_1 = 500 \text{ mV}$ (left), $V = V_{mpp}$ (middle), and $V_2 = 650 \text{ mV}$ (right) for the nominal bulk resistivities 1, 10 and $22 \Omega\text{cm}$ FZ bulk material. It holds $V_1 < V_{mpp} < V_2$. For lower voltages, the majority carrier density decreases significantly for high ρ_0 near the rear contact. Please note the different color scales. The shown 3D standard domains feature local rear contacts (see Fig. 7.1).

(right). Furthermore, the majority carrier density p is shown for $V = V_{\text{mpp}}$ (middle), while it holds $V_1 < V_{\text{mpp}} < V_2$, as shown in Fig. 7.5. Please note the different color scales.

For $1 \Omega\text{cm}$ bulk material, the majority carrier density is distributed homogeneously, driven by the bulk doping concentration of $\rho_0 = 1.5 \times 10^{16} \text{ cm}^{-3}$, as the calculated solar cell is operating under LLI conditions (see Fig. 7.11). For $\rho_0 > 1 \Omega\text{cm}$, the majority carrier distribution becomes inhomogeneous, according to the transition to HLI conditions (see Fig. 7.11). Due to the diode characteristics, $p \sim \exp(qV/k_B T)$ increases exponentially with V .

In Fig. 7.12 at $\rho_0 = 22 \Omega\text{cm}$ ($V = V_1$), an increased majority carrier density in the volume in comparison to $10 \Omega\text{cm}$ bulk material can be observed. At the same time the majority carrier density right above the rear contacts is significantly lower, holding values close to the corresponding N_A . Whereas in $10 \Omega\text{cm}$ bulk material a factor of about two appears within the local p close to the rear contact and far away from it, in $22 \Omega\text{cm}$ bulk material the factor rises to about seven. Towards $V = V_2$ the difference of the local p decreases/remains at a factor of two for both bulk resistivities, but with overall increasing carrier density.

Under mpp conditions, the local majority carrier density right above the rear contact is in the order of magnitude of the base doping concentration, due to the high recombination at the rear contact. Therefore, with decreasing base doping concentration, the effective series resistance increases close to the rear contact. The majority carrier density in the rest of the bulk overall is increased. The higher p in the bulk material, the higher is the recombination rate in this area. This effect of enhanced recombination can be seen in the IV curves in Fig. 7.5 and will be further discussed in Chap. 7.4. With increasing ρ_0 a current density drop occurs at decreasing voltages. Interestingly, a shunted area would cause the same IV characteristics, as this would mean as well increasing recombination losses with increasing voltage.

In Fig. 7.13 (above) the local bulk minority (left) and majority carrier densities (right) under mpp conditions are shown for FZ material as a function of the nominal bulk resistivity ρ_0 for $L_p = 1000 \mu\text{m}$. The local positions in the opposite corners of the symmetry element are shown, as well as the densities in the center of the standard domain and the average values of the whole bulk, as can be seen in the inset (below). Far from the rear contact (at the center and the opposite corners of the rear contact of the standard domain regarding L_p), Δn increases significantly with increasing ρ_0 reflecting the bulk average (line), which is already shown in Fig. 7.10. Above the rear

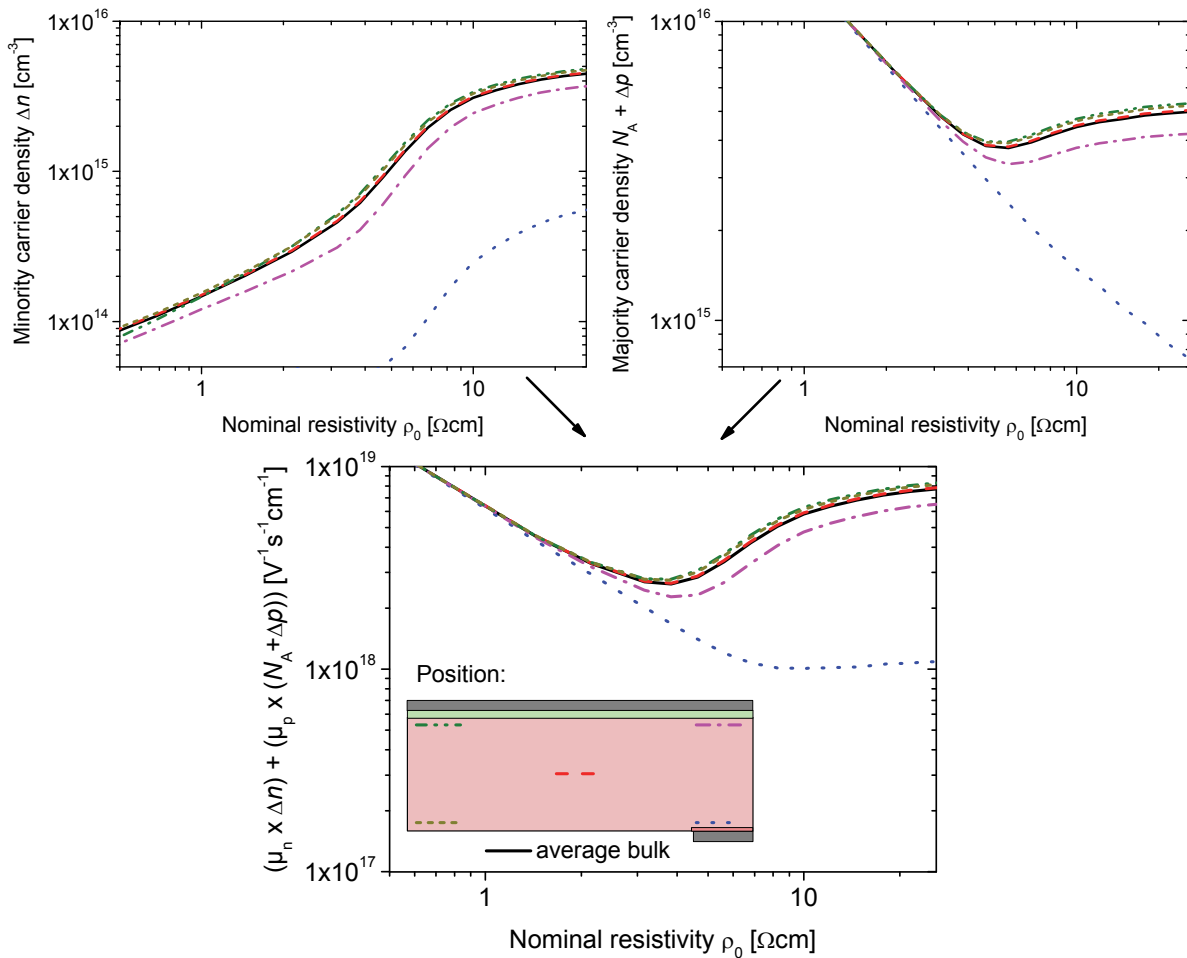


Fig. 7.13: Above: minority and majority carrier densities Δn and p , respectively, at different local positions in the calculated standard domain (below, inset) of FZ p-Si with $L_P = 1000 \mu\text{m}$. Below: sum of Δn and p , weighted by the carrier mobilities μ_n and μ_p of electrons and holes, respectively, which is proportional to the local conductivity. The behavior directly above the rear contact (dotted) limits the solar cell characteristics and equals qualitatively the FF behavior in Fig. 7.9.

contact close to the front emitter (dash dotted), Δn is already reduced for all ρ_0 by roughly 20%. Close to the rear contact (dotted), Δn is significantly reduced by one order of magnitude in comparison to the average density in the bulk. The bulk average of p decreases until $\rho_0 \approx 5 \Omega\text{cm}$, forming a minimum and increasing for higher ρ_0 according to the increasing Δp , as already observed in Fig. 7.10. Far from the rear contact, p behaves like the bulk average showing slightly increased values (for $\rho_0 > 3 \Omega\text{cm}$), in agreement to the Δn behavior. Above the rear contact close to the front emitter a reduction of p for $\rho_0 > 3 \Omega\text{cm}$ in comparison to the bulk average can be observed as well, but still showing the same qualitative behavior. In contrast, close to the rear contact, p decreases continuously reflecting the decrease of N_A (see Fig. 7.10).

The sum of Δn and p is given in Fig. 7.13 (below), weighted by the carrier mobilities μ_n and μ_p of electrons and holes, respectively, which have been determined by the

numerical simulations. As $\mu_{n/p}(N)$ does not change as much as the carrier concentrations, the sum is dominated by the behavior of Δn and p . As this weighted sum is proportional to the analytical expression for the conductivity, the tendencies can be interpreted as local conductivities in the bulk material. For all considered positions except right above the rear contact, the qualitative behavior is equal to the characteristics of the majority carrier density, featuring a local minimum in the range of $\rho_0 = 4$ to $6 \Omega\text{cm}$. This is consistent to the observations done in Fig. 7.10, but does not comply very well with the local extrema of the FF or R_s behavior, respectively, shown in Fig. 7.9 (please note that the figures feature the same x-scale for better comparison).

As a consequence of the increasing Δn and decreasing p directly above the rear contact (Fig. 7.13, above), the weighted sum of both densities (Fig. 7.13, below) decreases continuously until $\rho_0 \approx 10 \Omega\text{cm}$, and increases slightly with further increasing ρ_0 . Due to current crowding at the local contact, the local carrier density is very relevant. This local conductance behavior limits the series resistance of the solar cell and limits the FF , which shows the same characteristics for the entire considered range of ρ_0 .

If the region above the rear contact would be locally doped with a constant doping concentration, the series resistance losses should be reduced significantly. In Fig. 7.14 a region of $(50 \times 50 \times 50) \mu\text{m}^3$ close to the rear contact has been doped in the simulation with $N_A = 10^{16} \text{cm}^{-3}$, whereas ρ_0 in the bulk material has been varied. In comparison to the R_s , also shown in Fig. 7.9, the lumped series resistance reduces significantly,

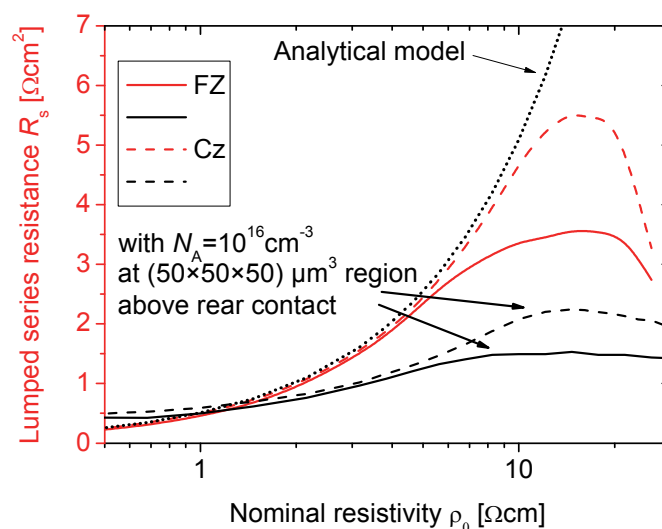


Fig. 7.14: Numerical simulations of the lumped series resistance R_s for FZ (line) and Cz (dash) bulk material, including the analytical model, shown in Fig. 7.9. Introducing a doped region of $(50 \times 50 \times 50) \mu\text{m}^3$ with $N_A = 10^{16} \text{cm}^{-3}$ close to the rear contact reduces significantly the lumped series resistance, confirming the local influence of the rear area above the contact.

confirming the local influence of the rear area above the contact. For $\rho_0 \leq 1 \Omega\text{cm}$ in Fig. 7.14, R_s is slightly increased, as the doping concentration in the mentioned $(50 \times 50 \times 50) \mu\text{m}^3$ region is here below the N_A in the rest of the bulk material.

In contrast to this theoretical assumption of a constantly doped $(50 \times 50 \times 50) \mu\text{m}^3$ region, a deeper diffused local BSF, which could be realized experimentally, would have a positive effect on the local series resistance losses as well. Up to now a Gaussian BSF profile with a peak concentration $N_{\text{peak}} = 1 \times 10^{20} \text{cm}^{-3}$ and a depth $d_{\text{BSF}}(N_A = 10^{16} \text{cm}^{-3}) = 0.1 \mu\text{m}$, introduced in Chap. 7.1.3, has been used in the simulations. In Fig. 7.15, d_{BSF} is varied by maintaining N_{peak} , for the same nominal bulk resistivities as in Fig. 7.12. The results for the FF (left) and V_{oc} (right) are displayed, relative to the results with $d_{\text{BSF}} = 0.1 \mu\text{m}$. For $1 \Omega\text{cm}$ bulk material a constant benefit in V_{oc} of $\sim 1\%$ due to a decreased recombination of minority carriers at the rear contact can be observed, whereas no significant ΔFF is achieved. For $10 \Omega\text{cm}$ bulk material, ΔV_{oc} is also constant, as the diffusion barrier for $d_{\text{BSF}} \geq 2 \mu\text{m}$ shields nearly all minority carriers from recombining at the highly recombination active rear contact. But in contrast to the $1 \Omega\text{cm}$ material, ΔFF increases proportionally to d_{BSF} , up to $\Delta FF = 5\%$ for $d_{\text{BSF}} = 10 \mu\text{m}$. Thus, the shape of the BSF has not only an influence on V_{oc} , but also influences significantly the FF losses for high resistive solar cells featuring local rear contacts. For $22 \Omega\text{cm}$ bulk material, ΔFF is even slightly higher, but shows the same linear tendency as for $10 \Omega\text{cm}$ bulk material. Here, the benefit in V_{oc} is reduced, as $V_{\text{oc}}(d_{\text{BSF}} = 0.1 \mu\text{m}) = 714 \text{mV}$ is already at a very high level.

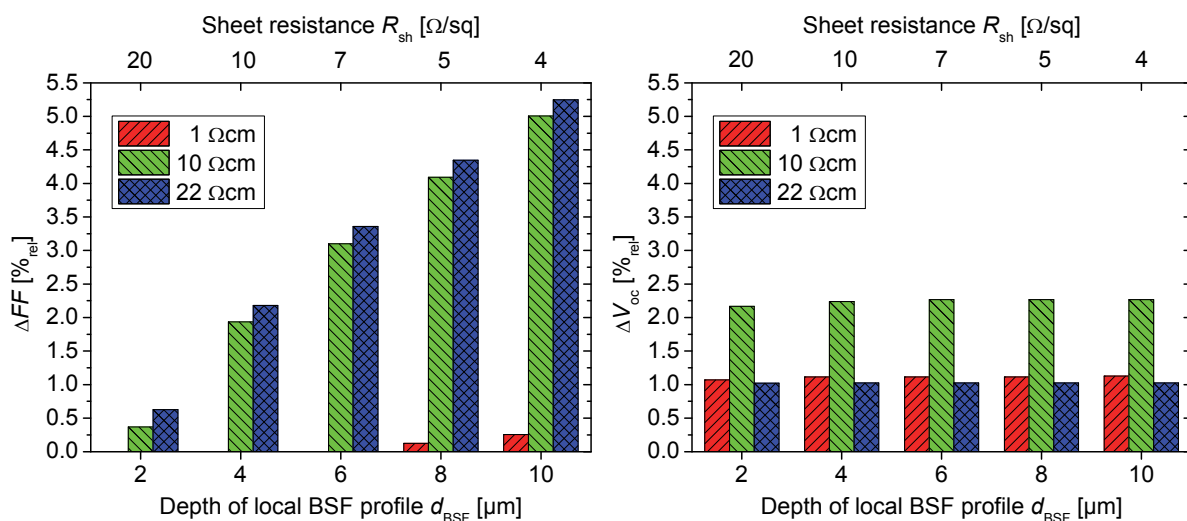


Fig. 7.15: Relative change of FF and V_{oc} by varying the depth d_{BSF} of the Gaussian local BSF profile ($N_{\text{peak}} = 10^{20} \text{cm}^{-3}$). Values are displayed relative to the results with $d_{\text{BSF}} = 0.1 \mu\text{m}$. Whereas for $1 \Omega\text{cm}$ bulk material ΔV_{oc} is dominant, for $\rho_0 \geq 10 \Omega\text{cm}$ a significant linear increase of FF with increasing d_{BSF} is observed.

It has been shown that with decreasing base doping concentration, the minority carrier density increases, leading to a conductivity modulation for $\rho_0 > 5$ to $8 \text{ } \Omega\text{cm}$ (dependent on whether FZ or Cz bulk material is considered) in large parts of the bulk material. Locally, in the bulk area close to the rear contact, the R_s is dominated by N_A , which leads to increasing R_s with increasing ρ_0 . Driven by this local effect, Δn increases in the bulk region with increasing ρ_0 . As a consequence, more recombination activity occurs in the bulk material, which is quantified in the following chapter.

7.4 Recombination losses in the bulk material

It could be observed in the previous chapter that the absolute carrier concentration increases with increasing ρ_0 , while the local conductivity close to the rear contact is significantly reduced. As a consequence of increased carrier density in the bulk material, the recombination rate is increased. The limiting bulk recombination mechanisms are given in Fig. 7.16. FZ bulk material is Auger limited and, thus, does not feature any SRH recombination losses. For FZ $1 \text{ } \Omega\text{cm}$ bulk material (Fig. 7.16, left) the Auger recombination rate R_{Auger} is relatively high at low voltages and remains constant until $\sim 450 \text{ mV}$. Due to the decreasing current at high voltages and, thus, an increase of the carrier densities, R_{Auger} increases continuously. With increasing ρ_0 , R_{Auger} decreases for low voltages, as a result of the lowered doping concentration. At the same time the incipient rise of R_{Auger} with increasing V shifts towards lower voltages. Here, the effect of a lower conductance near the rear contact occurs, favoring an accumulation of charge carriers in the bulk material. For $22 \text{ } \Omega\text{cm}$ bulk material, R_{Auger} initiates below $10^{13} \text{ cm}^{-3}\text{s}^{-1}$, but rises exponentially by orders of magnitude to a value above $3 \times 10^{18} \text{ cm}^{-3}$. The lower ρ_0 , the lower is the local conductance near the rear contact, and the sooner majority carriers accumulate in the bulk material, which leads to increased recombination. The increased recombination influences the voltage dependent current density and becomes visible with increasing ρ_0 at decreasing voltages. This can be directly seen in the IV curve simulations in Fig. 7.5, which correspond to the recombination rates shown in Fig. 7.16.

For low quality Cz bulk material (Fig. 7.16, right) with $[\text{O}_i] = 1 \times 10^{18} \text{ cm}^{-3}$, the Auger recombination characteristic shows nearly the same behavior as in FZ bulk material, but is slightly lower due to overall lower carrier densities. However, the limiting recombination rate for this high $[\text{O}_i]$ is clearly SRH recombination according to Eq. (2.38). The SRH recombination rate R_{SRH} is for all considered ρ_0 and V higher than R_{Auger} . For voltages below $\sim 430 \text{ mV}$ the qualitative behavior of R_{SRH} of different ρ_0 to each other is similar to the behavior of R_{Auger} , related to the injection level, but at an

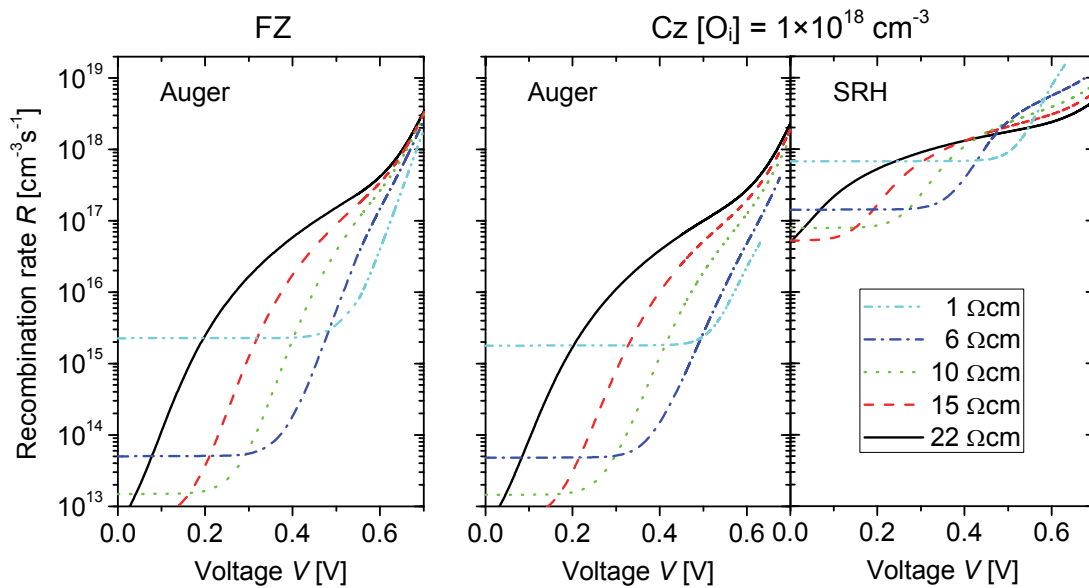


Fig. 7.16: Limiting bulk recombination mechanisms for FZ (left) and Cz (right) bulk material dependent on the applied voltage V for different nominal base resistivities ρ_0 .

orders of magnitude higher recombination level. In contrast to the R_{Auger} behavior, R_{SRH} shows a cross-over point at about 430 mV for $\rho_0 > 1 \Omega\text{cm}$, where R_{SRH} becomes lower for higher ohmic material towards higher voltages. This is due to the injection dependent behavior of the SRH lifetimes. As τ_{Auger} features a monotonous decrease with increasing Δn , τ_{SRH} increases from LLI to HLI conditions, as mentioned in Chap. 7.2.2. This R_{SRH} characteristic is directly correlated to the cross-over behavior observed in Fig. 7.5. Schmidt *et al.* [200] reported as well FF losses due to injection dependent recombination, but the observed results show quantitative deviations to the here presented observations. This is because the calculations presented in [200] are based on 1D simulations, set up with the program PC1D [122]. Thus, they include injection dependent effects, but are not able to describe local 3D effects, as reported in this work.

It can be concluded that recombination losses are closely interacting with transport losses, which can only be investigated properly, by taking 3D effects into account.

7.5 Optimization of analytical modeling

Recently, a comprehensive analytical study [190] has been presented to estimate the optimum bulk resistivity and corresponding contact distances, as mentioned in Chap. 7.1. These analytical calculations were restricted to LLI conditions, which is not fulfilled for high resistivity material, as could be observed in Chap. 7.2 and 7.3 via numerical calculations. Under one sun illumination, significantly increased minority carrier densities occur at mpp or open-circuit conditions, leaving the LLI regime. In

this chapter, results of the analytical model will be compared to numerical calculations, based on the same set of physical models and input parameters, and its extent of validity will be figured out. In continuation, the analytical model will be extended in order to account for effects beyond LLI and, thus, enhance its accuracy in this regime.

The content of this chapter has been developed in close collaboration with the doctoral thesis of A. Kimmerle and parts of it have been published in [176].

7.5.1 Comparison of analytical and numerical modeling

To compare the classical analytical model, based on the work presented in Ref. [190] and the numerical results, based on the model presented in foregoing sub-chapters, the physical models used in the calculations have to be exactly the same. Therefore, identical models, as given in Tab. 3.2, have been used for comparison. The rear side of the numerically calculated device has been performed as given in Chap. 7.1.1, whereas for the analytical model an effective surface recombination velocity

$$S_{\text{eff}} = \frac{D_e}{h} \left(\frac{R_{S,\text{back}}}{\rho \cdot h} + \frac{D_e}{f \cdot h \cdot S_{\text{met}}} - 1 \right)^{-1} + \frac{S_{\text{pass}}}{1-f}, \quad (7.4)$$

given by Fischer [197] has been used. More details of the series resistance contribution of $R_{S,\text{back}}$ of the base and rear side can be found in [190]. With the bulk diffusion length L_{bulk} , calculated with Eq. 3.5, the effective diffusion length holds

$$L_{\text{eff}} = L_{\text{bulk}} \frac{1 + \frac{S_{\text{eff}} \cdot L_{\text{bulk}}}{D_e} \cdot \tanh(h / L_{\text{bulk}})}{\frac{S_{\text{eff}} \cdot L_{\text{bulk}}}{D_e} + \tanh(h / L_{\text{bulk}})}. \quad (7.5)$$

The shallowly doped front emitter has been modeled analytically according to [126] to a very low dark saturation current density of $j_{0e} = 3 \text{ fA/cm}^2$, which has been used in the analytical calculations. The generation profile of the numerical simulation is reproduced for the analytical calculations with very good agreement to a parameterization given in [190].

In Fig. 7.17 results can be seen for rear contact distance variations. The classical non-injection dependent analytical model (dash) is compared to the numerical simulations (line) for different nominal base resistivities. The short-circuit current density is very well reproduced for $\rho_0 < 10 \text{ } \Omega\text{cm}$ in the analytical calculations, not exceeding a difference of $\Delta j_{\text{sc}} > 0.1 \text{ mA/cm}^2$ over the whole considered range. For $10 \text{ } \Omega\text{cm}$ base material and $L_p < 400 \text{ } \mu\text{m}$ the difference yields 0.2 mA/cm^2 , which is still below 0.5%.

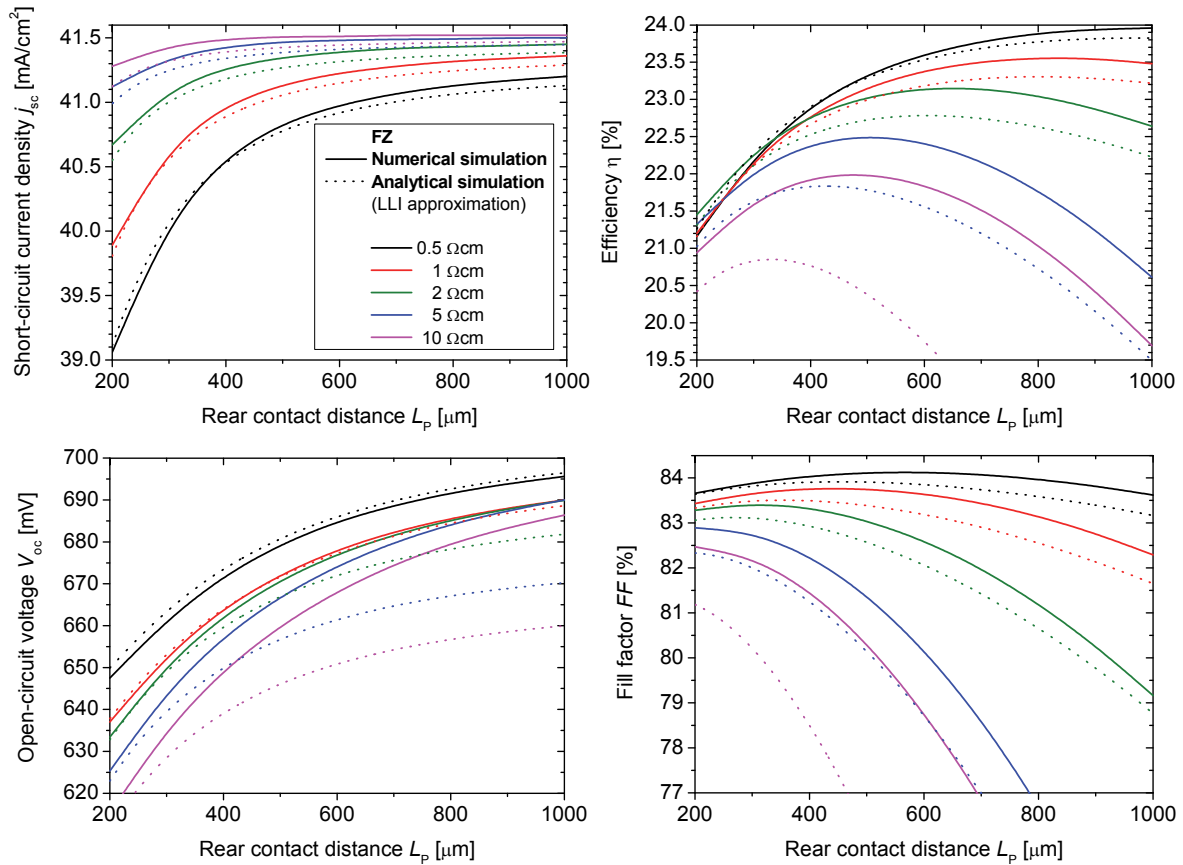


Fig. 7.17: Numerically (line) and analytically (dot) calculated solar cell parameters for a FZ p -type Si device in LLI approximation [190]. The nominal bulk resistivity ρ_0 and the rear contact distance L_p have been varied.

For $\rho_0 = 0.5 - 1 \Omega\text{cm}$ the V_{oc} shows very good agreement, whereas the FF is slightly underestimated in the analytical calculations, leading as well to a slightly underestimated η of up to 0.3% absolute. However, the optimum rear contact distance $L_{p,opt}$ is predicted very well by the analytical calculations. At $\rho_0 = 2 \Omega\text{cm}$ the prediction of $L_{p,opt}$ is still good with a deviation of $\sim 50 \mu\text{m}$, although a significantly increased deviation of V_{oc} with increasing L_p can be observed. For $\rho_0 > 2 \Omega\text{cm}$, V_{oc} is very well predicted for the smallest considered $L_p = 200 \mu\text{m}$, where nearly no lateral currents occur. With increasing L_p , V_{oc} becomes increasingly underestimated up to a deviation of 4% for 10 Ωcm base material and $L_p = 1000 \mu\text{m}$. This is mainly caused by neglecting Δp in the dark saturation current density of the bulk:

$$j_{ob} = \frac{q \cdot D_p \cdot n_1^2}{N_A \cdot L_{eff}} \quad (7.6)$$

Nevertheless, the main deviation for high resistive material consists of the detrimentally underestimated FF . The relative maximum deviation for 5 Ωcm material does not exceed 4%, but yields up to 23% for 10 Ωcm bulk material, resulting in

different $L_{P,opt}$ for the numerical and analytical predictions of a factor of 1.5. Thus, injection dependent effects need to be considered in analytical calculations for highly predictive modeling. A first approach will be discussed in Chap. 7.5.2.

7.5.2 High level injection effects in analytical modeling

Especially at high rear contact distances in low resistive base material could be observed a strong deviation in comparison to numerical results in Chap. 7.5.1, mainly due to the negligence of injection dependent effects in the analytical equations used in [190]. Therefore, the analytical equations are modified and extended in a first attempt in order to improve the prediction capabilities of analytical modeling.

The model presented in Ref. [190] is based on the two-diode equation, introduced in Eq. (3.7) in Chap. 3.2. As $j_{02} \equiv 0$ in this approach, the equation reduces to the one-diode model, shown in Eq. (3.3). The external applied voltage V minus the product of series resistance R_s and current density j denotes the voltage at the junction $V_{\text{junction}} = V - R_s \cdot j(V)$, which is used in the following. The global parallel resistance R_p is set to $1 \text{ M}\Omega\text{cm}^2$, not impacting the calculations at all.

To account for injection dependent effects in the determination of j_{mpp} , V_{mpp} and V_{oc} , the minority carrier density $\Delta n_{\text{junction}}$ at the junction is related to the voltage drop

$$V_{\text{junction}} = \frac{k_B T}{q} \cdot \ln \left(\frac{\Delta n_{\text{junction}} (\Delta n_{\text{junction}} + N_A)}{n_i^2} \right) . \quad (7.7)$$

Therefore, the injection dependence at the rear side has been accounted for by a self-consistent iterative process, using Eqs. (7.4) and (7.5):

$$\Delta n_{\text{rear}} = \Delta n_{\text{junction}} \cdot \exp \left(- \frac{d}{L_{\text{eff}}(\Delta n_{\text{bulk}}, \Delta n_{\text{rear}})} \right) . \quad (7.8)$$

Δn_{rear} is the minority carrier density at the rear side of the solar cell. To consider diffusion interactions of the electric fields of the positive and negative particles, D_e is replaced by the ambipolar diffusion constant $D_{\text{amb}}(\Delta n_{\text{bulk}})$. More details on D_{amb} can be found in Ref. [43]. It is important to mention, that Eq. (7.8) holds only at open-circuit conditions and, thus, can be seen as a first approximation. In analogy to Eq. (7.8), a mean minority carrier density in the bulk,

$$\Delta n_{\text{bulk}} = \frac{L_{\text{eff}}}{d} (\Delta n_{\text{junction}} - \Delta n_{\text{rear}}) , \quad (7.9)$$

is defined for the determination of τ_{bulk} in the Cz material, as the iteration process also includes the SRH equations (Eq. (2.41)), the injection-dependent surface recombination velocities $S_{\text{pass}}(\Delta n_{\text{rear}})$ and $S_{\text{met}}(\Delta n_{\text{rear}})$ and the bulk diffusion length according to Eq. (3.5). The iteration yields to an effective base dark saturation current density

$$j_{0b,\text{eff}} = \frac{q \cdot D_{\text{amb}}(\Delta n_{\text{bulk}}) \cdot n_i^2}{(N_A + \Delta n_{\text{junction}}) \cdot L_{\text{eff}}(\Delta n_{\text{bulk}}, \Delta n_{\text{rear}})}, \quad (7.10)$$

which is used in the one-diode equation (see Eq. (3.3)) as $j_{01} = j_{0e} + j_{0b,\text{eff}}$.

The series resistance $R_s = R_{s,\text{base,light}}$ includes spreading resistance losses [194-199], due to the point contacts at the rear side. The contribution of the front side is zero, consistent to the numerical setup. $R_{s,\text{base,light}}$ depends on the carrier concentration and mobility, leading to an effectively reduced resistivity, as observed in Chap. 7.2. Therefore, in first approximation an injection dependent effective illuminated resistivity ρ_{light} is used, taking into account the hole density, neglecting the conductivity due to injected electrons. The resistance per contact is scaled with the factor

$$\frac{\rho_{\text{light}}}{\rho_{\text{dark}}} = \frac{(q \cdot \mu_p \cdot (N_A + \Delta n))^{-1}}{(q \cdot \mu_p \cdot N_A)^{-1}}, \quad (7.11)$$

with the injection dependent mobility μ_p . ρ_{dark} denotes the resistivity without including Δn .

In Fig. 7.18 the IV curves are shown for FZ base material for the nominal bulk resistivities $\rho = 1, 2, 5$ and $10 \Omega\text{cm}$. For $1 \Omega\text{cm}$ base material, the LLI approximation (denoted as “LLI”) coincides very well with the numerical simulations, leading to a difference in FF of $\leq 1\%$ compared to the numerical simulations. For higher ohmic material the IV curves deviate increasingly in the range around the mpp and the V_{oc} becomes underestimated; as already observed in Fig. 7.17. By assuming an increased j_{0b} , which provides a realistic V_{oc} (denoted in Fig. 7.18 as “LLI (with V_{oc} from HLI)”, the overall voltage of the entire IV curve is shifted towards higher values, but the shape of the numerical simulation cannot be reproduced. An injection dependent correction (denoted as “HLI”), based on the previously introduced modifications, leads to an improved accordance around mpp conditions, but overestimates notably V_{oc} towards increasing bulk resistivities, indicating further high level injection effects.

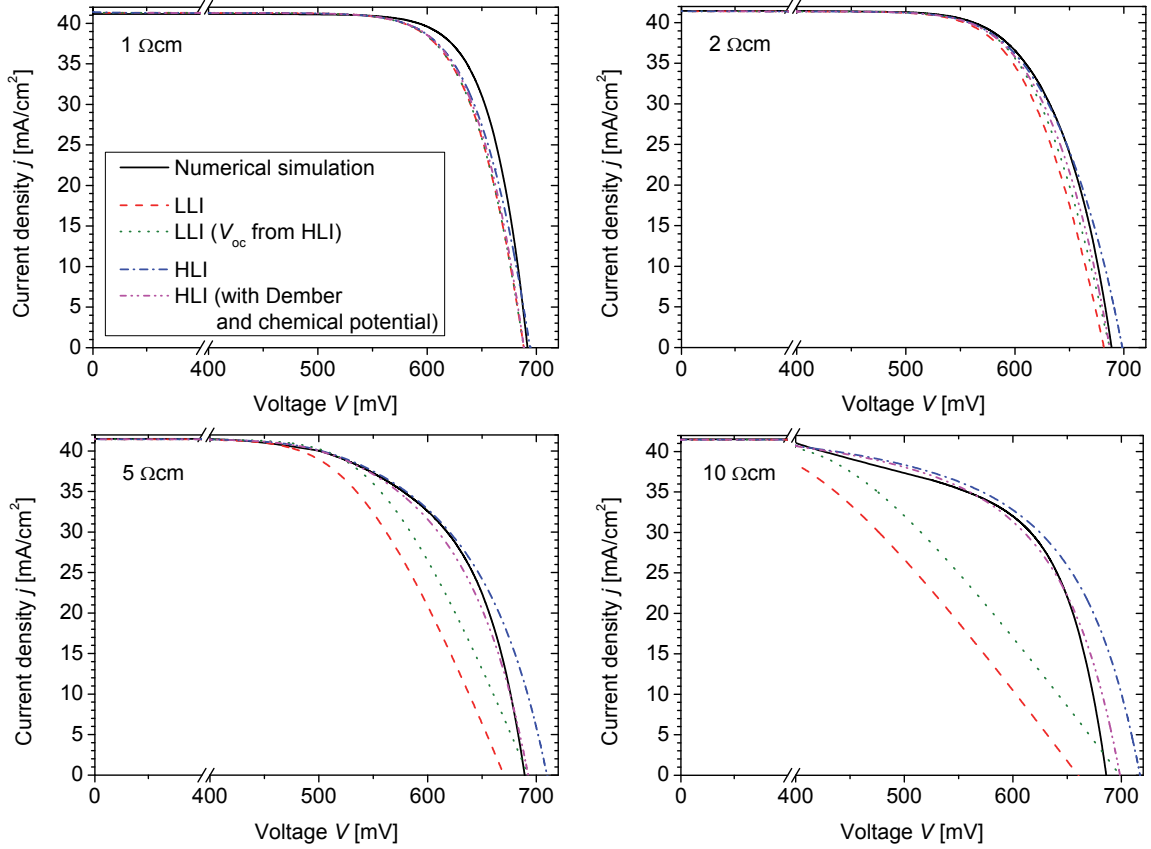


Fig. 7.18: Analytically calculated IV curves for FZ p-Si solar cells featuring nominal resistivities from 1 to 10 Ωcm . Shown are results for the LLI approximation (dash) and for LLI with an decreased j_{ob} , which provides the same V_{oc} (dot). Furthermore, calculations are shown for the HLI approximation presented in this chapter, without (dash dot) and with (dash dot dot) accounting for the corrections caused by the difference in the chemical potential at the metal contact and the junction and the Dember effect. The numerical results are shown for comparison (line).

Thus, due to the different concentrations of majority carriers at the metal surface and at the junction, the difference in the chemical potential (see Chap. 2.2) is accounted for according to

$$\Delta V_X = \frac{k_B T}{q} \cdot \ln \left(\frac{\Delta n_{\text{junction}} + N_A}{\Delta n_{\text{contact}} + N_A} \right) . \quad (7.12)$$

Furthermore, to account for the different diffusion velocities of electrons and holes, relevant in inhomogeneously distributed carrier density distributions, the Dember voltage ΔV_{Dember} is introduced:

$$\Delta V_{\text{Dember}} = \frac{\mu_n - \mu_p}{\mu_n + \mu_p} \cdot \frac{k_B T}{q} \cdot \ln \left(\frac{\Delta n_{\text{contact}} \cdot (\mu_n + \mu_p) + \mu_p N_A}{\Delta n_{\text{junction}} \cdot (\mu_n + \mu_p) + \mu_p N_A} \right) . \quad (7.13)$$

Details may be found in [43]. As a first approach, the injection density at the rear contact is approximated by

$$\Delta n_{\text{contact}} = \Delta n_{\text{junction}} \cdot \exp\left(-\frac{d}{L_{\text{eff}}(S_{\text{eff}} = S_{\text{met}})}\right), \quad (7.14)$$

neglecting the fraction of the rear side featuring a passivated surface for the evaluation of L_{eff} , whereas Δn_{bulk} and Δn_{rear} have been accounted for according to the iteration process mentioned above.

By additionally accounting for these effects, which are in accordance with [197], the analytically calculated IV curve for bulk resistivities $\rho > 1 \text{ } \Omega\text{cm}$ leads to a significantly improved accordance to the numerically determined results, as shown in Fig. 7.18 (denoted as ‘‘HLI (with Dember and chemical potential)’’). A minor deviation appears around mpp conditions, most likely due to the simplistic estimation of $\Delta n_{\text{contact}}$ and due to the neglected electron conductivity.

7.5.3 Injection dependent analytical simulation results

In Fig. 7.19 the same variations for FZ bulk material are shown as in Fig. 7.17, but the analytical calculations are extended by the HLI corrections, as mentioned above. Thereby, the results for j_{sc} are nearly unchanged, fitting the numerical results very well. Whereas the analytically calculated efficiencies do not change very much for $\rho \leq 2 \text{ } \Omega\text{cm}$, a significant enhancement can be observed for $\rho > 2 \text{ } \Omega\text{cm}$ towards increasing rear contact distances, in comparison to Fig. 7.17 featuring calculations based on the LLI approximation. However, towards highly resistive materials, V_{oc} is increasingly overestimated, as the estimation of the Dember voltage is a challenging task. The injection density at the contact becomes increasingly overestimated with increasing bulk resistivities by the above mentioned approach, which serves as base for the calculation of the Dember effect. Thus, the Dember voltage is increasingly underestimated. As a consequence, the FF is increasingly underestimated as well, as this parameter is calculated from j_{sc} , η and V_{oc} in the analytical approach. Nevertheless, a significant enhancement of the prediction of the optimum rear contact distance $L_{\text{P,opt}}$ could be achieved, as can be seen in the optimum efficiencies in Fig. 7.19 (above, right). Here, the deviation of $L_{\text{P,opt}}$ from analytical and numerical calculations does not exceed a factor of 1.2 for $10 \text{ } \Omega\text{cm}$ bulk material.

FZ bulk material with its very high charge carrier lifetimes sets high demands on the analytical calculations. Therefore, the industrially more relevant case for Cz bulk

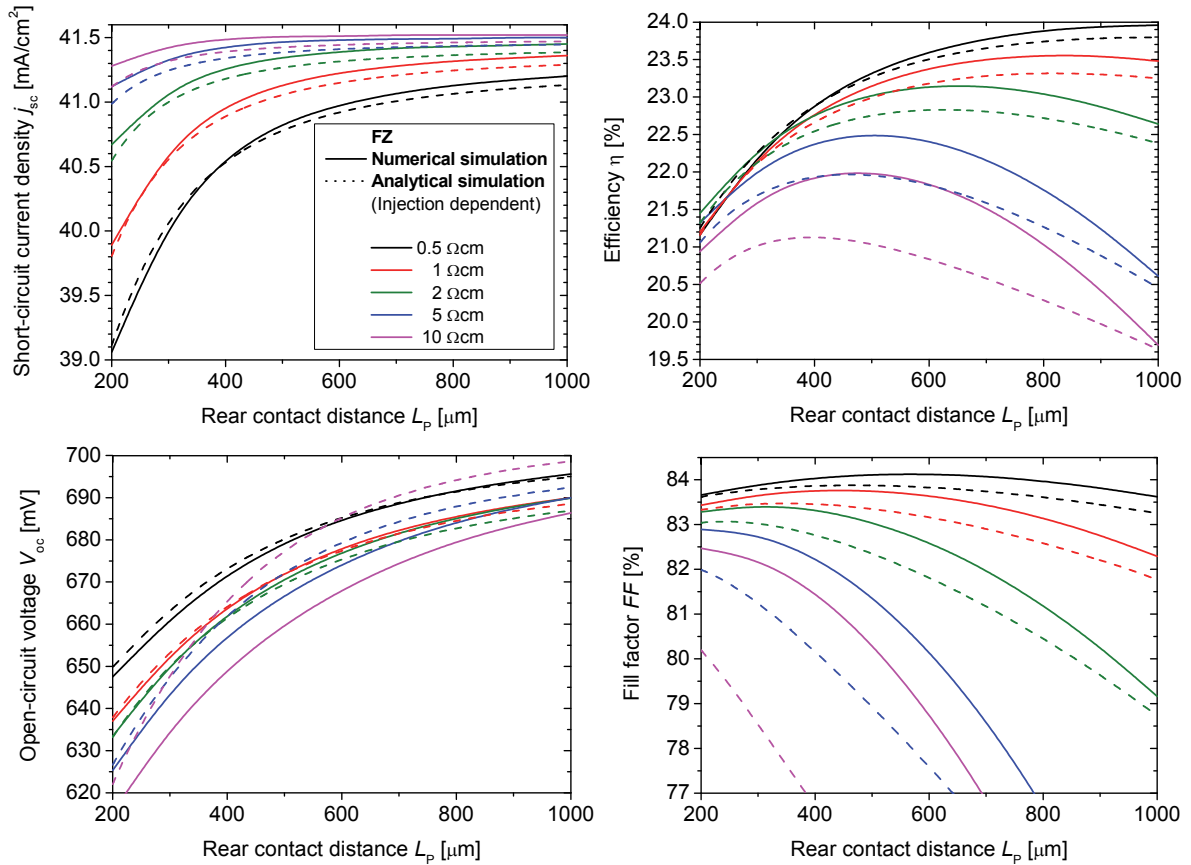


Fig. 7.19: Numerically (line) and analytically (dot) calculated solar cell parameters for a FZ p-type Si device, considering all HLI effects discussed in this chapter. The nominal bulk resistivity ρ_0 and the rear contact distance L_p have been varied.

material is investigated as well on base of the HLI corrections discussed above. An interstitial oxygen contamination of $[\text{O}_i] = 1 \times 10^{18} \text{ cm}^{-3}$ has been considered for the calculation of the degraded bulk lifetimes according to Eq. (7.1). Results are shown in Fig. 7.20. Due to the injection dependent bulk lifetime in Cz material, the analytical predictions improve strongly for high ohmic bulk materials. While the efficiencies in 10 Ωcm FZ bulk material deviate below 0.5% absolute, the deviation in the considered Cz bulk material reduces to below 0.3% absolute. The deviation of $L_{p,\text{opt}}$ does not exceed a factor of 1.1. Please note that for more realistic structures featuring non-idealized front sides, the deviations might be further decreased, since the parameters series resistance and the saturation current density of the solar cell are not fully determined by the bulk properties, leading finally to slightly lowered injection densities. However, injection dependence need to be considered in analytical calculations of solar cells with strongly injection dependent recombination as occurs e.g. in compensated material or highly resistive material featuring high bulk lifetimes as arising e.g. in n -type Si bulk material.

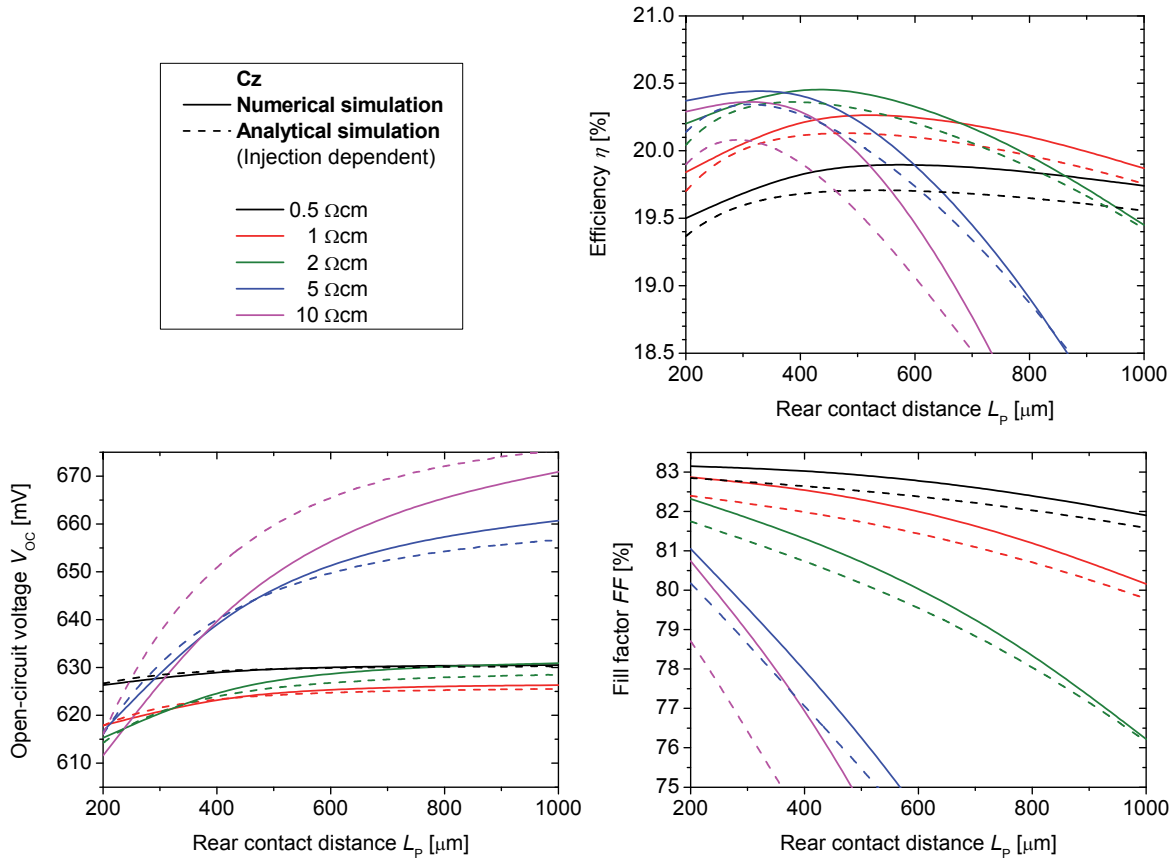


Fig. 7.20: Numerically (line) and analytically (dot) calculated solar cell parameters for a Cz *p*-type Si device, considering all HLI effects discussed in this chapter. An interstitial oxygen contamination of $[O_i] = 1 \times 10^{18} \text{ cm}^{-3}$ has been considered for the calculation of the degraded bulk lifetimes according to Eq. (7.1).

7.6 Conclusions

In this chapter, lateral conductance effects of locally contacted rear surface passivated *p*-Si solar cell concepts are investigated. The optimum rear contact distances L_P for different solar cell thicknesses and a broad range of nominal bulk resistivities ρ_0 are calculated. These variations are presented for (i) high-quality float-zone (FZ) and (ii & iii) Czochralski (Cz)-grown *p*-Si material with a very low ($[O_i] = 6 \times 10^{17} \text{ cm}^{-3}$) and a very high interstitial oxygen content of $[O_i] = 1 \times 10^{18} \text{ cm}^{-3}$ in the bulk material, which detrimentally influences the effective carrier lifetimes τ_{eff} . The results are published in [177].

A characteristic current density-voltage behavior for the considered FZ and Cz bulk materials for different base resistivities ρ_0 ($L_P = 1000 \text{ } \mu\text{m}$) could be observed via numerical 3D simulation, consistent to experimentally determined results [201]. For better understanding, the *FF* behavior is compared to numerically determined R_s losses under mpp conditions, occurring in the standard domain. It turned out that in high ohmic base material with high rear contact distances, high injection effects in

combination with local bulk transport effects need to be considered in order to understand the effects occurring in the bulk material.

Analytical modeling based on the comprehensive model presented in [190] shows good agreement with numerical modeling in LLI conditions. Towards HLI conditions, as arising e.g. in highly resistive bulk material with $\rho_0 > 2 \Omega\text{cm}$, results deviate significantly and injection dependent modeling is required. Thus, HLI corrections for the analytical calculations are presented, leading to an enhanced prediction of the optimum rear contact distance $L_{p,\text{opt}}$ in comparison to numerical simulation results. Results of these analytical considerations are partially published in [176].

8 Bifacial *n*-type silicon solar cells for upconversion applications

*In this chapter, calculations are presented for the optimization of bifacial *n*-type Si solar cells for upconversion applications. Based on the calculation results, solar cells were fabricated and a prototype upconverter could be placed at the rear side of the solar cells. To the author's knowledge, the measured quantum efficiencies exceed previously published results [206] with respect to the illumination intensity. The results of this chapter were achieved in close collaboration with J. Frank in the framework of her diploma thesis [207], which was supervised by the author of this work and S. Fischer in the context of his PhD thesis. Results of this chapter will be published in [208].*

8.1 Introduction

Solar cells made from materials with a single band gap, like silicon, utilize the solar spectrum incompletely. A photon can only contribute to the power generation in the solar cell, if it carries enough energy to produce an electron-hole pair. Therefore, the long-wavelength part of the solar spectrum with photon energies below the band gap energy $E_g = 1.13$ eV ($\lambda \sim 1100$ nm) at room temperature is lost. About 20% of the energy of the incident photon current remains unused. These losses are visualized in Fig. 8.1.

Due to upconversion the long-wavelength range of the incident sunlight can be made accessible for power conversion [209-211]. The operating principle of a system of solar cell and upconverter is shown in Fig. 8.2. Photons featuring energies $E_{h\nu} \geq E_g$ can be directly absorbed by the solar cell, while photons with $E_{h\nu} < E_g$ pass through a bifacial solar cell and enter the upconverter, which is mounted on the rear side of the solar cell. The upconverter absorbs two or more low-energy photons and, subsequently, emits a photon with higher energy than the band gap energy of Si. This may in turn be used by the solar cell to generate electricity. Trupke *et al.* determined the theoretical maximum efficiency of such a system to be 40.2% [210]. Efficient upconversion that can be used to increase the efficiency of silicon solar cells, was reported for Er^{3+} based upconverter materials [206, 212, 213].

Erbium based upconverting materials show efficient upconversion of photons with wavelengths around $\lambda = 1523$ nm. To exploit the photons in the wavelength range

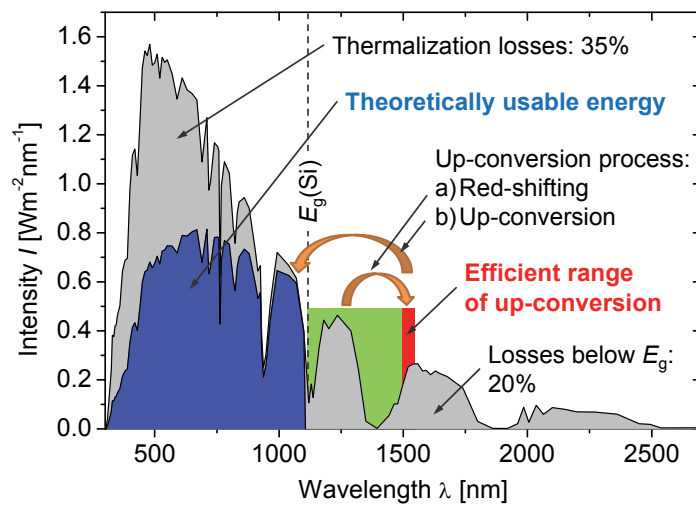


Fig. 8.1: Standardized irradiation spectrum AM1.5G (grey) and the part of the spectrum, theoretically accessible by a single-junction Si solar cell (blue). Losses occur due to thermalization processes of excess energy of highly energetic photons and due to photon energies $E_{hv} < E_g$ that are not sufficient to generate electron-hole pairs in Si. Combined with a down-shifting upconverter system, the efficiency of the solar cell can be enhanced. In such a system, photons with energies below E_g (green) are red-shifted to the spectral range of efficient upconversion by an erbium based upconverters around $\lambda = 1523$ nm (red). The upconverter converts two photons with $E < E_g$ into one photon with $E > E_g$.

between the band gap of Si and the range of efficient upconversion, the energies of these intermediate photons should be red-shifted to the range of efficient upconversion, as shown in Fig. 8.1. This concept is called spectral concentration, because the photon flux density in the range of efficient upconversion is increased [214].

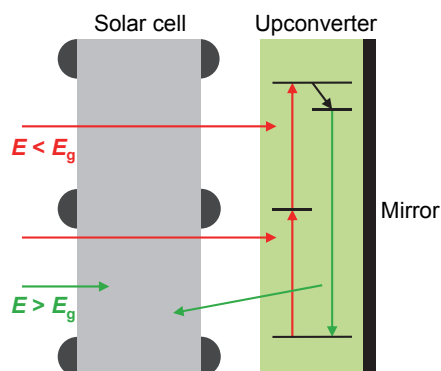


Fig. 8.2: Operating principle of a system of solar cell and upconverter after Trupke and Würfel [215]. The solar cell is transparent for photons featuring lower energies than the band gap energy (red). These are absorbed by the upconverter at the rear side of the solar cell. The upconverter emits high-energetic photons (green), which can be absorbed by the solar cell.

Upconversion is a non-linear process due to the fact that always two or more photons need to be absorbed in order to generate one high-energy photon. Thus, the quantum yield increases with the irradiance. Therefore, Goldschmidt *et al.* [214] proposed a system, which includes not only the bifacial solar cell and the upconverter, but also components for a spectral and spatial concentration of the transmitted light. Fig. 8.3 shows a sketch of the proposed setup [214, 216].

The spectral concentration can be realized by nanocrystalline quantum dots that absorb photons in the near infrared spectral range and re-emit them red-shifted. By the size of the nanocrystalline quantum dots, its band gap energy and, thus, its emitted wavelength can be adjusted [217, 218]. The entire area behind the solar cell is covered by a fluorescent concentrator consisting of nanocrystalline quantum dots, embedded in a transparent matrix. Photons transmitted by the solar cell are absorbed by the quantum dots and red-shifted in the absorption range of the upconverter. The fluorescent concentrator guides the red-shifted photons towards the upconverter by total internal reflection. The upconverter covers only a fraction of the rear side of the solar cell and is attached locally in order to achieve an additional spatial concentration of the radiation entering the upconverter, leading to a further enhanced quantum yield of the upconversion process.

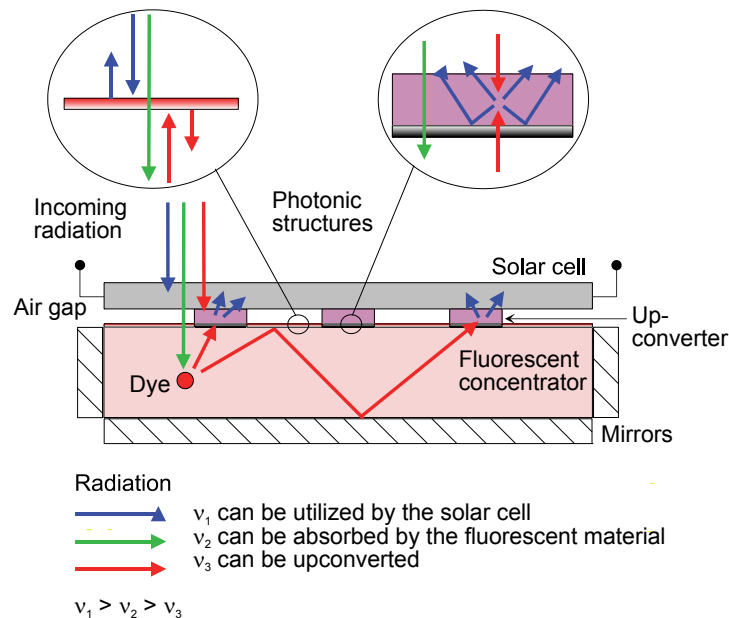


Fig. 8.3: Concept of an advanced system of bifacial solar cell and upconverter [214]. Long-wavelength light transmitted by the solar cell is red-shifted by nanocrystalline quantum dots inside a matrix forming a fluorescent concentrator, to a wavelength in the absorption range of the upconverter, leading to a spectral concentration. Due to a local application of the upconverter medium, a spatial concentration is achieved, improving the quantum yield of the upconverter. The light trapping of the fluorescent concentrator can be enhanced by photonic structures with wavelength-selective reflection at the surface of the concentrator. The figure has been taken from [216].

In previous experimental analyses, the focus has been set mainly on the upconverter material. Hence, available solar cells were used that had not been specifically optimized for the use in conjunction with upconverter materials [206, 212, 213, 219]. In this chapter, the question is addressed, how the solar cells can be adapted to maximize the impact of upconversion on the overall conversion efficiency. For this analysis, a system like presented in Fig. 8.3 has been taken as a reference. In such an upconverter system, the solar cells need to fulfill three requirements. First, the solar cell should have a very high transmittance for photons with wavelengths $\lambda > 1200$ nm in order to illuminate the upconverting system placed on the rear side of the solar cell. This aspect is particularly important, because the efficiency of the upconversion process increases with increasing illumination intensity. Second, the solar cell should utilize the upconverted photons with high efficiency. These two requirements mean that the solar cell needs to have an adapted, bifacial functionality. Third, the solar cells themselves need to have a high efficiency to ultimately optimize the system of solar cell and upconverter.

In the first part of this chapter, the simulation model is presented that allows to simulate the solar cell behavior under illumination with the emission of the upconverter, the parameterization of the upconverter characteristics, and the interaction of solar cell and upconverter. This model is subsequently used to optimize the optical properties of the solar cell. The second part deals with the fabrication and characterization of the solar cells that were prepared based on the findings presented in the first part. Upconverter samples are applied to different kind of solar cells, and the external quantum efficiency of the whole system of upconverter and solar cell is measured.

It can be seen in Chap. 3.4.2 (see Fig. 3.8) that front and rear side textured solar cells with a diffuse rear side reflector (as it is e.g. the fluorescent concentrator) are able to yield same photogeneration current densities j_{ph} as one-sided textured solar cells. At the same time, both-sided textured solar cells feature equivalently high transmission for the long wavelength range as planar solar cells. In contrast, one-sided textured solar cells feature very low transmission, due to internal reflection at the rear side. Thus, both-sided textured solar cells might be the best choice for upconversion applications.

However, as the upconverter system is topic of actual research, planar bifacial solar cells have been produced in this work for first experiments in order to achieve both, reasonable upconversion efficiencies and clearly defined surfaces for the application of the upconversion medium at the rear side of the solar cell.

8.2 Optimizing the solar cell structure using simulation models

In order to optimize the solar cell structure, the system out of solar cell and the upconverter, as well as their interaction has to be modeled.

8.2.1 Solar cell simulation model

For optical simulations of bifacial solar cells it is convenient to model the illumination from the front and rear side separately, so the spectrum and angular distribution of the rear side illumination can be defined independently. Thus, e.g. the rear side illumination of albedo collecting solar cells [220], diffuse rear reflectors (see Chap. 3.4.2) or upconverting solar cells can be calculated in a versatile manner. Thereby, it is assumed that the optical generation rates for the front and rear side illumination can be calculated independently. Subsequently, the recombination rates have to be added in the electrical simulation.

Two separate simulations have been used, one for the illumination of the front side and one for the illumination of the rear side. In order to determine the rear side illumination, the transmission of the front side illumination behind the solar cell is detected and weighted by the conversion efficiencies of the upconverter system. Further details are given in the following.

8.2.2 Modeling the impact of upconversion onto the solar cell performance

To assess the impact of upconversion on the overall solar cell performance, not only the used upconverter material, but also the overall upconversion system presented in Fig. 8.3 has to be considered. This includes more complex components, such as nanocrystalline quantum dots in a matrix material, forming a fluorescent concentrator.

In the presented model, the usage of the upconverter material $\beta\text{-NaY}_{0.8}\text{Er}_{0.2}\text{F}_4$ has been assumed, which will be used in the experimental section (see Chap. 8.4) as well. This material absorbs efficiently photons in the wavelength range from 1490 nm to 1550 nm and shows upconversion luminescence predominantly around 980 nm [221]. In Fig. 8.4, the experimentally determined integrated quantum yield η_{UC} as a function of the excitation wavelength is shown, obtained by integrating over all wavelengths of the emitted light:

$$\eta_{\text{UC}} = \frac{\Phi_{\text{UC}}}{\Phi_{\text{in}}} \quad . \quad (8.1)$$

η_{UC} specifies the ratio of the photon flux density Φ_{UC} , which is emitted by the upconverter at wavelengths below 1200 nm, and the incident photon flux density Φ_{in}

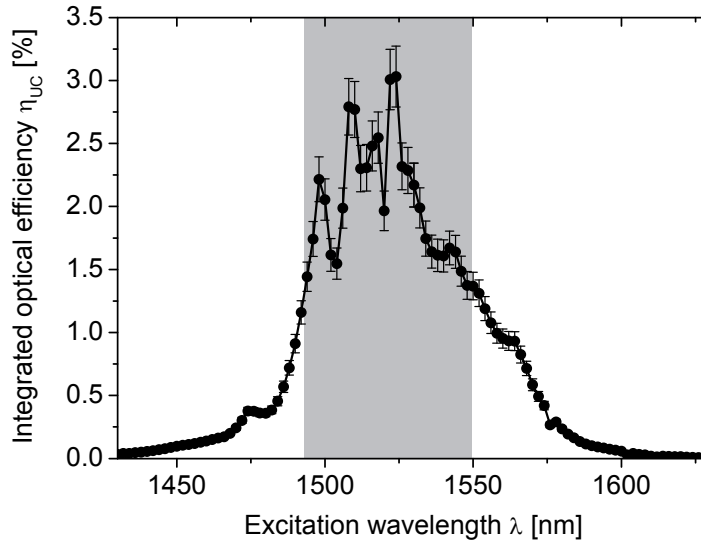


Fig. 8.4: Integrated quantum yield of the upconverter $\beta\text{-NaY}_{0.8}\text{Er}_{0.2}\text{F}_4$, dependent on the wavelength by monochromatic excitation [206, 222]. The illumination intensity holds 880 W/m^2 . In the wavelength range from $\lambda = 1490$ to 1550 nm the quantum yield of the upconversion holds $> 50\%$ of its maximum value.

impinging on the upconverter [206]. At a wavelength of $\lambda = 1523 \text{ nm}$ the upconverter attains its maximum efficiency η_{UC} of $\sim 3.0\%$ for an irradiance of 880 Wm^{-2} . This implies that at least 6% of the incident photons have been used since at least two photons are required to create an upconverted photon.

The experimentally determined dependence of the upconversion quantum yield on the incident irradiance I is shown in Fig. 8.5, citing results that have been presented in [222]. For the use in the calculations presented in this chapter, the dependency has been parameterized [206]:

$$\eta_{\text{UC}}(\Phi_{\text{in}}) = c_1 \cdot \Phi_{\text{in}}^{m-1} + c_2 \quad , \quad (8.2)$$

with the constants c_1 and c_2 and m , which is a measure for the non-linearity of the system. With this model, the photon flux density Φ_{UC} of the upconverted light can be directly calculated for any given incident photon flux density Φ_{in} .

For the simulations the approximation is assumed that all photons, which are transmitted by the solar cell, with a wavelength $\lambda < 1550 \text{ nm}$ are either directly utilized by the upconverter, or absorbed by the nanocrystalline quantum dots, re-emitted and guided without losses to the upconverter. Together with an assumed uniform quantum yield of the upconversion process over the entire effective spectral range, these highly idealized assumptions lead to the simplification that all transmitted photons with

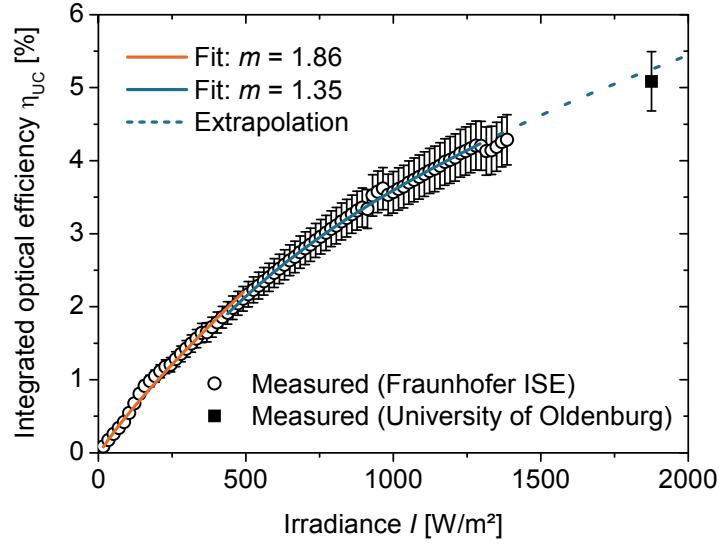


Fig. 8.5: Integrated quantum yield of the upconverter $\beta\text{-NaY}_{0.8}\text{Er}_{0.2}\text{F}_4$, dependent on the incident photon flux density Φ_{in} at a wavelength $\lambda = 1523 \text{ nm}$ [206, 222]. The maximum Φ_{in} shown in the graph corresponds to an illumination intensity of 2000 W/m^2 for $\lambda = 1523 \text{ nm}$.

$\lambda < 1550 \text{ nm}$ contribute to the upconversion with the same efficiency. The transmitted photon flux density Φ_{trans} behind the solar cell can be calculated via

$$\Phi_{trans} = \int_{300\text{nm}}^{1550\text{nm}} Trans_{SC}(\lambda) \cdot AM1.5G_{ph}(\lambda) d\lambda \quad . \quad (8.3)$$

with $Trans_{SC}(\lambda)$ being the transmission of the solar cell, and $AM1.5G_{ph}(\lambda)$ the incident solar spectrum in units of photons per flux density. The IEC 60904-3 norm spectrum [76] has been used throughout the calculations presented in this work. The upconverter does not necessarily cover the complete active area of the solar cell A_{SC} . Due to the fluorescence concentrator the light can be guided to the upconverter area, as shown in Fig. 8.3, and is consequently spatially concentrated. This spatial concentration is accounted for by a concentration factor K , arising from the ratio between the total area of the solar cell A_{SC} and the area A_{UC} , where the upconverter is located.

$$K = \frac{A_{SC}}{A_{UC}} \quad . \quad (8.4)$$

With the presented assumptions that no losses occur due to the spatial concentration, the incident photon flux density holds $\Phi_{in} = K \cdot \Phi_{trans}$. Φ_{trans} is the transmitted photon flux density.

Using the parameter model that gives $\eta_{UC}(\Phi_{in})$ and Eq. (8.3), the photon flux density of upconverted photons can be calculated via

$$\Phi_{UC} = \Phi_{trans} \cdot \eta_{UC}(\Phi_{in}) \quad \text{with} \quad \Phi_{in} = K \cdot \Phi_{trans} \quad . \quad (8.5)$$

Please note that Eq. (8.5) assumes that the upconverted photons are evenly distributed over the complete solar cell area. This is not a very strong simplification, given the fact that in a real system many upconverter spots would be distributed over the whole solar cell surface to keep the average path length short within the fluorescent concentrator, which the light has to travel until it reaches the upconverter. Furthermore, considering the emission spectrum of the upconverter, which is predominantly centered around 980 nm, the emitted photons also have a considerable penetration depth within silicon, which should lead to a rather even distribution of absorbed upconverted photons within the solar cell. Luminescence from higher transitions of the Er^{3+} with higher energies than the one centered around 980 nm contribute less than 1% to the emission of upconverted photons [221]. Therefore, these transitions can be neglected in the model. Furthermore, the emission spectrum centered around 980 nm, which shows a sharp peak and a width of about 30 nm, has been simplified to a monochromatic emission at $\lambda = 980$ nm.

The light, which is transmitted by the solar cell, needs to be weighted according to the upconversion properties for coupling back into the solar cell. and coupled back. The irradiance I_{UC} due to upconversion emission can be easily calculated by

$$I_{UC} = \Phi_{UC} \cdot \frac{hc}{980\text{nm}} \quad , \quad (8.6)$$

with the simplification of a monochromatic emission. h denotes the Planck constant, and c is the velocity of light in vacuum. Since the emission of the upconverter is uniformly distributed in all directions in space, the illumination of the rear side of the solar cell is isotropic. While the front side illumination is simulated perpendicular to the standard domain, light coming from the upconverter or from the fluorescent concentrator, respectively, is coupled diffusely into the simulated structure.

In the simulation a refractive index of $n = 1.5$ for the fluorescent concentrator and the upconverter material has been assumed.

To assess the impact of the upconverter onto the overall system performance, and to understand the different aspects relevant to this, three figures of merits that describe the performance of the individual components and of the overall system has been defined. Thereby, it has been concentrated on the optical performance, such that any effects of the electrical performance of the solar cell could not hide the aspects of interest.

The parameter Abs_0 indicates which fraction of incident photons is absorbed in the solar cell, if no upconverter is placed behind to solar cell, which is equivalent to an upconversion quantum yield of zero:

$$Abs_0 = \frac{\Phi_{abs}}{\Phi_{in}} = \frac{\int A(\lambda) \cdot AM1.5G_{ph}(\lambda) d\lambda}{\int AM1.5G_{ph}(\lambda) d\lambda} \quad (8.7)$$

Φ_{abs} indicates the absorbed photon flux density. $A(\lambda)$ denotes the spectrally resolved absorption probability in Si, calculated from numerical simulation. Thus, Abs_0 is a measure for the efficiency of the solar cell without the upconverter. The solar spectrum $AM1.5G_{ph}(\lambda)$ is given in units of photons per wavelength interval $s^{-1}cm^{-2}$.

Abs_{UC} denotes the fraction of photons of the AM1.5G spectrum from the upconversion process, which can potentially generate electron-hole pairs in the solar cell:

$$Abs_{UC} = 0.5 \cdot Trans \cdot Abs_r \quad \text{with}$$

$$Trans = \frac{\Phi_{trans}}{\Phi_{in}} = \frac{\int Trans(\lambda) \cdot AM1.5G_{ph}(\lambda) d\lambda}{\int AM1.5G_{ph}(\lambda) d\lambda} \quad , \quad (8.8)$$

$$Abs_r = \frac{\Phi_{abs,r}}{\Phi_{in,r}} = \frac{\int A_r(\lambda) \cdot UC_{ph}(\lambda) d\lambda}{\int UC_{ph}(\lambda) d\lambda} \quad .$$

It includes the transmitted fraction $Trans$ of the incident photons of the AM1.5G spectrum and the fraction of the photons Abs_r , re-emitted by the upconverter and absorbed by the solar cell. The integrations cover the relevant wavelength range from $\lambda = 300$ to 1550 nm. A_r denotes the absorption of the solar cell with illumination from the rear side and $UC_{ph}(\lambda)$ is the emission spectrum of the upconverter. Thereby, a perfect upconverter holds a quantum yield of 50%, because at least two photons are necessary to create one photon with higher energy.

The overall percentage of absorbed photons in the solar cell is:

$$Abs_x = Abs_0 + \eta_{UC} \cdot Trans \cdot Abs_r \quad . \quad (8.9)$$

Here, x denotes the quantum yield of the upconversion. Abs_x is eventually the parameter, which needs to be maximized.

8.2.3 Optimization of anti-reflection coatings

The front side of the solar cell should have a low reflection in the entire wavelength range from $\lambda = 300 - 1550$ nm, such that photons in the wavelength range below 1150 nm can be efficiently utilized directly by the solar cell, and such that photons

with longer wavelength have a chance to reach an upconverter. High transmission can be achieved with the help of an anti-reflection coating (ARC). Fig. 8.6 shows a selection of dielectric layers available at Fraunhofer ISE. Ellipsometry measurements to determine n and k in the considered wavelength range have been performed at Fraunhofer IAF. In the case of this work, the ARC at the front side should minimize reflection losses in the entire wavelength range from $\lambda = 300 - 1550$ nm. As with one anti-reflection layer the reflection can only be optimally reduced for one specific wavelength, it is advantageous to use a layer system of two or three layers. A further increase in the number of layers would not improve significantly the anti-reflection effect [223]. To achieve best anti-reflection results, the refractive indices of the coatings should be evenly distributed within $n = 3.5$ from Si and $n = 1$ from air (or another environmental medium). For a three-layer system, both lower and higher refractive materials are needed. Kraus [223] suggests silicon-rich silicon carbide with $n = 2.4$ and porous SiO_2 with $n = 1.2$. Layers with these properties were not available at Fraunhofer ISE. Therefore, two-layer systems were theoretically analyzed and later applied to the produced Si solar cells. Promising material combinations are layer systems with SiN_x as the first, higher refractive index layer with $n = 1.99$, and SiO_2 ($n = 1.47$) or MgF_2 ($n = 1.39$) as the second lower refractive index layer (all values at a wavelength of $1.0 \mu\text{m}$). TiO_2 with a refractive index of $n = 2.07$ in combination with MgF_2 has the highest potential anti-reflection effect, for which reason an optimization will be performed in detail in the following. However, the etching rates of TiO_2 depend strongly on the deposition circumstances and, thus, etching TiO_2 represents a process step prone to failure in the production of the solar cells. Therefore, the optima for systems of SiN_x and SiO_2 or MgF_2 , respectively, are given as well.

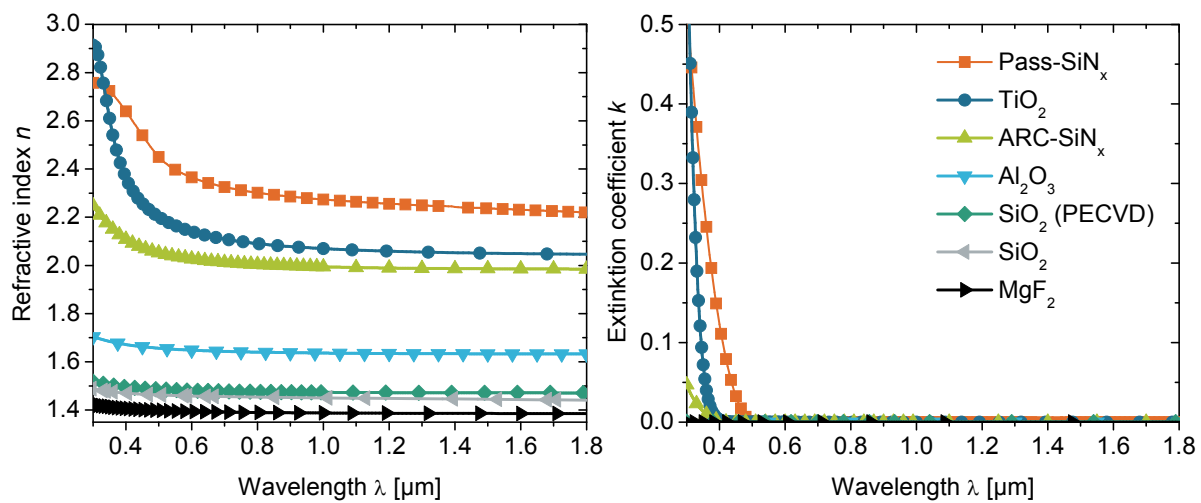


Fig. 8.6: Overview of refraction indices n (left) and extinction coefficients k (right) of dielectric layers.

To enhance the surface passivation, all investigated structures feature a 10 nm thick Al_2O_3 layer between Si and the first anti-reflection layer. Due to the thinness of the Al_2O_3 layer, it has a minor effect on the optical properties.

Fig. 8.7 shows results of these variations for planar bifacial solar cells. The coating thicknesses leading to the highest direct absorption of incident photons in the solar cell (Abs_0) are around 50 nm TiO_2 and 80 nm MgF_2 (Fig. 8.7, (a)). For a $\text{SiN}_x/\text{SiO}_2$ layer stack, the optimum thicknesses are 50 nm SiN_x and 70 nm SiO_2 . With MgF_2 as second ARC on top of the SiN_x , the SiN_x layer holds the same thickness, but the MgF_2 layer needs to be 85 nm, which is a little bit thicker than the SiO_2 layer for the optimum case. In the following, layer systems with these thicknesses will be referred to as “Cell_{opt}”.

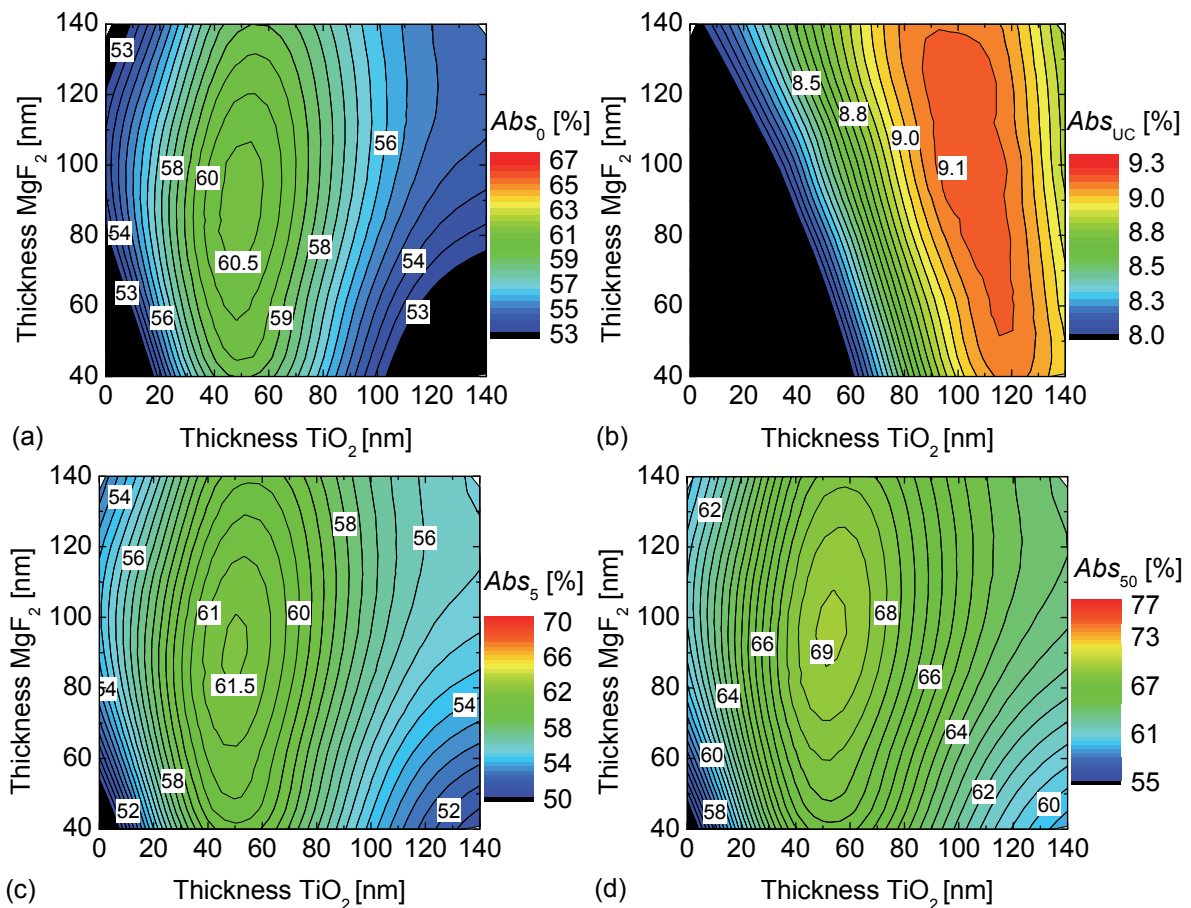


Fig. 8.7: Optimization of ARC layer thicknesses for the front side of planar bifacial solar cells for upconversion applications. The parameter Abs_0 (a) reflects the efficiency of the solar cell without upconverter. Abs_{UC} (b) is a measure for the efficiency yield of the upconverter. Abs_5 (c) and Abs_{50} (d) describe the system consisting of solar cell and upconverter with a quantum yield of the upconverter of 5% and 50%, respectively.

The layer thicknesses have to be larger to achieve the highest absorption within the solar cell for photons stemming from upconversion (Abs_r). Fig. 8.7 (b) indicates optimum layer thicknesses in the range of 110 nm TiO_2 and 110 nm MgF_2 . Thicker layers shift the reflection minima towards the infrared, increasing the transmission in this wavelength range. However, this increases the reflection in the visible spectral range, reducing the solar cell efficiency. The SiN_x/MgF_2 stack features the same optimum thicknesses as the SiN_x/SiO_2 stack within a tolerance of ± 5 nm. Layer systems following this scheme are denoted as “UC_{opt}” throughout the chapter.

Considering the entire system of solar cell and upconverter with upconversion efficiencies of 5% Abs_{05} (Fig. 8.7, (c)) and 50% Abs_{50} (Fig. 8.7, (d)), it can be seen that the optimum layer thickness depends on the quantum yield of the upconversion. With increasing upconversion efficiency, the optimum shifts slightly towards thicker layers. However, this effect is fairly small, even at the highest quantum yield of 50%.

Fig. 8.8 shows the same layer thickness optimization, but for both-sided textured solar cells. The same trends as in planar solar cells can be observed and the respective optimum layer thicknesses are approximately the same, even if the overall absorption in the Si bulk material is significantly enhanced due to enhanced light trapping properties (please note that Fig. 8.7 and Fig. 8.8 feature the same scales, respectively, for better comparison). In contrast, Abs_{UC} reaches about the same maximum value as in the case of a planar solar cell. The upconversion effect is therefore similar for both surface structures, but the influence on the layer thickness is less for textured Si bulk material. Therefore, the optimum with or without upconverter does not shift significantly and, thus, representing a system which combines good cell performance with the demand for a high transmission of the solar cell.

The requirements for the ARC at the rear side of the solar cell are easier to accomplish than at the front. Only the infrared part of the spectrum has to be considered. Photons coming from the upconverter with a wavelength around $\lambda = 980$ nm need to be coupled into the solar cell efficiently and transmission of photons with wavelengths beyond 1150 nm should be high as well. In the configuration where the upconverter is only coupled locally to the solar cell, the good incoupling efficiency at 980 nm is only required for the areas where the upconverter is attached. For the rest of the solar cell area, the reflection for wavelengths below 1150 nm can be high to increase the efficiency by which photons are utilized by the solar cell. In the configuration presented in Fig. 8.3, this function of a rear reflector is carried out by the spectrally selective photonic structure on top of the fluorescent concentrator. Hence, it can be

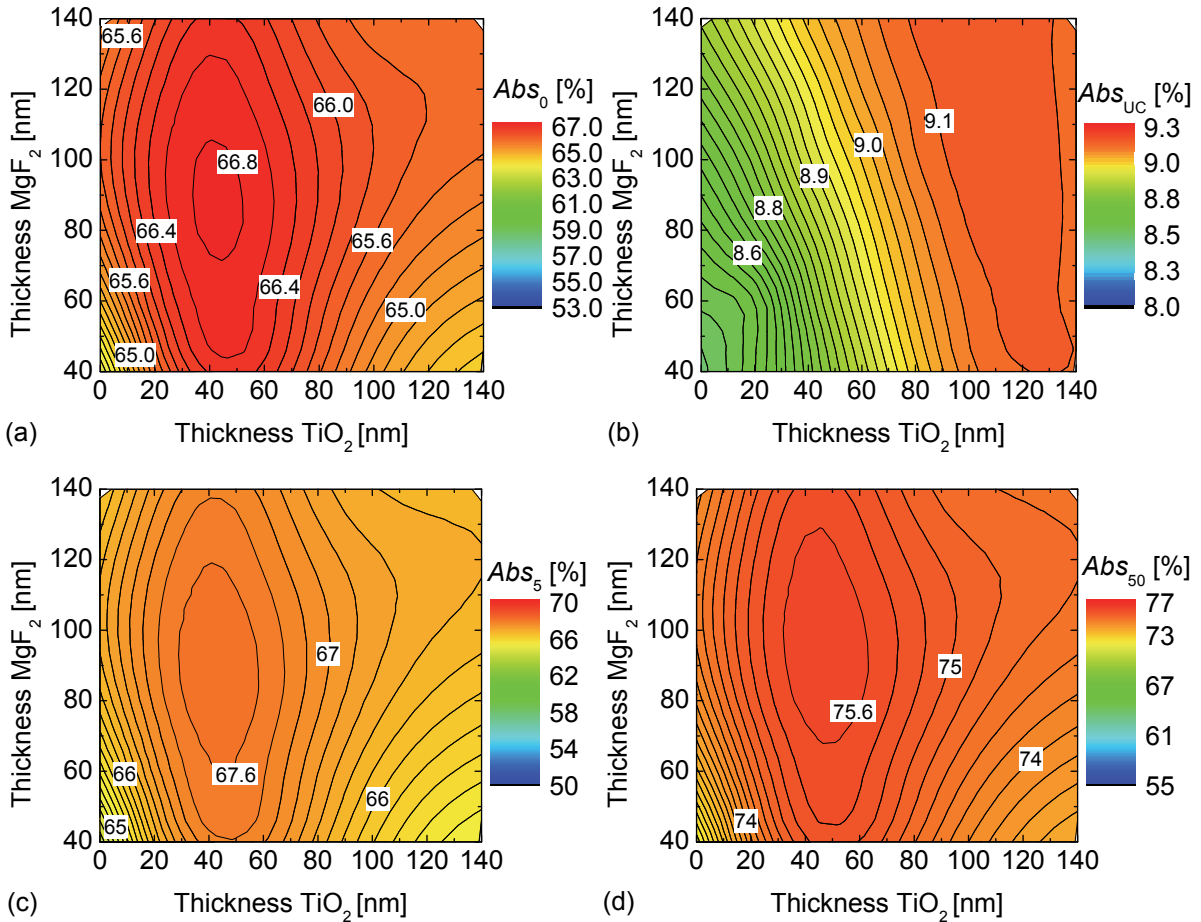


Fig. 8.8: Optimization of ARC layer thicknesses for the front side of both-sided textured bifacial solar cells for upconversion applications. In comparison to the calculations featuring planar solar cells, shown in Fig. 8.7, significantly higher cell efficiencies can be achieved.

ignored here. This leads to a small underestimation of the overall system efficiency, but in the light of the highly idealized assumptions made in the rest of this work, which tend to lead to an overestimation, this can be neglected. The rear side of the solar cell structure is optimized against $n = 1.5$, the refractive index of the carrier material in which the effective upconverter is embedded. Due to this higher n (in contrast to air with $n = 1$ at the front side), a single anti-reflection layer has shown to be most appropriate. As the upconverter acts as a diffuse reflector, only Abs_{UC} needs to be optimized in good approximation.

The most promising ARC for the rear side of the solar cell is TiO₂, due to its optical properties. An optimization of the TiO₂ ARC layer thicknesses for the rear side of planar and both-sided textured bifacial solar cells is shown in Fig. 8.9. Because of the above mentioned experimental challenges, SiN_x has been used, featuring similar results, due to comparable refractive indices. Again, the calculations have been performed with an additional 10 nm thick Al₂O₃ layer, necessary for good electrical

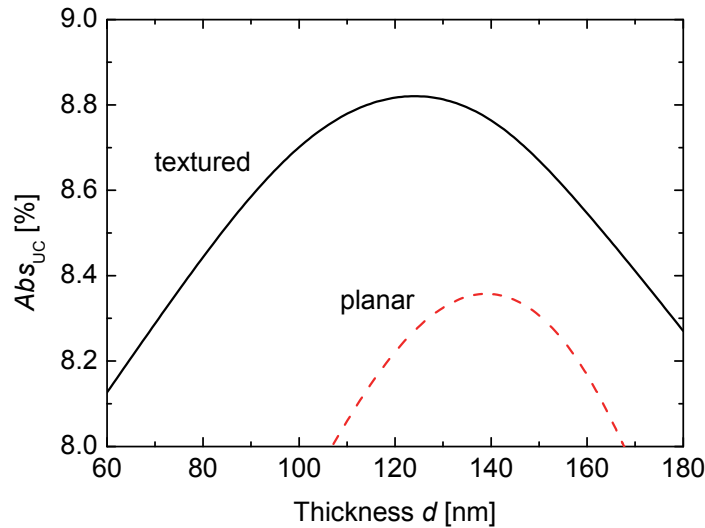


Fig. 8.9: Optimization of the TiO_2 ARC layer thicknesses for the rear side of planar and both-sided textured bifacial solar cells for upconversion applications.

surface passivation properties. During the optimization of the rear side, it has been assumed for the front side coating a layer stack of 10 nm Al_2O_3 , 50 nm TiO_2 , and 90 nm MgF_2 . As result, a TiO_2 layer thickness of $d = 140$ nm for planar bifacial solar cells lead to the highest Abs_{UC} , as shown in Fig. 8.9. Calculating the planar structure with SiN_x as rear side anti-reflection layer, the optimum thickness is with 120 nm slightly lower, due to the different n values. For both-sided textured solar cells, the optimum layer thickness for TiO_2 and also for SiN_x holds 120 nm.

Resulting simulated optical properties for planar and both-sided textured solar cells featuring the UC_{opt} are exemplarily presented in Fig. 8.10. As one can see for planar

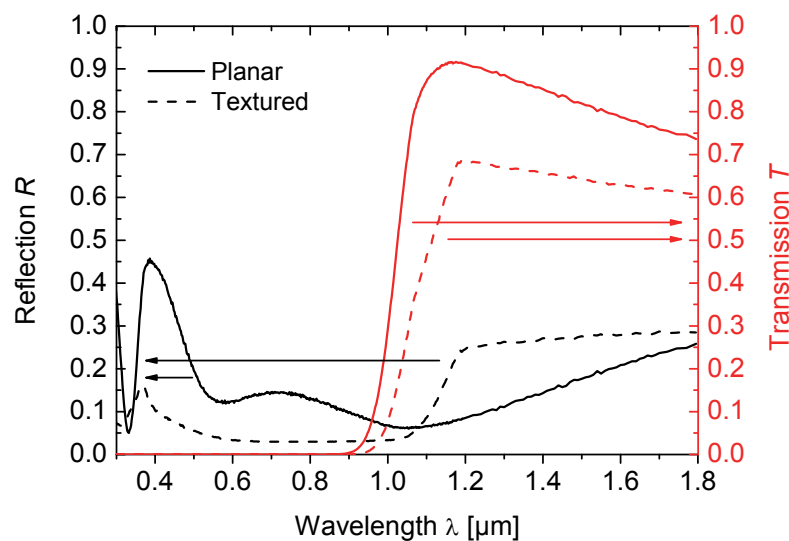


Fig. 8.10: Comparison of the wavelength dependent calculated reflection R (black) and transmission T (red) for planar (line) and textured (dash) bifacial solar cells featuring the UC_{opt} .

solar cells, a high transmission of 80 to 90% is achieved in the spectral range $1150 \text{ nm} < \lambda < 1550 \text{ nm}$, while reflection losses are low over the whole spectral range. Both-sided textured solar cells feature better reflection properties in absorption range of silicon, but feature beyond 1150 nm significantly less transmission, than planar solar cells.

8.2.4 Assessment of efficiency potential

Based on the previously performed optimizations, the efficiency potential for the considered upconversion system is calculated. The assumed solar cell parameters used for the simulations are summarized in Tab. 8.1. The solar cell geometry, consisting of e.g. front contact finger distance or finger width is chosen due to experimentally realizable structures at Fraunhofer ISE and, thus, not especially optimized.

For the assessment of the efficiency potential it is assumed that the transmitted light is both, spectrally and spatially concentrated on the upconverter. The spatial concentration is characterized by the factor K : $K = 1$ corresponds to a full-surface covering upconverter at the rear side of the solar cell, whereas for $K > 1$ the light transmitted by the solar cell is concentrated via a fluorescence concentrator and coupled into a partially applied upconverter. The optimum area ratio of upconverter and solar cell was investigated by Rist [224]. He concludes that high concentration factors K theoretically lead to an increase in the quantum yield of the upconversion, but on the other hand increased photon concentrations might cause significant reabsorption losses in the fluorescent concentrator. Based on first experimental data of appropriate quantum dots provided by the Heriot-Watt University Edinburgh, the reabsorption losses dominate the behavior, which would lead consequently to an optimum of $K = 1$. Thus, to achieve an effective efficiency gain of the entire system, the quantum efficiency of the actual experimentally realized quantum dots need to be increased. If a quantum efficiency of 90% is assumed, which might be experimentally achievable, $K = 5$ was determined [224] to be the optimum concentration factor.

Therefore, to estimate the gain in efficiency of the entire system consisting of bifacial Si solar cell, fluorescence concentrator with embedded quantum dots and $\beta\text{-NaY}_{0.8}\text{Er}_{0.2}\text{F}_4$ upconverter, $K = 1$ as well as $K = 5$ is considered in the simulations. In addition, the case of a very high geometric concentration of $K = 100$ is considered in order to define an upper limit for the potential efficiency gain. The fluorescence concentrator is assumed to be ideal, which means that no reabsorption occurs and the quantum efficiency of the quantum dots is 100%. This corresponds to a perfect spectral

Tab. 8.1: Overview of simulation parameters of the solar cell, optimized for upconversion applications at an illumination intensity of 1 sun.

Parameter	Numerical value
Surface morphology	Inverted pyramids (both-sided)
ARC: front side	50 nm TiO ₂ + 90 nm MgF ₂
ARC: rear side	120 nm TiO ₂
Contact finger distance	800 μm
Effective contact width of fingers	8 μm
Fraction of illuminated	0.952
External series resistance R_{grid}	0.17 Ωcm ²
Base doping concentration (P)	4.992×10 ¹⁵ cm ⁻³
Emitter (B)	$R_{\text{sh}} = 130 \text{ Ω/sq}; N_{\text{surf}} = 6 \times 10^{18} \text{ cm}^{-3}$
Local BSF (P)	$R_{\text{sh}} = 19 \text{ Ω/sq}; N_{\text{surf}} = 4 \times 10^{19} \text{ cm}^{-3}$
Width of BSF above contacts	30 μm
Electrical surface passivation	10 nm Al ₂ O ₃
Surface recombination velocity S_0	Front: 3× S_0 (S_0 according to Eq. (3.14)) Rear: 30 cm/s

concentration of the transmitted light from the solar cell to the absorption range of the upconverter. The resulting quantum yield of the upconversion η_{UC} is calculated for different radiation intensities and K values according to Eq. (8.2). Light with energies in the range of the band gap that might be reflected diffusely by the upconverter is not considered in the simulation, since this effect is independent of the upconversion and does not affect its efficiency gain $\Delta\eta$. This simplification is consistent to the assumption that each transmitted photon is red-shifted and absorbed by the upconverter.

The results of the simulations with 1 sun illumination are shown in Tab. 8.2 indicating that without additional spatial concentration of the transmitted light, the irradiance for the upconverter is too low to ensure a significant gain by the upconversion. With a quantum yield of the upconverter of $\eta_{\text{UC}} = 0.42\%$, the absolute increase in efficiency of the entire system is with $\Delta\eta = 0.02\%$ very low. By a concentration factor of $K = 5$, the absolute gain in efficiency can be increased to $\Delta\eta = 0.1\%$. For the more hypothetical case of $K = 100$, the irradiance reaches 7900 W/m² at the upconverter, which is outside

Tab. 8.2: Simulation results for a solar cell without upconverter and for the system consisting of solar cell and upconverter under consideration of different spatial concentration factors K at 1 sun. The quantum yield η_{UC} of the upconversion depends strongly on K . η denotes the total efficiency of the system consisting of solar cell, fluorescence concentrator and upconverter, and $\Delta\eta$ is the efficiency gain achieved by the upconversion, respectively.

K	Without upconverter	1	5	100
η_{UC} [%]	-	0.42	1.81	10.3
$\Delta\eta$ [%]	-	0.02	0.10	0.56
η [%]	22.21	22.23	22.31	22.77
j_{sc} [mA/cm ²]	39.03	39.07	39.20	39.98
FF [%]	81.2	81.2	81.2	81.2
V_{oc} [mV]	700.8	700.8	700.9	701.5

the range of validity of the parameterization shown in Fig. 8.5. The parameterization might be used up to irradiance values ≤ 2000 W/m². Thus, for the case $K = 100$, the quantum yield obtained from the simulation of the converter by means of the rate equation model described in [20] is used.

An increase of the quantum yield of the upconversion can also be achieved by illuminating directly the solar cell with concentrated sunlight. Simulation results featuring a tenfold concentration of the sunlight are given in Tab. 8.3. The relatively low solar cell efficiencies result from the fact that the simulated solar cell has not been optimized for concentration applications, reflected in the low fill factor $FF = 73.0 \pm 0.2\%$. For higher efficiencies in the first place the base resistivity and the contact finger distance need to be optimized [225]. Regardless of whether the cell design is optimized a notable increase in η_{UC} ($\Delta\eta = 0.14\%$) by the upconverter can be observed, even without an additional spatial concentration by the fluorescence concentrator ($K = 1$). By increasing the spatial concentration to $K = 5$, an absolute increase of the overall system efficiency of 0.35% is possible.

It can be concluded that the concentration of solar light is essential to achieve a significant increase in solar cell efficiency by the upconversion process. This can be done either by illuminating the solar cell with concentrated sunlight or by an active fluorescence concentrator behind the solar cell. Requirement for the realization of

Tab. 8.3: Simulation results for the system consisting of solar cell, fluorescence concentrator and upconverter under consideration of different spatial concentration factors K at 10 suns external concentration, analogous to the results shown in Tab. 8.2. The tenfold increased illumination intensity leads to a significant increase of the quantum yield of the upconverter.

K	Without upconverter	1	5	100
η_{UC} [%]	-	3.03	7.46	15.4
$\Delta\eta$ [%]	-	0.14	0.35	0.72
η [%]	21.70	21.84	22.05	22.42
j_{sc} [mA/cm ²]	390.5	393.4	397.5	404.9
FF [%]	73.1	73.0	73.0	72.8
V_{oc} [mV]	759.9	760.1	760.3	760.7

good fluorescence concentrators is a further optimization of nanocrystalline quantum dots. By the assumption of a realistic internal concentration factor $K = 5$, an absolute efficiency gain in the order of $\Delta\eta = 0.1\%$ to 0.4% might be achievable.

8.3 Fabrication of bifacial solar cells

8.3.1 Fabrication parameters

The design and fabrication of the solar cell was based on processes that are capable to yield high efficiency silicon solar cells. The solar cell structure is shown schematically in Fig. 8.11. It is based on the concept presented in 1981 by Cuevas *et al.* for highly efficient bifacial solar cells [226]. The solar cells are made on 200 μm thick 4" wafers of 10 Ωcm n -type FZ Si base material. On each wafer 7 cells were processed with the dimensions 2 x 2 cm^2 .

In order to achieve defined surface structures for the deposition of the upconverter medium, these first bifacial solar cells for upconversion applications feature planar surfaces. Furthermore, the transmission of sub-band gap photons is the highest for planar surfaces, thus maximizing the relative impact of the upconversion process (see Chap. 8.2). The solar cells feature metal contact finger grids consisting of a Ti/Pd/Ag stack system. The front and rear finger grids are aligned to each other in order to reduce shading losses. The contact finger distance is 800 μm . A sequence of the process steps is shown in Fig. 8.12.

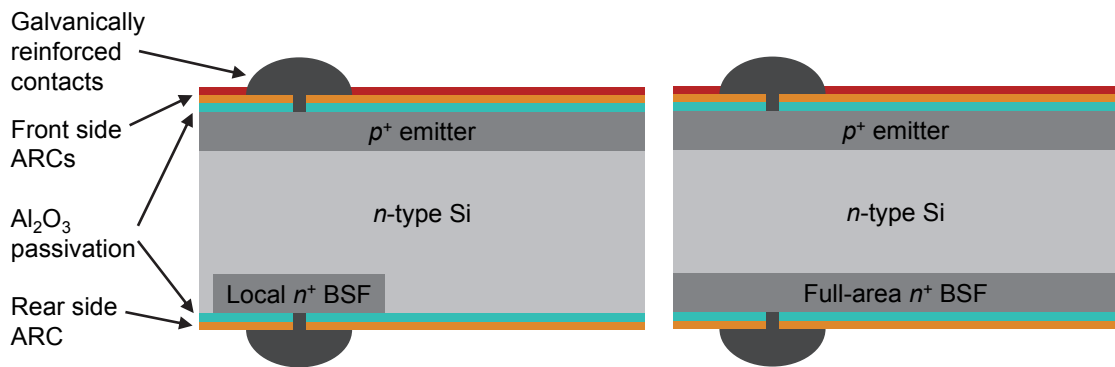


Fig. 8.11: Schematic of the solar cell concept with local (left) and full-area (right) BSF.

The emitter covers the entire front of the solar cell. To achieve a deep doping profile with a relatively low surface doping concentration, the wafers were exposed to an additional high-temperature step after boron diffusion. Half of the fabricated solar cell batch feature full-area phosphor diffused n^+ back surface fields (BSF) (Fig. 8.11, right), whereas the other half feature local n^+ BSFs below the contact areas with a width of $30\ \mu\text{m}$ (Fig. 8.11, left). The diffusion profiles of front and rear side are shown in Fig. 8.13. The boron doped emitter profiles feature a sheet resistance of $R_{\text{sh}} = 130\ \Omega/\text{sq}$, and the phosphor doped BSF profiles $R_{\text{sh}} = 19\ \Omega/\text{sq}$.

For surface passivation, $10\ \text{nm}$ thick Al_2O_3 layers were deposited by atomic layer deposition between silicon bulk material and ARC on the front and rear side of the solar cell. As Al_2O_3 saturates very well dangling bonds at the Si surface and features a strong negative surface charge density of $-9.9 \times 10^{13}\ \text{cm}^{-3}$ [111], it has ideal properties for the passivation of boron-doped surfaces [27, 227]. Al_2O_3 shows as well good



Fig. 8.12: Overview of the processing sequence for the fabrication of the bifacial solar cells.

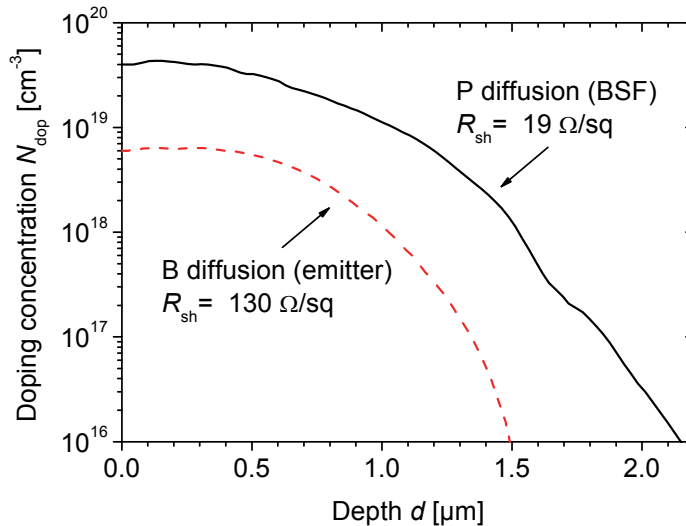


Fig. 8.13: Measured doping profiles of the B doped emitter and the P doped BSF profile of the bifacial Si solar cells, fabricated in this work.

passivation qualities on lowly phosphorus-doped surfaces [228] at an illumination intensity of 1 sun.

Following the results of Chap. 8.2, double-sided ARCs were applied on the front side of the solar cell. To investigate the different choices of materials and optimization schemes experimentally, both material systems, the $\text{SiN}_x/\text{MgF}_2$ stack and the $\text{SiN}_x/\text{SiO}_2$ stack, have been realized. For each material system, layers of different thicknesses were deposited, optimized for high transmission in the infrared and, thus, for a maximized upconversion effect (UC_{opt}), or optimized for high solar cell efficiencies (Cell_{opt}), as discussed in Chap. 8.2. The variations and ARC thicknesses are summarized in Tab. 8.4. The first anti-reflection layers of both, rear and front side, were deposited before metallization. These layers needed to be patterned by an etching process in order to create contact openings. The second anti-reflection layer on the front side of the solar cells was applied after metallization, consisting of PECVD SiO_2 or evaporated MgF_2 , respectively. Due to the different thicknesses of the ARCs in the different optimization schemes and, thus, varying reflection properties in the visible wavelength range, the color of the solar cell surface changes, as can be seen in Fig. 8.14. For the ARC of the rear side an ARC- SiN_x anti-reflection layer with a thickness of about 120 nm was applied.

After the etch-back process of the first anti-reflection layer (see Fig. 8.12), a thin metal contact grid of Ti, Pd and Ag was deposited, which is only 8 μm wide, in order to minimize recombination losses at the contacts. With a height of 0.2 μm the deposited contact fingers are far too thin for sufficient lateral conductance. Thus, contact fingers

Tab. 8.4: Overview of the variation of the double-layer ARCs of the front side of the solar cells. Two different materials for the 2nd ARC have been used, MgF₂ and SiO₂, and the layer thicknesses are optimized for both, high upconversion (UC_{opt}) and high solar cell efficiencies (Cell_{opt}). Due to an error in the processing sequence, the 1st ARCs for Cell_{opt} were deposited too thick (in brackets). Thus, the thicknesses of the 2nd ARCs were adjusted (in brackets).

Optimization	ARC front side		ARC rear side
	1 st ARC	2 nd ARC	
UC _{opt}	110 nm SiN _x	110 nm MgF ₂	120 nm SiN _x
Cell _{opt}	50 (85) nm SiN _x	85 (105) nm MgF ₂	120 nm SiN _x
UC _{opt}	105 nm SiN _x	105 nm SiO ₂	120 nm SiN _x
Cell _{opt}	50 (75) nm SiN _x	70 (90) nm SiO ₂	120 nm SiN _x

were thickened by electroplating. With this process sequence, it is possible to obtain contacts with a good aspect ratio of height and width featuring both, relatively low shading losses and low lateral series resistance losses [229]. For the galvanic thickening of the contact fingers with Ag⁺ ions, the metal fingers must feature a higher electro-chemical potential than the Ag electrode. Therefore, the velocity of Ag ablation depends on the voltage applied. In standard Si solar cells featuring a full-area rear side metallization, a voltage is applied at the rear side of the solar cell, forming a homogeneous potential over the entire solar cell and, thus, enabling a homogeneous deposition of Ag⁺ ions at the front finger grid. Bifacial solar cells do not feature an entire rear surface metallization and, thus, a voltage can only be applied point wise at the rear side for electroplating.

The produced solar cells were contacted at one point and submerged into the electrolyte solution. Due to a restricted conductivity of the Si wafer, the potential at the rear side of the wafer is not homogeneous. In the vicinity of the contacted area the

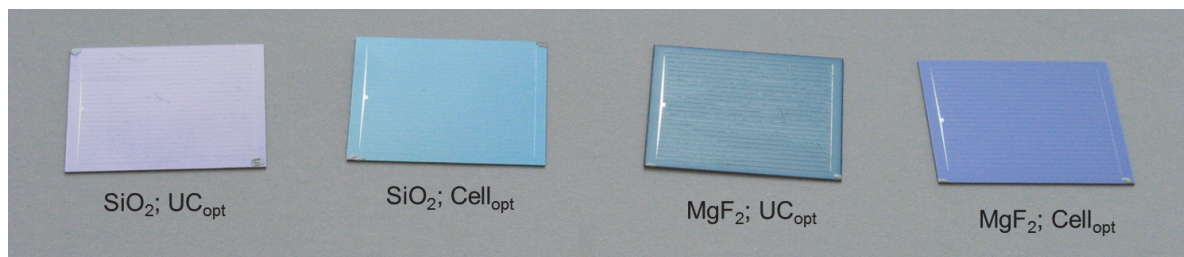


Fig. 8.14: Fabricated bifacial Si solar cells with a size of 2×2 cm². Due to the different thicknesses of the ARCs, the solar cells feature different colorations.

potential difference within wafer and Ag electrode is particularly high, and relatively thick Ag layer growth can be observed. In order to decrease this effect and to compensate thickness inhomogeneities, the wafers were contacted at the opposite side after half of the deposition time. However, the effect could be minimized, but not avoided. The solar cells with local BSF were most affected, leading to average plating thicknesses of $15 \mu\text{m}$ with a large standard deviation of $9 \mu\text{m}$. The solar cells featuring a surface-area covering BSF were less affected, due to the enhanced lateral conductivity of the phosphor doping at the rear side, This lead to an average plating thickness of $(12 \pm 5) \mu\text{m}$. Reduced electro-plating results into areas featuring too thin contact fingers, which causes a large lateral series resistance. A too thick Ag layer may cause adhesion problems of the metal finger and the Si bulk material, which might lead partially to a detachment of the finger grid from the wafer and consequently to a larger series resistance.

8.3.2 Measurement results

Optical and electrical characterization has been carried out. It was of special interest, how the variations of the anti-reflection coating parameters (see Tab. 8.4) and the different BSF configurations affect the electrical solar cell parameters. The measurement results are summarized in Fig. 8.15. Of each variation four to eleven solar cells were available for statistical analysis. The numbers at the top of the graphs indicate how many solar cells were analyzed in the specific variation. These numbers differ due to wafer breakage during the solar cell production. The average values, the maximum values and the standard deviations for each variation are shown.

The tendencies, whether the ARCs are optimized regarding high upconversion (UC_{opt}) or high solar cell efficiency ($Cell_{\text{opt}}$), are directly reflected in the results of j_{sc} (see Fig. 8.15). As discussed in Chap. 8.2, the $Cell_{\text{opt}}$ optimized solar cells featuring thinner ARCs result in significantly higher j_{sc} values, than the UC_{opt} optimized solar cells. These results are also reflected in the maximum efficiencies for the solar cells with full surface-area covering BSFs. Unfortunately, all $Cell_{\text{opt}}$ optimized solar cells featuring local BSFs broke during the processing and, thus, are not available for comparison. Due to a relatively high standard deviation of the different variations, a benefit of the MgF_2 ARC with $n_{\text{MgF}_2} = 1.40$ versus SiO_2 with $n_{\text{SiO}_2} = 1.48$ could not be observed from the data. However, as the optimum refractive index n_{opt} between the ARC- SiN_x layer ($n_{\text{ARC-SiN}_x} = 2.0$) and air ($n_{\text{air}} = 1.0$) is $n_{\text{opt}} = 1.41$, the differences should have been relatively small anyway (see Fig. 8.6).

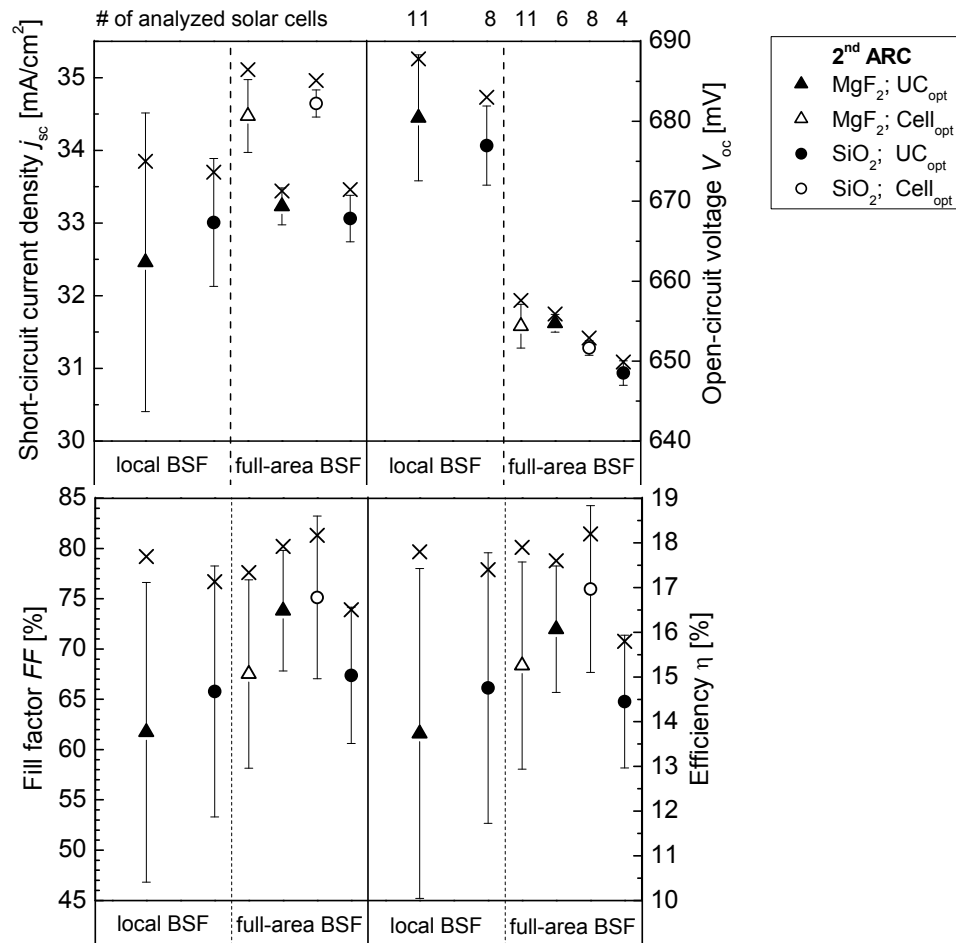


Fig. 8.15: Overview of the measured solar cell parameters. The solar cells vary in material and thickness of the front side ARCs. Furthermore, cells with local and full-area BSF were produced. The $Cell_{opt}$ solar cells featuring local BSFs failed during production. Shown are the arithmetic means, the standard deviations, and the highest achieved value (indicated by a cross), respectively.

Remarkably higher error bars for solar cell results with local BSF can be observed (see Fig. 8.15), in comparison to the results of the cells featuring full-area BSFs. Furthermore, the significantly reduced FF s, reflected by the average values, are an indication for increased resistance losses. This interpretation is backed by the finding that overall reduced voltages were observed for the affected solar cells in the IV characteristics, as exemplarily shown in Fig. 8.16. Here, the solar cell with (i) best, (ii) an average and (iii) worst efficiency is shown. The tendency of the IV curves indicates a problem consisting of increased series resistance losses [81]. Possible reasons are that the openings for the local P diffusion were not etched properly, leading to undiffused areas below the contacts and, thus, a poor contact formation. Another possible source of error is a mismatch of at least $15\ \mu\text{m}$ between contact grid and the locally doped regions, leading to the same consequence of a poor contact formation.

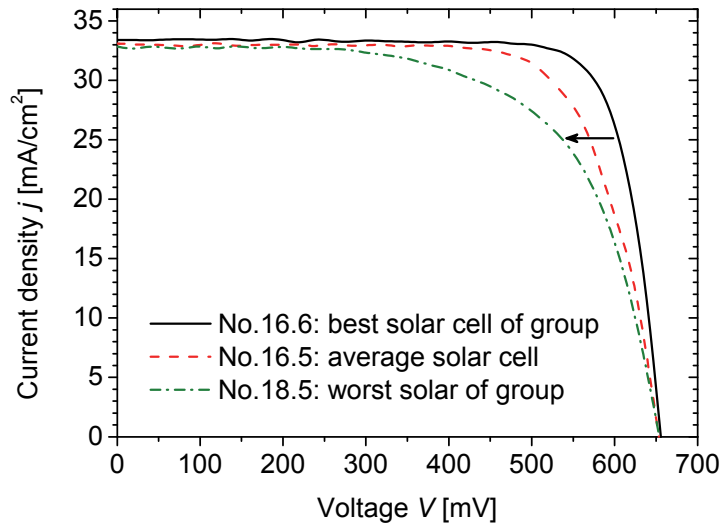


Fig. 8.16: *IV curves of solar cells featuring an MgF_2 front side ARC and local BSF. The result of the solar cell with (i) best, (ii) an average and (iii) worst efficiency are shown. The tendency of the IV curves indicates a series resistance problem [81].*

As mentioned in Chap. 8.3.1, too less or too thick electro-plated finger areas might lead to series resistance problems as well.

Regardless of the series resistance losses, the solar cells with local BSF achieve much higher V_{oc} values. The maximum values of comparable solar cells with local BSFs are about 30 mV higher than for solar cells featuring full-area BSFs. This is in agreement with experimental data of Al_2O_3 passivated surfaces featuring high phosphorus doping concentrations at the surface, which yield relatively high dark saturation current densities [230]. In the case of low phosphorus doping concentrations below the Al_2O_3 layer, very low recombination rates can be achieved.

Numerical simulations of the structure yield as well a similar difference in V_{oc} of about 30 mV. Thereby, a surface recombination velocity of $S_0 = 10$ cm/s was assumed for the passivated rear side of the solar cell with local BSFs. For the solar cell with full-area BSF, $S_0 = 5 \times 10^3$ cm/s is taken for the nitride passivated surface, according to [99]. Therefore, the use of local BSFs might be the most promising, but also more fragile approach, in which more care has to be taken during processing.

8.4 Measurements of bifacial solar cells with upconverter

8.4.1 Method to determine the external quantum efficiency of the system of solar cell and upconverter

In this chapter, the current gain of bifacial solar cells with upconverter applied to the rear side is experimentally determined. The solar cell upconverter system is illuminated by an infrared laser. For this purpose, a Santec Laser ECL-210 was used,

providing monochromatic light with wavelengths in the range of 1430 to 1530 nm. During the work on this paper, however, stable operation of the laser could only be achieved in the wavelength range up to 1515 nm. The output power can be varied continuously up to 10 mW. More details on the used setup and the measurement method can be found in [206, 222]. The short-circuit current density j_{sc} of the solar cell measured under illumination with the laser consists of upconverted laser light as well as parasitic scattered light. Therefore, the laser beam is modulated by a chopper with frequency ν before striking the solar cell. The signal S_{sc} , measured by a lock-in amplifier, is proportional to the fraction of j_{sc} that is induced by the upconverted laser light. In order to deduce from S_{sc} on the EQE of the entire system of Si solar cell and upconverter, a reference cell measurement $S_{sc,ref}$ is performed under the same illumination conditions. The EQE_{ref} of the germanium reference solar cell is known with an uncertainty of $\Delta\text{EQE} = 1\%$ absolute from measurements with another calibrated setup. The EQE of interest of the Si solar cell with applied upconverter can therefore be calculated by [206]:

$$\text{EQE}(\lambda, I) = \text{EQE}_{ref}(\lambda) \frac{j_{sc,UC}(\lambda, I)}{j_{sc,ref}(\lambda, I)} = \text{EQE}_{ref}(\lambda) \frac{\chi \cdot S_{sc,UC}(\lambda, I)}{\chi \cdot S_{sc,ref}(\lambda, I)} \quad (8.10)$$

Under the same illumination conditions, the proportionality constant χ , linking the measurement signal and j_{sc} , is the same for both measurements. Therefore the EQE can be directly determined by the ratio of the signals. As upconversion is a non-linear process, the EQE is not only dependent on λ , but also on the illumination irradiance I of the laser.

Fig. 8.17 shows the dependence of the EQE on the excitation wavelength for an irradiance of 880 Wm^{-2} for the combination of the upconverter with the solar cell 16.6, featuring full-area BSF, MgF_2 as uppermost ARC at the front side (UC_{opt}). As already mentioned, for the investigated wavelength region, accessible during the experiments, the highest integrated quantum yield of $(2.8 \pm 0.2)\%$ was observed at an excitation wavelength of 1508 nm. The local maximum at this wavelength reaches about 90% of the overall maximum, which would be reached at an excitation wavelength of $\lambda = 1523 \text{ nm}$ [206]. At the used wavelength $\lambda = 1508 \text{ nm}$ of the laser, the reference cell has an $\text{EQE}_{ref} = (82 \pm 1)\%$. The irradiance I of the excitation could be determined based on the measured current J_{ref} of the reference solar cell via

$$I = \frac{J_{ref}}{q \cdot \text{EQE}_{ref} \cdot A_{laser}} \cdot \frac{hc}{1508 \text{ nm}} \quad (8.11)$$

with $A_{laser} = (3.8 \pm 0.3) \text{ mm}^2$ being the solar cell area illuminated by the laser beam.

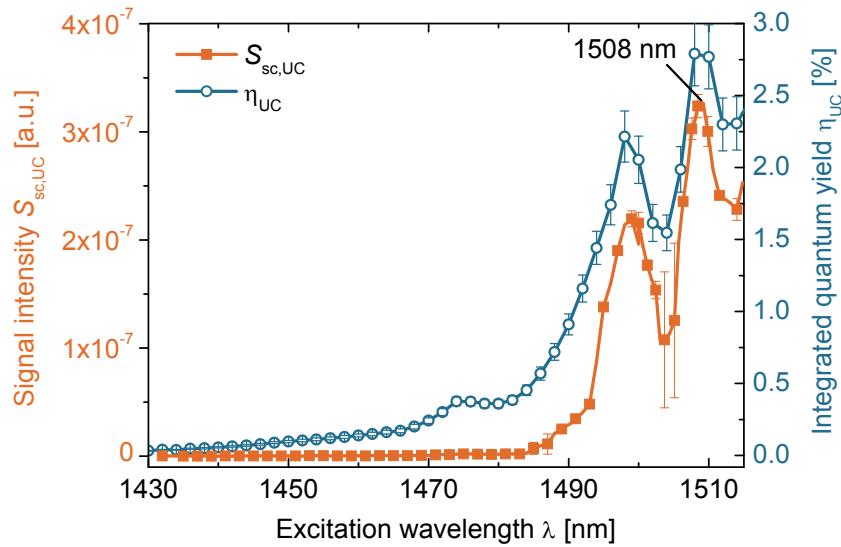


Fig. 8.17: Measured signal intensity $S_{sc,UC}$ of a bifacial solar cell with upconverter, dependent on the excitation wavelength. The signal is proportional to the quantum yield η_{UC} of the upconverter, which is plotted for comparison [206, 222].

8.4.2 Used upconverter samples and optical coupling with solar cell

As an upconverter material $\beta\text{-NaY}_{0.8}\text{Er}_{0.2}\text{F}_4$ has been used. This upconverter was produced by Dr. K.W. Krämer at the University of Bern. $\beta\text{-NaY}_{0.8}\text{Er}_{0.2}\text{F}_4$ is a microcrystalline powder. For the application of the upconverter to the solar cell, a more solid form is required. Therefore, the $\beta\text{-NaY}_{0.8}\text{Er}_{0.2}\text{F}_4$ powder was embedded in the polymer perfluorocyclobutyl (PFCB). This work was carried out by Aruna Ivaturi in the group of Prof. Dr. B.S. Richards at the Heriot-Watt University in Edinburgh. For the measurements, the bifacial solar cells were mounted on a copper frame, which is set on top of a PTFE chuck, as can be seen in Fig. 8.18. The embedded upconverter was optically coupled to the solar cell by an index matching liquid (IML) and sticks to the solar cell surface by adhesion. In order to match the refractive index of the

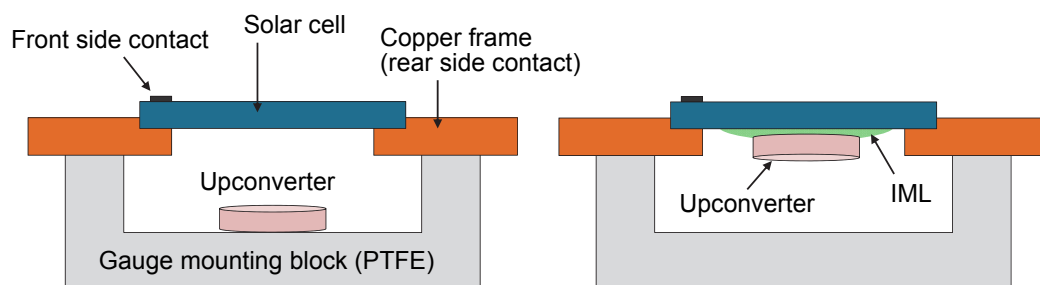


Fig. 8.18: Schematic of the measurement chuck used for upconversion measurements. The upconverter was placed on the ground of the measurement block (left) or coupled directly to the solar cell (right) via adhesion by an index matching liquid (IML), featuring with $n = 1.52$ the same refractive index as the upconverter.

upconverter ($n = 1.5$) by the IML, the “immersion oil Type 300” from Cargille Laboratories featuring a refractive index of $n = 1.52$ and a high viscosity has been used.

For testing, if the optical coupling via the IML increases significantly the signal intensity, the EQE of two different solar cells (15.7 and 9.4) have been determined with the two measurement setups shown in Fig. 8.18, respectively. Solar cell 15.7 features a full-area BSF (Cell_{opt}) and 9.4 a local BSF (UC_{opt}). The results are shown in Fig. 8.19, indicating a significant increase of the quantum efficiency of the system with optical coupling by the IML. By the IML, reflection losses between the solar cell and the upconverter are significantly minimized. This effect can be estimated by the Fresnel equations. Due to a refractive index of 1.52 instead of one behind the solar cell, the transmission of the solar cell is increased by about 6%, since the refractive index contrast to the Si is reduced.

Moreover, all transmitted photons impinge directly on the upconverter, without being reflected at the surface of the upconverter. Thereby, the irradiance reaching the upconverter is approximately 10% higher than without IML. Due to the higher irradiance, the quantum yield of the upconverter increases by about 10%, so in total about 22% more upconverted photons are available. Furthermore, reflection losses occur at the rear side of the solar cell, whereby in total about 35% more upconverted photons can be used by the solar cell than in the setup without IML. In this estimation, only the difference of the refractive indices of IML and air were taken into account.

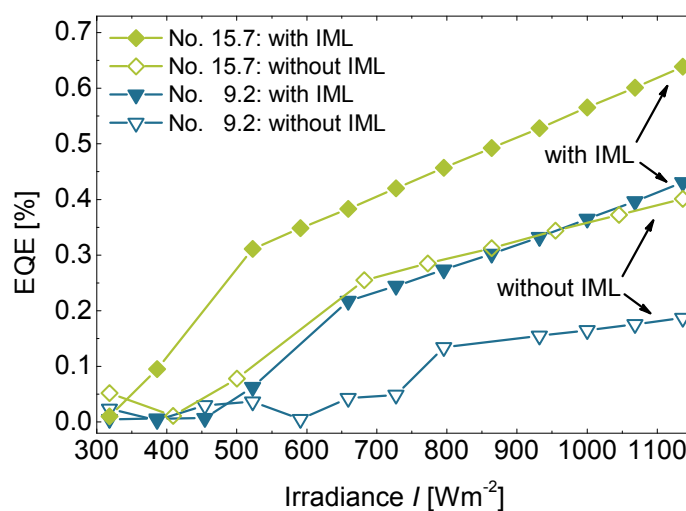


Fig. 8.19: External quantum efficiency of the solar cells 15.7 and 9.4, dependent on the irradiance I of the laser at $\lambda = 1508$ nm. The upconverter is placed with or without IML behind the solar cell, according to Fig. 8.18. In the setup with IML (Fig. 8.18, right), the EQE is significantly increased, due to an increased absorption in the upconverter and an enhanced coupling of the re-emitted light into the solar cell.

Without direct attaching of the upconverter with the IML on the solar cell a gap between solar cell and upconverter may cause losses. For example, only a fraction of the upconverted light directly enters the solar cell, the rest strikes the inner walls of the measuring block, which have a reflectivity of $> 95\%$. Because of the strong positive effect of the IML, all subsequent measurements are performed with IML.

8.4.3 Results

The measurements of the EQE in dependence on the excitation irradiance were carried out for several solar cells. For this purpose the solar cells featuring the highest efficiencies of each variation were chosen (see Fig. 8.15). In all experiments, the same upconverter sample was used. The results of these measurements are summarized in Fig. 8.20. Such measurements were previously performed by Fischer *et al.* [206], in which a back-contact back-junction (BCBJ) solar cell was used as bifacial solar cell [231]. The best previously achieved measurement result is plotted in Fig. 8.20 for comparison. With respect to the low irradiance, at the time being these results had featured the highest EQE for the system solar cell and upconverter, reported in literature [206]. The excitation wavelength of the laser used in these experiments had been $\lambda = 1522$ nm.

It can be seen that due to the non-linear behavior, the EQE of the system consisting of solar cell and upconverter increases with the irradiance I . For some solar cells, the achieved EQE values are significantly higher than those reported in literature. Significant differences are visible for the different types of solar cells. As the same upconverter sample was used, the observed differences in the EQE can be attributed to the properties of the corresponding solar cells. From theoretical considerations, we would expect that the EQE is mainly determined by the transmission of the solar cell at the excitation wavelength of $\lambda = 1508$ nm, and to a lower extent by the EQE of the rear side of the solar cell in the emission region of the upconverter around 980 nm. Therefore the different configurations for the ARC coatings should have the strongest impact.

However, the biggest differences can be found between the EQE of the systems featuring solar cells with local BSF on the one hand, and full-area BSF on the other hand. As can be seen in Tab. 8.5, neither the transmissions nor the EQEs of the solar cells featuring local BSF is lower than for solar cells with full-area BSF, respectively. However, the EQEs given in Tab. 8.5 are determined with the use of bias light with an intensity of one sun. The irradiation only by the upconverted light is in the order of magnitude of less than 0.01 suns. Moreover, only a small area of the solar cell, a few

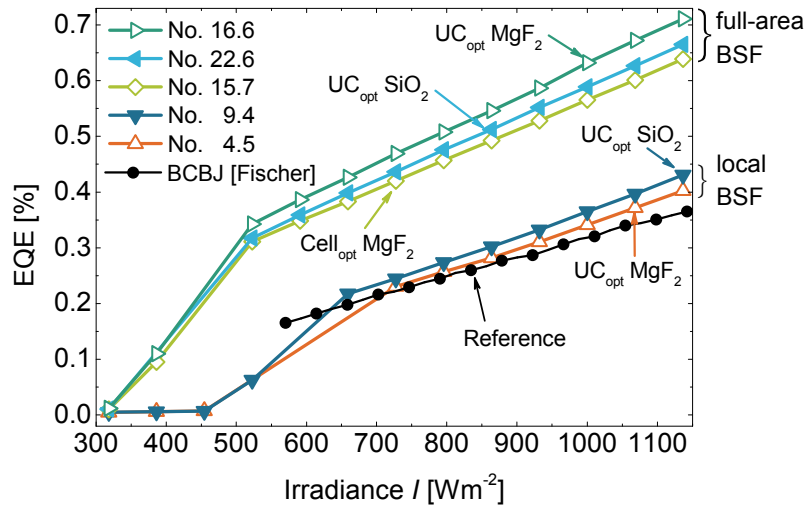


Fig. 8.20: External quantum efficiency of different solar cells with upconverter, dependent on the illumination intensity I of the laser at $\lambda = 1508$ nm. As reference, the EQE of a back-contact back-junction (BCBJ) solar cell with upconverter is plotted [206].

mm^2 , is illuminated. At these low irradiation intensities, the recombination at the rear side of the solar cells with local BSF increases significantly, caused by a reduced surface passivation of the Si surface with Al_2O_3 due to the low minority carrier density at the rear side of the solar cells [110, 232]. The good surface passivation properties of Al_2O_3 on lowly doped n -type Si surfaces is based mainly on the electrical shielding of electrons from the surface by the negative surface charge of Al_2O_3 [110]. Thereby, an inversion layer exists at the surface, in which the electrons are minority charge carriers. The effective surface recombination velocity S_{eff} of a passivation with inversion layer is strongly injection dependent. For very low excess charge carrier densities Δn a strong increase in S_{eff} is observed, which is attributed to increased volume recombination in the depletion region [110, 232]. This effect has been investigated in detail for p -type Si surfaces with SiO_2 [233] or SiN_x passivation [234] and can also be observed on Al_2O_3 -passivated n -type Si surfaces [110, 235]. Thus, for a measurement of the EQE of the system solar cell/upconverter with an additional bias illumination, results for the system with and without full-area BSF, respectively, should be in the same order of magnitude. In solar cells featuring full-area BSF no inversion layer exists, due to the much higher surface doping concentration at the rear side. Thus, the injection dependence of the carrier density is significantly reduced and does not occur in latter observed manner.

Apart from the strong effect of the back surface field, it can be seen in Fig. 8.20 that the solar cells having ARC coatings following the UC_{opt} scheme tend to lead to a higher EQE than the solar cell featuring the Cell_{opt} scheme. The sequential order

between the UC_{opt} ARC with MgF₂ and SiO₂ is, however, different for the solar cells with full-area and local BSF, respectively.

In Tab. 8.5 all measured solar cells are listed with the corresponding measured EQE of the rear side of the cells and the transmissions, respectively. From these data, it can be seen that differences in EQE can be attributed, apart from the effect of the BSF, to the different transmissions of the solar cells. A comparison of the results, shown in Fig. 8.20, and the measured transmissions (see Tab. 8.5) shows an explicit correlation of the data, featuring a stronger effect on the behavior of the system, than a comparison of the EQEs of the rear sides of the solar cells and of the entire system. The variations of the transmission are caused on the one hand by the different thicknesses of the ARCs for UC_{opt} and Cell_{opt}, and on the other hand by different shading losses caused by the contact fingers. Simulations show that due to the varying plating thicknesses, the shading losses of the solar cells may vary by about 2%. The material of the uppermost front anti-reflection layer, being SiO₂ or MgF₂, respectively, has only a minor influence on the transmission of the solar cells, which is negligible compared to the effect of the contact grid.

In conclusion, for a high current gain of the Si solar cells by the upconversion, the transmission of the solar cells should be optimized in the first place - the efficiency of the solar cell itself is secondary. Therefore, the high transmission of the planar Si solar cells with optimized ARCs, produced in this work, is the main reason why higher EQE

Tab. 8.5: Overview of the bifacial solar cells, on which the EQE measurements were performed, shown in Fig. 8.20. Given are the EQEs of the rear sides of the solar cells at $\lambda = 980$ nm as well as its transmissions at an excitation wavelength of $\lambda = 1508$ nm.

No.	Identifier	BSF	2 nd front ARC	Rear side EQE at $\lambda=980$ nm	Transmission at $\lambda=1508$ nm
BCBJ	Data from [30]			~ 76%	(40 ± 5)%*
16.6	UC _{opt}	full-area	MgF ₂	76.8%	84.2%
22.6	UC _{opt}	full-area	SiO ₂	78.2%	82.1%
15.7	Cell _{opt}	full-area	MgF ₂	76.9%	80.8%
9.4	UC _{opt}	local	SiO ₂	79.4%	86.8%
4.5	UC _{opt}	local	MgF ₂	67.7%	84.8%

* Transmission at $\lambda=1522$ nm

values were achieved than in [206], although the back-contact back-junction Si solar cell used in [206] was illuminated with a more suitable wavelength, achieving a higher quantum yield of the upconverter.

8.5 Conclusions

In this chapter, bifacial monocrystalline Si solar cells have been optimized for upconversion applications via numerical simulations. An upconverter absorbs two photons with energies $E < E_g$ smaller than the band gap energy of silicon, and convert them into a photon with $E > E_g$. These upconverted photons can be subsequently utilized by the solar cell. Therefore, the simulation setup had to be extended in order to account for the quantum yield of the erbium based upconversion medium β -NaY_{0.8}Er_{0.2}F₄, which is placed at the rear side of the solar cell. Solar cells with both-sided textured surfaces feature best properties in terms of cell efficiency and transmission in the long-wavelength range $\lambda > 1200$ nm in favor of an efficient upconversion process. Planar solar cells feature even higher transmission potential in the long-wavelength range, but significantly lower solar cell efficiencies, as the light trapping capabilities are reduced substantially. One-sided textured solar cells feature high efficiencies, but relatively low transmission for photons with $E > E_g$, due to an enhanced internal reflection (see Fig. 3.8), which make them inappropriate for upconversion applications.

Therefore, the anti-reflection layer of both-sided and planar bifacial Si solar cells have been optimized via simulations. For the rear side of the solar cells, a single-layer ARC consisting of a 120 nm thick TiO₂ or SiN_x layer has been identified as optimum, independent of the surface morphology. For the optimization of the front side ARC layer system, a compromise must be found between the optimization of high cell efficiency (Cell_{opt}) and the optimization of a large upconversion effect (UC_{opt}), tending to thicker layers. Suitable coating systems are two-layer anti-reflection systems of SiN_x or TiO₂, followed by SiO₂ or MgF₂ as a second anti-reflective layer.

Based on simulations, an assessment of the potentially achievable efficiency enhancement $\Delta\eta$ due to upconversion has been set up. For this purpose a bifacial solar cell with and without upconverter was simulated. In the simulation of the upconversion system it has been assumed that behind the solar cell a fluorescence concentrator is attached, which concentrates the photons transmitted by the solar cell spectrally and spatially on the upconverter, according to the concept shown in Fig. 8.3. Thus, depending on the external concentration of the incident light illuminating the solar cell, an absolute efficiency increase in the order of $\Delta\eta = 0.1\%$ to 0.4% is possible.

Increasing the quantum yield of the upconverter is topic of actual research. By more efficient upconverter media, the efficiency could be further increased.

In order to achieve well defined surfaces for the further development of the upconverter system, planar bifacial Si solar cells were produced and characterized, which differ by the used ARCs, and the rear diffusion profiles (local or full-area BSF). With local BSFs, potentially higher efficiencies might be achievable, but inversion layer effects caused too low charge carrier densities for effective passivation properties at the rear side of the solar cells, higher EQE values could be measured with solar cells featuring full-area BSFs (see Fig. 8.20). However, due to technological challenges in the fabrication of the bifacial solar cell structure, especially the results of the solar cells featuring local BSFs scatter significantly. Here e.g. problems with the adhesion of the contact fingers caused substantial series resistance losses.

The current benefit caused by the upconversion could be confirmed experimentally by measuring the EQE in the infrared spectral region around 1500 nm of different bifacial Si solar cells with applied upconverter. Here, the solar cell was illuminated with an infrared laser, and the transmitted laser light from the solar cell is converted by the upconverter into short-wavelength light, which can be absorbed by the solar cell. These measured EQEs are shown in Fig. 8.20. The EQE depends primarily on the transmission probabilities of the respective solar cell. With the planar solar cells produced in this work, significantly higher EQE values could be measured in comparison to previously performed measurements with back-contact back-junction Si solar cells, published in [206]. With respect to the used illumination intensity, the presented measurements constitute the highest EQE values for a system consisting of Si solar cell and upconverter, reported in literature so far.

9 Conclusions and outlook

The focus of the present work is the *analysis and simulation of crystalline silicon solar cells*.

The rapid development of novel solar cell concepts requires an accurate and reliable modeling to obtain a better physical understanding of the solar cells, as well as to reduce the number of time consuming and expensive experimental investigations. In order to get a rough overview about industrially relevant silicon solar cell concepts in production and their efficiency potential, an overview over different solar cell architectures is presented in the introduction. Thereby, the loss mechanisms of each solar cell concept are analyzed to be aware of their main losses in order to identify the certain efficiency restrictions.

The necessary theoretical background of solar cell physics and its methodical approach to the simulation of crystalline solar cells are introduced in the following two chapters and illustrated by practical examples.

For a better physical understanding and a higher accuracy of the numerical simulations of silicon solar cells, a further improvement and development of physical models and their parameterization is essential. In this work, the exact modeling of highly doped layers turned out to be a key task. Thus, the effect of *free carrier absorption* (FCA) is discussed in detail, a parasitic absorption process which might reduce significantly the amount of photons, potentially generating electron-hole pairs in highly doped silicon. Existing parameterizations given in literature are mostly set up on the base of data in the mid-wavelength infrared. In this work, these models are evaluated in the wavelength range $\lambda = 1.0 - 2.0 \mu\text{m}$, including the relevant range for silicon solar cells. Therefore, test samples have been produced featuring different boron and phosphorus doped diffusion profiles, covering a broad range of sheet resistances, and the corresponding reflection curves have been measured. Numerical device simulations have been calibrated to reference samples, showing very good accordance to the measured results. The test structures have been simulated, including the different FCA parameterizations given in literature. Thereby, significant deviations within the results of the existing FCA models for $\lambda = 1.0 - 2.0 \mu\text{m}$ could be observed. By a comparison of simulated results and experimental data it turned out that most existing models over- or underestimated the effect of FCA significantly. Therefore, new parameters are presented on base of an existing mathematical approach, which is easy to implement in numerical simulations in order to enhance the quantification of photogeneration losses.

On base of these new parameters, FCA losses are quantified for phosphorus and boron doped silicon.

Strong aluminum doped layers play currently an important role in industrially produced solar cells, but as well especially as emitter in new n -type silicon solar cells. An advanced method for precise modeling of *highly aluminum-doped p^+ silicon* ($\text{Al-}p^+$) is presented, as numerical device simulations of silicon regions with aluminum doping have been a challenging task so far. A recently published minority carrier lifetime parameterization as a function of the aluminum acceptor density N_A , reported for simulation purposes, turned out to be not suitable to describe $\text{Al-}p^+$ regions in good accordance with experimental data, such as the saturation current density j_0 or the open-circuit voltage V_{oc} of solar cells. Thus, the effects of different recombination losses on the saturation current densities of $\text{Al-}p^+$ regions, the influence of lateral profile inhomogeneities, and incomplete ionization of the aluminum acceptors have been analyzed in detail. The simulation results have been validated within a broad range of experimental data. As a result, it could be demonstrated that defect recombination in $\text{Al-}p^+$ regions seems to be the major loss mechanism. Depth inhomogeneities especially influence thin profiles with high recombination active surfaces, but in most cases these can be neglected in device simulations. However, due to a much higher ionization energy compared to other acceptor atoms, as for example boron, incomplete ionization has an explicit impact on the saturation current densities, due to a significant decrease of the electrically active aluminum concentration. Taking this effect into account, excellent agreement of measured and calculated $j_{0,\text{Al}}$ values has been achieved. The average Shockley-Read-Hall (SRH) lifetime in the $\text{Al-}p^+$ region has been determined to $\tau_{\text{Al-}p^+} = 270$ ns. Furthermore, measured data of an n -type silicon solar cell, where the $\text{Al-}p^+$ region acts as p^+ rear emitter, have been compared to simulations including the presented model, demonstrating very good agreement. From that it can be concluded that SRH defect recombination in combination with incomplete ionization has to be accounted for in accurate modeling of highly Al-doped Si.

Under the use of this method for precise modeling of $\text{Al-}p^+$ regions, a detailed analysis on the optimization of *n^+np^+ silicon solar cells with aluminum-alloyed rear p^+ emitter* for industrial applications is presented. By means of 2D and 3D numerical simulations, the potential and the limiting factors of this solar cell concept are identified, by sequentially focusing on effects of the front side, the bulk material and the rear side. For n^+np^+ solar cells with non-passivated full-area $\text{Al-}p^+$ rear emitter, conversion efficiencies of up to 20% are realistic. Additionally, an effective surface passivation of the $\text{Al-}p^+$ emitter should increase the efficiency by 1% absolute, leading to an

efficiency potential close to 21% for this solar cell concept. Presently, effort is spent on the realization of $< 100 \mu\text{m}$ thick n^+np^+ solar cells with an efficiency of $> 20\%$ in order to drive down production costs. To achieve this goal, diffractive rear side gratings might be necessary in order to enhance the path length of the light within the solar cell and, thus, to enhance the absorption probability of such thin structures.

Large area rear side passivated silicon solar cells are currently one of the most interesting structures that are in the process of transition to industrial production. As a high-efficiency approach, lateral conductance effects of *locally contacted rear surface passivated p-Si solar cells* are investigated. The optimum rear contact distances L_P for different solar cell thicknesses and a broad range of nominal bulk resistivities ρ_0 are calculated. These variations are presented for high-quality float-zone (FZ) and Czochralski (Cz)-grown p -type silicon material with a very low and a very high interstitial oxygen content in the bulk material, which detrimentally influences the effective carrier lifetimes τ_{eff} , not shown before in this extent. A characteristic current density-voltage behavior for the considered FZ and Cz bulk materials for different base resistivities ρ_0 ($L_P = 1000 \mu\text{m}$) could be observed via numerical 3D simulation, consistent to experimentally determined results. For better understanding, the FF behavior is compared to numerically determined R_S losses under mpp conditions, occurring in the standard domain. It turned out that in high ohmic base material with high rear contact distances, high injection effects in combination with local bulk effects need to be considered in order to understand the effects occurring in the bulk material. Analytical modeling based on a comprehensive model published in literature shows good agreement with numerical modeling in low-level injection conditions. Towards high-level injection conditions, as arising e.g. in highly resistive bulk material with $\rho_0 > 2 \Omega\text{cm}$, results deviate significantly and injection dependent modeling is required. Thus, high-level injection corrections for the analytical calculations are presented, leading to an enhanced prediction of the optimum rear contact distance $L_{P,\text{opt}}$ in comparison to numerical simulation results. However, the implemented injection dependence in the analytical model should be further improved in subsequent work, as it is essential for the calculation of solar cells with strongly injection dependent recombination as e.g. in compensated material or highly resistive material featuring high bulk carrier lifetimes as arising in n -type Si bulk material.

As a future orientated solar cell concept, *bifacial monocrystalline Si solar cells* have been optimized for *upconversion applications* via numerical simulations. An upconverter absorbs two photons with energies $E < E_g$ smaller than the band gap energy of silicon, and is able to convert them into a photon with $E > E_g$, which is coupled back into the solar cell. Therefore, the simulation setup had to be extended in

order to account for the quantum yield of the erbium based upconversion medium β -NaY_{0.8}Er_{0.2}F₄, which is placed at the rear side of the solar cell. One-sided textured bifacial silicon solar cells turned out to be not suitable for upconversion applications, as they feature too much internal reflection and, thus, too less transmission in the long-wavelength range. Both-sided and planar bifacial solar cells feature significantly enhanced transmission properties in the long-wavelength range. Thus, for both solar cell structures, the anti-reflection coatings (ARC) have been optimized via simulations. For the rear side of the solar cells, a single-layer ARC consisting of a 120 nm thick TiO₂ or SiN_x layer has been identified as optimum, independent of the surface morphology. For the optimization of the front side ARC layer system, a compromise must be found between the optimization of high solar cell efficiency and the optimization of a large upconversion effect, tending to thicker layers. Suitable coating systems are two-layer anti-reflection systems of SiN_x or TiO₂, followed by SiO₂ or MgF₂ as a second anti-reflective layer. Based on simulations, an assessment of the potentially achievable efficiency enhancement $\Delta\eta$ due to upconversion has been set up. For this purpose a bifacial solar cell with and without upconverter has been simulated. Depending on the external concentration of the incident light illuminating the solar cell, a realistic absolute efficiency increase in the order of $\Delta\eta = 0.1\%$ to 0.4% should be possible with the used erbium based upconverter. Planar bifacial Si solar cells have been produced and characterized. The current benefit caused by the upconversion could be confirmed experimentally by measuring the EQE in the infrared of different bifacial silicon solar cells with applied upconverter. With the planar solar cells produced in this work, significantly higher EQE values could be measured in comparison to previously performed measurements with back-contact back-junction silicon solar cells. With respect to the used illumination intensity, latter measurements highlighted so far the highest EQE values for a system consisting of silicon solar cell and upconverter, reported in literature. In subsequent work, both-sided textured silicon solar cells for upconversion applications should be produced, featuring the determined optimized ARC layers, as they hold a much higher solar cell efficiency potential in comparison to planar solar cells. Due to further enhanced upconverter media, which are subject of current research, the system efficiency could be further increased significantly, leading to $\Delta\eta > 0.4\%$.

10 Bibliography

- [1] IPCC, *Fourth Assessment Report: Climate change (AR4)*. Intergovernmental Panel on Climate Change, (2007)
- [2] R. Rohde, R.A. Muller, R. Jacobsen, E. Muller, S. Perlmutter, A. Rosenfeld, J. Wurtele, D. Groom, and C. Wickham, *A new estimate of the average earth surface land temperature spanning 1753 to 2011*, in *The Third Santa Fe Conference on Global and Regional Climate Change* (2012)
- [3] R.A. Muller, J. Curry, D. Groom, R. Jacobsen, S. Perlmutter, R. Rohde, A. Rosenfeld, C. Wickham, and J. Wurtele, *Decadal variations in the global atmospheric land temperatures*. Dept. of Physics, University of California, Berkeley, CA, USA, (2012)
- [4] P.D. Jones and A. Moberg, *Journal of Climate*, **16** (2), 206-23, (2003).
- [5] M.J. Menne and C.N. Williams, *Journal of Climate*, **18** (20), 4271-86, (2005).
- [6] P. Brohan, J.J. Kennedy, I. Harris, S.F.B. Tett, and P.D. Jones, *Journal of Geophysical Research Atmospheres*, **111** (D12), D12106, (2006).
- [7] J. Hansen, R. Ruedy, M. Sato, and K. Lo, *Reviews of Geophysics*, **48** (4), RG4004, (2010).
- [8] I.T.A. Report, *Climate change*. Intergovernmental panel on climate change, (2001)
- [9] H.-J. Schellnhuber, D. Messner, C. Leggewie, R. Leinfelder, N. Nakicenovic, S. Rahmstorf, S. Schlacke, J. Schmid, and R. Schubert, *Kassensturz für den Weltklimavertrag - Der Budgetansatz*. Wissenschaftlicher Beirat der Bundesregierung Globale Umweltveränderungen, Berlin, Germany, (2009)
- [10] H. Graßl, J. Kokott, M. Kulesa, J. Luther, F. Nuscheler, R. Sauerborn, H.-J. Schellnhuber, R. Schubert, and E.-D. Schulze, *Welt im Wandel - Energiewende zur Nachhaltigkeit*. 2003, Berlin: Wissenschaftlicher Beirat der Bundesregierung Globale Umweltveränderungen (WBGU).
- [11] M. Rüdiger, H. Steinkemper, M. Hermle, and S.W. Glunz, *IEEE Journal of Photovoltaics*, DOI: 10.1109/JPHOTOV.2013.2293196, (2013).
- [12] Sentaurus TCAD, *Technology computer aided design (TCAD)*. Synopsys: Zürich, Switzerland)
- [13] R. Brendel, ed. *Thin-Film Crystalline Silicon Solar Cells - Physics and Technology*, WILEY-VCH GmbH & Co. KGaA, Weinheim, (2003)
- [14] P. Löngen, W.C. Sinke, C. Leguijt, A.W. Weeber, P.F.A. Alkemade, and L.A. Verhoef, *Applied Physics Letters*, **65** (22), 2792-4, (1994).

- [15] M. Rauer, C. Schmiga, M. Glatthaar, and S.W. Glunz, *IEEE Journal of Photovoltaics*, **3** (1), 206-11, (2013).
- [16] M. Hörteis, D. Grote, S. Binder, A. Filipovic, D. Schmidt, and S.W. Glunz *Fine line printed and plated contacts on high ohmic emitters enabling 20% cell efficiency*, in *Proceedings of the 34th IEEE Photovoltaic Specialists Conference*, Philadelphia, USA, 2005-10 (2009).
- [17] G. Hahn, *Status of selective emitter technology*, in *Proceedings of the 25th European Photovoltaic Solar Energy Conference and Exhibition*, Valencia, Spain, 1091-6 (2010).
- [18] A. Mohr, P. Engelhart, C. Klenke, S. Wanka, A.A. Stekolnikov, M. Scherff, R. Seguin, S. Tardon, T. Rudolph, M. Hofmann, F. Stenzel, J.Y. Lee, S. Diez, J. Wendt, W. Brendle, S. Schmidt, J.W. Müller, P. Wawer, M. Hofmann, P. Saint-Cast, J. Nekarda, D. Erath, J. Rentsch, and R. Preu, *20%-efficient rear side passivated solar cells in pilot series designed for conventional module assembling*, in *Proceedings of the 26th European Photovoltaic Solar Energy Conference and Exhibition*, Hamburg, Germany, 2150-3 (2011).
- [19] P. Engelhart, D. Manger, B. Klöter, S. Hermann, A.A. Stekolnikov, S. Peters, H.-C. Ploigt, A. Eifler, C. Klenke, A. Mohr, G. Zimmermann, B. Barkenfelt, K. Suva, J. Wendt, T. Kaden, S. Rupp, D. Rychtarik, M. Fischer, and J.W. Müller, *Q.ANTUM - Q-Cells next generation high-power silicon solar cell & module concept*, in *Proceedings of the 26th European Photovoltaic Solar Energy Conference and Exhibition*, Hamburg, Germany, 821-6 (2011).
- [20] B. Sun, J. Sheng, S. Yuan, C. Zhang, Z. Feng, and Q. Huang, *Industrially feasible casting-mono crystalline solar cells with PECVD AlO_x/SiN_x rear passivation stack towards 19.6% efficiency*, in *Proceedings of the 38th IEEE Photovoltaic Specialists Conference*, Austin, Texas, 1125-8 (2012).
- [21] Y. Gassenbauer, K. Ramspeck, B. Bethmann, K. Dressler, J.D. Moschner, M. Fiedler, E. Brouwer, R. DroBler, N. Lenck, F. Heyer, M. Feldhaus, A. Seidl, M. Muller, and A. Metz, *IEEE Journal of Photovoltaics*, **PP** (99), 1-6, (2012).
- [22] K. Bothe, R. Sinton, and J. Schmidt, *Progress in Photovoltaics: Research and Applications*, **13**, 287-96, (2005).
- [23] S.W. Glunz, S. Rein, J.Y. Lee, and W. Warta, *Journal of Applied Physics*, **90** (5), 2397-404, (2001).
- [24] L.J. Geerligs, I.G. Romijn, A.R. Burgers, N. Guillevin, A.W. Weeber, J.H. Bultman, W. Hongfang, L. Fang, Z. Wenchao, L. Gaofei, H. Zhiyan, X. Jingfeng, and A. Vlooswijk, *Progress in low-cost n-type silicon solar cell technology*, in *Proceedings of the 38th IEEE Photovoltaic Specialists Conference*, Austin, Texas, 1701-4 (2012).

- [25] J. Zhao and A. Wang, *Applied Physics Letters*, **88** (24), 242102, (2006).
- [26] V. Mertens, T. Ballmann, J.Y. Lee, M. Junghänel, F. Stenzel, L. Brandt, A. Schulze, P. Engelhart, J.W. Müller, P. Wawer, and K.H. Küsters, *Influence of base resistivity on solar cell parameters of double-side contacted rear junction solar cells*, in *Proceedings of the 2nd International Conference on Crystalline Silicon Photovoltaics*, Leuven, Belgium, 53-8 (2012).
- [27] J. Benick, B. Hoex, M.C.M. van de Sanden, W.M.M. Kessels, O. Schultz, and S.W. Glunz *Applied Physics Letters*, **92** (253504), 253504/1-3, (2008).
- [28] S.W. Glunz, J. Benick, D. Biro, M. Bivour, M. Hermle, D. Pysch, M. Rauer, C. Reichel, A. Richter, M. Rüdiger, C. Schmiga, D. Suwito, A. Wolf, and R. Preu, *n-type silicon - enabling efficiencies > 20% in industrial production*, in *Proceedings of the 35th IEEE Photovoltaic Specialists Conference*, Honolulu, Hawaii, USA, (2010).
- [29] D. Suwito, U. Jäger, J. Benick, S. Janz, M. Hermle, and S.W. Glunz *IEEE Transactions on Electron Devices*, **57** (8), 2032-6, (2010).
- [30] D. De Ceuster, P. Cousins, D. Rose, D. Vicente, P. Tipones, and W. Mulligan, *Low Cost, high volume production of >22% efficiency silicon solar cells*, in *Proceedings of the 22nd European Photovoltaic Solar Energy Conference*, Milan, Italy, 816-9 (2007).
- [31] N. Bateman, P. Sullivan, C. Reichel, J. Benick, and M. Hermle, *High quality ion implanted boron emitters in an interdigitated back contact solar cell with 20% efficiency*, in *Proceedings of the 1st International Conference on Silicon Photovoltaics*, Freiburg, Germany, **8**, 509-14 (2011).
- [32] M. Hermle, J. Benick, N. Bateman, and S.W. Glunz *N-type silicon solar cells with implanted emitter*, in *Proceedings of the 26th European Photovoltaic Solar Energy Conference and Exhibition*, Hamburg, Germany, 875-8 (2011).
- [33] G. Galbiati, V.D. Mihailitchi, R. Roescu, A. Halm, L.J. Koduvelikulathu, R. Kopecek, K. Peter, and J. Libal, *IEEE Journal of Photovoltaics*, **3** (1), 560-5, (2013).
- [34] M. Hermle, F. Granek, O. Schultz-Wittmann, and S.W. Glunz, *Shading effects in back-junction back-contacted silicon solar cells*, in *Proceedings of the 33rd IEEE Photovoltaic Specialists Conference*, San Diego, USA, (2008).
- [35] H. Sakata, Y. Tsunomura, H. inoue, S. Taira, T. Baba, H. Kanno, T. Kinoshita, M. Taguchi, and E. Maruyama, *R&D progress of next-generation very thin HITtm solar cells*, in *Proceedings of the 25th European Photovoltaic Solar Energy Conference and Exhibition*, Valencia, Spain, 1102-5 (2010).
- [36] P.J. Cousins, D.D. Smith, H.-C. Luan, J. Manning, T.D. Dennis, A. Waldhauer, K.E. Wilson, G. Harley, and W.P. Mulligan, *Generation 3: Improved*

- performance at lower cost*, in *Proceedings of the 35th IEEE Photovoltaic Specialists Conference*, Honolulu, Hawaii USA, 000275 - 8 (2010).
- [37] D.D. Smith, P.J. Cousins, A. Masad, A. Waldhauer, S. Westerberg, M. Johnson, T. Xiuwen, T. Dennis, G. Harley, G. Solomon, R. Seung, M. Shepherd, S. Harrington, M. Defensor, A. Leygo, P. Tomada, W. Junbo, T. Pass, L. Ann, L. Smith, N. Bergstrom, C. Nicdao, P. Tipones, and D. Vicente, *Generation III high efficiency lower cost technology: Transition to full scale manufacturing*, in *Proceedings of the 38th IEEE Photovoltaic Specialists Conference*, Austin, Texas, 1594-7 (2012).
- [38] S. Janz, P. Voisin, D. Suwito, M. Peters, M. Hermle, and S.W. Glunz, *Photonic crystals as rear-side diffusers and reflectors for high efficiency silicon solar cells*, in *Proceedings of the 24th European Photovoltaic Solar Energy Conference*, Hamburg, Germany, 1529-33 (2009).
- [39] P. Voisin, M. Peters, H. Hauser, C. Helgert, E.-B. Kley, T. Pertsch, B. Bläsi, M. Hermle, and S.W. Glunz *Nanostructured back side silicon solar cells*, in *Proceedings of the 24th European Photovoltaic Solar Energy Conference*, Hamburg, Germany, 1997-2000 (2009).
- [40] R.M. Swanson, *Approaching the 29% limit efficiency of silicon solar cells*, in *Proceedings of the 31st IEEE Photovoltaic Specialists Conference*, Orlando, USA, 889-94 (2005).
- [41] S.M. Sze, *Semiconductor devices, physics and technology*, ed. M.H. AT&T Bell Laboratories, New Jersey. 1985, New York, Chichester, Brisbane, Toronto, Singapore: John Wiley & Sons.
- [42] S. Rein, *Lifetime spectroscopy: a method of defect characterization in silicon for photovoltaic applications*. 1st ed, ed. R. Hull, et al. 2005, Berlin Heidelberg: Springer.
- [43] P. Würfel, *Physics of Solar Cells - From principles to new concepts*. 2005, Weinheim: Wiley-Vch Verlag GmbH & Co KGaA.
- [44] S.M. Sze, *Physics of semiconductor devices*. 2nd ed. 1981, New York: John Wiley & Sons, Inc.
- [45] J.R. Chelikowsky and M.L. Cohen, *Physical Review B*, **14** (2), 556-82, (1976).
- [46] M.A. Green, *J. Appl. Phys.*, **67** (6), 2944-54, (1990).
- [47] A.B. Sproul and M.A. Green, *Journal of Applied Physics*, **70** (2), 846-54, (1991).
- [48] P.P. Altermatt, A. Schenk, F. Geelhaar, and G. Heiser, *Journal of Applied Physics*, **93** (3), 1598-604, (2003).
- [49] A. Schenk, *Journal of Applied Physics*, **84** (7), 3684-95, (1998).

- [50] P. Würfel, S. Finkbeiner, and E. Daub, *Applied Physics A (Materials Science Processing)*, **60**, 67-70, (1995).
- [51] P. Würfel, *Physics of solar cells - from basic principles to advanced concepts*. 2nd ed. 2009, Weinheim: Wiley-VCH Verlag GmbH & Co. KGaA.
- [52] T. Trupke, M.A. Green, P. Würfel, P.P. Altermatt, A. Wang, J. Zhao, and R. Corkish, *Journal of Applied Physics*, **94** (8), 4930, (2003).
- [53] P.P. Altermatt, F. Geelhaar, T. Trupke, X. Dai, A. Neisser, and E. Daub, *Applied Physics Letters*, **88**, 261901-1-3, (2006).
- [54] R. Häcker and A. Hangleiter, *Journal of Applied Physics*, **75** (11), 7570-2, (1994).
- [55] L. Huld, N.G. Nilsson, and K.G. Svantesson, *Applied Physics Letters*, **35** (10), 776-7, (1979).
- [56] W. Lochmann and A. Haug, *Solid State Communications*, **35** (7), 553-6, (1980).
- [57] J. Dziewior and W. Schmid, *Applied Physics Letters*, **31** (5), 346-8, (1977).
- [58] A. Hangleiter and R. Häcker, *Physical Review Letters*, **65** (2), 215-18, (1990).
- [59] M.J. Kerr and A. Cuevas, *Journal of Applied Physics*, **91** (4), 2473-80, (2002).
- [60] P.P. Altermatt, *Journal of Computational Electronics*, **10** (3), 314-30, (2011).
- [61] A. Richter, S.W. Glunz, F. Werner, J. Schmidt, and A. Cuevas, *Physical Review B*, **86** (16), 165202, (2012).
- [62] K. Jaeger and R. Hezel, *A novel thin silicon solar cell with Al₂O₃ as surface passivation*, in *Proceedings of the 18th IEEE Photovoltaic Specialists Conference*, Las Vegas, Nevada, USA, 1752-3 (1985).
- [63] R. Hezel and K. Jaeger, *Journal of the Electrochemical Society*, **136** (2), 518-23, (1989).
- [64] W. Shockley and W.T.J. Read, *Physical Review*, **87** (5), 835-42, (1952).
- [65] R.N. Hall, *Physical Review*, **87**, 387, (1952).
- [66] D.K. Schroder, *Semiconductor Material and Device Characterization*. 1st ed. 1990, New York: John Wiley & Sons.
- [67] J.S. Blakemore, *Semiconductor statistics*. 2nd ed. 1987, New York, USA: Dover Publications.
- [68] R.A. Smith, *Semiconductors*. 1st ed. 1961, New York, NY, USA: Cambridge University Press.
- [69] D.K. Schroder, R.N. Thomas, and J.C. Swartz, *IEEE Journal of Solid-State Circuits*, **SC-13** (1), 180-7, (1978).

- [70] M.A. Green, *Silicon solar cells: advanced principles and practice*. 1995, Sydney, Australia: Centre for Photovoltaic Devices and Systems UNSW.
- [71] W. Spitzer and H.Y. Fan, *Physical Review*, **108** (2), 268-71, (1957).
- [72] E. Barta, *Infrared Physics*, **17** (2), 111-9, (1977).
- [73] R.A. Smith, *Semiconductors*. 2nd edition ed. 1978, New York, USA: Cambridge University Press.
- [74] E. Conwell and V.F. Weisskopf, *Physical Review*, **77** (3), 388-90, (1950).
- [75] J. Isenberg and W. Warta, *Applied Physics Letters*, **84** (13), 2265-7, (2004).
- [76] IEC, *Photovoltaic devices - part 3: measurement principles for terrestrial photovoltaic (PV) solar devices with reference spectral irradiance data*. . 2nd ed. International Standard, IEC 60904-3. 2008: International Electrotechnical Commission.
- [77] W. Shockley, *Bell System Tech. J.*, **28**, 435-89, (1949).
- [78] M. Hermle, *Analyse neuartiger Silizium- und III-V-Solarzellen mittels Simulation und Experiment*, Dissertation, Universität Konstanz, (2008)
- [79] K. Lee and A. Nussbaum, *Solid-State Electronics*, **23** (6), 655-60, (1980).
- [80] K.R. McIntosh, P.P. Altermatt, and G. Heiser, *Depletion-region recombination in silicon solar cells: when does $m_{DR} = 2$?*, in *Proceedings of the 16th European Photovoltaic Solar Energy Conference*, Glasgow, UK, **1**, 251-4 (2000).
- [81] S.W. Glunz, *Ladungsträgerrekombination in Silicium und Siliciumsolarzellen*, Dissertation, Universität Freiburg, (1995)
- [82] H. Murrmann and D. Widmann, *IEEE Transactions on Electron Devices*, **16** (12), 1022-4, (1969).
- [83] H.A. Macleod, *Thin film optical filters*. 3rd ed. 2001: Taylor & Francis.
- [84] M.A. Green, *Solar Energy Materials & Solar Cells*, **92** (11), 1305-10, (2008).
- [85] J. Greulich, N. Wöhrle, M. Glatthaar, and S. Rein, *Energy Procedia*, **27**, 234-9, (2012).
- [86] J. Foley, A. van Dam, S. Feiner, and J. Hughes, *Computer graphics: Principles and Practice*. 1990, Amsterdam: Addison-Wesley Publishing Company.
- [87] M.A. Green, *Progress in Photovoltaics: Research and Applications*, **10**, 235-41, (2002).
- [88] C. Ulbrich, S. Fahr, J. Üpping, M. Peters, T. Kirchartz, C. Rockstuhl, R. Wehrspohn, A. Gombert, F. Lederer, and U. Rau, *Physica Status Solidi A*, **205** (12), 2831-43, (2008).

- [89] A. Goetzberger, J.C. Goldschmidt, M. Peters, and P. Löper, *Solar Energy Materials & Solar Cells*, **92** (12), 1570-8, (2008).
- [90] K. Tvingstedt, S. Dal Zilio, O. Inganas, and M. Tormen, *Optics Express*, **16** (26), 21608-15, (2008).
- [91] E. Garnett and P. Yang, *Nano Letters*, **10** (3), 1082-7, (2010).
- [92] M. Peters, M. Rüdiger, H. Hauser, M. Hermle, and B. Bläsi, *Progress in Photovoltaics: Research and Applications*, **20** (7), 862-73, (2012).
- [93] M. Peters, M. Rüdiger, B. Bläsi, and W. Platzer, *Optics Express*, **18** (S4), A584-93, (2010).
- [94] A. Mellor, I. Tobías, A. Martí, and A. Luque, *Solar Energy Materials and Solar Cells*, **95** (12), 3527-35, (2011).
- [95] M. Wellenzohn and R. Hainberger, *Optics Express*, **20** (S1), A20-7, (2011).
- [96] I.M. Peters, *Photonic concepts for solar cells*, Dissertation, Universität Freiburg, (2009)
- [97] J. Frank, M. Rüdiger, S. Fischer, J.C. Goldschmidt, and M. Hermle, *Energy Procedia*, **27**, 300-5, (2012).
- [98] A. Goetzberger, B. Voß, and J. Knobloch, *Sonnenenergie: Photovoltaik*. 1994, Stuttgart: Teubner Studienbücher Physik.
- [99] P.P. Altermatt, J.O. Schumacher, A. Cuevas, S.W. Glunz, R.R. King, G. Heiser, and A. Schenk, *Journal of Applied Physics*, **92** (6), 3187-97, (2002).
- [100] D.B.M. Klaassen, *Solid-State Electronics*, **35** (7), 953-9, (1992).
- [101] D.B.M. Klaassen, *Solid State Electronics*, **35** (7), 961-7, (1992).
- [102] T. Trupke, M.A. Green, P. Würfel, P.P. Altermatt, A. Wang, J. Zhao, and R. Corkish, *Journal of Applied Physics*, **94** (8), 4930-7, (2003).
- [103] P.P. Altermatt, J. Schmidt, G. Heiser, and A.G. Aberle, *Journal of Applied Physics*, **82** (10), 4938-44, (1997).
- [104] S. Rein and S.W. Glunz, *Applied Physics Letters*, **82** (7), 1054-56, (2003).
- [105] P.P. Altermatt, H. Plagwitz, R. Bock, J. Schmidt, R. Brendel, M.J. Kerr, and A. Cuevas, *The surface recombination velocity at boron-doped emitters: comparison between various passivation techniques*, in *Proceedings of the 21st European Photovoltaic Solar Energy Conference*, Dresden, Germany, 647-50 (2006).
- [106] B. Hoex, J. Schmidt, R. Bock, P.P. Altermatt, M.C.M. van de Sanden, and W.M.M. Kessels, *Applied Physics Letters*, **91** (112107), 112107/1-3, (2007).
- [107] K.R. McIntosh and L.P. Johnson, *Journal of Applied Physics*, **105**, 124520, (2009).

- [108] J. Dicker, *Charakterisierung von hocheffizienten Rückseitenkontaktzellen*, Diplomarbeit, Universität Freiburg, (1998)
- [109] B. Hoex, S.B.S. Heil, E. Langereis, M.C.M. van de Sanden, and W.M.M. Kessels, *Applied Physics Letters*, **89** (042112), 042112/1-3, (2006).
- [110] B. Hoex, J. Schmidt, P. Pohl, M.C.M. van de Sanden, and W.M.M. Kessels, *Journal of Applied Physics*, **104**, 044903, (2008).
- [111] J. Benick, A. Richter, T.-A. Li, N.E. Grant, K.R. McIntosh, Y. Ren, K.J. Weber, M. Hermle, and S.W. Glunz, *Effect of a post-deposition anneal on Al₂O₃/Si interface properties*, in *Proceedings of the 35th IEEE Photovoltaic Specialists Conference*, Honolulu, Hawaii, USA, (2010).
- [112] G. Agostinelli, P. Choulat, H.F.W. Dekkers, E. Vermariën, and G. Beaucarne, *Rear surface passivation for industrial solar cells on thin substrates*, in *Proceedings of the 4th World Conference on Photovoltaic Energy Conversion*, Waikoloa, Hawaii, USA, 1004-8 (2006).
- [113] J. Schmidt, A. Merkle, R. Brendel, B. Hoex, M.C.M. van de Sanden, and W.M.M. Kessels, *Progress in Photovoltaics: Research and Applications*, **16** (6), 461-6, (2008).
- [114] G. Dingemans and W.M.M. Kessels, *Journal of Vacuum Science & Technology A*, **30** (4), 040802, (2012).
- [115] R.R. King, R.A. Sinton, and R.M. Swanson, *IEEE Transactions on Electron Devices*, **37** (2), 365-71, (1990).
- [116] R.R. King and R.M. Swanson, *IEEE Transactions on Electron Devices*, **38** (6), 1399-409, (1991).
- [117] A. Cuevas, P.A. Basore, G. Giroult-Matlakowski, and C. Dubois, *Surface recombination velocity and energy bandgap narrowing of highly doped n-type silicon*, in *Proceedings of the 13th European Photovoltaic Solar Energy Conference*, Nice, France, 337-42 (1995).
- [118] D.E. Kane and R.M. Swanson, *Measurement of the emitter saturation current by a contactless photoconductivity decay method (silicon solar cells)*, in *Proceedings of the 18th IEEE Photovoltaic Specialists Conference*, Las Vegas, Nevada, USA, 578-83 (1985).
- [119] B. Michl, D. Impera, M. Bivour, W. Warta, and M.C. Schubert, *Progress in Photovoltaics: Research and Applications*, DOI: 10.1002/pip.2293, (2012).
- [120] B.T. Michl, M. Rüdiger, J.A. Giesecke, M. Hermle, W. Warta, and M.C. Schubert, *From injection dependent lifetime to solar cell efficiency*, in *Proceedings of the 26th European Photovoltaic Solar Energy Conference and Exhibition*, Hamburg, Germany, 1058-62 (2011).

-
- [121] B. Michl, M. Rüdiger, J. Giesecke, M. Hermle, W. Warta, and M.C. Schubert, *Solar Energy Materials & Solar Cells*, **98**, 441-7, (2012).
- [122] D.A. Clugston and P.A. Basore, *PCID version 5: 32-bit solar cell modeling on personal computers*, in *Proceedings of the 26th IEEE Photovoltaic Specialists Conference*, Anaheim, California, USA, 207-10 (1997).
- [123] M. Engelhardt, *LTSpice/SwitcherCAD III*. Linear Technology Corporation (2007)
- [124] M. Rüdiger, J. Greulich, A. Richter, and M. Hermle, *IEEE Transactions on Electron Devices*, **60** (7), 2156-63, (2013).
- [125] M. Rauer, M. Rüdiger, C. Schmiga, H. Strutzberg, M. Bähr, M. Glatthaar, and S.W. Glunz, *Journal of Applied Physics*, **114**, 203702, (2013).
- [126] A. Kimmerle, A. Wolf, U. Belledin, and B. Biro, *Energy Procedia*, **8**, 275-81, (2011).
- [127] S. Solmi, A. Parisini, R. Angelucci, A. Armigliato, D. Nobile, and L. Moro, *Physical Review B*, **53** (12), 7836-41, (1996).
- [128] E. Hecht, *Optics*. 4th ed. International ed. ed. 2002, Amsterdam: Addison-Wesley Longman.
- [129] M. Rüdiger, M. Rauer, C. Schmiga, and M. Hermle, *Journal of Applied Physics*, **110**, 024508, (2011).
- [130] M. Rüdiger, M. Rauer, C. Schmiga, M. Hermle, and S.W. Glunz, *Energy Procedia*, **8**, 527-32, (2011).
- [131] P. Altermatt, S. Steingrube, Y. Yang, C. Sprodowski, T. Dezhdar, S. Koc, B. Veith, S. Herrman, R. Bock, K. Bothe, J. Schmidt, and R. Brendel, *Highly predictive modelling of entire Si solar cells for industrial applications*, in *Proceeding of the 24th European Photovoltaic Solar Energy Conference*, Hamburg, 901-6 (2009).
- [132] J.R. Davis, Jr., A. Rohatgi, R.H. Hopkins, P.D. Blais, P. Rai-Choudhury, J.R. McCormick, and H.C. Mollenkopf, *IEEE Transactions on Electron Devices*, **ED-27** (4), 677-87, (1980).
- [133] P. Rosenits, T. Roth, S.W. Glunz, and S. Beljakowa, *Applied Physics Letters*, **91** (12), 122109/1-3, (2007).
- [134] P. Rosenits, T. Roth, and S.W. Glunz, *Applied Physics Letters*, **99** (23), 1, (2011).
- [135] O. Krause, H. Ryssel, and P. Pichler, *Journal of Applied Physics*, **91** (9), 5645-9, (2002).
- [136] D.W. Fischer and J.J. Rome, *Physical Review B*, **27** (8), 4826-32, (1983).

- [137] R.L. Marchand and C.-T. Sah, *Journal of Applied Physics*, **48** (1), 336-41, (1977).
- [138] J. Schmidt and R.A. Sinton, *Defect characterization by temperature and injection-dependent lifetime spectroscopy*, in *Proceedings of the 3rd World Conference on Photovoltaic Energy Conversion*, Osaka, Japan, 947-50 (2003).
- [139] A. Rohatgi, J.R. Davis, R.H. Hopkins, and P.G. McMullin, *Solid State Electronics*, **26**, 1039-51, (1983).
- [140] J. Schmidt, *Applied Physics Letters*, **82** (13), 2178-80, (2003).
- [141] C. Schmiga, H. Nagel, and J. Schmidt, *Progress in Photovoltaics: Research and Applications*, **14** (6), 533-9, (2006).
- [142] C. Schmiga, M. Rauer, M. Rüdiger, K. Meyer, J. Lossen, H.-J. Krokoszinski, M. Hermle, and S.W. Glunz *Aluminium-doped p^+ silicon for rear emitters and back surface fields: results and potentials of industrial n- and p-type solar cells*, in *Proceedings of the 25th European Photovoltaic Solar Energy Conference and Exhibition*, Valencia, Spain, 1163-8 (2010).
- [143] M. Rauer, C. Schmiga, M. Hermle, and S.W. Glunz, *Passivation of screen-printed aluminium-alloyed emitters for back junction n-type silicon solar cells*, in *Proceedings of the 24th European Photovoltaic Solar Energy Conference*, Hamburg, Germany, 1059-62 (2009).
- [144] M. Rauer, C. Schmiga, M. Hermle, and S.W. Glunz, *Physica Status Solidi A*, **207**, 1249-51, (2009).
- [145] R.A. Sinton, A. Cuevas, and M. Stuckings, *Quasi-steady-state photoconductance, a new method for solar cell material and device characterization*, in *Proceedings of the 25th IEEE Photovoltaic Specialists Conference*, Washington DC, USA, 457-60 (1996).
- [146] F. Huster and G. Schubert, *ECV doping profile measurements of aluminium alloyed back surface fields*, in *Proceedings of the 20th European Photovoltaic Solar Energy Conference*, Barcelona, Spain, 1462-5 (2005).
- [147] R. Bock, J. Schmidt, R. Brendel, H. Schuhmann, and M. Seibt, *Journal of Applied Physics*, **104** (4), 1-5, (2008).
- [148] K. Misiakos and D. Tsamakis, *Journal of Applied Physics*, **74** (5), 3293-7, (1993).
- [149] P.P. Altermatt, A. Schenk, and G. Heiser, *Journal of Applied Physics*, **100** (11), 113714, (2006).
- [150] P.P. Altermatt, A. Schenk, B. Schmithusen, and G. Heiser, *Journal of Applied Physics*, **100** (11), 113715, (2006).

- [151] J. Schmidt, N. Thiemann, R. Bock, and R. Brendel, *Journal of Applied Physics*, **106** (9), 093707, (2009).
- [152] R. Bock, P.P. Altermatt, J. Schmidt, and R. Brendel, *Semiconductor Science and Technology*, **25** (10), 105007, (2010).
- [153] S.M. Sze, *Semiconductor devices, Physics and Technology*. . 2nd ed. 2002, New York, NY, USA: John Wiley & Sons Inc. .
- [154] M. Rüdiger, C. Schmiga, M. Rauer, M. Hermle, and S.W. Glunz, *IEEE Transactions on Electron Devices*, **59** (5), 1295-303, (2012).
- [155] M. Rüdiger, C. Schmiga, M. Rauer, M. Hermle, and S.W. Glunz, *Optimisation of industrial n-type silicon solar cells with aluminium-alloyed rear emitter by means of 2D numerical simulation*, in *Proceedings of the 25th European Photovoltaic Solar Energy Conference and Exhibition*, Valencia, Spain, 2280-6 (2010).
- [156] H. Nagel, C. Schmiga, B. Lenkeit, G. Wahl, and W. Schmidt, *17%-efficient screen-printed n-type Cz silicon solar cell featuring aluminium-alloyed back junction*, in *Proceedings of the 21st European Photovoltaic Solar Energy Conference*, Dresden, Germany, 1228-34 (2006).
- [157] C. Schmiga, M. Hörteis, M. Rauer, K. Meyer, J. Lossen, H.-J. Krokoszinski, M. Hermle, and S.W. Glunz *Large-area n-type silicon solar cells with printed contacts and aluminium-alloyed rear emitter*, in *Proceedings of the 24th European Photovoltaic Solar Energy Conference*, Hamburg, Germany, 1167-70 (2009).
- [158] F. Book, T. Wiedenmann, G. Schubert, H. Plagwitz, and G. Hahn, *Energy Procedia*, **8**, 487-92, (2011).
- [159] R. Bock, R. Hesse, J. Schmidt, R. Brendel, J. Maier, B. Geyer, J. Koopmann, and H. Kerp, *n-Type Cz-silicon solar cells with screen-printed alluminium-alloyed rear emitter*, in *Proceedings of the 25th European Photovoltaic Solar Energy Conference and Exhibition*, Valencia, Spain, 1449-52 (2010).
- [160] C. Gong, E. van Kerschaver, J. Robbelein, N.E. Posthuma, S. Singh, J. Poortmans, and R. Mertens, *High efficient n-type back-junction back-contact silicon solar cells with screen-printed Al-alloyed emitter*, in *Proceedings of the 25th European Photovoltaic Solar Energy Conference and Exhibition*, Valencia, Spain, 1424-8 (2010).
- [161] R. Kopecek, A. Halm, A. Popescu, K. Peter, C. Vázquez, and N. Fukushima, *Aluminium rear emitter large area n-type Cz-Si solar cells for industrial application*, in *Proceedings of the 25th European Photovoltaic Solar Energy Conference and Exhibition*, Valencia, Spain, 2381-6 (2010).

- [162] V.D. Mihailetchi, D.S. Sainova, L.J. Geerligs, and A.W. Weeber, *17.4% efficiency solar cells on large area and thin n-type silicon with screen-printed aluminium-alloyed rear emitter*, in *Proceedings of the 22nd European Photovoltaic Solar Energy Conference*, Milan, Italy, 837-40 (2007).
- [163] Y. Veschetti, T. Schutz-Kuchly, S. Manuel, S. Gall, and D. Heslinga, *High efficiency solar cells by optimization of front surface passivation on n-type rear Al alloyed emitter structure*, in *Proceedings of the 25th European Photovoltaic Solar Energy Conference and Exhibition*, Valencia, Spain, 2265-7 (2010).
- [164] R. Woehl, R. Keding, M. Rüdiger, H. Gentischer, F. Clement, J. Wilde, and D. Biro, *20% efficient screen-printed and aluminium-alloyed back-contact back-junction cells and interconnection scheme of point-shaped metalized cells*, in *Proceedings of the 37th IEEE Photovoltaic Specialists Conference*, Seattle, Washington, USA, 48-52 (2011).
- [165] R. Woehl, M. Hörteis, and S.W. Glunz *Advances in OptoElectronics*, **2008** (ID 759340), 1-7, (2008).
- [166] A. Cuevas, G. Giroult-Matlakowski, P.A. Basore, C. DuBois, and R.R. King, *Extraction of the surface recombination velocity of passivated phosphorus-doped silicon emitters*, in *Proceedings of the 1st World Conference on Photovoltaic Energy Conversion- WCPEC*, Waikoloa, Hawaii, USA, **2**, 1446-9 (1994).
- [167] M.B. Spitzer, S.P. Tobin, and C.J. Keavney, *IEEE Transactions on Electron Devices*, **31** (5), 546-50, (1984).
- [168] D.L. Meier, V. Chandrasekaran, H.P. Davis, A.M. Payne, S. Wang, J.E. O'Neill, Y.-W. Ok, F. Zimbardi, and A. Rohatgi, *n-Type, ion implanted silicon solar cells and modules*, in *Proceedings of the 37th IEEE Photovoltaic Specialists Conference*, Seattle, Washington, USA, (2011).
- [169] M. Hermle, F. Granek, O. Schultz, and S.W. Glunz, *Journal of Applied Physics*, **103**, 054507, (2008).
- [170] R.J. Schwartz, M.S. Lundstrom, and R.D. Nasby, *IEEE Transactions on Electron Devices*, **28** (3), 264-9, (1981).
- [171] M. Hörteis, *Fine-line printed contacts on crystalline silicon solar cells*, Dissertation, Universität Konstanz, (2009)
- [172] A. Fell, S. Hopman, and F. Granek, *Applied Physics A: Materials Science & Processing*, **104** (1), 165-70, (2011).
- [173] C. Schmiga, M. Hermle, and S.W. Glunz *Towards 20% efficient n-type silicon solar cells with screen-printed aluminium-alloyed rear emitter*, in *Proceedings*

- of the 23rd European Photovoltaic Solar Energy Conference*, Valencia, Spain, 982 (2008).
- [174] R. Bock, J. Schmidt, and R. Brendel, *Applied Physics Letters*, **91** (112112), 1-3, (2007).
- [175] J. Krause, R. Woehl, M. Rauer, C. Schmiga, J. Wilde, and D. Biro, *Solar Energy Materials and Solar Cells*, **95** (8), 2151-60, (2011).
- [176] A. Kimmerle, M. Rüdiger, A. Wolf, M. Hermle, and D. Biro, *Energy Procedia*, **27**, 219-26, (2012).
- [177] M. Rüdiger and M. Hermle, *Japanese Journal of Applied Physics*, **51** (10NA07), 1-3, (2012).
- [178] A.W. Blakers, A. Wang, A.M. Milne, J. Zhao, and M.A. Green, *Applied Physics Letters*, **55** (13), 1363-5, (1989).
- [179] E. Schneiderlochner, R. Preu, R. Ludemann, and S.W. Glunz, *Progress in Photovoltaics*, **10** (1), 29-34, (2002).
- [180] M. Schöfthaler, U. Rau, W. Füssel, and J.H. Werner, *Optimization of the back contact geometry for high efficiency solar cells*, in *Proceedings of the 23rd IEEE Photovoltaic Specialists Conference*, Louisville, Kentucky, USA, 315-20 (1993).
- [181] S. Sterk and S.W. Glunz, *Simulation in high efficiency solar cell research*, in *Proceedings of the 5th International Conference on Simulation of Semiconductor Devices and Processes*, Vienna, **5**, 393-6 (1993).
- [182] S. Sterk, J. Knobloch, and W. Wettling, *Progress in Photovoltaics: Research and Applications*, **2** (1), 19-26, (1994).
- [183] A.G. Aberle, G. Heiser, and M.A. Green, *Journal of Applied Physics*, **75** (10, pt.1), 5391-405, (1994).
- [184] U. Rau, *Three dimensional simulation of the electrical transport in high efficiency solar cells*, in *Proceedings of the 12th European Photovoltaic Solar Energy Conference*, Amsterdam, The Netherlands, 1350-3 (1994).
- [185] P.P. Altermatt, G. Heiser, and M.A. Green, *Progress in Photovoltaics: Research and Applications*, **4** (5), 355-67, (1996).
- [186] P.P. Altermatt, G. Heiser, A.G. Aberle, A. Wang, J. Zhao, S.J. Robinson, S. Bowden, and M.A. Green, *Progress in Photovoltaics: Research and Applications*, **4** (6), 399-414, (1996).
- [187] P.P. Altermatt, G. Heiser, X. Dai, J. Jürgens, A.G. Aberle, S.J. Robinson, T. Young, S.R. Wenham, and M.A. Green, *Journal of Applied Physics*, **80** (6), 3574-86, (1996).

- [188] K.R. Catchpole and A.W. Blakers, *Modelling of the PERC structure with stripe and dot back contacts*, in *Proceedings of the 16th European Photovoltaic Solar Energy Conference*, Glasgow, UK, 1719-22 (2000).
- [189] K.R. Catchpole and A.W. Blakers, *Solar Energy Materials and Solar Cells*, **73** (2), 189-202, (2002).
- [190] A. Wolf, D. Biro, J.-F. Nékarda, S. Stumpp, A. Kimmerle, S. Mack, and R. Preu, *Journal of Applied Physics*, **108** (124510), 1-13, (2010).
- [191] D. Kray, M. Hermle, and S.W. Glunz, *Progress in Photovoltaics: Research and Applications*, **16**, 1-15, (2008).
- [192] D. Kray and S.W. Glunz, *Progress in Photovoltaics: Research and Applications*, **14**, 195-201, (2006).
- [193] A. Cuevas, M. Stuckings, J. Lau, and M. Petracic, *The recombination velocity of boron diffused silicon surfaces*, in *Proceedings of the 14th European Photovoltaic Solar Energy Conference*, Barcelona, Spain, 2416-9 (1997).
- [194] R.H. Cox and H. Strack, *Solid State Electronics*, **10**, 1213-8, (1967).
- [195] B. Gelmont and M. Shur, *Solid-State Electronics*, **36** (2), 143-6, (1993).
- [196] B. Gelmont, M.S. Shur, and R.J. Mattauch, *Solid-State Electronics*, **38** (3), 731-4, (1995).
- [197] B. Fischer, *Loss analysis of crystalline silicon solar cells using photoconductance and quantum efficiency measurements*, Dissertation, Universität Konstanz, (2003)
- [198] P. Saint-Cast, M. Rüdiger, A. Wolf, M. Hofmann, J. Rentsch, and R. Preu, *Journal of Applied Physics*, **108**, 013705, (2010).
- [199] S. Karmalkar, P.V. Mohan, H.P. Nair, and R. Yeluri, *Electron Devices, IEEE Transactions on*, **54** (7), 1734-43, (2007).
- [200] J. Schmidt, A. Cuevas, S. Rein, and S.W. Glunz, *Fill factor limitations and non-ideal diode behaviour of Czochralski silicon solar cells due to light-induced recombination centres*, in *Proceedings of the 17th European Photovoltaic Solar Energy Conference*, Munich, Germany, 1396-9 (2001).
- [201] A. Grohe, *Einsatz von Laserverfahren zur Prozessierung von kristallinen Silizium-Solarzellen*, Dissertation, Universität Konstanz, (2007)
- [202] D. Pysch, A. Mette, and S.W. Glunz, *Solar Energy Materials & Solar Cells*, **91**, 1698-706, (2007).
- [203] M. Wolf and H. Rauschenbach, *Advanced Energy Conversion*, **3**, 455-79, (1963).

- [204] K.C. Fong, K.R. McIntosh, and A.W. Blakers, Progress in Photovoltaics: Research and Applications, DOI: 10.1002/pip.216, (2011).
- [205] R.J. Handy, Solid-State Electronics, **10**, 765-75, (1967).
- [206] S. Fischer, J.C. Goldschmidt, P. Löper, G.H. Bauer, R. Brüggemann, K. Krämer, D. Biner, M. Hermle, and S.W. Glunz Journal of Applied Physics, **108** (4), 044912, (2010).
- [207] J. Frank, *Simulation von bifacialen Solarzellen für Photovoltaiksysteme mit Hochkonvertern*, Diplomarbeit, Universität Freiburg, (2012)
- [208] M. Rüdiger, S. Fischer, J. Frank, A. Ivaturi, B.S. Richards, K.W. Krämer, M. Hermle, and J.C. Goldschmidt, *Bifacial n-Type Silicon Solar Cells for Upconversion Applications*, (in preparation for publication).
- [209] T. Trupke, M.A. Green, and P. Würfel, Journal of Applied Physics, **92** (7), 4117-22, (2002).
- [210] T. Trupke, A. Shalav, B.S. Richards, P. Würfel, and M.A. Green, Solar Energy Materials & Solar Cells, **90** (18-19), 3327-38, (2006).
- [211] P. Gibart, F. Auzel, J.C. Guillaume, and K. Zahraman, Japanese Journal of Applied Physics, **35** (8), 4401-2, (1996).
- [212] A. Shalav, B.S. Richards, and M.A. Green, Solar Energy Materials & Solar Cells, **91** (9), 829-42, (2007).
- [213] B. Ahrens, P. Löper, J.C. Goldschmidt, S.W. Glunz, B. Henke, P.-T. Miclea, and S. Schweizer, Physica Status Solidi A, **205** (12), 2822-30, (2008).
- [214] J.C. Goldschmidt, P. Löper, and M. Peters, *Solarelement mit gesteigerter Effizienz und Verfahren zur Effizienzsteigerung*, in *Deutsches Patent*. Fraunhofer-Gesellschaft zur Förderung der angewandten Forschung e.V.: Bundesrepublik Deutschland (2007)
- [215] P. Würfel and T. Trupke, Physik Journal, **2** (12), 45-51, (2003).
- [216] J.C. Goldschmidt, P. Löper, S. Fischer, S. Janz, M. Peters, S.W. Glunz, G. Willeke, E. Lifshitz, K. Krämer, and D. Biner, *Advanced Upconverter Systems with Spectral and Geometric Concentration for high Upconversion Efficiencies*, in *Proceedings IUMRS International Conference on Electronic Materials*, Sydney, Australia, 307-11 (2008).
- [217] A. Sashchiuk, L. Langof, R. Chaim, and E. Lifshitz, Journal of Crystal Growth, **240**, 431-8, (2002).
- [218] J.M. Pietryga, R.D. Schaller, D. Werder, M.H. Stewart, V.I. Klimov, and J.A. Hollingsworth, Journal of the American Chemical Society, **126**, 11752-3, (2004).

- [219] J.C. Goldschmidt, S. Fischer, P. Löper, K.W. Krämer, D. Biner, M. Hermle, and S.W. Glunz *Solar Energy Materials and Solar Cells*, **95** (7), 1960-3, (2011).
- [220] K. Jaeger, G. Bende, W. Hoffmann, and R. Hezel, *Performance of bifacial MIS-inversion layer solar cells encapsulated in novel albedo collecting modules*, in *Proceedings of the 23rd IEEE Photovoltaic Specialists Conference*, Louisville, Kentucky, USA, 1235-9 (1993).
- [221] S. Fischer, J.C. Goldschmidt, K.W. Krämer, D. Biner, M. Hermle, and S.W. Glunz *Calibrated photoluminescence measurements of the upconverter NaYF₄:20% ER³⁺ for silicon solar cells*, in *Proceedings of the 25th European Photovoltaic Solar Energy Conference and Exhibition*, Valencia, Spain, 657-61 (2010).
- [222] S. Fischer, *Photonenmanagement für neuartige Silizium-Solarzellen*, Diplomarbeit, Universität Freiburg, (2009)
- [223] O. Kraus, *Entwicklung von breitbandigen Antireflex-Beschichtungen für III-V-Mehrfachsolarzellen*, Diplomarbeit, Universität Regensburg, (2010)
- [224] T. Rist, *Modellierung und Charakterisierung von Fluoreszenzkonzentrator- und Hochkonvertersystemen*, Diplomarbeit, Universität Freiburg, (2012)
- [225] R. Woehl, M. Rüdiger, D. Erath, D. Stüwe, R. Preu, and D. Biro, *Structuring technology and simulation of high efficiency back-contact back-junction silicon solar cells under low concentration*, in *AIP Conference Proceedings*, Freiburg, Germany, **1277**, 53-7 (2010).
- [226] A. Cuevas, A. Luque, J. Eguren, and J. Del Alamo, *Solar Cells*, **3** (4), 337-40, (1981).
- [227] J. Schmidt, F. Werner, B. Veith, D. Zielke, S. Steingrube, P.P. Altermatt, S. Gatz, T. Dullweber, and R. Brendel, *Energy Procedia*, **15**, 30-9, (2012).
- [228] G. Dingemans, R. Seguin, P. Engelhart, M.C.M. van den Sanden, and W.M.M. Kessels, *Physica Status Solidi RRL*, **4** (1-2), 10-2, (2010).
- [229] S. Greil, *Charakterisierung und Optimierung der lichtinduzierten Galvanik (LIP) von Silber zur Verstärkung der Vorderseitenkontakte an kristallinen Siliciumsolarzellen*, Diplomarbeit, Technische Universität Bergakademie Freiberg, (2008)
- [230] B. Hoex, M.C.M. van de Sanden, J. Schmidt, R. Brendel, and W.M.M. Kessels, *Physica Status Solidi RRL*, **6** (1), 4-6, (2012).
- [231] A. Mohr, T. Roth, and S.W. Glunz, *Progress in Photovoltaics: Research and Applications*, **14** (7), 663-74, (2006).

-
- [232] S. Steingrube, P.P. Altermatt, D. Zielke, F. Werner, J. Schmidt, and R. Brendel, *Reduced passivation of silicon surfaces at low injection densities caused by H-induced defects*, in *Proceedings of the 25th European Photovoltaic Solar Energy Conference and Exhibition*, Valencia, Spain, 1748-54 (2010).
- [233] S.W. Glunz, D. Biro, S. Rein, and W. Warta, *Journal of Applied Physics*, **86** (1), 683-91, (1999).
- [234] S. Dauwe, J. Schmidt, and R. Hezel, *Very low surface recombination velocities on p- and n-type silicon wafers passivated with hydrogenated amorphous silicon films*, in *Proceedings of the 29th IEEE Photovoltaics Specialists Conference*, New Orleans, Louisiana, USA, 1246-9 (2002).
- [235] M. Bivour, M. Rüdiger, C. Reichel, K.-U. Ritzau, M. Hermle, and S.W. Glunz, *Energy Procedia*, **8**, 185-92, (2011).
- [236] P.P. Altermatt, A. Schenk, G. Heiser, and M.A. Green, *The influence of a new band gap narrowing model on measurements of the intrinsic carrier density in crystalline silicon*, in *Proceedings of the 11th International Photovoltaic Science and Engineering Conference*, Sapporo, Japan, 719-20 (1999).

11 Appendix

11.1 Abbreviations

Variable	Meaning
2D	Two dimensional
3D	Three dimensional
Ag	Silver
Al	Aluminum
Al ₂ O ₃	Aluminum oxide
Al- p^+	Al-doped p^+ Si
AM1.5G	Standard global radiation spectrum
ARC	Anti-Reflection Coating
B	Boron
BCBJ	Back-contact back-junction
BSF	Back Surface Field
Cell _{opt}	Optimization for high solar cell efficiency
CRU	Climate Research Unit
c-Si	Crystalline silicon
Cz	Czochralski
ECV	Electrochemical Capacitance–Voltage
EQE	External quantum efficiency
FCA	Free Carrier Absorption
FDTD	Finite Different Time Domain
FSF	Front Surface Field
FZ	Float-Zone
GISS	Goddard Institute for Space Studies
HLI	High-level injection

IEC	International Electrotechnical Commission
IML	Index matching liquid
IPCC	Intergovernmental Panel on Climate Change
LFC	Lase-Fired Contact
LLI	Low-level injection
MgF ₂	Magnesium difluoride
mpp	Maximum power point
NASA	National Aeronautics and Space Administration
NCDC	National Climatic Data Center
NH ₄ HF ₆	Ammonium bifluoride
NOAA	National Oceanic and Atmospheric Administration
<i>n</i> -Si	Phosphorus doped silicon
P	Phosphorus
PECVD	Plasma Enhanced Chemical Vapor Deposition
PERC	Passivated Emitter and Rear Cell
PERL	Passivated Emitter, Rear Locally-diffused
PL	Photoluminescence
<i>p</i> -Si	Boron doped silicon
PTFE	Polytetrafluoroethylene (commercially known as Teflon)
RCWA	Rigorous Coupled Wave Analysis
SEM	Scanning Electron Microscope
Si	Silicon
SiN _x	Silicon nitride
SiO ₂	Silicon dioxide
SRH	Shockley-Read-Hall
TCAD	Technology Computer Aided Design
TiO ₂	Titanium dioxide
TMM	Transfer Matrix Method
UC _{opt}	Optimization for high upconversion efficiency

UC_{ph}	Upconverter emission spectrum
Γ	Phonon
$\beta\text{-NaY}_{0.8}\text{Er}_{0.2}\text{F}_4$	Erbium based upconverter material
γ	Photon

11.2 Glossary

Variable	Dimension	Meaning
$[B_s]$	cm^{-3}	Substitutional boron concentration
$[O_i]$	cm^{-3}	Interstitial oxygen concentration
A	-	Absorption
Ab_{s_0}	-	Absorbed photons in the solar cell without upconverter
Ab_{s_r}	-	Photon absorption in solar cell, after re-emission by upconverter
$Ab_{s_{UC}}$	-	Fraction of photons from upconversion process, potentially generating electron-hole pairs
$A_{f/r}$	-	Absorption for front/rear side illumination
A_{laser}	mm^2	Illuminated solar cell surface by laser beam
A_r	-	Solar cell absorption with illumination from rear side
A_{SC}	cm^2	Total solar cell area
A_{UC}	-	Solar cell area, covered by upconverter
B	cm^3s^{-1}	Coefficient of radiative recombination
B_{LLI}	cm^3s^{-1}	Transition probability under low-level injection
$C_{FCA,n/p}$	-	Coefficient of free carrier absorption for n/p -Si
$C_{n/p}$	cm^6s^{-1}	Auger coefficient
$c_{n/p}$	s^{-1}	Coefficient coefficient of capture rate
$c_{n/p}^*$	$\text{cm}^{-3}\text{s}^{-1}$	Capture rate of electrons/holes
d	μm	Diffusion profile depth
D	cm^2s^{-1}	Diffusivity of interstitial Al in Si
d	μm	Sample thickness
d_{Al}	μm	Thickness of deconvoluted Al- p^+ profile
D_{amb}	cm^2s^{-1}	Ambipolar diffusion constant
$D_{C/V}$	$\text{cm}^{-3}\text{eV}^{-1}$	Density of states in the conduction/valence band
$D_{e/h}$	cm^2s^{-1}	Diffusion constant of electrons/holes

E	eV	Energy
E_{bgn}	eV	Reduction of the band gap due to band gap narrowing
E_C	eV	Lowest energy in the conduction band
E_F	eV	Fermi energy
$E_{F,e/h}$	eV	Quasi Fermi distribution of electrons/holes
E_g	eV	Band gap energy
$E_{h\nu}$	eV	Photon energy
$e_{n/p}$	$\text{cm}^{-3}\text{s}^{-1}$	Emission rate of electrons/holes
E_t	eV	Energy of defect level
E_V	eV	Highest energy in the conduction band
f	-	Occupation probability
FF	%	Fill factor
FF_0	%	Fill factor of an ideal diode
f_t	-	Occupation probability with an electron
G	$\text{cm}^{-3}\text{s}^{-1}$	Generation rate
g	-	Degeneracy factor
$g_{\text{eh/eeh/ehh}}$	-	Enhancement factor
$G_{n/p}$	$\text{cm}^{-3}\text{s}^{-1}$	Generation rate of electrons/holes
G_{ph}	$\text{cm}^{-3}\text{s}^{-1}$	Photogeneration rate
h	μm	Edge length of local rear contacts
I	Wm^{-2}	Illumination intensity
I_0	Wm^{-2}	Initial beam intensity
j	mA/cm^2	Current density
j_0	mA/cm^2	Dark saturation current density
$j_{0,\text{Al}}$	mA/cm^2	Saturation current density within Al- p^+ profile
$j_{0,\text{total}}$	mA/cm^2	Total saturation current density
$j_{01/02}$	mA/cm^2	Dark saturation current densities of two-diode model
j_{0b}	mA/cm^2	Dark saturation current density of the bulk
j_{gen}	mA/cm^2	Generated photo-current density
J_{in}	mA/cm^2	Incident current density

$j_{\max,160\mu\text{m}}$	mA/cm^2	Theoretical current density maximum for a 160 μm thick wafer
j_{mpp}	mA/cm^2	Current density at maximum power point
$j_{\text{n/p}}$	mA/cm^2	Current density of electrons/holes
j_{ph}	mA/cm^2	Photogeneration current density
j_{ph}	mA/cm^2	Photocurrent density
$j_{\text{ph,rel}}$	mA/cm^2	Relative photogeneration current density
j_{sc}	mA/cm^2	Short-circuit current density
k	-	Symmetry factor
K	-	Concentration factor
k_{Si}	-	Extinction coefficient of silicon
$L_{\text{e/h}}$	cm	Diffusion length of electrons/holes
L_{eff}	μm	Effective diffusion length
L_{p}	μm	Rear contact distance
MAE	-	Mean Absolute Error
$m_{\text{e/h}}^*$	kg	Effective mass of electrons/holes
$m_{\text{l/t}}^*$	kg	Longitudinal/transversal effective electron mass
$m_{\text{th,e/h}}^*$	kg	Thermal effective electron/hole mass
n	cm^{-3}	Electron density
N	cm^{-3}	Charge carrier concentration
n_0	cm^{-3}	Equilibrium electron concentration in the conduction band
N_0	cm^{-3}	Normalized carrier concentration
n_1	cm^{-3}	SRH density of electrons
$n_{1/2}$	-	Ideality factors
$N_{\text{A/D}}$	cm^{-3}	Doping concentration of acceptors/donors
N_{abs}	cm^{-3}	Absorbed photon concentration
$N_{\text{C/V}}$	cm^{-3}	Effective density of states of electrons/holes
N_{dop}	cm^{-3}	Doping concentration
N_{dose}	cm^{-2}	Area doping concentration

$N_{\text{FSF,peak}}$	cm^{-3}	FSF peak doping concentration
$n_{\text{i,eff}}$	cm^{-3}	Effective intrinsic carrier concentration
N_{in}	cm^{-3}	Incident photon concentration
n_{s}	cm^{-2}	Surface charge carrier density of electrons
n_{Si}	-	Refractive index of silicon
N_{t}	cm^{-3}	Defect concentration
N_{t}^*	cm^{-3}	Effective defect density
N_{trans}	cm^{-3}	Transmitted photon concentration
p	cm^{-3}	Hole density
p_0	cm^{-3}	Equilibrium hole concentration in the valence band
p_1	cm^{-3}	SRH density of holes
PFF_{bulk}	%	Pseudo fill factor
P_{in}	mW/cm^2	Incident light power density
P_{mpp}	mW/cm^2	Light power density at maximum power point
p_{s}	cm^{-2}	Surface charge carrier density of holes
$P\eta_{\text{bulk}}$	%	Pseudo efficiency
Q_{f}	e/cm^2	Fixed surface charge
R	-	Reflectance
R_0	-	Reflectance
R_{Auger}	$\text{cm}^{-3}\text{s}^{-1}$	Auger recombination rate
$R_{\text{f/r}}$	-	Reflection for front/rear side illumination
R_{measured}	-	Measured reflection curve
$R_{\text{n/p}}$	$\text{cm}^{-3}\text{s}^{-1}$	Recombination rate of electrons/holes
R_{p}	Ωcm^2	Parallel resistance
R_{R}	-	Reflection of diffuse rear reflector
$R_{\text{radiative}}$	$\text{cm}^{-3}\text{s}^{-1}$	Radiative recombination rate
R_{s}	Ωcm^2	Series resistance
$R_{\text{s,ext}}$	Ωcm^2	Series resistance for contacts, fingers and busbars
R_{sh}	Ω/sq	Sheet resistance

R_{sim}	-	Simulated reflection curve
R_{SRH}	$\text{cm}^{-3}\text{s}^{-1}$	SRH recombination rate
R_{surface}	$\text{cm}^{-2}\text{s}^{-1}$	Surface recombination rate
S_0	cm/s	Surface recombination velocity
$S_{0,\text{contact}}$	cm/s	Surface recombination velocity at contacts
$S_{0,\text{front}}$	cm/s	Surface recombination velocity at the front side
$S_{0,\text{met}}$	cm^{-3}	Surface recombination velocity at rear contact
$S_{0,\text{min}}$	cm/s	Surface recombination velocity of minority carriers
$S_{0,\text{pass}}$	cm^{-3}	Surface recombination velocity at rear passivation
S_{eff}	cm/s	Effective surface recombination velocity
$S_{\text{n/p}}$	cm/s	Surface recombination velocity of electrons/holes
$S_{\text{sc,UC}}$	a.u.	Measured signal intensity
T	K	Temperature
$T(\lambda)$	-	Transmission
T_0	K	Normalized temperature
$T_{\text{f/r}}$	-	Transmission for front/rear side illumination
V	mV	Voltage
V_{junction}	mV	Voltage at the junction
V_{mpp}	mV	Voltage at maximum power point
V_{oc}	mV	Open-circuit voltage
$v_{\text{th,e/h}}$	cm/s	Thermal charge carrier velocity
w	μm	Front finger distance
w_{finger}	μm	Front finger width
Φ_{in}	$\text{cm}^{-2}\text{s}^{-1}$	Incident photon flux density
Φ_{T}	$\text{cm}^{-2}\text{s}^{-1}$	Transmitted photon flux density
Φ_{UC}	$\text{cm}^{-2}\text{s}^{-1}$	Photon flux density
Δj	mA/cm^2	Current density loss
$\Delta j_{\text{Auger,base}}$	mA/cm^2	Auger current density loss in the base of the solar cell
Δj_{front}	mA/cm^2	Current density loss at the front side of the solar cell

$\Delta j_{\text{optical}}$	mA/cm^2	Optical current density loss
Δj_{ph}	mA/cm^2	Photocurrent density increase
Δj_{rear}	mA/cm^2	Current density loss at the rear side of the solar cell
$\Delta j_{\text{SRH,base}}$	mA/cm^2	SRH current density loss in the base of the solar cell
$\Delta n/p$	cm^{-3}	Minority carrier density of electrons/holes
Δn_{bulk}	cm^{-3}	Minority carrier density in the bulk
$\Delta n_{\text{contact}}$	cm^{-3}	Injection density at the rear contact
$\Delta n_{\text{junction}}$	cm^{-3}	Minority carrier density at the junction
Δn_{rear}	cm^{-3}	Minority carrier density at the rear side
ΔV_{Dember}	mV	Dember voltage
ΔV_{X}	mV	Difference in the chemical potential
α	eV/K	Constant of band gap parameterization
α	cm^{-1}	Absorption
$\alpha_{\text{FCA,n/p}}$	cm^{-1}	Free carrier absorption in <i>n/p</i> -Si
α_{Si}	cm^{-1}	Absorption of silicon
β	K	Constant of band gap parameterization
ε	As/Vm	Electrical field constant in a medium
ε_0	As/Vm	Electrical field constant in vacuum
η	%	Efficiency
$\eta_{\text{e/h}}$	eV	Electro-chemical potential of electrons/holes
η_{UC}	%	Integrated quantum yield of upconversion
φ	V	Electrostatic potential
φ	-	Exponent of free carrier absorption for <i>p</i> -Si
λ	μm	Wavelength
$\mu_{\text{e/h}}$	eV	Chemical potential of electrons/holes
$\mu_{\text{n/p}}$	s/kg	Charge carrier mobility of electrons/holes
ρ	Ωcm	Resistivity
ρ_0	Ωcm	Nominal resistivity

ρ_{dark}	Ωcm	Resistivity without including Δn
ρ_{light}	Ωcm	Effective illuminated resistivity
ρ_p	As/cm^3	Volume charge density
σ	-	Standard deviation
$\sigma_{n/p}$	cm^2	Capture cross section of electrons/holes
τ	μs	Excess charge carrier lifetime
$\tau_{\text{A,CE}}$	μs	Coulomb enhanced Auger lifetime
$\tau_{\text{Al-p}^+}$	μs	Average SRH carrier lifetime in Al- p^+ region
τ_{Auger}	μs	Charge carrier lifetime due to Auger recombination
τ_{bulk}	μs	Excess charge carrier lifetime in the bulk
$\tau_{\text{bulk,xy}}$	μs	Local bulk excess carrier lifetime
τ_d	μs	Degraded excess carrier lifetime
τ_{eff}	μs	Effective minority carrier lifetime
$\tau_{n0/p0}$	μs	Capture time constant of electrons/holes
$\tau_{\text{radiative}}$	μs	Charge carrier lifetime due to radiative recombination
τ_{SRH}	μs	Charge carrier lifetime due to SRH recombination
τ_{total}	μs	Total excess charge carrier lifetime
ω	-	Phong-exponent [86]
ξ	-	Exponent of free carrier absorption for n -Si

11.3 Physical constants

Variable	Value	Dimension	Meaning
c	2.998×10^8	m / s	Velocity of light in vacuum [43]
ϵ_0	8.85×10^{-12}	As / Vm	Electric constant [43]
h	4.136×10^{-15}	eV s	Planck constant [43]
n_i	9.65×10^{-9}	cm ⁻³	Intrinsic carrier concentration [48]
π	3.14159	-	Mathematical constant
k_B	8.617×10^{-5}	eV / K	Boltzmann constant [43]
$E_{g,0}$	1.175	eV	Band gap energy at $T = 0$ K [236]
m_0	9.109×10^{-31}	kg	Electron rest mass [153]
q	1.602×10^{-19}	As	Elementary charge [43]

12 List of publications

12.1 Refereed journal papers

M. Rüdiger, S. Fischer, J. Frank, A. Ivaturi, B.S. Richards, K.W. Krämer, M. Hermle, J.C. Goldschmidt, *Bifacial n-type Silicon Solar Cells for Upconversion Applications*, (in preparation for publication).

M. Rüdiger, J. Greulich, A. Richter, M. Hermle, *Parameterization of Free Carrier Absorption in Highly Doped Silicon for Solar Cells*, IEEE Transactions on Electron Devices, Vol. 60, No. 7, pp. 2156-2163 (2013).

M. Rüdiger, H. Steinkemper, S.W. Glunz, M. Hermle, *Numerical Current Density Loss Analysis of Industrially Relevant Crystalline Silicon Solar Cell Concepts*, IEEE Journal of Photovoltaics, DOI: 10.1109/JPHOTOV.2013.2293196 (2013).

M. Rauer, **M. Rüdiger**, C. Schmiga, H. Strutzberg, M. Bähr, M. Glatthaar, S.W. Glunz, *Incomplete ionization of aluminum in silicon and its effect on accurate determination of doping profiles*, Journal of Applied Physics, 114, 203702, (2013).

R. Woehl, **M. Rüdiger**, D. Biro, J. Wilde, *All-Screen-Printed Back-Contact Back-Junction Silicon Solar Cells with Aluminum-Alloyed Emitter and Demonstration of Interconnection of Point-Shaped Metallized Contacts*, DOI: 10.1002/pip.2418 (2013).

S. Fischer, A. Ivaturi, B. Fröhlich, **M. Rüdiger**, A. Richter, K. Krämer, B. Richards, J.C. Goldschmidt, *Upconverter Silicon Solar Cell Devices for Efficient Utilization of Sub-Band-Gap Photons under Concentrated Solar Radiation*, IEEE Journal of Photovoltaics, DOI: 10.1109/JPHOTOV.2013.2282744 (2013).

M. Rüdiger, M. Hermle, *Numerical Analysis of Locally Contacted Rear Surface Passivated Silicon Solar Cells*, Japanese Journal of Applied Physics 51, 10NA07, pp. 1-3 (2012).

M. Rüdiger, C. Schmiga, M. Rauer, M. Hermle, S.W. Glunz, *Efficiency Potential of n-Type Silicon Solar Cells with Aluminum-Doped Rear p^+ Emitter*, IEEE Transactions on Electron Devices, Vol. 59, No. 5, pp. 1295-1303 (2012).

J. Frank, **M. Rüdiger**, S. Fischer, J.C. Goldschmidt, M. Hermle, *Optical simulation of bifacial solar cells*, Energy Procedia, Vol. 27, pp. 300 - 305 (2012).

A. Kimmerle, **M. Rüdiger**, A. Wolf, M. Hermle, D. Biro, *Validation of Analytical Modelling of Locally Contacted Solar Cells by Numerical Simulations*, Energy Procedia, Vol. 27, pp. 219 - 226 (2012).

B. Michl, **M. Rüdiger**, J.A. Giesecke, M. Hermle, W. Warta, M.C. Schubert, *Efficiency limiting bulk recombination in multicrystalline silicon solar cells*, Solar Energy Materials & Solar Cells 98, pp. 441-447 (2012).

M. Peters, **M. Rüdiger**, H. Hauser, M. Hermle, B. Bläsi, *Diffraction Gratings for Crystalline Silicon Solar Cells – Optimum Parameters and Loss Mechanisms*, Progress in Photovoltaics, Vol. 20 (7), pp. 862 - 873 (2012).

J.A. Giesecke, T. Niewelt, **M. Rüdiger**, M. Rauer, M.C. Schubert, W. Warta, *Broad range injection-dependent minority carrier lifetime from photoluminescence*, Solar Energy Materials & Solar Cells 102, pp. 220-224 (2012).

K. Rühle, M. Rauer, **M. Rüdiger**, J. Giesecke, T. Niewelt, C. Schmiga, S.W. Glunz, M. Kasemann, *Passivation layers for indoor solar cells at low irradiation intensities*, Energy Procedia, Vol. 27, pp. 406 - 411 (2012).

M. Rüdiger, M. Rauer, C. Schmiga, M. Hermle, *Effect of incomplete ionization for the description of highly aluminium-doped silicon*, Journal of Applied Physics **110**, 024508 (2011).

M. Rüdiger, M. Rauer, C. Schmiga, M. Hermle, S.W. Glunz, *Accurate modeling of aluminum-doped silicon*, Energy Procedia, Vol. 8, pp. 527 - 532 (2011).

J. Greulich, M. Glatthaar, F. Fertig, F. Clement, B. Thaidigsmann, A. Fallisch, D. Biro, **M. Rüdiger**, M. Hermle, S. Rein, *Intrinsic effects of double side collecting silicon solar cells*, Energy Procedia, Vol. 8, pp. 160 - 166 (2011).

M. Bivour, **M. Rüdiger**, C. Reichel, K.-U. Ritzau, M. Hermle, S.W. Glunz, *Analysis of the Diffused Front Surface Field of n-type Silicon Solar Cells with a-Si/c-Si Heterojunction Rear Emitter*, Energy Procedia, Vol. 8, pp. 160 - 166 (2011).

M. Peters, **M. Rüdiger**, B. Bläsi, W. Platzer, *Electro – optical simulation of diffraction in solar cells*, Optics Express, Vol. 18, Issue S4, pp. A584-A593 (2010).

P. Saint-Cast, **M. Rüdiger**, A. Wolf, M. Hofmann, J. Rentsch, R. Preu, *Advanced analytical model for the effective recombination velocity of locally contacted surfaces*, Journal of Applied Physics **108**, 013705 (2010).

S. Kluska, F. Granek, **M. Rüdiger**, M. Hermle, S.W. Glunz, *Modeling and optimization study of industrial n-type high-efficiency back-contact back-junction silicon solar cells*, *Solar Energy Materials & Solar Cells*, **94** (3), pp. 568–577 (2010).

M. Rüdiger, T. Trupke, P. Würfel, T. Roth, S.W. Glunz, *Influence of photon reabsorption on temperature dependent quasi-steady-state photoluminescence lifetime measurements on crystalline silicon*, *Applied Physics Letters*, **92**, 222112 (2008).

T. Roth, **M. Rüdiger**, W. Warta, S.W. Glunz, *Electronic properties of titanium in boron-doped silicon analyzed by temperature-dependent photoluminescence and injection-dependent photoconductance lifetime spectroscopy*, *Journal of Applied Physics*, **104**, 074510 (2008).

12.2 Refereed papers presented at international conferences

B. Steinhauser, **M. Rüdiger**, U. Jäger, J. Benick, M. Hermle, *Optimization of Local BSF Formation for n-Type Solar Cells Allowing Large Base Resistivity Variation*, *SiliconPV – 2nd International Conference on Crystalline Silicon Photovoltaics*, M-A-36 (2012).

C. Schmiga, M. Rauer, **M. Rüdiger**, M. Glatthaar and S.W. Glunz, *Status and Perspectives of n-type Silicon Solar Cells with Aluminium-alloyed Rear Emitter*, 27th European Photovoltaic Solar Energy Conference and Exhibition, Frankfurt, Germany, pp. 915-918 (2012).

M. Rüdiger, M. Hermle, A. Wolf, S.W. Glunz, *Numerical analysis of locally contacted rear surface passivated solar cells*, *Technical Digest*, 21st International Photovoltaic Science and Engineering Conference PVSEC-21, Fukuoka, Japan, 5A-10-03 (2011).

B.T. Michl, **M. Rüdiger**, J.A. Giesecke, M. Hermle, W. Warta, M.C. Schubert, *From injection dependent carrier lifetime to solar cell efficiency*, 26th European Photovoltaic Solar Energy Conference and Exhibition, Hamburg, Germany, pp. 1058-1062 (2011).

M. Hermle, J. Benick, **M. Rüdiger**, N. Bateman, S.W. Glunz, *N-type silicon solar cells with implanted emitter*, 26th European Photovoltaic Solar Energy Conference and Exhibition, Hamburg, Germany, pp. 875-878 (2011).

R. Woehl, R. Keding, **M. Rüdiger**, H. Gentischer, F. Clement, J. Wilde, D. Biro, *20% efficient screen-printed and aluminum-alloyed back-contact back-junction cells and interconnection scheme of point-shaped metalized cells*, 37th IEEE Photovoltaic Specialists Conference (PVSC), Seattle, USA, pp. 48-52 (2011).

D. Pelzer, M. Peters, H. Hauser, **M. Rüdiger**, B. Bläsi, *Diffraction structures for advanced light trapping in silicon solar cells*, 23rd Workshop on Quantum Solar Energy Conversion - (QUANTSOL 2011), Bad Hofgastein, Austria, (2011).

M. Rüdiger, C. Schmiga, M. Rauer, M. Hermle, S.W. Glunz, *Optimisation of Industrial n-Type Silicon Solar Cells with Aluminium-Alloyed Rear Emitter by Means of 2D Numerical Simulation*, 25th European Photovoltaic Solar Energy Conference and Exhibition / 5th World Conference on Photovoltaic Energy Conversion, Valencia, Spain, pp. 2280-2286 (2010).

M. Peters, **M. Rüdiger**, M. Hermle, B. Bläsi, *Photonic crystals in solar cells: a simulation approach*, Proc. SPIE 7725, 772514); DOI: 10.1117/12.853865 (2010).

M. Peters, **M. Rüdiger**, D. Pelzer, H. Hauser, M. Hermle, B. Bläsi, *Electro-Optical Modelling of Solar Cells with Photonic Structures*, 25th European Photovoltaic Solar Energy Conference and Exhibition / 5th World Conference on Photovoltaic Energy Conversion, Valencia, Spain, pp. 87-91 (2010).

M.C. Schubert, **M. Rüdiger**, B. Michl, F. Schindler, W. Kwapil, J. Giesecke, M. Hermle, W. Warta, R. Ferre, R. Wade, K. Petter, *The Role of Material Quality in EWT and Standard Solar Cells on Multicrystalline Standard and UMG Silicon Material*, 25th European Photovoltaic Solar Energy Conference and Exhibition / 5th World Conference on Photovoltaic Energy Conversion, Valencia, Spain, pp. 2464-2468 (2010).

R. Woehl, **M. Rüdiger**, D. Erath, D. Stüwe, R. Preu, D. Biro, *Structuring Technology and Simulation of High Efficiency Back-Contact Back-Junction Silicon Solar Cells Under Low Concentration*, AIP Conference Proceedings, Volume 1277, pp. 53-57 (2010).

M. Peters, J.C. Goldschmidt, **M. Rüdiger**, P. Voisin, H. Hauser, S. Janz, M. Hermle, B. Bläsi, *Diffraction gratings in solar cells and how to model them*, 22nd Workshop on Quantum Solar Energy Conversion - (QUANTSOL 2010), Brigels, Swiss (2010).

C. Schmiga, M. Rauer, **M. Rüdiger**, K. Meyer, J. Lossen, H.-J. Krokoszinski, M. Hermle, S.W. Glunz, *Aluminium-Doped p+ Silicon for Rear Emitters and Back Surface Fields: Results and Potentials of Industrial n- and p-Type Solar Cells*, 25th European Photovoltaic Solar Energy Conference and Exhibition / 5th World Conference on Photovoltaic Energy Conversion, Valencia, Spain, pp. 1163-1168 (2010).

S.W. Glunz, J. Benick, D. Biro, M. Bivour, M. Hermle, D. Pysch, M. Rauer, C. Reichel, A. Richter, **M. Rüdiger**, C. Schmiga, D. Suwito, A. Wolf, R. Preu, *n-type silicon – enabling efficiencies > 20% in industrial production*, 35th IEEE Photovoltaic Specialists Conference (PVSC), Honolulu/Hawaii, USA, pp. 50-56 (2010).

P. Saint-Cast, **M. Rüdiger**, S. Lude, A. Wolf, D. Kania, M. Hofmann, J. Rentsch, R. Preu, *Advanced Analytical Models of Loss Calculation on PERC Structure*, 19th International Photovoltaic Solar Energy Conference (PVSEC), Jeju, Korea, CSI3-I-1 (2009).

S. Kluska, F. Granek, **M. Rüdiger**, M. Hermle, S.W. Glunz, *Characterization and Modeling of Back-Contact Back-Junction Silicon Solar Cells*, 24th European Photovoltaic Solar Energy Conference and Exhibition, Hamburg, Germany, pp. 950-954 (2009).

M. Rüdiger, T. Roth, W. Warta, S.W. Glunz, *Temperature-Dependent Quasi-Steady-State Photoluminescence Lifetime Measurements for Defect Spectroscopy*, 23rd European Photovoltaic Solar Energy Conference and Exhibition, Valencia, Spain, pp. 1333-1337 (2008).

T. Roth, **M. Rüdiger**, T. Trupke, R.A. Bardos, S.W. Glunz, *Titanium-related Defect Levels in Silicon analyzed by temperature-dependent Photoluminescence Lifetime Spectroscopy*, 33rd IEEE Photovoltaic Specialists Conference, San Diego, USA, DOI: 10.1109/PVSC.2008.4922479 (2008).

T. Roth, P. Rosenits, **M. Rüdiger**, W. Warta, S.W. Glunz, *Comparison of Photoconductance and Photoluminescence-based Lifetime Measurement Techniques*, International Conference on Electronic Materials IUMRS-ICEM 2008, Sydney, Australia (2008).

M. Rüdiger, T. Trupke, P. Würfel, R.A. Bardos, T. Roth, *Influence of Photon Reabsorption on Temperature Dependent Quasi-Steady-State Photoluminescence Lifetime Measurements on Crystalline Silicon*, 22nd European Photovoltaic Solar Energy Conference and Exhibition, Milan, Italy, pp. 386-389 (2007).

T. Roth, **M. Rüdiger**, P. Rosenits, S. Diez, T. Trupke, R.A. Bardos, S.W. Glunz, *Photoluminescence Lifetime Spectroscopy – Surface Recombination Analysis*, 22nd European Photovoltaic Solar Energy Conference and Exhibition, Milan, Italy, pp. 1002-1005 (2007).

P. Würfel, T. Trupke, **M. Rüdiger**, T. Puzzer, E. Schäffer, W. Warta, S.W. Glunz, *Diffusion lengths of silicon solar cells from luminescence images*, 22nd European Photovoltaic Solar Energy Conference, Milan, Italy, pp. 390-393 (2007).

T. Trupke, R.A. Bardos, M.D. Abbott, P. Würfel, E. Pink, Y. Augarten, F.W. Chen, K. Fisher, J.E. Cotter, M. Kasemann, **M. Rüdiger**, S. Kontermann, M.C. Schubert, M. The, S.W. Glunz, W. Warta, D. Macdonald, J. Tan, A. Cuevas, J. Bauer, R. Gupta, O. Breitenstein, T. Buonassisi, G. Tarnowski, A. Lorenz, H.P. Hartmann, D.H. Neuhaus, J.M. Fernandez, *Progress with luminescence imaging for the characterisation of silicon wafers and solar cells*, 22nd European Photovoltaic Solar Energy Conference and Exhibition, Milan, Italy, pp. 22-31 (2007).

T. Roth, **M. Rüdiger**, S. Diez, T. Trupke, R.A. Bardos, S.W. Glunz, “Temperature- and Injection-Dependent Photoluminescence Lifetime Spectroscopy”, 21st European Photovoltaic Solar Energy Conference and Exhibition, Dresden, Germany, pp. 593-596 (2006).

12.3 Diploma thesis

M. Rüdiger, *Analyse von Defekten in Silizium mittels Photolumineszenz-Spektroskopie*, Universität Freiburg, Oktober 2007.

13 Deutsche Zusammenfassung und Ausblick

Die vorliegende Arbeit behandelt die *Analyse und Simulation von kristallinen Silizium-Solarzellen*.

Die rasante Entwicklung von neuartigen Solarzellenkonzepten erfordert eine genaue und zuverlässige Modellierung, um ein besseres physikalisches Verständnis der Solarzellen zu erlangen, sowie die Anzahl an zeitaufwendigen und teuren experimentellen Untersuchungen zu minimieren. Um einen groben Überblick über industriell relevante Silizium-Solarzellenkonzepte in der Produktion und deren Effizienzpotenzial zu erhalten, werden mehrere Solarzellenarchitekturen in der Einleitung vorgestellt. Die Verlustmechanismen dieser Solarzellenkonzepte werden quantifiziert, um deren hauptsächlich begrenzenden Rekombinationsverluste zu identifizieren, die letztendlich begrenzend auf die Effizienz wirken.

Der notwendige theoretische Hintergrund der Physik der Solarzellen und der methodische Ansatz zur Simulation von Solarzellen sind in den beiden folgenden Kapiteln vorgestellt und anhand von praktischen Beispielen untermauert.

Zugunsten eines besseren physikalischen Verständnisses von Silizium-Solarzellen ist eine fortwährende Verbesserung und Entwicklung von physikalischen Modellen und deren Parametrisierung unerlässlich. In dieser Arbeit erwies sich die exakte Modellierung hochdotierter Schichten als eine Schlüsselaufgabe. Somit wird der Einfluss der *freien Ladungsträgerabsorption* (FCA) im Detail diskutiert. Hierbei handelt es sich um eine parasitäre Form der Lichtabsorption, die in hochdotiertem Silizium signifikant die Anzahl an Photonen reduzieren kann, die potenziell zur Erzeugung von Elektron-Loch-Paaren zur Verfügung stehen. Die meisten bestehenden Parametrisierungen in der Literatur basieren auf Daten im mittleren Infrarotbereich, da FCA hier z.B. in optischen Charakterisierungsmethoden Anwendung findet. In der vorliegenden Arbeit werden diese existierenden Modelle im Wellenlängenbereich $\lambda = 1.0 - 2.0 \mu\text{m}$ ausgewertet, der den relevanten Bereich für Silizium-Solarzellen mit einschließt. Zu diesem Zweck wurden Proben mit unterschiedlichen Bor- und Phosphor-Diffusionsprofilen hergestellt, die ein breites Spektrum an Schichtwiderständen aufweisen. Die entsprechenden Reflexionskurven der Proben wurden gemessen. Numerische Bauelementsimulationen wurden an experimentellen Referenzproben kalibriert. Unter Berücksichtigung der verschiedenen in der Literatur gegebenen FCA-Parametrisierungen wurden die diffundierten Teststrukturen simuliert. Dabei konnten signifikante Unterschiede zwischen den Ergebnissen der FCA-Modelle beobachtet werden. Durch einen Vergleich zwischen simulierten Ergebnissen und

experimentellen Daten stellte sich heraus, dass die meisten Modelle den Effekt von FCA im untersuchten Wellenlängenbereich signifikant über- oder unterschätzen. Aus diesem Grund wurden im Rahmen dieser Arbeit neue Parameter für einen bestehenden, einfach in numerische Simulationen integrierbaren mathematischen Ansatz aufgestellt. Diese Parametrisierung hat den Gültigkeitsbereich $\lambda = 1.0 - 2.0 \mu\text{m}$ und erlaubt es, in künftigen Rechnungen die Genauigkeit der Quantifizierung der Photogenerationsverluste zu erhöhen. Auf Basis dieser Parametrisierung wurden durch FCA hervorgerufene Verluste der Photogenerationsstromdichte in phosphor- und bordotiertem Silizium zur Veranschaulichung exemplarisch dargestellt.

Stark Aluminium dotierte Schichten spielen in aktuell industriell hergestellten Solarzellen, aber insbesondere auch als Emitter in neuen n -Typ Solarzellen eine wichtige Rolle. Es wurde eine Methode zur genauen *Modellierung von stark Aluminium dotiertem p^+ Silizium ($\text{Al-}p^+$)* vorgestellt, da sich numerische Bauelementsimulationen solcher Regionen bisher als schwierig herausgestellt hatten. Eine kürzlich veröffentlichte Parametrierung der Minoritätsladungsträgerlebensdauer als Funktion der Aluminiumakzeptordichte N_A ergab nur bedingt eine Übereinstimmung mit experimentellen Daten, wie der Sättigungsstromdichte j_0 oder der Leerlaufspannung V_{oc} von Solarzellen, und erwies sich somit als weniger geeignet. Daher wurden die Auswirkungen verschiedener Rekombinationsverluste auf die Sättigungsstromdichten von $\text{Al-}p^+$ Regionen, wie insbesondere der Einfluss von Profilinghomogenitäten und unvollständiger Ionisierung von Aluminiumakzeptoren, sukzessive untersucht. Die Simulationsergebnisse sind in einem weiten Bereich durch experimentelle Daten validiert. Es zeigte sich, dass Defektrekombination in $\text{Al-}p^+$ Regionen den größten Verlustmechanismus darstellt. Der Einfluss von Profilinghomogenitäten wirkt sich primär bei dünnen $\text{Al-}p^+$ Profilen aus, kann aber in den meisten Fällen in Bauelementsimulationen vernachlässigt werden. Aluminiumakzeptoratome weisen im Vergleich zu anderen Akzeptoren, wie zum Beispiel Bor, eine deutlich höhere Ionisierungsenergie auf. Durch unvollständige Ionisierung ergibt sich eine signifikante Abnahme der elektrisch aktiven Aluminiumkonzentration und somit eine explizite Auswirkung auf die Rekombinationsstromdichte j_0 in der $\text{Al-}p^+$ Region. Unter Berücksichtigung dieses Effektes ergab sich eine ausgezeichnete Übereinstimmung von gemessenen und berechneten j_0 . Eine durchschnittliche Shockley-Read-Hall (SRH) Ladungsträgerlebensdauer in der $\text{Al-}p^+$ Region von $\tau_{\text{Al-}p^+} = 270 \text{ ns}$ konnte bestimmt werden. Durch die Implementierung des erarbeiteten Modells in eine Solarzellensimulation zeigen die modellierten Offenklemspannungen sehr gute Übereinstimmung zu gemessenen Werten. Daraus kann die Schlussfolgerung gezogen werden, dass für eine exakte

Simulation von stark Aluminium dotiertem Silizium SRH Defektrekombination in Kombination mit unvollständiger Ionisierung berücksichtigt werden müssen.

Unter der Verwendung dieses Modells wurde eine detaillierte Analyse zur Optimierung von n^+np^+ Silizium-Solarzellen mit Aluminium legiertem rückseitigen p^+ Emitter für industrielle Anwendungen durchgeführt. Mittels 2D und 3D Simulationen konnte das Potenzial und die begrenzenden Faktoren dieses Solarzellenkonzeptes identifiziert werden. Hierbei wurden die Einflüsse der Vorderseite, des Basismaterials und der Rückseite sequentiell betrachtet. Für n^+np^+ Solarzellen mit nicht-passiviertem vollflächigen Al- p^+ Emitter können unter realistischen Annahmen Wirkungsgrade von bis zu 20% erreicht werden. Darüber hinaus kann eine effektive Oberflächenpassivierung des Al- p^+ Emitters die Effizienz um ca. 1% absolut erhöhen, was zu einem Effizienzpotenzial für dieses Solarzellenkonzept nahe 21% führt. Aktuelle Arbeiten an diesem Zellkonzept konzentrieren sich auf die Herstellung von dünneren Solarzellen mit Dicken im Bereich $< 100 \mu\text{m}$ und Effizienzen $> 20\%$. Hier wird der Einsatz von diffraktiven Rückseitenstrukturen sehr interessant, da sie den Lichtweg innerhalb des Siliziums und somit die Absorptionswahrscheinlichkeit erhöhen.

Großflächige rückseitenpassivierte Solarzellen gehören zur Zeit zu den interessantesten Strukturen, die unmittelbar vor dem Übergang in die industrielle Produktion stehen. In lokal rückseitig passivierten p -Typ Silizium-Solarzellen wurden Effekte der lateralen Leitfähigkeit untersucht, die sich in 3D Strukturen ausbilden. In diesem Zusammenhang wurde der optimale Rückseitenkontaktabstand L_p für unterschiedliche Solarzellendicken und eine Vielzahl von nominalen Widerständen ρ_0 berechnet. Diese Variationen wurden für hochwertiges Floatzone (FZ) als auch für Czochralski (Cz) gezogenes p -Typ Siliziummaterial, letzteres mit einem sehr niedrigen und einem sehr hohen Gehalt an interstitiellem Sauerstoff, welcher sich nachteilig auf die effektive Ladungsträgerlebensdauer τ_{eff} auswirkt, durchgeführt. Ein charakteristisches Strom-dichte-Spannungs-Verhalten der betrachteten FZ und Cz Materialien für unterschiedliche Basisresistivitäten ρ_0 ($L_p = 1000 \mu\text{m}$) konnte über numerische 3D-Simulation beobachtet werden, die sich konsistent zu experimentell ermittelten Ergebnissen verhalten. Es stellte sich heraus, dass in hochohmigem Basismaterial mit großen Rückseitenkontaktabständen sowohl Hochinjektionseffekte als auch lokale Effekte im Basismaterial berücksichtigt werden müssen, um diese Volumenphänomene zu verstehen. Eine analytische Modellierung auf Basis eines umfassenden in der Literatur vorgestellten Modells zeigt eine gute Übereinstimmung mit der numerischen Modellierung unter Niederinjektionsbedingungen. Jenseits der Niederinjektions- in Richtung Hochinjektionsbedingungen, wie es z.B. in hochohmigem Basismaterial mit $\rho_0 > 2 \Omega\text{cm}$ der Fall ist, führen die analytischen Berechnungen zu steigenden

Abweichungen. Somit wurden Hochinjektionskorrekturen für die analytischen Berechnungen entwickelt, die zu einer verbesserten Vorhersage des optimalen Rückseitenkontaktabstandes L_p für höherohmiges Basismaterial führen. Dennoch sollten diese im analytischen Modell implementierten injektionsabhängigen Effekte in weiterführenden Arbeiten noch verbessert werden, da sie von großer Wichtigkeit für die Berechnung von Solarzellen mit stark injektionsabhängiger Rekombination sind. Hierzu zählen z.B. überkompensierte Materialien oder hochohmige Materialien mit hohen Ladungsträgerlebensdauern, wie sie in n -Typ Siliziummaterial vorkommen.

Als sehr zukunftsorientiertes Solarzellenkonzept wurden *bifaciale monokristalline Silizium-Solarzellen für Hochkonversionsanwendungen* über numerische Simulationen optimiert. Hochkonverter absorbieren zwei Photonen mit Energien $E < E_g$ kleiner als die Bandlückenenergie des Siliziums, und emittieren ein Photon mit $E > E_g$, welches von einer Silizium-Solarzelle absorbiert werden kann. Hierzu musste das Simulationsmodell erweitert werden, um die Quantenausbeute des Erbium basierten Hochkonvertermediums $\beta\text{-NaY}_{0.8}\text{Er}_{0.2}\text{F}_4$ berücksichtigen zu können, das auf der Rückseite der Solarzelle angebracht wird. Einseitig texturierte bifaciale Silizium-Solarzellen haben sich für Hochkonversionsanwendungen nur als bedingt geeignet erwiesen, da sie eine sehr hohe interne Rückseitenreflexion aufweisen und somit bei Photonenenergien $E < E_g$ zu wenig Licht transmittieren. Beidseitig texturierte und planare Solarzellen weisen hier wesentlich höhere Transmissionsgrade auf. Daher wurden die Antireflexbeschichtungen (ARC) für diese Solarzellenstrukturen numerisch optimiert. Für die Rückseite der Solarzellen hat sich eine einlagige ARC bestehend aus einer 120 nm dicken TiO_2 oder SiN_x Schicht als optimal herausgestellt, unabhängig von der Oberflächenmorphologie. Bei der Optimierung der vorderseitigen ARCs muss ein Kompromiss zwischen dem Erreichen eines hohen Wirkungsgrades der Solarzellen oder eines großen Hochkonversionseffektes gefunden werden. Geeignete Schichtsysteme sind zweilagige ARCs bestehend aus SiN_x oder TiO_2 für die erste abgechiedene Schicht, gefolgt von SiO_2 oder MgF_2 als eine zweite ARC. Basierend auf den Simulationen wurde eine Abschätzung der potenziell erreichbaren Effizienzsteigerung $\Delta\eta$ durch den verwendeten Hochkonverter vorgenommen. Zu diesem Zweck wurde eine bifaciale Solarzelle mit und ohne Hochkonverter simuliert. Abhängig von der Konzentration des extern einfallenden Lichtes auf die Solarzelle, sind realistische absolute Effizienzsteigerung in der Größenordnung von $\Delta\eta = 0.1\%$ bis 0.4% mit dem verwendeten Erbium basierten Hochkonvertermedium erreichbar. Basierend auf den Simulationen wurden planare bifaciale Silizium-Solarzellen hergestellt und charakterisiert. Ein durch die Hochkonversion hervorgerufener Stromgewinn konnte experimentell durch die Messung der externen Quanteneffizienz

(EQE) im Infraroten an verschiedenen Systemen aus Solarzelle und Hochkonverter bestätigt werden. Mit den im Rahmen dieser Arbeit hergestellten planaren Solarzellen konnten deutlich höhere EQE Werte im Vergleich zu bisherig durchgeführten Messungen mit dem gleichen Hochkonvertersystem an rückseitenkontaktierten rückseitig sammelnden Silizium-Solarzellen gemessen werden. In Bezug auf die verwendeten Beleuchtungsintensität markierten letztere Messungen die bisher höchsten in der Literatur vorkommenden EQE-Werte für ein System bestehend aus Silizium-Solarzelle und Hochkonverter. In weiterführenden Arbeiten sollten beidseitig texturierte bifaciale Silizium-Solarzellen mit den hier ermittelten optimalen ARC Systemen hergestellt werden. Diese weisen im Vergleich zu planaren Solarzellen ein deutlich höheres Effizienzpotenzial auf. Des Weiteren könnte durch effizientere Hochkonversionsmedien, die Gegenstand aktueller Forschung sind, die Effizienz noch signifikant gesteigert werden, um $\Delta\eta > 0.4\%$ zu erreichen.

Danksagung

An dieser Stelle möchte ich mich bei allen bedanken, die zum Gelingen dieser Arbeit beigetragen haben.

Mein besonderer Dank gilt:

Prof. Dr. Gerhard Willeke für die Übernahme der Betreuung dieses Promotionsvorhabens,

Prof. Dr. Thomas Dekorsy für die Übernahme des Zweitreferats,

Dr. Stefan W. Glunz für die Vergabe dieser Promotionsarbeit, viele konstruktive Impulse und seinen mitreißenden Enthusiasmus,

Dr. Martin Hermle für die sehr gute wissenschaftliche Betreuung und viele konstruktive Diskussionen,

Dr. Wilhelm Warta für fruchtbare Diskussionen und wertvolle Hinweise,

Judith Frank und **Tim Niewelt** für eine sehr gute und freundschaftliche Zusammenarbeit im Rahmen ihrer Diplomarbeiten,

meinen Bürokollegen **Bernhard Michl, Michael Rauer, Christian Schmiga, Martin Bivour, Dr. Jochen Hohl-Ebinger, Holger Seifert** und **Dr. Pauline Berger**, für viele fruchtbare Diskussionen und eine sehr angenehme Arbeitsatmosphäre,

Dr. Gergő Létay für seine stetige Hilfsbereitschaft und **Dr. Peter Fuß-Kailuweit, Johannes Greulich** und **Dr. Jonas Schön** für die konstruktive Zusammenarbeit im Rahmen der numerischen Solarzellensimulation,

Armin Richter, Dr. Christian Reichel, Dr. Jan Benick, Dr. Robert Woehl, Achim Kimmerle, Dr. Andreas Wolf, Bernd Steinhauser und **Sven Kluska** für fruchtbare Diskussionen, eine sehr gute Zusammenarbeit und hilfreiche Tipps bei technologischen Fragestellungen,

Dr. Martin Schubert für wertvolle Impulse und Zusammenarbeit im Bereich der Charakterisierung,

Dr. Marius Peters, Dr. Hubert Hauser und **Dominik Pelzer** für konstruktiven Austausch bei optischen Fragestellungen,

Dr. Jan Christoph Goldschmidt und **Stefan Fischer** für die sehr gute Zusammenarbeit im Rahmen der Arbeiten zur Hochkonversion,

Karola Rühle und **Dr. Pierre Saint-Cast** für eine fruchtbare Zusammenarbeit,

Dr. Philipp Löper für viele wertvolle physikalische Impulse und eine großartige Freundschaft,

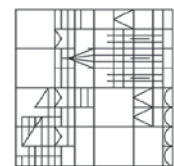
Heiko Steinkemper für Korrekturlesen

und allen Mitarbeitern der Bereiche **SEC**, **PTQ** und **MST** für die äußerst gute Zusammenarbeit und angenehme Arbeitsatmosphäre.

Mein ganz besonderer Dank gilt meiner Frau **Isabel Romero Espejo**, meinen Töchtern **Carla** und **Mila**, sowie meinen Eltern **Gertrud** und **Bernd Rüdiger**, die mir die Kraft und die Motivation für das Gelingen dieser Arbeit gegeben haben.

The rapid development of novel solar cell concepts requires an accurate and reliable modeling to obtain a better physical understanding of the solar cells, as well as to reduce the number of time consuming and expensive experimental investigations. In order to get a rough overview about industrially relevant crystalline silicon solar cell concepts in production and their efficiency potential an overview over different solar cell architectures is presented at the beginning of this work.

For a higher accuracy of the numerical simulations of crystalline silicon solar cells, the effect of free carrier absorption is discussed in detail. Also, an advanced method for precise modeling of highly aluminum-doped p^+ silicon is presented. By using this method, a detailed analysis on the optimization of n^+np^+ silicon solar cells with aluminum-alloyed rear p^+ emitter for industrial applications is shown. As a high-efficiency approach, lateral conductance effects of locally contacted rear surface passivated p -Si solar cells are investigated. Furthermore, as a future orientated solar cell concept, bifacial monocrystalline Si solar cells for upconversion applications have been optimized via numerical simulations.



Universität
Konstanz

ISBN 978-3-8396-0638-4

